Muon performance aspects and measurement of the inclusive ZZ production cross section through the four lepton final state with the ATLAS experiment at the LHC

Dissertation zur Erlangung des naturwissenschaftlichen Doktorgrades
der Bayerischen Julius-Maximilians-Universität Würzburg

vorgelegt von

Jochen Meyer

aus Würzburg

Dezember 2012
(Tag der Promotion: 17. April 2013)

1. Gutachter: Prof. Dr. Thomas Trefzger
2. Gutachter: Prof. Dr. Raimund Ströhmer

Lehrstuhl für Physik und ihre Didaktik
Physikalisches Institut
Julius-Maximilians-Universität Würzburg

Zusammenfassung

Der **L**arge **H**adron **C**ollider (LHC) ist der leistungsfähigste Teilchenbeschleuniger unserer Tage. Der Ringbeschleuniger erzeugt Teilchenkollisionen bei einer nie zuvor in einem Labor erreichten Schwerpunktenergie im Bereich von Teraelektronenvolt. Damit hat eine neue Ära in der Hochenergie-Teilchenphysik begonnen, in der eine der präzisesten Theorien der Physik, das Standardmodell der Teilchenphysik, bei diesen hohen Energien überprüft werden kann. Diesem Zweck dienen insbesondere die vier großen Experimente, “**A** **T**oroidal **L**HC **A**pparatu**S**” (ATLAS), “**C**ompact-**M**uon-**S**olenoid” (CMS), “**L**arge **H**adron **C**ollider **b**eauty” (LHCb) und “**A** **L**arge **I**on **C**ollider **E**xperiment” (ALICE), welche am LHC aufgebaut sind. Neben der Erkundung des Hochenergieverhaltens der etablierten Bestandteile des Standardmodells, ist es ein Hauptanliegen das in dem Modell enthaltene Higgs Boson zu finden, welches bei allen bisherigen Bemühungen nicht nachgewiesen werden konnte. Dem Boson kommt eine wichtige Rolle zu, denn es erlaubt eine Erklärung der Massen von Fermionen und von schweren, elektroschwachen Eichbosonen. Obgleich der Erfolg des Standardmodells in seiner Beschreibung der Natur unumstritten ist, gibt es Schwachpunkte aufgrund von Beobachtungen, die die Existenz bislang unentdeckter Teilchen und Wechselwirkungen andeuten. Aus diesem Grund werden zudem Suchen nach Physik jenseits des Standardmodells von den LHC Experimenten betrieben.

Um die ausgewiesenen Ziele zu erreichen, sind wesentliche Aspekte zum einen Präzisionsmessungen, um die Vorhersagen des Standardmodells eingehend zu testen, und zum anderen eine Auswertung aller mit den Detektoren zugänglichen Informationen, um Phänomene neuer Physik früh zu erkennen und Analysen daraufhin zu optimieren. Beide Herausforderungen gehen einher mit einem ausgezeichneten Verständnis der Detektoren. Einen unumgänglichen Beitrag dieses Wissen zu erlangen leistet eine realitätsgetreue Simulation, die teilweise neuer Techniken der Implementierung bedarf, um die komplexen Messanlagen zu beschreiben. Die hier präsentierte Forschungsarbeit wurde im Rahmen der ATLAS Kollaboration durchgeführt, wobei ein besonderer Schwerpunkt auf Messungen des Myon-Spektrometers liegt. Daher ist ein erstes zentrales Thema die Leistungsfähigkeit des Spektrometers hinsichtlich der von ihm identifizierten physikalischen Objekte, die Verträglichkeit aufgenommener Daten mit der existierenden Simulation sowie deren Verbesserung und schließlich die Erweiterung des Akzeptanzbereichs. Nachdem das exzellente Verhalten und Verständnis des Myon-Spektrometers demonstriert ist, befasst sich ein zweiter Teil mit einem physikalischen Anwendungsbereich gefundener Myonen.

Die elektroschwache Kraft ist Teil des Standardmodells und verursacht die Wechselwirkung der schweren, elektroschwachen Eichbosonen mit Fermionen sowie ihre Selbstwechselwirkung. In Proton-Proton Kollisionen werden solche Bosonen produziert, die jedoch sofort wieder in ein Fermionen-Paar zerfallen. Im Falle des Z Bosons, welches solch ein Eichboson ist, entstehen entgegengesetzt geladene oder neutrale Fermionen der selben Generation, darunter auch Myonen. Die verschiedenen Zerfallsmodi sind bereits an anderen Beschleunigern als dem LHC bestimmt worden. Die gleichzeitige Produktion zweier Z Bosonen wurde jedoch aufgrund des sehr kleinen Wirkungsquerschnittes weniger exakt an diesen Einrichtungen gemessen. Die entsprechenden, mit dem ATLAS Experiment gewonnenen Resultate, übersteigen alle vorherigen Messungen hinsichtlich ihrer Statistik und Genauigkeit. Wie sie aus beobachteten Ereignissen mit vier geladenen Leptonen gewonnen werden, ist in dieser Arbeit ausgeführt. Besonders betont wird die gesteigerte Signalaufnahme durch die Erweiterung des Akzeptanzbereichs des Myon-Spektrometers sowie alternative Methoden zur Abschätzung von Untergrundereignissen. Außerdem werden Auswirkungen auf die Erforschung von Kopplungen dreier Z Bosonen sowie Überschneidungen mit der Suche nach dem Higgs Boson des Standardmodells erläutert.

Abstract

The "**L**arge **H**adron **C**ollider" (LHC) is currently the most powerful particle accelerator. It provides particle collisions at a center of mass energy in the Tera-electronvolt range, which had never been reached in a laboratory before. Thereby a new era in high energy particle physics has began. Now it is possible to test one of the most precise theories in physics, the Standard Model of particle physics, at these high energies. The purpose is particularly served by four large experiments installed at the LHC, namely "**A** **T**oroidal **L**HC **A**pparatu**S**" (ATLAS), the "**C**ompact-**M**uon-**S**olenoid" (CMS), the "**L**arge **H**adron **C**ollider **b**eauty" (LHCb) and "**A** **L**arge **I**on **C**ollider **E**xperiment" (ALICE). Besides exploring the high energy behavior of the well-established portions of the Standard Model, one of the main objectives is to find the Higgs boson included in the model, but not discovered by any preceding effort. It is of tremendous importance since fermions and heavy electroweak gauge bosons acquire mass because of this boson. Although the success of the Standard Model in describing nature is already undisputed, there are some flaws due to observations inexplicable within this theory only. Therefore searches for physics beyond the Standard Model are promoted at the LHC experiments as well.

In order to achieve the defined goals, crucial aspects are firstly precise measurements, to verify Standard Model predictions in detail, and secondly an evaluation of as much information as accessible by the detectors, to recognize new phenomena as soon as possible for subsequent optimizations. Both challenges are only possible with a superior understanding of the detectors. An inevitable contribution to attain this knowledge is a realistic simulation, partially requiring new implementation techniques to describe the very complex instrumentation. The research presented here is performed under the patronage of the ATLAS collaboration with a special focus on measurements done with muon spectrometer. Thus a first central issue is the performance of the spectrometer in terms of physics objects that are recognized by the device, the compatibility of data and the existing simulation as well as its improvement and finally the extension of the acceptance region. Once the excellent behavior and comprehension of the muon spectrometer is demonstrated, a second part addresses one physics use case of reconstructed muons.

The electroweak force is part of the Standard Model and causes the interaction of heavy electroweak gauge bosons with fermions as well as their self-interaction. In proton-proton collisions such gauge bosons are produced. However, they decay immediately into a pair of fermions. In case of the Z boson, which is one of the gauge bosons, oppositely charged fermions of the same generation, including muons, emerge. The various decay modes are determined precisely at particle accelerators other than the LHC. However, the associated production of two Z bosons is measured less exactly at those facilities because of a very low cross section. The corresponding results acquired with the ATLAS experiment exceed all previous measurements in terms of statistics and accuracy. They are reported in this thesis as obtained from the observation of events with four charged leptons. The enhancement of the signal yield based on the extension of the muon spectrometer acceptance is especially emphasized as well as alternative methods to estimate background events. Furthermore, the impact on the probing of couplings of three Z bosons and intersection with the search for the Standard Model Higgs boson are pointed out.

Contents

Chapter 1

Introduction

The Standard Model of particle physics is one of the best-established theories in the history of physics. It was formulated in the $50s$ and $60s$ of the last century and tested since by various experimental setups. With time and the development of corresponding technologies it is checked from low energies up to the Tera-electronvolt scale. Although the theoretical predictions derived from the Standard Model give a good description of nature, there are several theoretical and experimental shortcomings. The most prominent one of today is the generation of fermion and heavy gauge boson masses induced by the Higgs mechanism, which predicts a particle with a mass of the order of 100 GeV or more, however, without former experimental confirmation. In addition phenomena like neutrino masses or dark matter are not explained by the Standard Model but observed by experiments. On the other hand there are strict predictions of some quantities in the electroweak sector of the theory for example which are not yet determined with the same accuracy.

To further explore the Standard Model, the "**L**arge **H**adron **C**ollider" (LHC) has provided proton-proton collisions at a center of mass energy of 7 TeV or 8 TeV, which had not yet been reached by any other particle accelerator. Therefore the mounted experiments are able to verify or discard theoretical predictions in an environment not accessible before in a laboratory. This thesis presents studies performed with "**A** **T**oroidal **L**HC **A**pparatu**S**" (ATLAS) as one of the experiments at the LHC. The ATLAS detector is a state of the art multi-purpose particle detector built to recognize, reconstruct and record final state particles produced in hard scattering processes. To accomplish this task it comprises a calorimetric system as well as various tracking devices and an elaborated software structure. Measurements with the dedicated muon spectrometer are one of the core themes of this work.

The thesis is structured as follows: Chapter 2 gives a theoretical introduction to the Standard Model with a special focus on the electroweak sector of the theory and the occurring heavy gauge bosons. The Higgs mechanism is explained in more detail and the experimental status without any results of the LHC is presented. In chapter 3 the accelerator facility is introduced and some physics implications of the high center of mass energies are reported. Some more details on the several components of the ATLAS detector and the subsequent data acquisition as well as processing are given, too.

The ATLAS software framework is expounded in chapter 4. It describes the simulation chain starting from theoretical input up to the corresponding predictions of detector output. Since the processing of actual data enters the same framework at some point, considerable information on the reconstruction of physical objects is given. Another focus is the software representation of the muon spectrometer. It is explained in chapter 4.2.1 and becomes a subject in chapter 5 dealing with the performance of the muon spectrometer.

The measurement of the muon inclusive spectrum and the estimation of the heavy flavor fraction is reported in section 5.1. The experimental technique is based on template fit functions which are applied on a well-chosen kinematic variable suitable to disentangle the various origins of the muon. Multiple scattering contributions to the muon momentum resolution are addressed in section 5.2. A data sample is constructed for comparison to simulation and occurring differences are pointed out. The final section 5.3 of this chapter provides studies regarding the quality and performance of muons reconstructed in a high pseudorapidity region. Those muons are used in the following to extend the acceptance of the spectrometer for physics measurements.

The main result reported in chapter 6 is the inclusive ZZ production cross section measured through the four charged lepton final state in proton-proton collisions at a center of mass energy of $\sqrt{s} = 7$ TeV. The event as well as the object selection and the analysis strategy are explicitly described. Explanations on the selection of muons with high pseudorapidity and the corresponding gain in signal yield are given. An alternative method to estimate background events is introduced to cross check the results received from the method used for the determination of the cross section. Finally section 6.7 includes further implications of the measurement like the testing for neutral triple gauge couplings of three Z bosons. Those couplings are predicted by the Standard Model with higher precision, namely to be zero on tree-level, than the current limits set by experiments. In addition, a comparison with the search for the Standard Model Higgs boson through the $H \to ZZ^{(*)} \to 4\ell$ channel is provided. This study is congeneric in terms of the event and object selection and aims to find the missing piece of the Standard Model which has not been discovered at previous accelerators. The thesis ends with a summary in chapter 7.

The appendices hold various supporting and auxiliary material on the different subjects. They are referred to at the appropriate parts in the text.

Chapter 2

Standard Model of particle physics

This chapter gives a short introduction to one of the most successful theories in physics, the "Standard Model of particle physics" (SM). Firstly, there is a basic explanation of the gauge symmetries used to build the model and the interactions arising. The focus is on the electroweak theory and its breakdown to the electromagnetic and weak interaction via the Higgs mechanism. The strong interaction is only mentioned as a side remark, though it is not less important. The fundamental particles and their properties, as well as the free parameters that are not fixed by the model, are introduced. The chapter finally ends with some examples of observations that give evidence for physics beyond the SM, since it is not possible to describe them in a convenient way in this theory, if at all.

2.1. Currents and gauge symmetries

A first approach is to look at the currents present in nature and the corresponding formalism in the SM. More than a century ago, charged weak currents were first observed by Antoine Becquerel and Marie and Pierre Curie with the discovery of radioactivity and the β decay as part of nuclear decay chains. In the $70s$ of the last century, there was also evidence for the neutral weak current claimed to be observed in the heavy liquid bubble chamber Gargamelle [1] at the proton synchrotron of the European organization for nuclear physics (CERN). Short time later, it was confirmed in the United States at the National Accelerator Laboratory [2], today known as Fermilab. Besides the weak currents, a neutral electromagnetic current acting for charged particles was measured, too. It was first observed by Patrick Blackett who recognized electron-positron pair production in a cloud chamber. To describe the currents in a mathematical way, there was a theory developed in parallel to the continuing experimental studies, which eventually should end up as the Standard Model of particle physics. In this theory the electromagnetic current is written as a vector current acting for both, the left handed and right handed fermions. The charged and neutral weak current is expressed by a vector-axialvector (V-A) current which only acts for left handed fermions like it is observed. To obtain these currents one has to start with the weak currents J_i^μ and the hypercharge current J_Y^μ. In their explicit form, they read

$$\begin{array}{ll} J_1^\mu & = \frac{1}{2}\left(\bar{\ell}_L\gamma^\mu\nu_L + \bar{\nu}_L\gamma^\mu\ell_L\right) \\ J_2^\mu & = \frac{i}{2}\left(\bar{\ell}_L\gamma^\mu\nu_L - \bar{\nu}_L\gamma^\mu\ell_L\right) \\ J_3^\mu & = \frac{1}{2}\left(\bar{\nu}_L\gamma^\mu\nu_L - \bar{\ell}_L\gamma^\mu\ell_L\right) \\ J_Y^\mu & = -\left(\bar{\nu}_L\gamma^\mu\nu_L + \bar{\ell}_L\gamma^\mu\ell_L + 2\bar{\ell}_R\gamma^\mu\ell_R\right) \end{array} \tag{2.1}$$

with the left (right) handed Dirac spinor $\ell_{L(R)}$ for a generic, charged lepton and ν_L for the neutrino. In general these spinors are vectors of four complex components with special transformation behavior and used to describe any kind of particle in any state. However, the observation of currents acting only for specific helicity states inspired a notation separating left and right handed particles. For high energies (e.g. $m \ll E$) the Dirac spinors are eigenstates of the γ_5 matrix and the left (right) handed components of the particles $\ell_{L(R)}$ and ν_L, identified with their helicity states, can be projected out by the operators $P_{L/R}$ comprising the γ_5 matrix. A more detailed description is in appendix A. In a next step the isospin T is introduced and the left and right handed components are sorted into multiplets depending on their isospin quantum number determined by the generators $\boldsymbol{T^i}$. The left handed components ℓ_L (with $T_3 = +1/2$) and ν_L (with $T_3 = -1/2$) are forming an isospin doublets L ($T = 1/2$) while the right handed one ℓ_R is an isospin singlets R ($T = 0$). To stay more conceptional, quarks and more complicated features like the flavor structure or right handed neutrinos, which could be introduced at this point, are skipped for the moment and the following explanations are restricted to the leptonic case only. The mentioned generators $\boldsymbol{T^i}$ of the weak currents and the generator $\boldsymbol{Y}$ of the hypercharge current satisfy the commutation relations

$$\begin{aligned} \left[\boldsymbol{T^i}, \boldsymbol{T^j}\right] &= i\epsilon^{ijk}\boldsymbol{T^k} \\ \left[\boldsymbol{T^i}, \boldsymbol{Y}\right] &= 0 \end{aligned} \tag{2.2}$$

which is the algebra of a $SU(2) \otimes U(1)$ group. The $SU(2)$ is matched to the weak current and therefore called $SU(2)_L$ while the $U(1)$ is related to the hypercharge and named $U(1)_Y$. The need for local gauge invariance, which is discussed later, gives rise to gauge fields connected to the generators:

$$\begin{aligned} SU(2)_L &\longrightarrow W_\mu^1,\ W_\mu^2,\ W_\mu^3 \\ U(1)_Y &\longrightarrow B_\mu \end{aligned} \tag{2.3}$$

Since all the basic fields are introduced, it is possible to write the free Lagrangian for the leptons and gauge fields respectively

$$\mathcal{L}^{\text{free}}_{\text{leptons}} = \bar{\mathsf{R}} i\partial\!\!\!/ \mathsf{R} + \bar{\mathsf{L}} i\partial\!\!\!/ \mathsf{L} = \bar{\ell} i\partial\!\!\!/ \ell + \bar{\nu} i\partial\!\!\!/ \nu \tag{2.4}$$

$$\mathcal{L}^{\text{free}}_{\text{gauge}} = -\tfrac{1}{4} W^i_{\mu\nu} W^{i\ \mu\nu} - \tfrac{1}{4} B_{\mu\nu} B^{\mu\nu} \tag{2.5}$$

where $W^i_{\mu\nu}$ denotes the strength tensor of the $SU(2)_L$ which is a common strength tensor of non-Abelian groups whereas $B^{\mu\nu}$ is the strength tensor of the Abelian group $U(1)_Y$. Up to this stage all fields are massless. For the gauge fields this is obvious, while for the leptons one could think about writing a mass term. However, such a mass term would mix left and right handed fields and therefore violate the gauge invariance of the theory. Because the gauge invariance should be guaranteed, it is not possible to introduce these mass terms.

The given Lagrangian does not respect local gauge invariance either, because transforming the lepton fields according to $\mathsf{L} \to \mathsf{L}' = U_{\mathsf{L}}\mathsf{L}$ and $\mathsf{R} \to \mathsf{R}' = U_{\mathsf{R}}\mathsf{R}$ with a unitary transformation $U_{\mathsf{L}(\mathsf{R})}$ would lead to additional terms. So, it is required to add terms which cancel contributions occurring due to gauge transformations. Technically this is done by constructing the so called covariant derivative, which is

$$\begin{aligned} \mathsf{L} &: \quad \partial_\mu + i\tfrac{g}{2}\tau^i W^i_\mu + i\tfrac{g'}{2} Y B_\mu \\ \mathsf{R} &: \quad \partial_\mu + i\tfrac{g'}{2} Y B_\mu \end{aligned} \tag{2.6}$$

where Y denotes the isospin quantum number and τ^i are the Pauli matrices. The covariant derivatives introduce the interaction of fermions and gauge fields via the minimal couplings g and g' of the two gauge groups $SU(2)_L$ and $U(1)_Y$ respectively. Due to the fact that right handed fields do not interact weakly the covariant derivative misses the term $i\frac{g}{2}\tau^i W^i_\mu$.

Since the section started with observed currents without any hint for gauge bosons, which are now implied by the gauge fields, it is reasonable to match the theoretical currents (2.1) introduced at the beginning to charged weak currents $J^\mu_\pm$ and the electromagnetic current J^μ_{em} which are measured directly and initially motivated the development of the theory. Indeed, the combination gives

$$\begin{aligned} J^\mu_\pm &= 2\left(J^\mu_1 \mp i J^\mu_2\right) \\ J^\mu_{\mathrm{em}} &= -\left(\bar{\ell}_L \gamma^\mu \ell_L + \bar{\ell}_R \gamma^\mu \ell_R\right) = J^\mu_3 + \tfrac{1}{2} J^\mu_Y \end{aligned} \tag{2.7}$$

The next step is to construct the physical gauge bosons predicted by the theory. The neutral hypercharge current J^μ_Y is untouched, but part of the set. With the combined generator $\boldsymbol{Q}$ of the electromagnetic current a relation between the quantum numbers Q and T_3 emerges in a natural way

$$Q = T_3 + \tfrac{1}{2} Y \tag{2.8}$$

which is known as Gell-Mann-Nishijima relation [3]. Using this equation and the electric charges $Q = 0, \pm 1$ of the corresponding particles, the hypercharge Y in equation (2.6) can be determined to be $Y_{\mathsf{L}_\ell} = -1$ and $Y_{\mathsf{R}_\ell} = -2$. To move towards the definition of the physical charged and neutral gauge bosons first of all one has to write down the Lagrangian accounting for the interaction of the fields which emerges from the covariant derivatives in equation (2.6). It reads

$$\mathcal{L}^{\mathrm{int}}_{\mathrm{leptons}} = \bar{\mathsf{L}} i \gamma^\mu \left(i \tfrac{g}{2} \tau^i W^i_\mu + i \tfrac{g'}{2} Y B_\mu\right) \mathsf{L} + \bar{\mathsf{R}} i \gamma^\mu \left(i \tfrac{g'}{2} Y B_\mu\right) \mathsf{R}\ . \tag{2.9}$$

Re-writing the charged snippet which includes only left handed fields in a slightly different manner one gets the expression

$$\mathcal{L}^{\mathrm{int},\ \mathsf{L}_{(\pm)}}_{\mathrm{leptons}} = -\tfrac{g}{2} \bar{\mathsf{L}} \gamma^\mu \begin{pmatrix} 0 & W^1_\mu - i W^2_\mu \\ W^1_\mu + i W^2_\mu & 0 \end{pmatrix} \mathsf{L} \tag{2.10}$$

which suggests to define the charged gauge bosons as

$$W^\pm_\mu = \tfrac{1}{\sqrt{2}} \left(W^1_\mu \mp i W^2_\mu\right)\ . \tag{2.11}$$

With this choice and the left handed doublet expanded, equation (2.10) becomes

$$\mathcal{L}^{\mathrm{int},\ \mathsf{L}_{(\pm)}}_{\mathrm{leptons}} = -\tfrac{g}{2\sqrt{2}} \left[\bar{\nu} \gamma^\mu (1 - \gamma_5) \ell W^+_\mu + \bar{\ell} \gamma^\mu (1 - \gamma_5) \nu W^-_\mu\right] \tag{2.12}$$

This reproduces exactly the (V-A) structure of the weak charged current. Calculating the amplitude of observed low energy phenomena like the muon decay [4] once within the Fermi theory [5] excluding the exchange of an intermediate vector boson and once including such a boson [6], one obtains the coupling of the weak currents depending on the mass of the intermediate boson (M_W) and the Fermi constant (G_F). The W boson was observed for the first time by the UA1 [7] and UA2 [8] experiments at the super proton synchrotron at CERN. Modern and very precise measurements of the Fermi constant G_F are performed at the Paul Scherrer Institute by the determination of the muon life time [9]. Relating these results with the results derived above which depend on the couplings g and g' one ends up with

$$\tfrac{g}{2\sqrt{2}} = \left(\tfrac{M_W^2\ G_F}{\sqrt{2}}\right)^{1/2}\ . \tag{2.13}$$

In contrast to the part of the interaction Lagrangian which is charged the neutral piece contains both left and right handed fermions and reads

$$\begin{aligned}\mathcal{L}^{\text{int, }(\mathsf{L}+\mathsf{R})_{(0)}}_{\text{leptons}} &= -g\bar{\mathsf{L}}\left(\gamma^\mu \tfrac{\tau^3}{2}\right)\mathsf{L}W^3_\mu - \tfrac{g'}{2}\left(\bar{\mathsf{L}}\gamma^\mu Y\mathsf{L} + \bar{\mathsf{R}}\gamma^\mu Y\mathsf{R}\right)B_\mu \\ &= -gJ^\mu_3 W^3_\mu - \tfrac{g'}{2}J^\mu_Y B_\mu\ .\end{aligned} \tag{2.14}$$

Obviously this expression is related to the electromagnetic current J^{em}_μ given in equation (2.7). One way to get the correct combination of the fields W^3_μ and B_μ to couple to the current is transcribing them in terms of new fields A and Z following a common rotation given by

$$\begin{pmatrix} A_\mu \\ Z_\mu \end{pmatrix} = \begin{pmatrix} \cos\theta_W & \sin\theta_W \\ -\sin\theta_W & \cos\theta_W \end{pmatrix} \begin{pmatrix} B_\mu \\ W^3_\mu \end{pmatrix} \tag{2.15}$$

with the Weinberg angle θ_W [10]. The trigonometric functions can be related to the gauge groups $SU_L(2)$ and $U_Y(1)$ and written as

$$\sin\theta_W = \tfrac{g'}{\sqrt{g^2+g'^2}} \qquad \text{and} \qquad \cos\theta_W = \tfrac{g}{\sqrt{g^2+g'^2}}\ . \tag{2.16}$$

Inserting the new fields and the Weinberg angle in the neutral interaction Lagrangian given in equation (2.14) it is possible to identify separately the part coupling to the electromagnetic field A_μ which is the photon and to the field Z_μ which is the Z boson

$$\begin{aligned}\mathcal{L}^{\text{int, }(\mathsf{L}+\mathsf{R})_0}_{\text{leptons}} = \ & -g\sin\theta_W\left(\bar{\ell}\gamma^\mu\ell\right)A_\mu \\ & -\tfrac{g}{2\cos\theta_W}\textstyle\sum_{\psi_i=\nu,\ell}\bar{\psi}_i\gamma^\mu\left(g^i_V - g^i_A\gamma_5\right)\psi_i Z_\mu\end{aligned} \tag{2.17}$$

Therefore the electromagnetic charge e can be expressed in terms of the Weinberg angle and gauge couplings according to the relation $e = g\sin\theta_W = g'\cos\theta_W$. First direct experimental evidence for the Z boson was also found by UA1 [11] and UA2 [12] experiments. The second line of equation (2.17) describes the neutral weak interaction. The corresponding observation is mentioned at the beginning of the section, and the SM makes a specific prediction for the vector (V) and axialvector (A) couplings of fermions to the Z boson:

$$g^i_V = T^i_3 - 2Q_i\sin^2\theta_W \qquad \text{and} \qquad g^i_A = T^i_3 \tag{2.18}$$

These quantities were extensively studied by the ALEPH, DELPHI, L3 and OPAL experiments which were installed at the Large Electron-Positron Collider at CERN [13]. This particle accelerator provided, amongst others, collision at a center of mass energy at the Z mass pole and it was possible to determine many important properties of the Z boson. They are combined with previous as well as subsequent measurement and summarized by the Particle Data Group [14]. For example the branching fractions of the Z boson into a pair of leptons is found to be approximately 3.4% while the branching fraction to hadrons is $\sim$ 70% and the not visible fraction is $\sim$ 20%.

Though this explanation seems already to give a rather complete picture of the electroweak theory, some aspects have been left out. Since in the given Lagrangians only flavor eigenstates occur there was no need to introduce flavor mixing. The common convention how to treat them is to choose the mixing matrix of the three lepton generations as the identity matrix and shift the mixing to the neutrino sector. This is possible because in the calculation of amplitudes only products of the mixing matrix of the neutrino sector times the one in the lepton sector occur.

For this reason one matrix can be chosen arbitrarily while the other one is fixed by the choice. The so called Pontecorvo-Maki-Nakagawa-Sakata (PMNS) matrix [15] describes the mixing of the neutrino flavors in case of massive neutrinos. Of course such a description would no longer be valid if neutral flavor changing currents were observed. Though an additional factor, the so called majorana phase, would still be possible like it is in charged weak currents, too.

Apart from leptons, neutrinos and the gauge bosons, the SM contains one more type of particles, the quarks. These fermions are $T_3 = \pm\frac{1}{2}$ fields and appear in three generations like the leptons. Roughly speaking, the down-type quarks correspond to charged leptons and up-type quarks to neutrinos, though right handed up-type quarks exist as well. The correspondence is especially true for the description of the flavor mixing, since for up-type quarks the mixing matrix is chosen to be unity while the Cabibbo-Kobayashi-Maskawa (CKM) matrix [16] is a full matrix present in the down-type quark sector. Regarding the electromagnetic charge quarks differ from leptons: up-type quarks carry a charge of $+\frac{2}{3}$ and down-type quarks are charged $-\frac{1}{3}$. This implies different hypercharges as well, which can be obtained by the Gell-Mann-Nishijima equation (2.8).

Apart from their electroweak behavior quarks are strongly interacting because they carry, besides the electric charge, a color charge. The strong force can be embedded in a gauge theory which is described by a unbroken $SU(3)$ symmetry group. Eight gauge bosons, the so called gluons, are introduced in this context and couple to the quarks. These bosons are colored and massless particles. One feature of the strong theory is color confinement [17], which is based on the fact that only color neutral particles are observed. Therefore quarks never appear as single particles in nature but only in hadrons which are bounded states, also known as SM resonances. If it is a two particle state composed of a quark and anti-quark it is called a meson, while baryons are three quark resonances.

type	spin	charge	symbol(s)	name(s)	interaction
charged lepton	$\pm\frac{1}{2}$	±1	e, μ, τ	electron, muon, tau lepton	electroweak
neutral lepton	$\pm\frac{1}{2}$	0	ν_e, ν_μ, ν_τ	electron/muon/tau neutrino	electroweak
charged electroweak gauge bosons	±1	±1	W	W boson	electroweak
neutral electroweak gauge bosons	±1	0	Z, γ	Z boson, photon	electroweak
up-type quarks	$\pm\frac{1}{2}$	$\pm\frac{2}{3}$	u, c, t	up/charm/top quark	electroweak strong
down-type quarks	$\pm\frac{1}{2}$	$\mp\frac{1}{3}$	d, s, b	down/strange/bottom quark	electroweak strong
strong gauge bosons	±1	0	g	gluon	strong

Table 2.1.: The well-established particle content of the Standard Model of particle physics.

The picture of the weak and strong theory summarized in the SM and presented in this section is quite complete. All well-established particles of the Standard Model are introduced and once more listed in table 2.1. The experimental observation of the gauge bosons is mentioned and their interaction with the remaining particles is pointed out in a theoretical description. Although it is not mentioned directly, the electromagnetic coupling $\alpha = \frac{e^2}{2\pi}$ was introduced via the electric charge and the couplings g as well as g'. Respectively the coupling of the strong force α_s was established parenthetically. Also mentioned are the three mixing angles of the lepton and quark sector and the possibility of a phase which can occur in each sector separately. All particles are massless up to this stage and no explanation of the mechanism was given which breaks the $SU(2)_L \times U(1)_Y$ down to the $U(1)_{\text{em}}$. This important part of the SM is addressed in the next section.

2.2. Higgs mechanism

The SM contains symmetries like isospin or strangeness which are known to be imperfect. The observation of heavy gauge bosons and therefore non-exact symmetries motivates a breakdown of the already-discussed gauge symmetries, since in general each non-broken symmetry leads to a conservation law. Two ways to perform symmetry breaking are to add a term to the Lagrangian that contributes very little to the overall results, but breaks the symmetry or to break the symmetry spontaneously, i.e. the Lagrangian remains invariant while the ground state does not. The second option is understood to be more natural, since no justification is needed for adding a term by hand and all required features emerge due to the presence of a new field or particle. Applying the Goldstone theorem [18] of spontaneous symmetry breaking on the SM is not convenient since for each broken generator a massless Goldstone boson would occur. Nature however shows the existence of a massless boson in combination with a heavy neutral and charged bosons, which implies a more sophisticated breakdown of $SU(2)_L \times U(1)_Y \to U(1)_{\text{em}}$ also accounting for the short range character of the electroweak interaction relying on massive intermediate particles. The one massless boson is the photon and related to the final $U(1)_{\text{em}}$ respected by the broken Lagrangian. Therefore the remaining part of the section will give a short theoretical sketch of the Higgs mechanism [19] that achieves the needed, massive gauge bosons.

First of all two complex fields ϕ^+ and ϕ^0 have to be introduced. They constitute a $T_3 = \pm 1/2$ scalar doublet of the form

$$\Phi \equiv \begin{pmatrix} \phi^+ \\ \phi^0 \end{pmatrix} \tag{2.19}$$

with hypercharge $Y = 1$ according to equation (2.8). The Lagrangian for this field reads

$$\mathcal{L}_{\text{scalar}} = \partial_\mu \Phi^\dagger \partial^\mu \Phi - V(\Phi^\dagger \Phi) \tag{2.20}$$

and consists of a free part which is the first term and an additional potential. In order to end up with the required preferences and a re-normalizable theory the potential has to be chosen as

$$V(\Phi^\dagger \Phi) = \mu^2 \Phi^\dagger \Phi + \lambda \left(\Phi^\dagger \Phi\right)^2 \tag{2.21}$$

with the a priori free parameters μ^2 and λ. In the case of $\mu^2 > 0$ the vacuum ground state is $\phi_0^0 = 0$ and for small oscillations the Lagrangian shows that both scalar fields acquire the mass $m^2 = \mu^2 > 0$. Therefore it is not possible to break the symmetry spontaneously in this way. However for $\mu^2 < 0$ it is possible. The potential in this case looks like that shown in figure 2.1.

The complete Lagrangian is symmetric under $SO(2)$ and has a continuum of distinct vacua, which are located at

$$\left\langle \left|\phi_0^0\right|^2 \right\rangle = \tfrac{-\mu^2}{2\lambda} \equiv \tfrac{v^2}{2} \tag{2.22}$$

where $v = \sqrt{-\frac{\mu^2}{\lambda}}$ is the vacuum expectation value. Within this setup the symmetry can be broken spontaneously by choosing a particular vacuum out of the continuum. One typical choice is

$$\langle \Phi \rangle_0 = \begin{pmatrix} 0 \\ v/\sqrt{2} \end{pmatrix} . \tag{2.23}$$

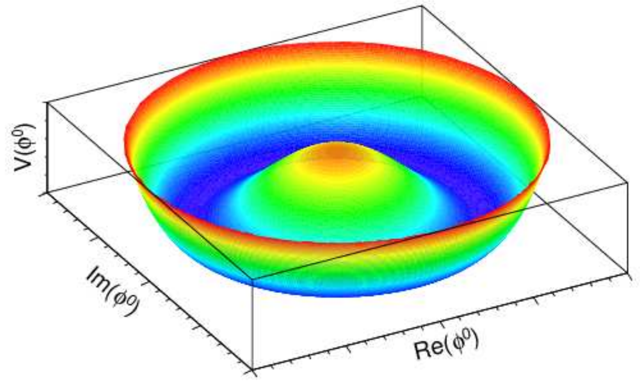

Figure 2.1.: Illustration of the potential $V(\Phi^\dagger\Phi)$.

After the breakdown the remaining symmetry is the $U(1)_{\mathrm{em}}$ which has to be respected by the Lagrangian and the vacuum. In addition the generator $\boldsymbol{Q}$ has to annihilate the vacuum. The special choice fulfills both requirements:

$$\begin{aligned} e^{i\alpha Q}\langle \Phi \rangle_0 &\simeq (1 + i\alpha Q)\langle \Phi \rangle_0 = \langle \Phi \rangle_0 \\ Q\langle \Phi \rangle_0 &= \left(T_3 + \tfrac{1}{2}Y\right)\langle \Phi \rangle_0 = 0 \end{aligned} \tag{2.24}$$

In order to show in a simple way how the heavy gauge bosons acquire their masses due to the broken generators $\boldsymbol{T_1}$, $\boldsymbol{T_2}$ and $(\boldsymbol{T_3} - \boldsymbol{Y}/2) = 2\boldsymbol{T_3} - \boldsymbol{Q}$ it is reasonable to parametrize the Higgs doublet (2.19) differently. A new field H is introduced and an expansion for small perturbations is done

$$\Phi \equiv \exp\left(i\frac{\tau^i}{2}\frac{\chi_i}{v}\right)\begin{pmatrix} 0 \\ (v + H/\sqrt{2}) \end{pmatrix} \simeq \langle \Phi \rangle_0 + \frac{1}{2\sqrt{2}}\begin{pmatrix} \chi_2 + i\chi_1 \\ 2H - i\chi_3 \end{pmatrix} = \frac{1}{\sqrt{2}}\begin{pmatrix} i\sqrt{2}\omega^+ \\ v + H - iz^0 \end{pmatrix} \tag{2.25}$$

where χ_i are general real parameters and τ^i are the Pauli matrices. The newly defined fields $\omega^\pm$ and z^0 are the scalar and pseudoscalar Goldstone bosons respectively. Performing a $SU(2)_L$ gauge transformation with $\alpha_i = \chi_i/v$, which is called the unitary gauge, the field becomes

$$\Phi \to \Phi' = \exp\left(-i\frac{\tau^i}{2}\frac{\chi_i}{v}\right)\Phi = \frac{(v + H)}{\sqrt{2}}\begin{pmatrix} 0 \\ 1 \end{pmatrix} . \tag{2.26}$$

Inserting this result into the general Lagrangian (2.20) in combination with the covariant derivative (2.6) to make it invariant under $SU(2)_L \otimes U(1)_Y$ leads to

$$\begin{aligned}\mathcal{L}_{\text{scalar}} =& \left|\left(\partial_\mu + ig\frac{\tau^i}{2}W^i_\mu + i\frac{g'}{2}YB_\mu\right)\frac{(v+H)}{\sqrt{2}}\begin{pmatrix}0\\1\end{pmatrix}\right|^2 - \mu^2\frac{(v+H)^2}{2} - \lambda\frac{(v+H)^4}{4} \\ =& \frac{1}{2}\partial_\mu H\partial^\mu H + \frac{g^2}{4}(v+H)^2\left(W^+_\mu W^{-\mu} + \frac{1}{2\cos^2\theta_W}Z_\mu Z^\mu\right) \\ & - \mu^2\frac{(v+H)^2}{2} - \lambda\frac{(v+H)^4}{4}\ .\end{aligned} \tag{2.27}$$

The second line is the result in terms of physical fields $W^\pm$ and Z^0. The Goldstone bosons $\omega^\pm$ and z^0 have vanished, and their degrees of freedom are absorbed in the longitudinal amplitudes of the gauge bosons. Interaction terms of the Higgs field and the gauge fields can be identified and have the pattern $yH^2\psi_\mu\psi^\mu$ or $y'H\psi_\mu\psi^\mu$, where $y^{(')}$ indicates the coupling and ψ is the gauge field. Terms which are quadratic in v are the mass terms of the gauge fields:

$$\begin{aligned}\tfrac{g^2v^2}{4}W^+_\mu W^{-\mu} + \tfrac{g^2v^2}{8\cos^2\theta_W}Z_\mu Z^\mu =& \ M_W^2 W^+_\mu W^{-\mu} + \tfrac{1}{2}M_Z^2 Z_\mu Z^\mu \\ =& \ M_W^2 W^+_\mu W^{-\mu} + \tfrac{M_W^2}{2\cos^2\theta_W}Z_\mu Z^\mu\end{aligned} \tag{2.28}$$

Obviously there is no term including A_μ. This means there is neither a leading order interaction of the photon with the Higgs field nor a photon mass. Because the $U(1)_{\text{em}}$ remains unbroken, this behavior is expected. The connection between the mass of the $W^\pm$ boson and the vacuum expectation value of the Higgs field and the low energy phenomena introduced via equation (2.13) allow an estimate of the vacuum expectation value:

$$v = \left(\sqrt{2}G_F\right)^{1/2} \simeq 246\ \text{GeV} \tag{2.29}$$

Once the vacuum expectation value of the Higgs is known, the next step is to calculate the gauge bosons' masses. The only quantities missing are the Weinberg angle θ_W, the electric charge e and the coupling constant α. The SM does not predict them, but they can be measured independently as $\sin^2\theta_W = 0.23146(12)$[14] and $\alpha \approx 1/137$ [20] like it is explained in the previous section. So the masses can be determined to be:

$$\begin{aligned}M_W^2 \ &= \tfrac{e^2v^2}{4\sin^2\theta_W} = \tfrac{\pi\alpha v^2}{\sin^2\theta_W} \simeq \left(\tfrac{37.3}{\sin\theta_W}\ \text{GeV}\right)^2 \sim (78\ \text{GeV})^2 \\ M_Z^2 \ &\simeq \left(\tfrac{37.3}{\sin\theta_W\cos\theta_W}\ \text{GeV}\right)^2 \sim (88\ \text{GeV})^2\end{aligned} \tag{2.30}$$

The agreement with the measured masses, $M_W = 80.385(15)$ GeV and $M_Z = 91.1876(21)$ GeV, is very good [14]. In equation (2.28) the remaining terms apart from mass and interaction terms of the gauge bosons and the Higgs boson are self interaction terms of the Higgs and a mass term

$$M_H = \sqrt{-2\mu^2}\ . \tag{2.31}$$

In spite of the good agreement of measurements with the SM including electroweak symmetry breaking via the Higgs mechanism and therefore the prediction of a Higgs particle, the value of μ^2 and in consequence the Higgs mass are not fixed by the theory itself. Since all other particles of the SM are well-established and measured with good precision the Higgs boson is the last missing piece to complete the picture. Later on there will be some more words on this and the experimental attempts for searches.

As a closing remark for this section it should be stressed that leptons can acquire their mass due to the Higgs boson as well. As pointed out in the previous section, pure lepton mass terms are forbidden because they break the gauge invariance. To solve this issue a direct interaction of the leptons and the Higgs is introduced with a strength called Yukawa coupling Y_ℓ. The corresponding Lagrangian reads

$$\begin{aligned}
\mathcal{L}_{\text{yuk}}^{\text{leptons}} &= -Y_\ell \left[\bar{\mathsf{R}}\left(\Phi^\dagger \mathsf{L}\right) + \left(\bar{\mathsf{L}}\Phi\right)\mathsf{R}\right] \\
&= -Y_\ell \frac{(v+H)}{\sqrt{2}} \left[\bar{\ell}_R \,(0\ 1) \begin{pmatrix} \nu_L \\ \ell_L \end{pmatrix} + \left(\bar{\nu}_L\ \bar{\ell}_L\right) \begin{pmatrix} 0 \\ 1 \end{pmatrix} \ell_R\right] \\
&= -\frac{Y_\ell v}{\sqrt{2}} \bar{\ell}\ell - \frac{Y_\ell}{\sqrt{2}} \bar{\ell}\ell H
\end{aligned} \tag{2.32}$$

Hence the generated lepton mass is $M_\ell = \frac{Y_\ell v}{\sqrt{2}}$ but is not fixed by the theory because there is no prediction for the value of the Yukawa coupling. The same is true for the quark sector. The same mechanism may be used to generate the quark masses, but again they are not fixed by the SM intrinsically.

2.3. Complete Standard Model

To get a complete although only schematic picture of the SM Lagrangian $\mathcal{L}_{\text{SM}}$ this section summarizes all previous explanations, and missing parts are added. The full formula is given in terms of physical gauge fields, and accordingly fermions are represented in their flavor eigenstates. For a basic understanding of possible interactions in scattering processes the actual terms of the Lagrangian which link the different fields are rather more important than their coefficients, which reflect the coupling strength. Therefore these constants are left out but the corresponding terms are marked with a box. Some of the missing couplings, which are crucial for this work can already be found in the previous sections.

The first five lines of the following expressions contain the free Lagrangian of the gauge fields $\mathcal{L}_{\text{gauge}}^{\text{free}}$ (2.5) and the Lagrangian of the Higgs field $\mathcal{L}_{\text{scalar}}$ (2.28) plus some self coupling terms not yet presented. Lines six and seven show the free leptonic Lagrangian $\mathcal{L}_{\text{leptons}}^{\text{free}}$ (2.4), the interaction Lagrangians $\mathcal{L}_{\text{leptons}}^{\text{int},\ \mathsf{L}_{(\pm)}}$ (2.12) and $\mathcal{L}_{\text{leptons}}^{\text{int},\ (\mathsf{L}+\mathsf{R})_0}$ (2.17) as well as the Yukawa terms for leptons $\mathcal{L}_{\text{yuk}}^{\ell}$. The remaining terms correspond to the quarks and their interactions including the strong force and its exchange particles, the gluons.

$$\begin{aligned}
\mathcal{L}_{\text{SM}} = \; & -\tfrac{1}{4} F_{\mu\nu} F^{\mu\nu} - \tfrac{1}{2} W_{\mu\nu}^{+} W^{-\ \mu\nu} + M_W^2 W_\mu^{+} W^{-\ \mu} \\
& -\tfrac{1}{4} Z_{\mu\nu} Z^{\mu\nu} + M_Z^2 Z_\mu Z^\mu + \tfrac{1}{2}\partial_\mu H \partial^\mu H - \tfrac{1}{2} M_H^2 H^2 \\
& + \boxed{W^+W^-A} + \boxed{W^+W^-Z} + \boxed{W^+W^-H} + \boxed{ZZH} + \boxed{HHH} \\
& + \boxed{W^+W^-AA} + \boxed{W^+W^-ZZ} + \boxed{W^+W^-AZ} + \boxed{W^+W^-W^+W^-} \\
& + \boxed{W^+W^-HH} + \boxed{ZZHH} + \boxed{HHHH} \\
& + \textstyle\sum_{\ell=e,\mu,\tau} \bar{\ell}\,(i\partial\!\!\!/ - M_\ell)\,\ell + \sum_{\nu_\ell=\nu_e,\nu_\mu,\nu_\tau} \bar{\nu}_\ell\,(i\partial\!\!\!/)\,\nu_\ell \\
& + \boxed{\bar{\ell}\ell A} + \boxed{\bar{\nu}_\ell \ell W^+} + \boxed{\bar{\ell}\nu_\ell W^-} + \boxed{\bar{\ell}\ell Z} + \boxed{\bar{\nu}_\ell \nu_\ell Z} + \boxed{\bar{\ell}\ell H} \\
& + \textstyle\sum_{\ell=q,\ldots,t} \bar{q}\,(i\partial\!\!\!/ - M_q)\,q - \tfrac{1}{4}\sum_{\alpha=1,\ldots,8} G_{\mu\nu}^{\alpha} G_{\alpha}^{\mu\nu} \\
& + \boxed{\bar{q}qA} + \boxed{\bar{u}dW^+} + \boxed{\bar{d}uW^-} + \boxed{\bar{q}qZ} + \boxed{\bar{q}qH} \\
& + \boxed{\bar{q}qg} + \boxed{ggg} + \boxed{gggg} \\
= \; & \mathcal{L}_{\text{gauge}} + \mathcal{L}_{\text{scalar}} + \mathcal{L}_{\text{leptons}}^{\text{free}} + \mathcal{L}_{\text{leptons}}^{\text{int}} + \mathcal{L}_{\text{yuk}}^{\ell} + \mathcal{L}_{\text{quarks}} + \mathcal{L}_{\text{yuk}}^{q} + \mathcal{L}_{\text{gluons}}
\end{aligned} \tag{2.33}$$

In theoretical particle physics scattering amplitudes may be calculated by the scattering matrix (S-Matrix) method [21]. Terms derived from the Lagrangian are inserted and integrations of the phase space are done. Although only the initial state and final state particles are known, higher order effects have to be take into account as well. Higher order in this context means that terms including greater powers of the occurring coupling constants are respected. A clever way to calculate amplitudes is to use Feynman diagrams [22]. In this representation particles and interactions are assigned to symbols that can be combined according to dedicated algebraic rules. Because this subject is not strongly related to the remaining work the reader is referred to textbooks like [23] to learn more about theoretical particle physics and the methods of calculating scattering processes.

The free parameters that enter in the SM Lagrangian $\mathcal{L}_{\mathrm{SM}}$ are the 12 fermion masses m_ℓ, m_ν, m_{u} and m_{d}, accompanied by the 6 mixing angles contained in the PMNS matrix for leptons and the CKM matrix for quarks plus, the two phases which can come along with the mixing or the Yukawa couplings of the fermions to the Higgs boson. Not fixed as well are the strong, weak and electromagnetic coupling constants. With the mass of the Z and the Higgs boson the number of free parameters adds up to be 25, though it should be stressed that the Weinberg angle θ_W and the W mass can only be precisely predicted with a fixed top quark and Higgs mass.

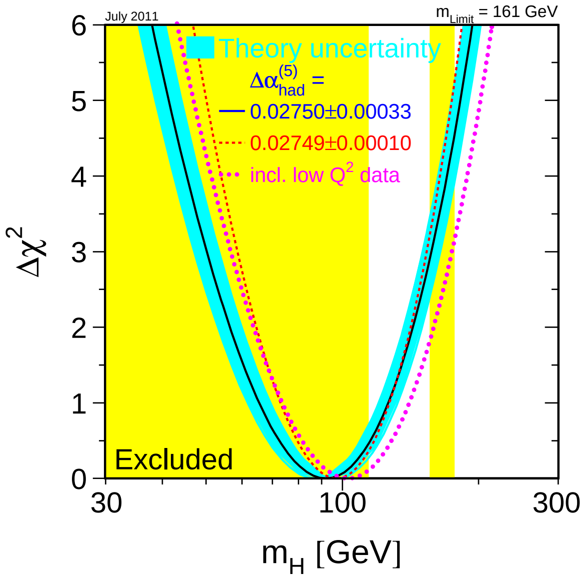

Figure 2.2.: The $\Delta\chi^2 = \chi^2 - \chi^2_{\mathrm{min}}$ of the Higgs mass as function of m_H [24]. For the line all hard scattering data with high momentum transfer obtained at the Standford Linear Collider, LEP and the Tevatron are used. Results of the LHC are not considered. An estimate for uncertainties due to missing higher order calculations is represented by the blue band. The yellow area denotes the 95% confidence level exclusion limit on m_H from direct searches. The dashed curves originate from calculations including another value of $\Delta\alpha^{(5)}_{\mathrm{had}}(m_Z^2)$ and measurements with low momentum transfer.

Therefore, one of the major topics of interest in theoretical as well as experimental particle physics is to prove that there is a Higgs boson and to measure its preferences. In figure 2.2 it is shown that there are quite good limits on the Higgs mass without taking into account any measurements of the experiments mounted to the Large Hadron Collider. In section 6.7.3 evidence for its existence is reported. Due to its mass and couplings the Higgs decays right after its production. The only chance to get knowledge about it is via its decay products. In figure 2.3 the branching ratios for the different decay channels calculated up to next to leading order are shown in dependence of the Higgs mass. However, the Higgs production is suppressed by several orders of magnitud compared to the production of other physics objects. The details are shown in figure 3.2 later on.

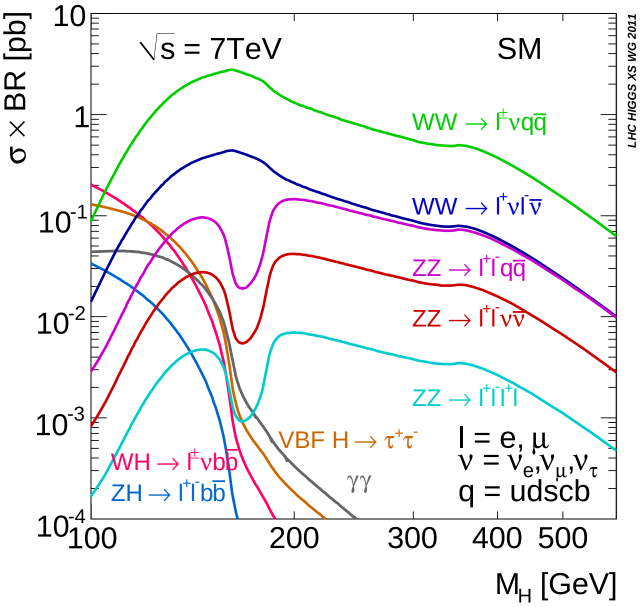

Figure 2.3.: Product of the SM Higgs boson production cross section times the decay branching ratios in proton-proton collisions at $\sqrt{s} = 7$ TeV as a function of the Higgs-boson mass [25]. In the channels of $H \rightarrow \tau^+\tau^-$, $\gamma\gamma$ or WW/ZZ ($\rightarrow$ 4 fermions) all production modes are summed while in the $H \rightarrow b\bar{b}$ channel only the vector-boson associated production is considered.

2.4. Possible extensions of the Standard Model

Although the SM is in very good agreement with current observations, it cannot be the full story. Since the 1990s measurements of solar and atmospheric neutrino rates show that flavor mixing should take place and the PMNS matrix was established. However such a mixing implies that neutrinos are not massless but massive particles. In order to explain those masses in the SM, an extension in this sector is needed. One of the most minimalistic explanations is to introduce right handed neutrinos which give mass to the left handed ones via the so called Seesaw mechanism [26]. But as yet there is no evidence for these additional particles. Astrophysical observations like rotation curves of galaxies, gravitational lensing and the cosmic microwave background [27] give indications for the existence of only very weakly interacting particles, the so called dark matter. The SM does also not provide a candidate particle which could explain these observations.

Apart from these two deficits the SM is also not without blemish from the theoretical point of view. Firstly the gauge couplings do not unify at high energies as one might want in order to have as few free parameters as possible. This kind of physics is described in so called Grand unified theories (GUTs) [28]. Besides this rather academic issue, there is a more crucial one linked to the Higgs mechanism called the hierarchy problem. Considering the unification of forces at a high energy scale [29] $m_{\mathrm{GUT}} \approx \mathcal{O}(10^{16}\ \mathrm{GeV})$ and a theory valid up to this scale, the higher-order quantum corrections to the Higgs mass are given by

$$\Delta m_H^2 = m_W^2 \mathcal{O}\left(\frac{m_{\mathrm{GUT}}^2}{m_W^2}\right) \quad . \tag{2.34}$$

With the Higgs vacuum expectation value given in equation (2.29) and the resulting W boson mass, it is required to perform a fine tuning over 26 orders of magnitude to predict a Higgs mass at the electroweak scale. Such a precise tweaking of parameters usually is avoided by any means because it is understood to be unnatural.

To explain these features or to avoid the occurring problems in the SM, new particles and additional interactions are introduced. The masses of the new particles are sufficiently big or their production cross section is small enough that limits derived from measurements are not violated. If there are new couplings introduced they are in most cases very small, so that besides a precise calculation, the measurement has to be very exact to detect the new physics. Promising extension of the SM nowadays are for example supersymmetry or extra dimensions. For these two examples the set of free parameters includes combinations that can be tested at current particle accelerators like the Large Hadron Collider introduced in the next chapter.

Chapter 3

Research facility and experimental setup

On 29 September 1954 the treaty for the organization of the Conseil Européen pour la Recherche Nucláire (CERN) was ratified by 12 countries of in those days Western Europe [30]. It has become one of the worldwide largest organization for basic and applied research and now contains countries from outside Europe as well. The related facility is located on the border of France and Switzerland close to Geneva. Beside several smaller experimental setups, it hosts a particle accelerator complex with four major experiments attached. In the first part this chapter gives a short introduction to the accelerator installations and the motivation of their construction. The purposes and main features of the mounted particle detectors are briefly present in the second part, while there is a special focus on the ATLAS experiment in the third section.

3.1. Large Hadron Collider (LHC)

The LHC machine [31, 32] is a state of the art particle collider using an accelerator technology based on superconducting magnets. In total the installation involves approximately 1200 dipole magnets that are designed to produce a maximal magnetic field of 8.3 T to force the particles on a circle. In addition to that, several more complex magnets like quadrupoles provide fields to continuously focus the beams. The acceleration itself is done by electric fields generated by radio frequent systems. Before entering the LHC ring the particles are pre-accelerated up to 450 GeV, merged to bunches and stored. This takes places in the injector chain [32] composed of the linear accelerator Linac2, the Proton Synchrotron Booster (PSB), the Proton Synchrotron (PS) and finally the Super Proton Synchrotron (SPS) as it is shown in figure 3.1.
The infrastructure located at CERN already existed and was used before by the Large Electron-Positron Collider (LEP). The main tunnel has a perimeter of 27 km and is placed approximately 100 m underground. The initial design of LHC has foreseen to deliver proton collisions with a center of mass energy of 14 TeV and an instantaneous luminosity of $L_{\text{design}} = 10^{34}$ cm^{-2} s^{-1} with this quantity defined as [34]

$$L = \frac{N_b^2 n_b f_{\text{rev}} \gamma_r}{4\pi \epsilon_n \beta^*} F(\theta_c, \sigma_z, \sigma^*) \approx \frac{N_b^2 n_b f_{\text{rev}}}{A} \tag{3.1}$$

where the number of particles per bunch N_b, the number of bunches per beam n_b, the revolution frequency f_{rev}, the relativistic gamma factor γ_r, the normalized transverse beam emittance ϵ_n and the beta function at the collision point β^* determine its value. The factor F is called geometric luminosity reduction factor and accounts for a proper treatment of the full crossing angle θ_c at the interaction point (IP) while also the root mean square (RMS) of the bunch length σ_z and the transverse RMS of the beam size σ^* enter. In most cases though the given approximation depending on the cross section area A is good enough.

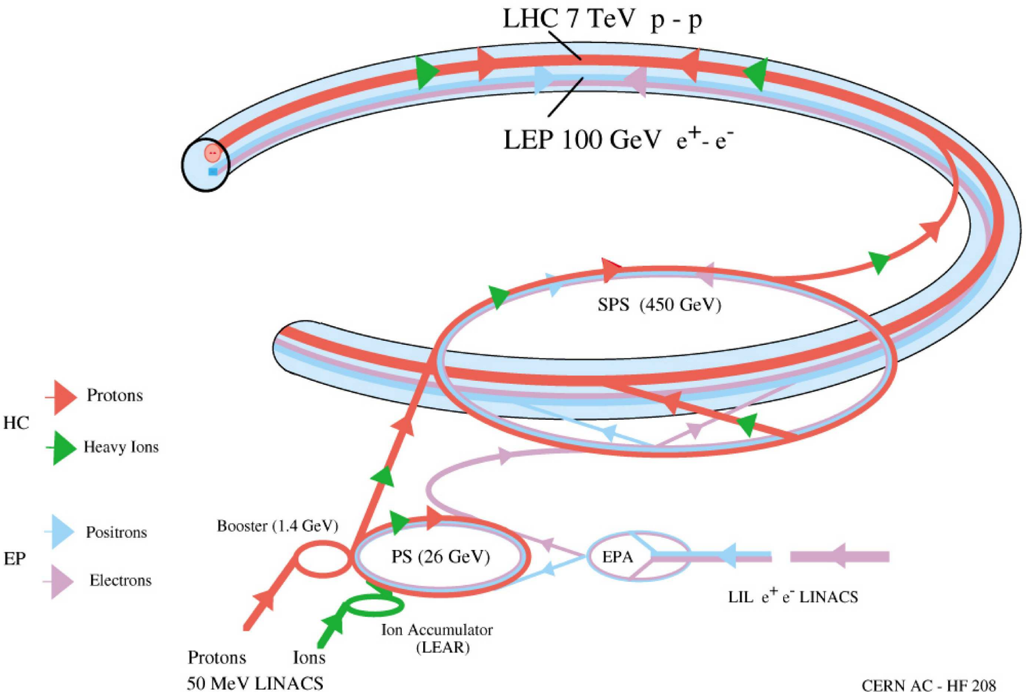

Figure 3.1.: The LHC and preceding injector complex [33].

To reach the design instantaneous luminosity at a revolution frequency of 11.2 kHz, there have to be 2808 bunches of 1.15×10^{11} protons squeezed to transverse a dimension of 16 µm. Due to some technical problems right after the start of the LHC in 2008 and a following maintenance phase, the design goals were not achieved for the first periods of data taking. In 2011 the machine was operating at a center of mass energy of 7 TeV with a maximum of 2100 bunches. The number of protons per bunch was increased up to 1.45×10^{11} while most of the time it was at nominal. The bunch spacing time in 2011 was chosen to be 75, 50 or 25 ns while most data was aquired in the 50 ns mode. The highest instantaneous luminosity attained in 2011 was 3.65×10^{33} cm^{-2} s^{-1} and 7.73×10^{33} cm^{-2} s^{-1} [35] in 2012. Both beat the previous world record of 4.31×10^{32} cm^{-2} s^{-1} [36] hold by the Tevatron which is a proton-anti-proton collider operating at 1.96 TeV center of mass energy. It is placed at the Fermi National Accelerator Laboratory in Illinois, USA. Despite the technical issues and the deviation of the initial design benchmark points from the ones attained, the LHC exceeded the Tevatron performance rather soon so that it ceased operation in 2011. Up to the closure the two installed experiments D0 and CDF collected an integrated luminosity of approximately 10 fb^{-1} each.

The data recorded by the LHC experiments in 2011, in one year of operation, improved or at least confirmed the results of Tevatron in a wide field. The explanation can be derived from figure 3.2 which shows the production rates of various physics objects. Due to the increase of the center of mass energy, the same number of interesting objects is produced with less integrated luminosity due to higher cross sections. The increase of rates also induced the CERN management to run LHC in 2012 with a center of mass energy of 8 TeV, and there will be another step to higher energies in the future.

An example related to chapter 6 is given in figure 3.3. While in 6.4 fb^{-1} and 1.9 fb^{-1} of Tevatron data 10 and 3 events had been identified by D0 [38] and CDF [39] as candidates of a pair of Z bosons decaying into electrons or muons, the ATLAS experiment found 66 of such candidate

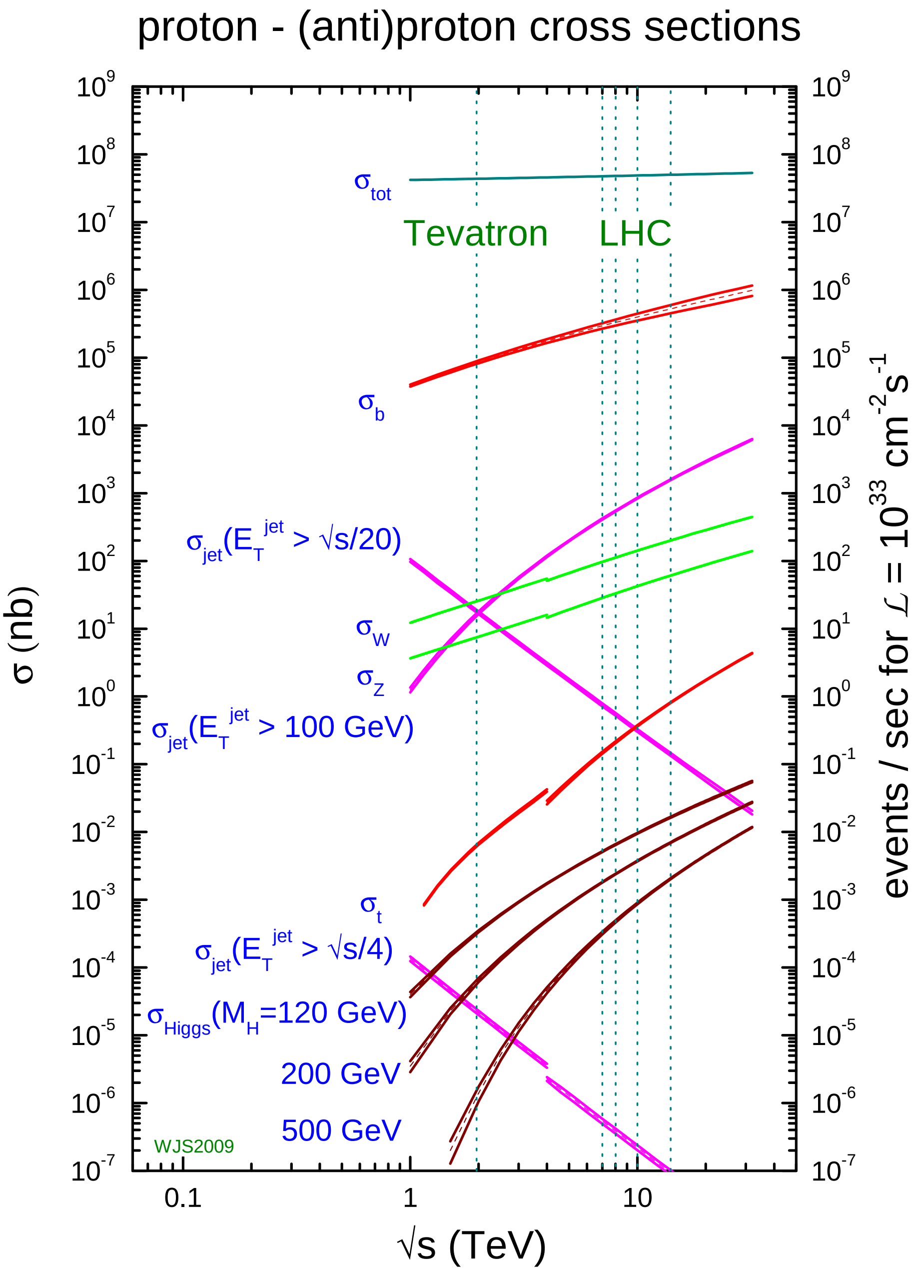

Figure 3.2.: The production cross section and the event rate for an instantaneous luminosity of $L = 10^{33}$ cm^{-2} s^{-1} for various objects of interest [37]. In violet the inclusive jet production cross sections are given for jets with an transverse energy E_T^{jet} above 5% of the center of mass energy, above 100 GeV and above 25% of the center of mass energy. The inclusive top quark and bottom quark production rates are indicated by the red bands while the green bands represent the gauge boson production rates. For a Higgs mass of $m_H = 120$, 200 and 500 GeV the brown bands give the production cross sections. The very top band indicates the total rate for all Standard Model processes summed up. At about 3 TeV the initial scattering process is changed from proton-antiproton to proton-proton collisions. Therefore a discontinuity appears in some of the bands. The horizontal lines are placed at 1.96 TeV what is the center of mass energy of the Tevatron. As well lines at 7, and 8 TeV are drawn which are the operating points for the LHC in 2011 and 2012 respectively. The line at 10 TeV indicates a possible scenario before the design value of 14 TeV is reached which is indicated by the line on the most right.

events in 4.6 fb^{-1} of data collected during 2011 [40] and 85 events in 5.8 fb^{-1} recorded in the first months of 2012 [41]. With CMS there are 54 of such candidate events found in 5.0 fb^{-1} recorded during 2011 data taking [42] and 71 candidate events in the first 5.26 fb^{-1} recorded during 2012 [43]. Of course, not only the rates of new and interesting objects are enhanced, but also those of objects already studied by previous experiments like those mentioned in chapter 2. Today such objects and processes are considered as background, but nevertheless it is important to understand and estimate them in an appropriate way. In addition circumstances like an increased number of interactions per bunch crossing, called pile up, become an important issue at LHC. In sections 5.3.5 and 6.5 these two topics are studied in more detail.

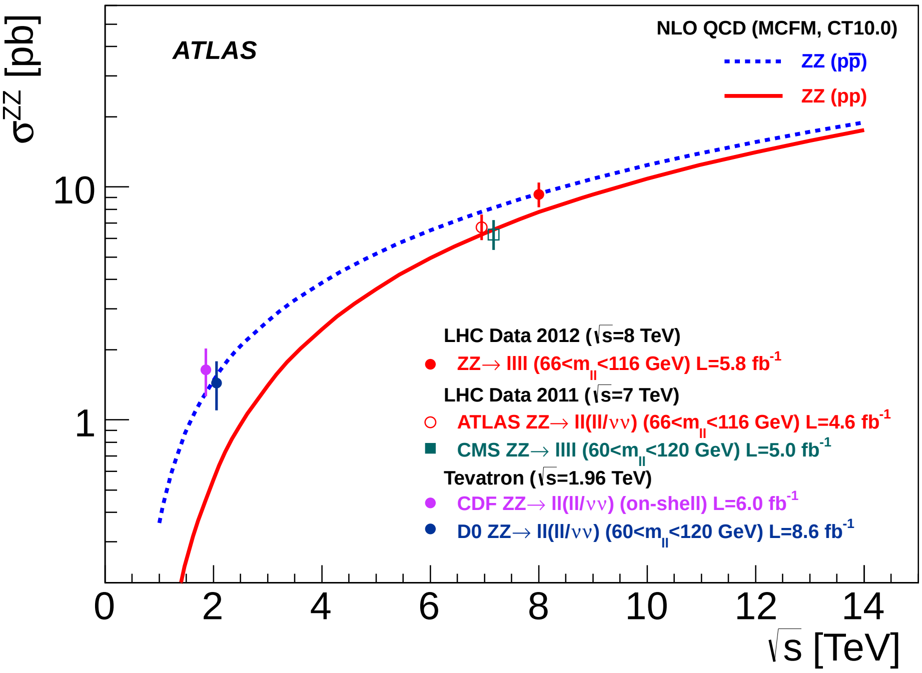

Figure 3.3.: The predicted inclusive Z boson pair production cross section as a function of the center of mass energy in proton-proton collisions (full line) and proton-antiproton collision (dashed line). The measurements at Tevatron and LHC based on the subsequent leptonic decay of both Z bosons are superimposed [40]. The result from the CMS experiment for $\sqrt{s} = 8$ TeV is $\sigma(pp \rightarrow ZZ) = 8.4 \pm 1.0(\text{stat.}) \pm 0.7(\text{sys.}) \pm 0.4(\text{lumi.})$ pb [43] and missing in the plot.

Due to the higher beam energy the kinematic structure of the proton has changed at LHC compared to Tevatron, i.e. there is a larger fraction of gluons accessible. In consequence heavy particles are more often produced via gluons in the initial state than it was the case for Tevatron. Therefore it is important for physics analysis to take into account these additional initial states accurately if comparisons with theoretical predictions are performed. The enhancement of the production involving a quark and an anti-quark, though, remained moderate, mainly because the colliding particles at LHC are protons while Tevatron was a proton-anti-proton collider. Figure 3.4 summarizes the explained effect and correlates the parton luminosity with the mass M_x of a produced particle. The derived functions are obtained by using a convenient set of parton distribution functions valid for the center of mass energies of interest.

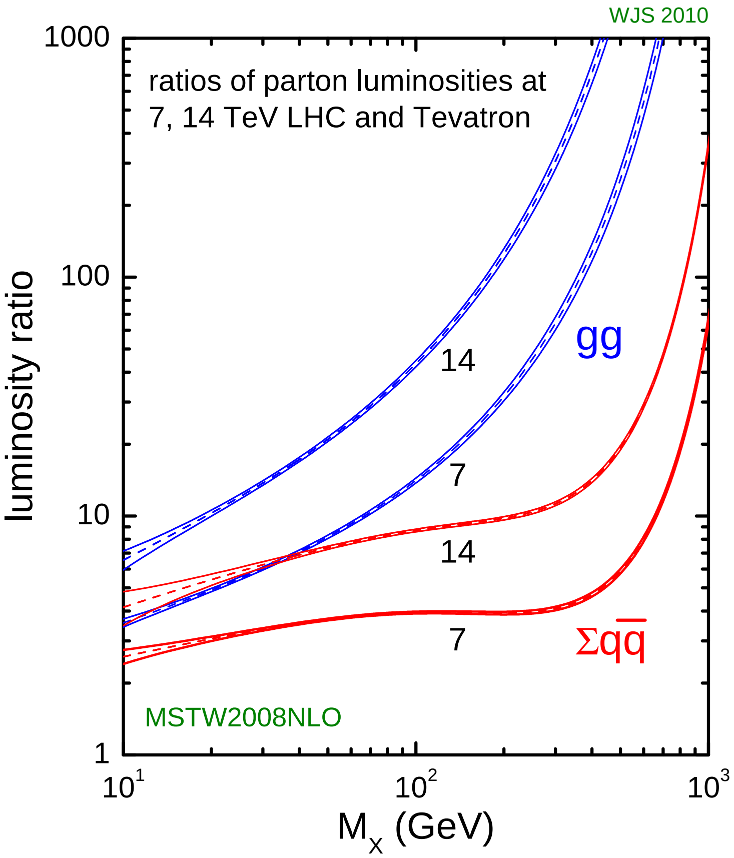

Figure 3.4.: The ratio of LHC to Tevatron parton luminosity for 7 and 14 TeV as function of the mass of a produced particle M_x [37].

3.2. LHC experiments

The four main experiments located at the LHC accelerator are called "**L**arge **H**adron **C**ollider **b**eauty" (LHCb), "**A** **L**arge **I**on **C**ollider **E**xperiment" (ALICE), "**C**ompact **M**uon **S**olenoid" (CMS) and "**A** **T**oroidal **L**HC **A**pparatu**S**" (ATLAS). LHCb [44] does not cover the full spacial angle around the interaction point, but is a forward detector. It contains a dedicated vertex detector to reconstruct precisely the vertex of the hard scattering process and additional secondary vertices originating from decays of particles produced in the collision. The physics this experiment primarily aims at is related to charge conjugation and parity (CP) violation in the B-hadron sector. The ALICE experiment [45] focuses on more special physics as well, namely measurements of the quark-gluon plasma like the one present right after the Big Bang. Therefore special runs of the LHC are performed for which the beams do not comprise protons but lead nuclei. The center of mass energy of the heavy ion collisions is 2.76 TeV per nucleon pair in 2011. The main challenge for such measurements is the very high number of particles in the final state caused by the numerous parton-parton interaction happening during a bunch crossing.
Also ATLAS [46] and CMS [47] record data from heavy ion collisions, though the large majority of data collected by these two experiments originates from proton-proton collisions. Both detectors are general multi-purpose detectors which cover close to the complete solid angle around the interaction point. The basic structure is the same for both: They possess a tracking system, which is the detector closest to the the beampipe. After that the calorimeters follow, while the

outer most detector is the muon spectrometer. The physics program for both experiments is very wide, including searches for the last missing part of the Standard Model, the Higgs Boson, as well as for physics beyond the Standard Model. For example there are dedicated search programs for heavy gauge bosons, Supersymmetry and extra dimensions. Nevertheless, the known portions of the Standard Model itself are also precisely investigated by the two experiments, starting with the rediscovery at center of mass energies never explored before at a collider. Figure 3.5 summarizes for example the cross sections for electroweak gauge boson production and top quark production as expected for the Standard Model and the corresponding measurement with the ATLAS detector. The measurement of the Z boson pair production, as part of this figure will be presented in more detail in chapter 6.

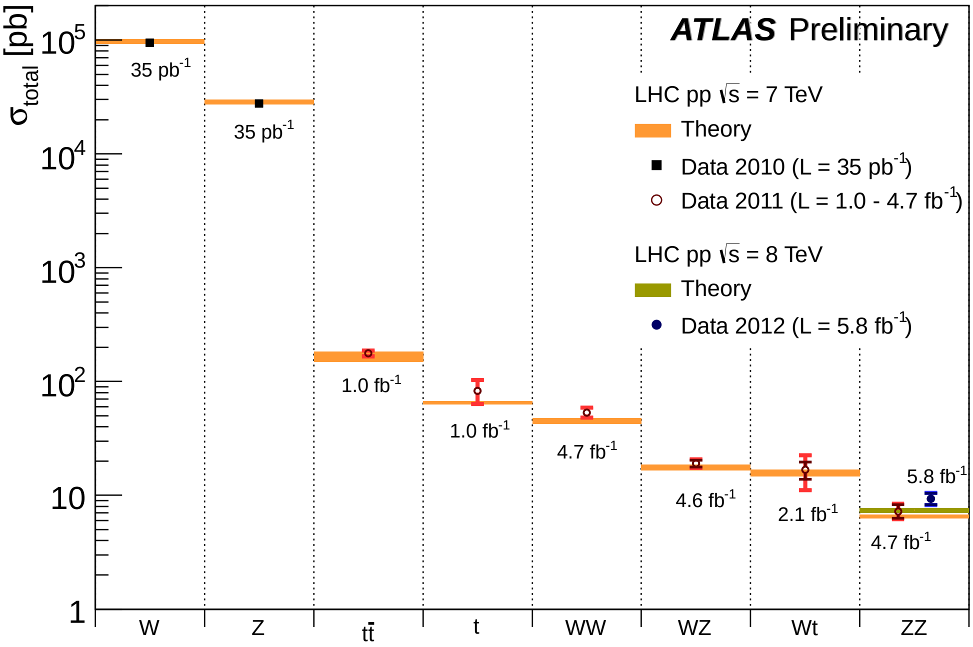

Figure 3.5.: Summary of several Standard Model total production cross sections predicted by theory. The corresponding measurements performed by the ATLAS experiment are superimposed [48].

3.3. A Toroidal LHC Apparatus (ATLAS)

The ATLAS detector [46], located at point 1 of the LHC, comprises various subsystems built to detect particles emerging from the scattering process at the interaction point. Particles that are unstable and therefore do not reach the detectors are commonly reconstructed via their decay products. The subdetectors are sensitive to different properties of a particle and are installed like an onion skin to achieve a unique identification over the covered solid angle. The inner most layer is a tracking system responding in general to all kind of charged particles. It is followed by an electromagnetic calorimeter which especially absorbs electrons and photons. The next layer is the hadronic calorimeter sensitive to strongly interacting particles. Minimal ionizing particles like muons are able to escape all these detectors, but create tracks in the muon spectrometer which is the outer most instrumentation. For a momentum measurement, the inner detector and muon spectrometer are embedded in magnetic fields. Particles which are only weakly interacting, like neutrinos, or not interacting at all, like those predicted by theories beyond the Standard Model, can be reconstructed by missing momentum. An overview image of the ATLAS experiment is given in figure 3.6.

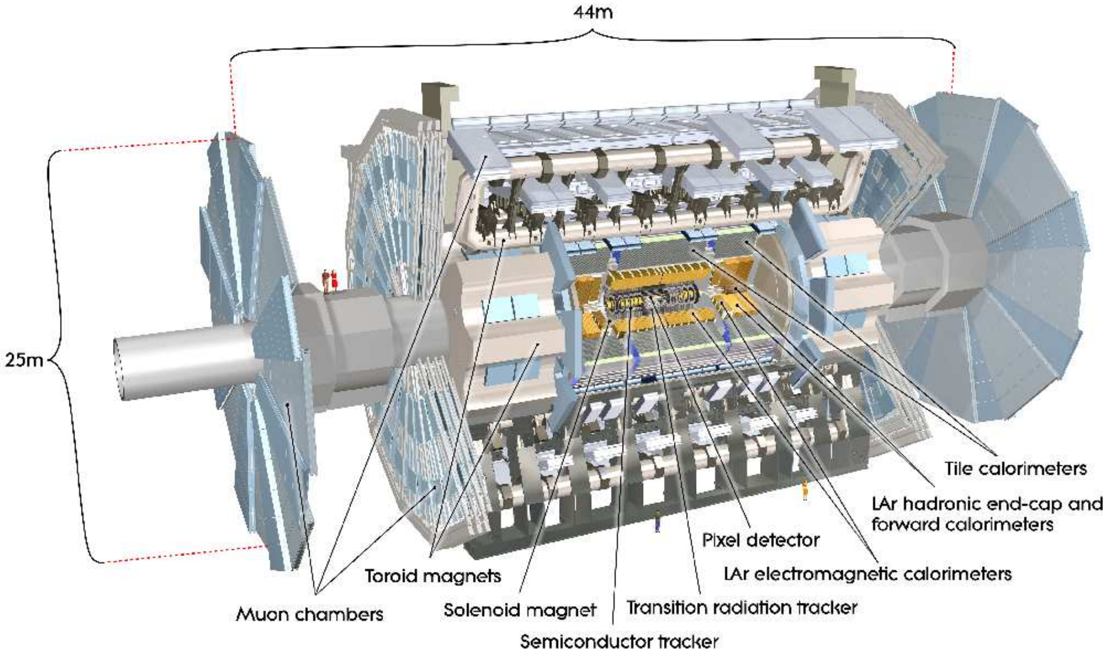

Figure 3.6.: An overview illustration of the ATLAS experiment [49].

The more central part of the detector, known as barrel, follows a cylindric geometry with the beampipe as rotation axis. Called end-caps and formed like discs with the beampipe in the center are those parts closing the barrel on its ends. For orientation, there is a right handed Cartesian coordinate system defined, with the origin in the middle of the detector which is the interaction point. The positive x-axis points to the center of the LHC ring while the positive y-axis points towards the earth's surface. The z-axis is defined accordingly and follows the beam lines. A-side denotes the side of the detector with positive values for z while the opposite side is called C-side.

In most cases though it is more convenient to use spherical instead of Cartesian coordinates. The ϕ-angle turns clockwise around the z-axis and starts at $y = 0$ and x positive. In complete ϕ measures 2π while the second angle, named θ, measures up to π in polar angle. It turns anti-clockwise around the x-axis and starts at $y = 0$ and z positive. The probability of the sum of momenta in z direction to be zero is negligible for hadron colliders since the hadron momentum is statistically distributed on the actually colliding partons. Therefore the produced particles are boosted in z direction, and it is reasonable to not use the angle θ, but a parametrization called pseudorapidity. It is defined as

$$\eta = -\ln\left[\tan\left(\frac{\theta}{2}\right)\right] = \frac{1}{2}\ln\left(\frac{|\vec{p}|+p_z}{|\vec{p}|-p_z}\right) \tag{3.2}$$

where $\vec{p}$ is the momentum of the particle and p_z is the longitudinal momentum which is here along the z-axis. The pseudorapidity is the zero mass approximation, i.e. for $E \approx |\vec{p}|$, of the rapidity which reads

$$y = \frac{1}{2} \ln \left(\frac{E + p_z}{E - p_z} \right) . \tag{3.3}$$

In high energy physics this approximation holds in most cases. In comparison to the angle θ, the advantage is that differences in this quantity are invariant under Lorentz boost along the z-axis. In this context another commonly used quantity is the spacial distance ΔR, which is given by

$$\Delta R = \sqrt{(\eta_i - \eta_j)^2 + (\phi_i - \phi_j)^2} = \sqrt{(\Delta\eta)^2 + (\Delta\phi)^2} \tag{3.4}$$

where $\eta_{i/j}$ and $\phi_{i/j}$ are the coordinates of two space points i and j. Since the momentum along the z-axis is unknown for the initial state, it is not possible to extract the full momentum of the system after the scattering. Although the approximation of negligible momenta of the incoming partons in the transversal plane, i.e. in the XY-plane, is very good. Therefore the transverse momenta of all final state particles should sum up to zero, which makes the individual transverse momentum p_{T} of a particle an important quantity in hadron collider physics. In consequence the previously mentioned missing momentum can only be measured as missing transverse energy $E_{\mathrm{T}}^{\mathrm{miss}}$.

3.3.1. Inner detector

The silicon pixel tracker, silicon strip tracker (SCT) and transition radiation tracker (TRT) make up the ATLAS inner detector [50]. All instruments are sensitive to charged particles which deposit a small fraction of energy. In the nominal acceptance region more than 40 of those deposits, called hits, are created by a typical charged particle and combined into a track by the subsequently applied reconstruction software. The inner detector is embedded in a solenoid magnetic field of 2 T. The field lines are along the z-axis and therefore charged particles are bent in the transversal plane. The curvature of the reconstructed track is used to determine the momentum of the particle.

The pixel detector and SCT use the same principle to detect charged particles. They are made out of doped semiconductors with a high bias voltage. A traversing charged particle creates electrons and holes which are separated by the applied voltage and collected by a cathode on the surface of the silicon. While there is a point-like cathode mounted to a pixel, which regularly is 50 µm long and 400 µm wide, the cathode is strip-like for a SCT, with the dimensions 80 µm × 12 cm. In order to suppress fake hits caused by noise of the electronics, there is a comparison of the analog signal to the threshold. The eventually recorded quantity is the time over threshold, which is longer for hits produced by actual particles than for noise. In fact, it is possible that neighboring pixels register a signal over threshold as well. For such cases the reconstruction software groups the signals into clusters and treats them as a single hit. The hit efficiency for both kind of detectors is above 99% within their geometrical acceptance and tracks in this region contain typically 3 hits in the pixel detector and about 8 hits in the SCT.

An illustration of the transversal plane in the barrel region of the inner detector is presented in figure 3.7. There are three layers of pixels. To provide best resolution for the primary vertex emerging from the hard scattering process and possible secondary vertices associated to particles decaying after a finite lifetime, the inner most pixel layer, also called B-layer , is mounted directly to the beryllium beam pipe. With a distance in z direction of 495, 580 and 650 mm from the inter action point, there are three end-cap disks on either side. In total there are 47232 individual pixels distributed on each of the 1744 pixel modules. Besides the four radial layers of the SCT shown in the figure, there are also 6 end-cap disks on either side. The first, third and sixth one consist of two layers glued back-to-back with an angular offset to improve the spacial resolution in the long dimension. The SCT end-cap disks are positioned at $|z|$ = 890, 1091, 1350, 1771, 2115 and 2608 mm and in total there are 15912 individual SCT sensor modules. Only tracks in the region up to $|\eta| \approx 2.5$ possess a sufficient amount of pixel and SCT hits to be reconstructed with an efficiency above $\sim 50\%$ although the outermost layer of the pixel end-caps covers up to $|\eta| < 2.69$ and the B-layer in the barrel reaches $|\eta| < 2.77$. Nevertheless $|\eta| = 2.5$ is usually declared to be the boarder of the inner detector acceptance.

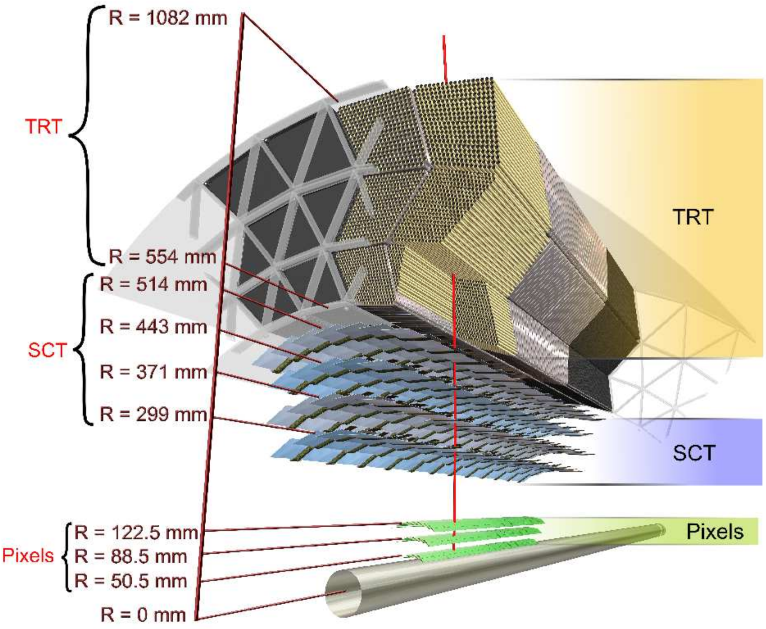

Figure 3.7.: Section of the transversal plane showing the inner detector in the barrel. The radial distance relative to the beam pipe is given for the various layers of the subdetectors [51].

Due to their proximity to the interaction point both the pixel detector and SCT are exposed to high radiation. To reduce radiation damage, they are cooled down to approximately −10°C by an evaporative cooling system using C_3F_8 as coolant. However, the TRT operates at room temperature and surrounds the silicon detectors according to figure 3.7. In consequence there are several isolators and heaters installed in between those two technologies. The TRT is composed of 52544 straws installed in parallel to the beam pipe in the central region and another 122880 straws in each end-cap placed perpendicular to the z-axis. A single straw has a diameter of 4 mm and is made out of carbondoped polyimide. It is kept at high voltage and acts as cathode while its conductivity is increased by a 0.2 µm thick layer of aluminium covering the inner surface. The anode wire is made out of gold-plated tungsten and on a potential of 1530 V. It passes through the center of the straw while the body is filled with a gas mixture of CO_2 and xenon. If a charged particle is traversing the straw, it ionizes some of the gas, and the emerging charge is collected at the anode after a certain drift time. This time is an accurate measure to determine the impact parameter of the track orthogonal to the wire. However, a measurement along the wire is not possible. Common tracks of charged particles possess about 35 hits in the complete

TRT. Due to the different capacitivity of the gas inside the straw compared to the outside region, there is also an emission of low energy transition radiation photons by charged particles. Those photons are absorbed by the gas and it is possible to distinguish electrons from other particles like charged hadrons. Table 3.1 summarizes the introduced instrumentations of the inner detector and gives in addition information on their resolution and coverage. For aligning the various sensors to each other a track based approach is chosen, but further explanations are omitted at this point.

Subdetector	Coverage	Spacial resolution [μm]	Hits per regular track
pixel barrel	$\lvert\eta\rvert < 2.5$	10 (R-ϕ), 115 (z)	3
pixel end-caps	$2.0 < \lvert\eta\rvert < 2.5$	10 (R-ϕ), 115 (R)	3
SCT barrel	$\lvert\eta\rvert < 1.5$	17 (R-ϕ), 580 (z)	8
SCT end-caps	$1.3 < \lvert\eta\rvert < 2.5$	17 (R-ϕ), 580 (R)	8
TRT barrel	$\lvert\eta\rvert < 1.0$	130	35
TRT end-caps	$0.8 < \lvert\eta\rvert < 2.0$	130	35

Table 3.1.: Coverage, spacial resolution and number of hits per regular track for the subdetectors of the inner detector.

Although the beam conditions monitor (BCM) does not contribute to the reconstruction of scattering processes in any physics analysis, it is important as it is the only component of the ATLAS detector allowed to trigger a dump of the beams. It consists of eight diamond sensors mounted on the beam pipe and positioned at $|z| = 184$ mm. Because of the very good time resolution, the BCM is able to distinguish particles approaching from the interaction point or from along the beam pipe in case the beams are not centered in the pipe. To protect the ATLAS detectors against dangerously high particle fluxes caused by beams brushing the pipe a beam dump can be initiated by the BCM safety system.

3.3.2. Calorimetry

The ATLAS calorimeter system [52] entirely surrounds the inner detector, as is shown in figure 3.6. The component next to the inner detector is the electromagnetic calorimeter while the hadronic calorimeter is installed behind it. Both of them are sampling calorimeters composed of absorbers and parts made out of an active medium. Highly energetic particles lose their energy due to interactions in the absorber material. For electrons the most important process is bremsstrahlung, for photons it is pair production and hadrons lose energy due to strong interactions. The secondary particles generated by these processes interact with the absorber as well. The procedure is repeated until the full energy is converted to secondary particles. A cascade, also called shower, emerges and develops typical shapes for different particle types. In the case of electrons for example, the shower is more regular and thinner than for hadrons which develop wider showers. Depending on the rapidity region, steel, lead, copper and in the very forward region also tungsten is used as absorber material.

To measure the energy of a shower, there is an active medium placed in-between the absorbers. Either liquid argon (LAr) or scintillating tiles are used in ATLAS to fulfill this purpose. In case of LAr, ionization takes place, and the occurring charge is collected as current in the cell. This technology is used for the calorimeters closer to the beam pipe since a continuous flow of the liquid argon is provided and in consequence there is no signal degradation due to radiation damage over the lifetime of ATLAS, despite the high radiation those parts are exposed to. The scintillating tiles are used further away from the beam pipe and are built out of doped polystyrene. Scintillation light is produced due to the absorbed radiation. In a second step optical fibers transfer the light to photomultiplier tubes installed in support structures behind the active volumes. For the tiles the signal is expected to be reduced by a few percent during the LHC lifetime due to radiation damage.

The design of the ATLAS calorimeter system satisfies the requirement to handle the significant variation of deposited energy in the range $|\eta| < 4.9$, i.e. over 178° in θ. The large coverage is especially important for the determination of missing energy in an event. The electromagnetic calorimeter has a thickness of about 20-30 radiation lengths and is capable of containing showers of electrons and photons up to 1 TeV. In addition approximately two thirds of hadronic showers are collected in this component as well. The barrel part of the electromagnetic calorimeter covers the region up to $|\eta| < 1.475$ and for the electromagnetic end-cap it is $1.375 < |\eta| < 3.2$. The thickness of the lead used in the electromagnetic calorimeter varies from 1.13 to 2.2 mm and there is a stainless steel support structure. The altering lead and liquid argon layers wave with the radius comparable to an accordion's geometry. This guarantees a full coverage in the ϕ-coordinate without any cracks.

There are three longitudinal sampling layers up to $|\eta| = 2.5$ and two for $2.5 < |\eta| < 3.2$ in the electromagnetic calorimeter. The first layer has the finest segmentation to achieve a good position measurement, the second one collects the majority of the shower while the third one is used to measure the tails. In detail the segmentation in the η-coordinate is varying from 0.003125 to 0.1 while for ϕ it is from 0.025 to 0.1. The reconstruction of the direction of flight for uncharged particles like photons benefits from this segmentation since they do not leave a track in the inner detector. In addition there are finely granulated portions of liquid argon without absorber layers installed right after the inner detector. They are called presamplers and behave like single layer liquid argon trackers. Because of the cryostat, the solenoid and the 1 to 4 radiation lengths caused by the inner detector, electromagnetic showers already start to develop before reaching the main part of the calorimeters. In the region $|\eta| < 1.8$, the presamplers help to correct for these losses of this development.

To measure the part of the hadronic shower exceeding the electromagnetic calorimeter, there is the hadronic calorimeter with a thickness of about 8-12 interaction lengths mounted subsequently. Up to $|\eta| < 1.7$ the tile technology is used while there is an additional division between the barrel up to $|\eta| < 1.0$ and extended barrel covering $0.8 < |\eta| < 1.7$. The scintillating tiles are 3 mm thick and installed with their thin side in z direction. They are alternating with steel absorbers of a thickness between 4 and 5 mm. The readout segmentation in the η and ϕ-coordinate is 0.1 for the complete tile calorimeter. On the outside of this detector at the radius of ~ 4.25 m, there is a cylindric steel yoke to support the tile calorimeter on the one hand and on the other hand to return the solenoid magnetic field. The magnetic field throughout the calorimeter is negligible. The hadronic end-cap calorimeter is based on liquid argon as active medium and copper plates as absorbers. It covers the region $1.5 < |\eta| < 3.2$ and has a segmentation of 0.1 to 0.2 in the η-coordinate while it is 0.1 for the ϕ-coordinate. In contrast to the electromagnetic calorimeter though there are just two sampling layers installed.

The barrel and extended barrel part of the tile calorimeter as well as the barrel and end-cap calorimeters using liquid argon are housed in separate cryostats due to service structures installed in-between. To get nevertheless as much information as possible on showers passing the crack between the cryostats, there are special scintillators mounted on the outside of the cryostats. As additional side effect the particle flux in the ATLAS muon spectrometer is reduced due to physically blocking parts of the gap. In the very forward region, i.e. for $3.1 < |\eta| < 4.9$, the forward calorimeter surrounds the beam pipe and closes the inner detector in the z direction. This calorimeter is composed of three modules which are 45 cm long each. There is one electromagnetic module consisting of copper and two hadronic modules made out of tungsten. Parallel to the beam pipe, there are holes drilled in the elements and copper or tungsten rods are inserted to work as electrodes. Liquid argon fills the remaining gap between the rods and hole walls. The segmentation is 0.8 to 5.4 in the x-coordinate and 0.6 to 4.7 in the y-coordinate. The resolution of the various parts of the calorimeter is desired to be:

calorimetry type	desired resolution
electromagnetic	$\sigma_E/E = 10\%/\sqrt{E} \oplus 0.7\%$
hadronic barrel and end-cap	$\sigma_E/E = 50\%/\sqrt{E} \oplus 3\%$
hadronic forward	$\sigma_E/E = 100\%/\sqrt{E} \oplus 10\%$

Table 3.2.: Desired resolution for the various calorimetry types installed in ATLAS.

3.3.3. Muon spectrometer

The outermost part of the ATLAS detector is the ATLAS muon spectrometer [53] which is embedded in a toroidal magnetic field. Although many of the muon's properties in terms of quantum numbers are similar to the ones of the electron, it is not stopped in the calorimeters. This is based on the classical fact that deflections of charged particles cause them to emit electromagetic radiation with an amplitude proportional to their acceleration. Besides the dependence on the charge of the deflecting nucleus and the incident particle, which is the same for electrons and muons, the intensity is proportional to the inverse of the squared mass of the incident particle. Therefore the emission of bremsstrahlung by muons is suppressed about forty thousand times more than for electrons since the muon is about two hundred times heavier than the electron. However, if the muon momentum is less than approximately 3 GeV, there is no reasonable track in the spectrometer due to energy losses and the bending in the magnetic field. An overview of the spectrometer is given in figure 3.8. There are four detector technologies operating independently in the muon spectrometer, namely monitored drift tubes (MDTs), cathode strip chambers (CSCs), thin gap chambers (TGCs) and resistive plate chambers (RPCs). While MDTs and CSCs provide a precise measurement of track segments approximately in the bending plane of the muon in order to determine the momentum accurately, the RPCs and TGCs are used for rapid response to trigger on events with muons in the final state and to provide a measurement of the missing coordinate. The region $|\eta| < 2.0$ is covered by three layers of MDT stations. Beyond, up to $|\eta| = 2.7$, the CSC technology is used in the inner most station layer because it is capable of handling the higher rates occurring in this region. For $|\eta| < 1.05$, i.e. in the barrel, there are three double layers of RPCs. Two of them are installed on the top and bottom of the middle station of MDTs while the third one is mounted on the outside of the outer layer of MDTs. The TGCs accomplish the triggering in region $1.05 < |\eta| < 2.4$, in the end-caps of the spectrometer. There are single TGC station layers in front of the inner and middle MDT stations and double layers of TGCs behind the middle MDT stations. For illustration purposes one quadrant of the ATLAS detector in the RZ-plane is shown in figure 3.9.

In the ϕ-coordinate there is a segmentation in 16 sectors expect for the TGCs which follow a more complicated division. The counting of the sectors starts at $y = 0$ on the side of positive x

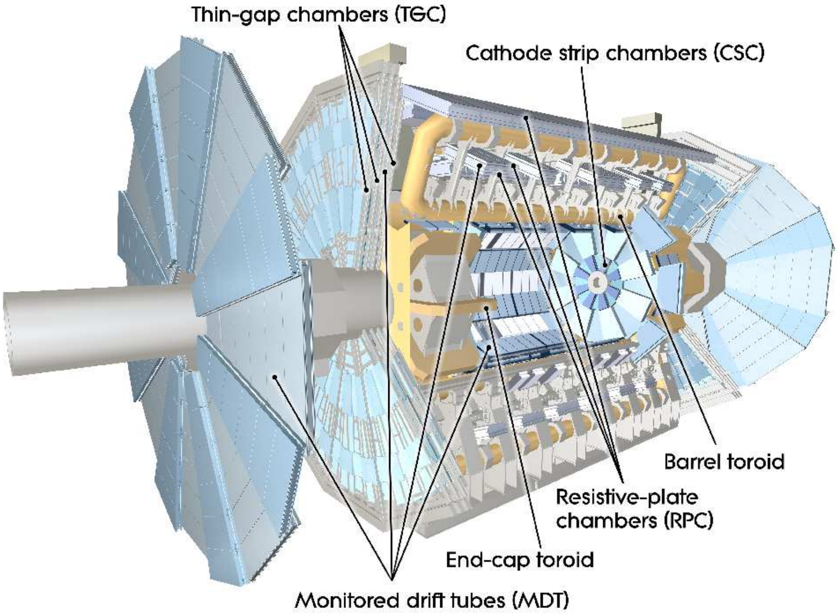

Figure 3.8.: Overview illustration of the ATLAS muon spectrometer including the barrel and end-cap toroids magnets[54].

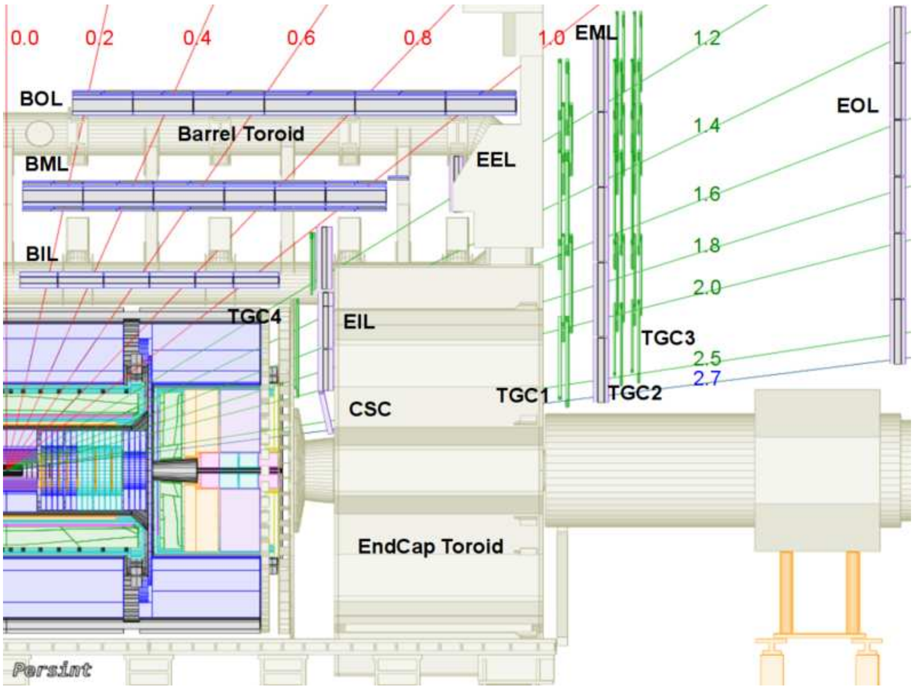

Figure 3.9.: Quadrant of the ATLAS detector in the RZ-profile [55].

values. The size of the chambers is alternating between larger ones in odd sectors and smaller ones in even sectors. There are further geometrical features not addressed here, like the absence of stations around $z = 0$ because of services for the inner detector and calorimeters, additional chambers installed in the end-cap during the shutdown in the winter 2011/2012, and special stations in regions difficult to cover.

Although there are four different technologies, the basic detection principle is ionization of a filling gas for all of them. An MDT is composed of an aluminum tube with a diameter of about 3 cm used as cathode and an anode which is a wire passing in the center of the tube. The length of the tubes varies from 1 to 6 m. The filling gas is a mixture of argon and CO_2 and the applied voltage is about 3 kV. Traversing charged particles ionize the gas. The emerging electrons are accelerated towards the anode, but at some point drift with a constant velocity due to collisions with the gas atoms. After a maximal drift time of 700 ns the anode is reached and a signal is created. With the knowledge of the connection between the drift time and the radius ("r-t-relation"), it is possible to determine the radial distance of the passing charged particle with respect to the wire. At the moment an accuracy of approximately 80 µm can be achieved. However, this information is not sufficient to build a full segment of the particle's trajectory. Therefore 3 to 4 layers of tubes are stacked into so called multi-layers, which have a width of 1 to 2 m. A full MDT station is subsequently built out of two multi-layers like it is illustrated in figure 3.10. The combination of the measurements in all tubes in a station eventually creates a segment, as shown in the sketch in the same figure. However, the size of the chamber induces deformations, and effects like gravitational sagging as well as thermal swelling become significant. For this reason an optical alignment system inside the chambers is used to monitor the position of the tubes all the time. Including the information of a second optical alignment system monitoring the positions of the stations relative to each other, it is possible to achieve resolutions up to 30 µm. This resolution, although, is perpendicular to the wires only since the coordinate along the wires is not accessible with the drift tubes.

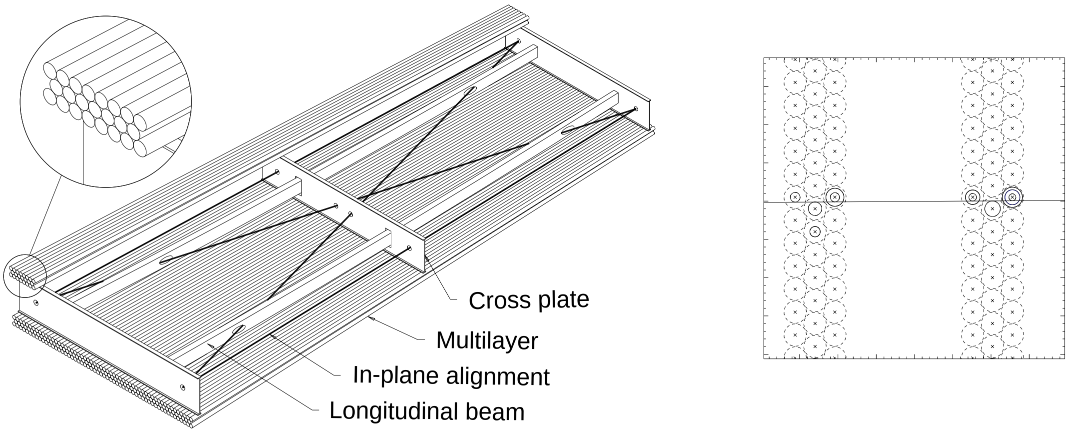

Figure 3.10.: Schematic illustration of a MDT chamber (left) with one incomplete multilayer in order to display the inner structures as well. Both multilayers are composed of three tube layers. Traversing particles create signals in the tubes (right) and a segment can be formed by a correct match of the resulting radii [53].

In case of the CSC technology both coordinates are measured. The cathodes are not cylindric, but plates, which are separated in strips and placed at the front and back of each chamber. Inside there is a mixture of argon and CO_2, and wires used as anodes run radially. The applied voltage is 1.9 kV. One set of strips is aligned in parallel to the wires while the other one is perpendicular. Again traversing charged particles cause ionization. The emerging charges are drifting to the electrodes. Compared to an MDT, the drift time in a CSC is rather small and amounts about 40 ns, so that higher particle rates can be handled. The drift time is used to determine the position of the ionization, and the cathode strips are read out providing both coordinates. A complete CSC station is composed of four layers of gas volumes.

For triggering on events with muons in the final state it is more important to provide fast response rather than high resolution. The TGC and RPC technologies satisfy this demand and make it possible to identify highly energetic muons within $10 - 25$ ns. The resolution is of the order of mm which is worse than the performance of the precision technologies. However, for the final track reconstruction the trigger chambers only provide the one coordinate not accessible by the precision chambers. The TGCs are, similar to the CSCs, multi-wire chambers, but there is less distance between the electrodes and the applied voltage is increased to 2900 kV. Therefore drift times are smaller and a faster response is achieved. One station comprises two to three gaps of 2.8 mm filled with CO_2 and C_5H_{12} gas. The gas gaps in the case of the RPCs measures 2 mm, and a station is commonly built out of two layers. There are two plates with high resistance bounding the gap and a voltage of 9.8 kV is applied in-between. Metallic strips, used for read out, are mounted and capacitively coupled to the plates. Once a charged particle ionizes the gas, there is a conducting channel established including electrical breakdown, and a signal is generated by the strips.

The magnetic field that bends charged particles traversing the muon spectrometer is created by three air-core toroidal magnets with 8 magnetic coils each, as is shown in figure 3.6. In the barrel region $|\eta| < 1.4$ the coils are placed in the small sectors and a bending power of $2.5 \text{ T} - \text{m}$ is provided. The coils in the end-cap are located in the large sectors, and on both sides a end-cap toroid in fit in the barrel toroid. The provided bending power in the region $1.6 < |\eta| < 2.7$ amounts to $5 \text{ T} - \text{m}$. Since there is no coupling of the toroid magnetic field and the solenoid magnetic field of the inner detector, two independent momentum measurements can be performed.

The muon spectrometer is able to operate completely independent from the other components of the ATLAS detector, a useful feature for collecting e.g. cosmic muons. There are only limited applications of this ability in the case of collision data, since inner detector and calorimeter measurements are very important to discriminate fake objects from real muons. In chapter 5 there are more studies provided regarding such topics.

3.3.4. Forward detectors

Three forward detectors, namely LUCID [56] (LUminosity measurement using Cherenkov Integrating Detector), ALFA [57] (Absolute Luminosity For ATLAS) and ZDC [58] (Zero Degree Calorimeter), are part of ATLAS and located at $|z| = 17$, 240 and 140 m from the interaction point. They provide information on the luminosity and are used to study diffractive physics. LUCID comprises aluminum tubes filled with C_4F_{10} in which charged particles emit Cherenkov radiation. It is possible to draw inferences from the measurement of the radiation's intensity about the luminosity. To calibrate LUCID it is possible to use measurements of elastic scattering performed by ALFA. This detector houses fiber tracker modules inside Roman pots which can be moved to 1 mm from the beam pipe. To determine the centrality of heavy-ion collision, there is a measurement of neutral particles performed by electromagnetic and hadronic modules in the ZDC. The modules are composed of quartz strips wedged between layers of tungsten and steel. To determine the absolute luminosity with rather small systematic uncertainties, van-der-Meer scans are performed in order to calibrate the visible luminosity while the introduced detecotors like LUCID or BCM in combination with minimum bias trigger scintillators are used to get relative luminosity measurements [59, 60].

3.3.5. Data acquisition, quality and processing

In order to collect collision data with the ATLAS experiment, the very basic requirement is colliding stable beams in the center of the experiment delivered by the LHC machine. Once LHC declares this condition to be fulfilled, the subdetectors of ATLAS ramp from a safe state with for example decreased voltages, up to the state optimized for data taking. Depending on the subdetector this procedure may take some minutes. In figure 3.11 the total integrated luminosity as a function of days is shown for the 2011 data taking period. This period is analyzed in most of the following chapters, but for data taken in 2010 and 2012 the data taking efficiency does not change by much.

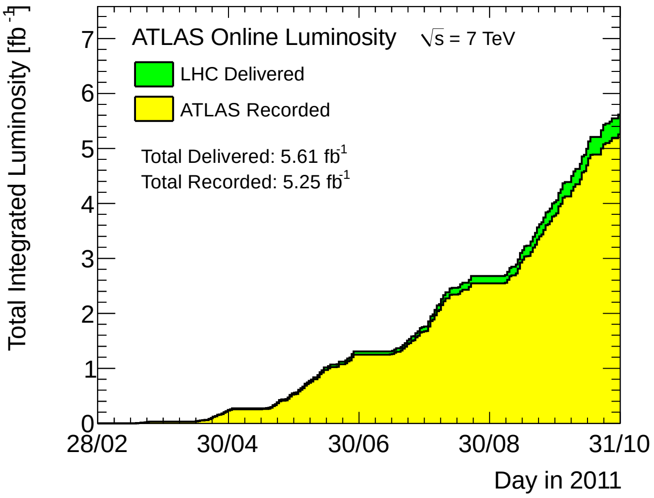

Figure 3.11.: Summed integrated luminosity [35] delivered by LHC (green) and recorded by the ATLAS experiment (yellow) as a function of days. The displayed time period includes the complete 2011 data taking of proton-proton collisions at $\sqrt{s} = 7$ TeV.

Independent of the presence of stable beams, ATLAS groups the data in so called runs which could last for hours. Besides runs comprising actual collision data for physics analysis recorded with the full detector, there are also dedicated runs including only parts of the detector. Those runs are mainly used for calibration purposes or special detector studies. Each run is divided in smaller units a few minutes long, called luminosity blocks. With the luminosity block boundary it is possible to address portions of data more easily and for example select only those with stable beams announced and with all instrumentations working properly. Accounting for problems on the level of the subdetectors, the data per luminosity block is classified as good or bad quality. Depending on the studied signature and in consequence the required detector components to measure this signature, it is possible to decide per luminosity block which data should enter the analysis. Most of the time all subdetectors deliver data of good quality, like it is reported in table 3.3 for 2011 data taking. In 2010 and 2012 there is no major difference in this performance. Because of varying filling configurations of the proton bunches in particular at the beginning of the data taking in 2010, it is required to demand an event to be associated to an actual bunch crossing via a bunch crossing identifier (BCID) for this time period.

subdetector	number of channels	approximate operational fraction	percentage of good quality data
pixels	80×10^6	95.0%	99.8%
SCT silicon strips	6.3×10^6	99.3%	99.6%
TRT transition radiation tracker	350×10^3	97.5%	99.2%
LAr EM calorimeter	170×10^3	99.9%	97.5%
tile calorimeter	9800	98.3%	99.2%
hadronic end-cap LAr calorimeter	5600	99.6%	99.2%
forward LAr calorimeter	3500	99.8%	99.5%
MDT muon drift tubes	350×10^3	99.7%	99.4%
CSC cathode strip chambers	31×10^3	96.0%	98.8%
RPC barrel muon chambers	370×10^3	97.1%	99.4%
TGC end-cap muon chambers	320×10^3	98.2%	99.1%

Table 3.3.: Data taking efficiency and fraction of good quality data per subdetector [61] during proton-proton collisions at $\sqrt{s} = 7$ TeV in 2011.

Even at luminosities below the design luminosity it is not possible to store all the events. An event size of about 1.5 MB with zero suppression already applied, i.e. only channels giving an actual signal are recorded, implies an output of about 60 TB each second if collisions happen every 25 ns. Since this rate can technically not be handled at the moment, rapid decisions have to be made if an event exhibits interesting signatures and should be kept or discarded forever. Currently the rate of 700 MB/ s for transferring data from point 1 to the CERN data processing center (Tier0) is limiting the output to a maximum of about 400 Hz. At Tier0 data can be processed with a rate of about 200 Hz. In consequence, for each event recorded another 200,000 have to be rejected. To accomplish this task, there is a three-tier trigger system implemented in the ATLAS data processing chain.

Physics objects are reconstructed at each level of the trigger with increasing granularity and precision. The level-one (L1) trigger arrives at a decision after 2.5 μs by searching for interesting objects and creating regions of interest (RoIs) attributed with an approximate transverse momentum measurement and defined by the calorimeter and muon spectrometer. Also a rough approximation of the missing and measured total transverse energy is provided at this stage. Inner detector information is not included at this stage. The output rate of this pure-hardware trigger is about 75 kHz. Until the selection is done, all event information is buffered in on-detector modules. Depending on the thresholds for a single object's transverse momentum in case of simple triggers or a combination of several objects and various thresholds for complex triggers, an event eventually passes the L1 trigger and is transfered to a computing farm for applying the level-two (L2) trigger.

At L2 also inner detector measurements are used and a simplified version of the reconstruction is performed in the RoIs. Besides a refined approximation of the missing transverse energy taking into account for example muons, there is a distinction of electrons and photons via the matching of a track and the calorimeter shower shape. A simplified classification of jets potentially including bottom quark decays is applied as well. In complete this takes about 40 ms per event and results in rates up to 3.5 kHz. The following level-three trigger, referred as event filter (EF), together with the L2 trigger are called high-level triggers since they are based on software. During the four seconds engrossed by the event filter a full event reconstruction is accomplished and the eventually desired rate of 200 - 400 Hz is achieved. The series of trigger requirements from L1 to the EF is referred to as a "trigger chain". In case of no further restriction on the events seeding the next trigger level, i.e. if all events selected by the L1 pass the full chain without any additional screening, this chain is called unprescaled otherwise it is prescaled. Especially for chains seeded by triggers with low thresholds on transverse momenta a prescale is applied nowadays.

Finally the events are grouped in streams comprising the output of dedicated trigger chains. For example the "muon stream" contains all events passing any muon trigger chain while the "e/γ stream" is the same but for any electron or photon trigger. These streams are not exclusive, e.g. for multi-lepton analyses considering both streams, care has to be taken that events passing muon and electron triggers are not counted twice. In total there are about 10 different streams that are eventually sent to the Tier0. There the complete event reconstruction is done once again including additional calibrations. Subsequently the data is distributed on the worldwide Large Computing Grid (LCG) [62]. Partially the reprocessing takes place there as well. The LCG is also used to simulate detector outputs like it is described in the following chapter or to run the individual analysis codes of the physicists.

Chapter 4
Software environment

In ATLAS there is a common software and computing framework called Athena [63] which provides various features. It interfaces to the simulation toolkit Geant4 [64] to produce large scale Monte Carlo samples, which are mandatory for physics analysis. All functionality is included to produce a simulated detector output in several steps. In addition all software needed to reconstruct physics objects out of the data and simulation is included. Athena also contains the specific software written to do physics analysis, i.e. to ascribe the physics objects to actual processes they are produced by. This chapter mainly focuses on the various steps done to obtain simulated detector output, with some aspects highlighted that involve the ATLAS muon spectrometer. For a better orientation in the process flow figure 4.1 gives a summary up front.

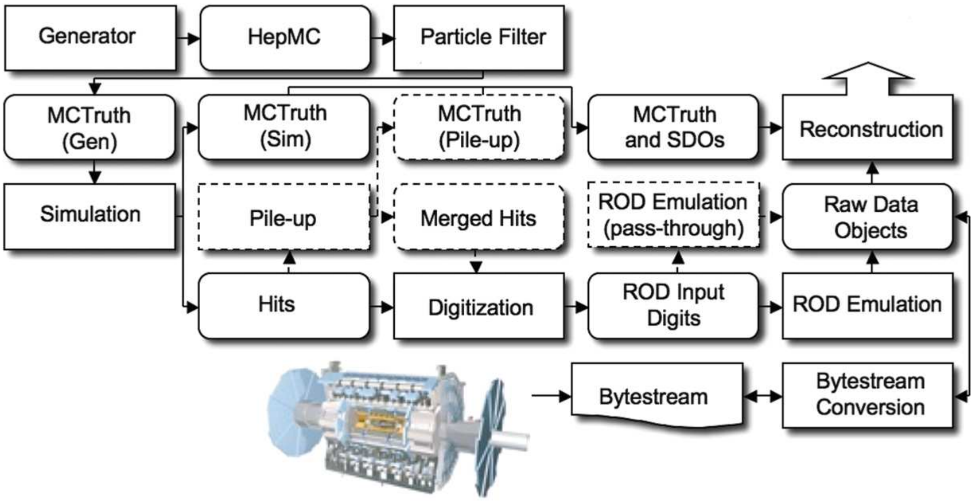

Figure 4.1.: Schematic flow of the ATLAS simulation software [65], from event generation (top left) to reconstruction (top right). Square-cornered boxes indicate algorithms while rounded boxes denote persistent data objects. Boxes corresponding to the pile-up portion of the chain are dashed since this is optional and only used in case events are overlaid. In the lower right corner it is shown how real data enters the scheme.

4.1. Generation of hard scattering processes

The first step to produce any detector output is to generate the physics processes that take place at the interaction point and before any detectors interactions. These are on the one hand the hard scattering process of the two colliding hadrons in the initial state and on the other hand the so called hadronization of the emerging quarks and gluons. The decay of τ leptons takes place at this step as well as final state radiation of leptons in general. For the simulation of the hard scattering there is a variety of tools available which calculate differential cross sections for the specific final states via their matrix elements. These tools consider either leading order, next to leading order or even higher order Feynman diagrams for the calculation. As an essential input all these codes rely on a parton distribution function (PDF). This function gives the probability to find a proton's constituent to have the momentum fraction x of the full proton momentum at an energy scale Q^2 and are available on leading, next to leading or higher order. The most common PDF sets are provided by the CTEQ collaboration [66] or the MSTW group [37]. Example matrix element generators commonly used in ATLAS are MC@NLO [67], Alpgen [68] or Sherpa [69].

As a matter of principle, the following hadronization and parton showering is deeply linked to the final state of the hard scattering process, since here additional quarks and gluons may occur despite being included in the calculation of the matrix element. To avoid such double counting, matching schemes are used which are either based on the energy of the partons, like in CKKW [70], or on the number of partons, like in MLM [71]. These two schemes however do not consider complete next to leading order matrix elements while the matching performed in MC@NLO and Powheg [72] includes such calculations. Finally the hadronization itself can be done based on the Lund string model or based on clusters. In the first model hadrons are produced by stretching (unphysical) strings between colored partons, which are allowed to break by introducing a quark-anti-quark pair until only Standard Model resonances are left over. This approach is used for example by the Pythia [73] code. The second model, applied by the generator software Herwig [74], splits gluons not perturbatively in quark-anti-quark pairs and forms color neutral clusters which decay depending on their mass until only resonances known from the Standard Model remain.

Due to enormous intersection of the generation of the hard scattering process and the following hadronization it is hard to draw a defined line between the different tasks. Some of the hadron shower programs for example also provide the calculation of dedicated hard scattering processes, while some of the libraries to calculate the matrix elements offer the possibility to simulate hadron showers as well. In addition there are dedicated tools used to describe special features of an event. Jimmy [75] models the underlying event more accurately and for a more correct description of the behavior of τ leptons and photons the tools Tauola [76] and Photos [77] are used. The results obtained by the various combinations of PDF sets, hard scattering generators and hadronization programs are not necessarily the same. Therefore it is a common approach to assign a systematic uncertainty describing this difference. Usually it is determined by using different setups and take the biggest difference as the uncertainty. Later this issue will be revisited.

In ATLAS the Athena framework is used to configure all the needed tools, to execute them and to take care of interfacing the specific outputs accordingly. The final output of the complete event generation step, the so called event file, includes besides other information regarding generator settings, all the particles that are created during the production with their Lorentz vectors and their particle data group identifier (PDGID). The latter is a signed integer that specifies the particle type and charge, e.g. -13 means μ^-. In addition each particle object holds information about its direct predecessor and is branded by an unique barcode which makes it possible later in the simulation chain to track back the full process and decay chain respectively. Since at the end of the hadronization not all the particles are stable but may have a finite lifetime and decay in the detectors, this information is attached as well. Finally the output file including all this information is stored and can be used as input for the next step, the full detector simulation. In particular the same event file can be used by different versions of the detector simulation software or even different simulation programs for validation purposes.

4.2. Full detector simulation

The next step to go from the generated hard scattering process to the corresponding detector outstream is to simulate the traveling of the emerged particles through the experiment and the sensitive parts used to detect them. For this purpose two very common toolkits are FLUctuating KAskades (FLUKA) [78] and GEometry ANd Tracking (Geant), which are both used by ATLAS. While FLUKA is mainly used for special issues like cavern background simulation outside the Athena framework, Geant is interfaced to Athena and used for all large scale production campaigns. Therefore in this work the focus is on the Geant or more precisely on the Geant4 [64] toolkit, which is fully written in the C++ programming language. At some point some concrete Geant4 versions will be referred to, but since they change with the Athena version first a general description is given.

The two major inputs for the Geant4 simulation toolkit are the event files, especially the Lorentz vectors and the type of the particles, and the physics configuration which defines the model how the particles behave. This configuration holds for example the information about which interaction model with matter should be applied on particles, e.g. according to which model they should loose energy, ionize or scatter. It also defines how non-stable resonances should decay and which shower shapes they will produce in the detectors. The specific input responsible for these models is also known as physics list. Examples are the quark-gluon string precompound model (QGSP) [79] or the Fritiof precompound model (FTFP) [80] which both can be combined with the Bertini intranuclear cascade (BERT) [81].

The actual approach of Geant4 to simulate the propagation of the particles is based on statistical methods, so called Monte Carlo methods. For this reason the simulated data is sometimes just called Monte Carlo. First the traveling of an academic particle which is non interacting and not charged through a simple block of matter is described. It propagates according to its Lorentz vector in one step to the surface of the matter block and enters it. In the next propagation step it again follows the Lorentz vector up to the next surface where it exits the block. Finally in the last step it travels until the boarder of the simulated volume is reached, where it is terminated. Since there is no physics involved in this propagation, no statistical method has entered. Nevertheless, Geant4 provides such particles, called geantinos, for validation purposes. For example they can be used to produce radiation length profiles of the detector model like those shown later.

If a real physics particle like a muon travels through the example block of matter things get slightly more complicated. In principle the three main regions, namely before, inside and beyond the block remain the same, though they may not be passed in just one step. Instead the interaction with the matter or other physics processes like bremsstrahlung are considered. The probability for each process and its impact follows distributions determined by the underlying physics law which was set by the user in the physics configuration of Geant4. At this point random numbers and the Monte Carlo method are used to decide the position in the distributions taking into account the properties of the material of interest and the particles properties like the momentum. Once an interaction takes place Geant4 processes an additional step. For the example of the muon there may be several steps inside the block due to scattering, ionization or other kinds of energy loss. If before and beyond the block of matter perfect vacuum is assumed only bremsstrahlung or the decay of the muon will take place. In both cases secondary particles will be produced which will interact with the environment as well. Therefore Geant4 considers them as well and applies the same step propagation.

Obviously the tracking through the detector of all final state particles emerging from a hard scattering immediately becomes very complex even for initially simple processes, because firstly the number of particles can increase rapidly due to decays or interactions of the primary particles. This is especially true if there is a magnetic field present which bends charged particles and has to be applied correctly in the stepping procedure. Secondly the detector model is of course not just a single block but quite complicated. All this makes the Geant4 simulation step the most CPU time and memory consuming step in the simulation, although it just handles the tracking through the detectors and not the detector response itself. Every time a sensitive part of the detector is passed during the particles' propagation and a detectable interaction takes place, this is recorded in the output file, called a hits file. Besides the position, additional information like the deposited charge, energy or particle type are saved depending on the detector technology. This information is used for input at the next step, called digitization, which simulates the actual detector response. All other quantities like the particles' momenta that were calculated during the tracking only exist in memory and are deleted after the simulation step.

Like the event generation, also the simulation and Geant4 itself are configured and interfaced by the Athena environment. The detector description, which is elaborated upon in the following section, is implemented in Athena and handed to Geant4. Due to this interfacing and the various components it is mandatory to have functional validation procedures to make sure that the subsequent steps are not fed with incomplete or false information. One validation algorithm is described in section 4.2.2. Last but not least it should be mentioned that the simulation is much more perfect compared to reality in the sense that for example condition effects like detailed misalignment or deformation of the detectors are not taken into account, since it would be unfeasible to apply such and guarantee the stability of the simulation program at the same time. These phenomena have non negligible impact especially on the resolution as will be pointed out later.

4.2.1. More realistic muon detector description to approach data resolution

Due to the different technologies and structures implemented in the ATLAS experiment their description in the software representation has to satisfy different needs. For all parts an accurate description on the level of millimeters or even below is required in order to produce simulated data as close to real data as possible. While the description of the actual detecting structures is mostly homogeneous and follows a cylindrical symmetry, the support structures are profoundly irregular, asymmetric and inhomogeneous. For the inner detectors and calorimeters the amount of dead material is rather assessable and regularly organized compared to the muon spectrometer. Although as mentioned before Athena is used to provide one common detector representation to Geant4. This section explains the approach chosen for the muon spectrometer software to describe the structures on the one hand precisely and on the other hand in a feasible way for the developers.

In the early design of the ATLAS simulation framework all subdetector developers agreed on using a package called `GeoModel` [82] to interface their description of detectors and structures to Geant4. In terms of programming technique for the implementation of a detector description this package follows quite closely the idea of bare Geant4, while some additional mechanisms are applied to save memory. In general the full detector description has to be implemented without any visual feedback in terms of C++ classes. After compiling the code and detector representation respectively, it is possible to get visual feedback of the `GeoModel` representation by a package called virtual point one (*VP1*) [83], which is integrated in Athena and therefore configured and launched only as part of the framework. It should be mentioned that the *VP1* package of course is not primarily used to give visual feedback to the developers of the detector representation, but to serve as an event display and therefore holds many other features for this purpose.

In the described approach quantities like dimensions and positions are mostly not hardcoded, but retrieved from a database. For the muon spectrometer this is a Oracle database and the tables follow the ATLAS Muon DataBase (AMDB) scheme [84]. This is especially true for the sensitive detector components and was true for most passive structures in the past. The disadvantages of such an approach are not hard to find: Fast turnarounds are not possible, and duty cycles as well as the maintenance are time consuming efforts in terms of developer time more than in terms of CPU time. In addition the detector description has to be fairly free of conflicts to get a first visual model. The main issues to mention are overlaps of volumes or shapes with corrupted surface definitions not visible in the first place. These types of bugs also jeopardize the stability of the full Geant4 simulation.

Rather soon it turned out that especially for passive structures of muon spectrometer another way had to be found because they mostly have irregular shapes that are rather hard to code neatly in terms of C++. In addition they are arranged inhomogeneously, have as contrasted with other parts of the detector dimensions between millimeters and several ten of meters and are often redesigned in more detail or added from scratch to describe reality more accurately. Therefore the approach of an ATLAS Generic Detector Description (AGDD) [85] was developed, which adapts some concepts of Geant4 and `GeoModel`, but exhibits fundamental differences. The AGDD approach starts from an `XML`-like ASCII input file and is in principle a chain of parsers and handlers that eventually provides a detector representation to any visitor program.

In the `XML` input file main structures like the toroids or shielding of the muon spectrometer are grouped in so called sections. The most basic building units are simple volumes like boxes or tubes connected with the material they are made of. These volumes are further on rearranged in simple composite volumes or composite volumes which involve a boolean operation like a subtraction. The dimensions used in the description are part of the `XML` file and available in separate elements. More details on the technical structure of the `XML` ASCII file and the available volume types is given in reference [86]. To give an idea of the final size of such an `XML` ASCII file Table 4.1 contains the current number of objects that are used to describe the dead material of the ATLAS muon spectrometer. Including also prototype structures and comments, the current version consists of approximately 10 thousand lines of code.

Category	amount
variables	1442
basic single volumes	498
simple composite volumes	265
composite boolean volumes	92
sections	14

Table 4.1.: Number of elements used to describe the ATLAS muon spectrometer in `XML` disentangled in different categories.

In Athena the package `AGDD2Geo` is available in terms of a service and ensures the correct passing of the `XML` to `GeoModel`. Firstly the TinyXML [87] parser is used to read the `XML` ASCII code. Basically the input file can be located anywhere, either on a database or in a local working area. This is possible because the path is specified in the python configuration of the service on the Athena initialization level. Therefore no database updates or recompiling is needed if a new test description is examined. Secondly a handler holds for each of the elements in `XML` a class which is used to build a new object according to the element. In the next most essential step

the generic detector description is built by using volume and positioner classes of AGDD. In contrast to Geant4 all volumes get already equipped with material properties at this level. Like the read-in this operation can be configured during the Athena initialization process so that it is greatly flexible. It is possible to choose single volumes, structures, full sections or everything available to be built.
The volume hierarchy does not strictly match a tree structure, since branches can be reclaimed or merged to save memory. The building process though follows a tree like flow. From the generic detector representation in memory it is possible to derive a convenient description in terms of any other classes or volumes and positioners respectively to satisfy any needs of visitor programs. In the case of `AGDD2Geo`, a `AGDD2GeoModelBuilder` class creates the according `GeoModel` representation that enters the flow foreseen by Athena. Apart from that, a `AGDD2G4Builder` is available, which can produce decent input for direct use in Geant4. Therefore the AGDD approach provides much more flexibility than an implementation in `GeoModel`, since two time consuming working steps, namely compiling and the maintenance of the database are not needed any longer.

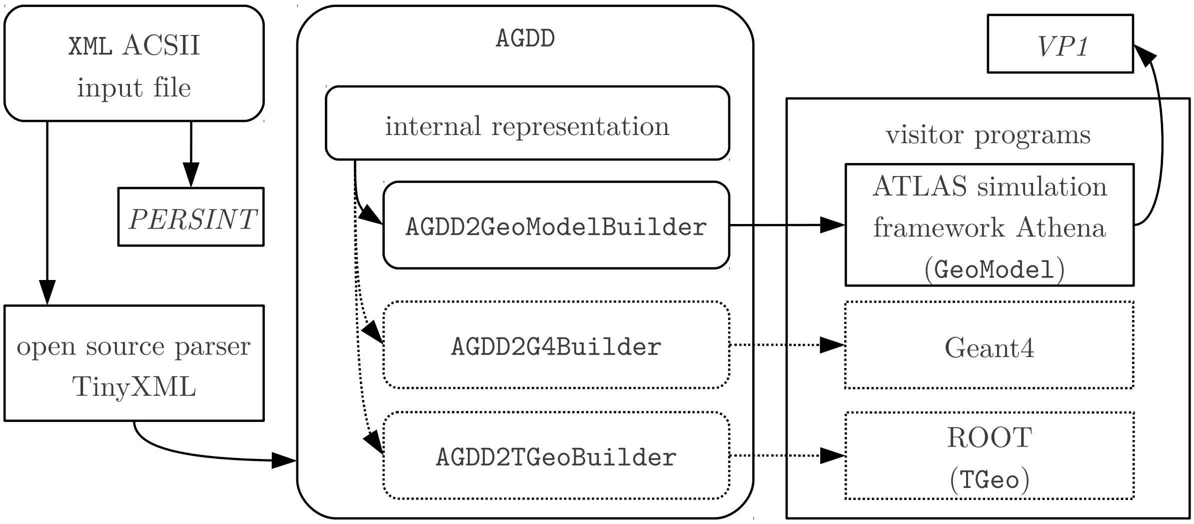

Figure 4.2.: Flow chart of the sequence of parsers and handlers to build a `XML` and AGDD based detector representation in the ATLAS simulation software [86]. Besides the visitor programs mentioned in the text, namely `GeoModel` and Geant4, this chart lists ROOT and the corresponding handler in addition.

Another advantage is the `XML` format itself. Common freeware like TinyXML or Xerces [88] provide powerful syntax debugging features that support the developer in the coding efforts. Besides this very basic benefit the even more relevant convenience is that PERSpective INTerative (*PERSINT*) [89] is able to perform a close to real time visualization of the implemented detector description using an internal parser. *PERSINT* is a stand alone program developed by the ATLAS collaboration that does not rely on Athena. It offers a GUI and is very intuitive to handle. Volumes or structures that the user wants to display can be easily selected using the mouse and a full 3D model can be moved dynamically. These two features in addition to an internal option to search for overlapping volumes are a very good combination to help the developer to find any conflicts which could impact the stability of the simulation once the detector description is inserted there. Like *VP1*, also *PERSINT* is not intended to solely visualize a detector representation but is an event display program. In addition it also includes the option to do fast tracking and reconstruction as well as producing radiation length maps or magnetic field maps. An action chart summarizing the described sequence of parsers, handlers and visualization programs is given in figure 4.2.

Nowadays no single structure of the dead material of the ATLAS muon spectrometer is implemented in terms of `GeoModel` classes any longer. Everything is migrated to the description in `XML` and extended there. Figure 4.3(a) is produced by *VP1* and shows a picture of the full set of the formerly used structures available in the `GeoModel` description, while figure 4.3(b) shows all parts available via AGDD displayed by *PERSINT*. Obviously the increase of complexity and amount of material introduced in the model accessible via AGDD affects the resolution of muons reconstructed from Monte Carlo data due to the more precise simulation. Corresponding studies are presented in more detail in section 5.2.

4.2.2. Validation of detector description implementation

Although the simulation is just the second step to a simulated detector output after the event generation and further steps can be used to correct for inaccurate modelings or mistakes in the implementation, it is of tremendous importance to do some validation already at this stage. Bugs introduced at this stage are rather difficult to spot after the output is processed further, and it is troublesome if the large scale Monte Carlo production campaigns which are expensive in terms of resources are found to be corrupted. Keeping in mind that the output solely holds the hits in the sensitive detectors, there are only very basic things to check so that additional algorithms have to be implemented to do more detailed examinations.

Nevertheless basic malfunctions can be recognized from the output. For example there are the validation packages `MuonHitTest` and `MuonEvtValidator` [90] available in the Athena framework. While the `MuonHitTest` algorithm dumps the number of hits per muon station, the `MuonEvtValidator` is used to superimpose two such dumps, which may be derived from two different outputs of the simulation step and therefore changed conditions in the simulation. Figure 4.4 shows an example plot produced by the `MuonEvtValidtor`. The superimposed Monte Carlo simulation samples had been produced with the same conditions, but with two different detector layouts for the ATLAS muon spectrometer, namely MuonSpectrometer-R.04.06 and MuonSpectrometer-R.05.01.02. Due to the Monte Carlo methods used for the simulation and slightly different random numbers, the number of hits in the stations is not exactly the same. The agreement is rather good and within the statistical uncertainties except for the stations CSL and BIM. For these two station types there are no hits at all for layout MuonSpectrometer-R.05.01.02, which indicates a programming mistake. Therefore this layout was fixed before it was release.

An example for a validation test which cannot be performed by analyzing the output of the simulation itself, but needs the implementation of a separate algorithm acting directly on the level of Geant4, is the production of a radiation length map. These maps display a projection of the thickness in terms of radiation lengths of the detector in a $\eta\phi$-plane. For purposes like this Athena provides a skeleton package named `G4UserAction`. It offers the basic structure to ask any information on propagating particles for each step taken, including information on the volume they travel through. Producing geantinos stepping from volume boundary to volume boundary and with Lorentz vectors binned in $\eta - \phi$, it is possible to store the sum of the step lengths multiplied by the specific radiation length of the passed volume and therefore create radiation length maps. Figures 4.5(a) presents such a map for the layout MuonSpectrometer-R.04.06 while figure 4.5(b) shows the thickness in terms of radiation lengths for layout MuonSpectrometer-R.05.01.02. In both cases only the radiation length of the ATLAS muon spectrometer is recorded

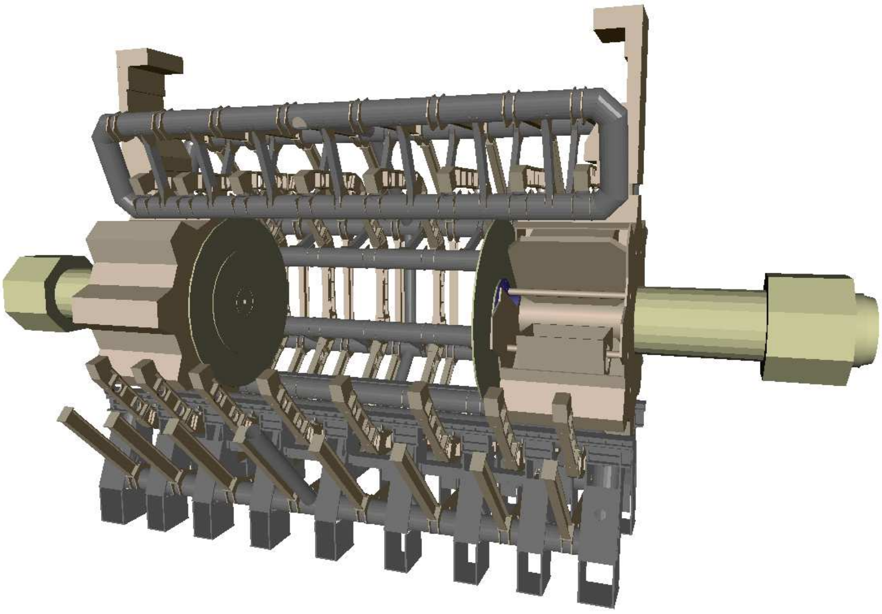

(a) Support structures as included in the muon spectrometer detector layout MuonSpectrometer-R.03.01 related to detector layout ATLAS-GEO-06-00-00 visualized by *VP1*. All volumes are implemented in terms of `GeoModel` classes.

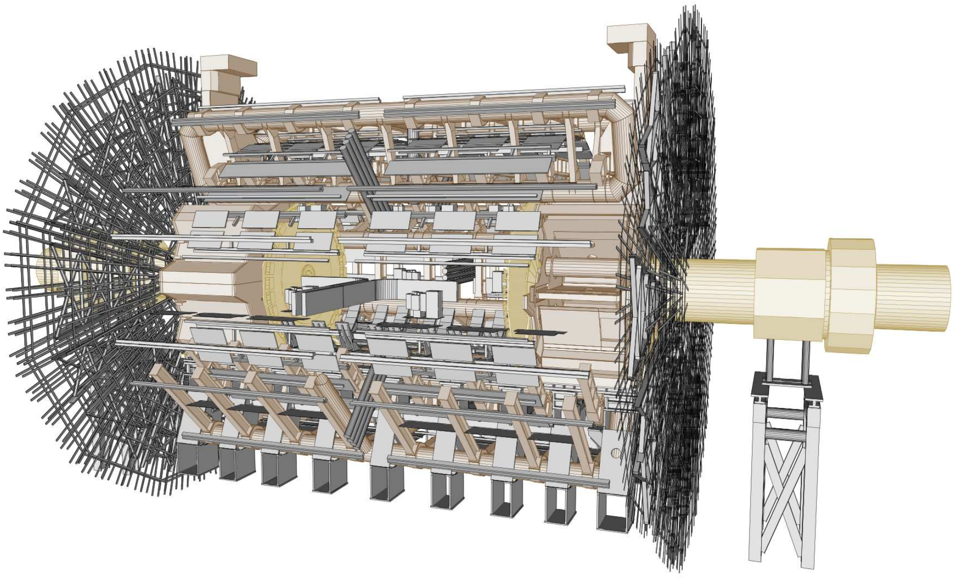

(b) Support structures as included in the muon spectrometer detector layout MuonSpectrometer-R.06.01 related to detector layout ATLAS-GEO-20-00-01 visualized by *PERSINT*. All volumes are implemented in terms of `XML` elements.

Figure 4.3.: Visual representations of the support structures present in the muon spectrometer displayed by *VP1* and *PERSINT* respectively.

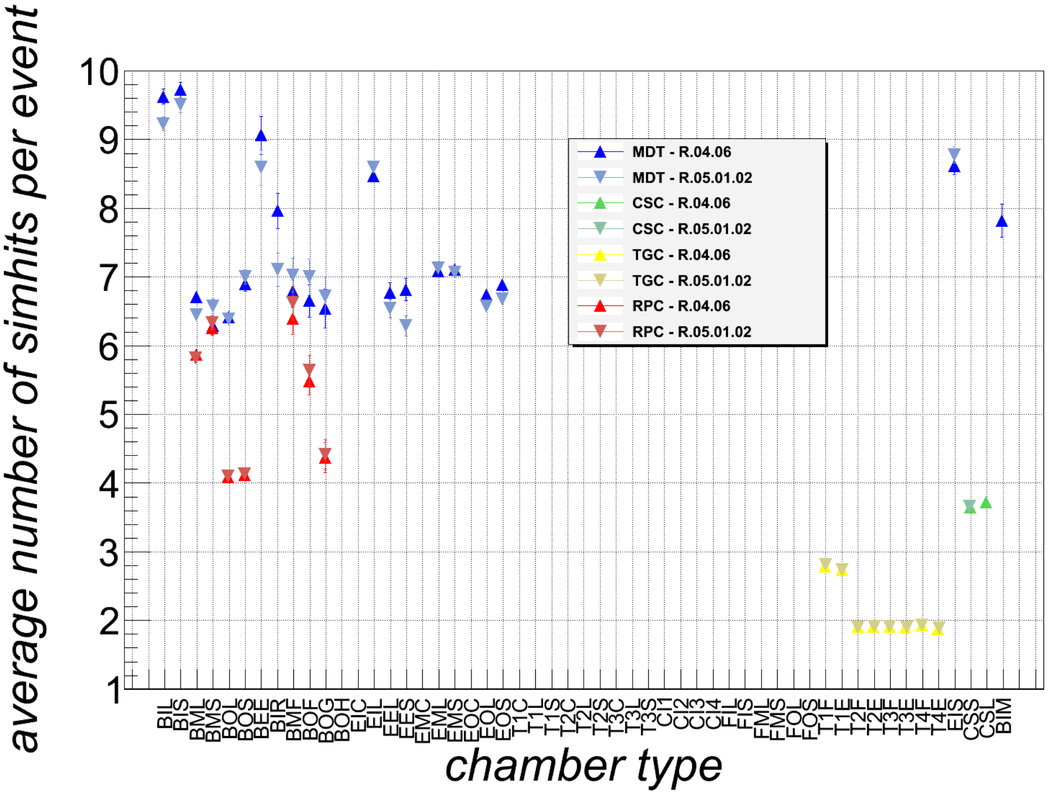

Figure 4.4.: Example plot of the `MuonEvtValidator` algorithm. In the legend the shortcut R.04.06 stands for MuonSpectrometer-R.04.06 while R.05.01.02 denotes MuonSpectrometer-R.05.01.02. More details can be found in the text.

while the inner detector and the calorimeters are skipped. Figure 4.5(c) shows the ratio of figures 4.5(b) divided by figure 4.5(a). Plots like these are a powerful tool to check if detector descriptions are interpreted correctly by the simulation program or if unexpected features occur.

To validate the proper functionality of new methods like the AGDD approach the explained radiation length maps are a very good handle. Actually, this procedure was used to show that there are no major differences in the simulation program between the description of the dead material placed in the ATLAS muon spectrometer either implemented directly in `GeoModel` or via `XML` and parsed by `AGDD2Geo`. For instance in the transition of the detector layouts presented in figure 4.5(c) the `GeoModel` description of the shielding system installed beyond $|\eta| \approx 1.2$ was replaced by the updated description within `XML`. The ratio of one for the predominant part of the area indicates that there is no difference, while the areas with a deviating ratio are expected since the description was updated there. Another more intuitive method for this specific validation task is to do it visually. By looking at the visual model of a structure in *VP1*, *PERSINT* and the visualization programs integrated in Geant4, it is possible to check if the interpretation and transformation of the `XML` into the various visitor programs' languages was done correctly. In figure 4.6 this is shown for a simple example, namely the service structures at $\eta \approx 0$.

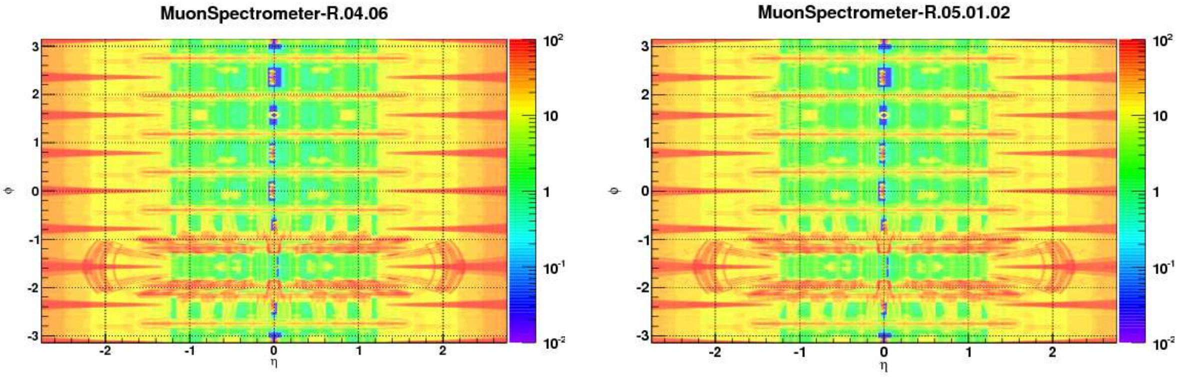

(a) Thickness in terms of radiation lengths for the muon spectrometer detector layout MuonSpectrometer-R.04.06 related to detector layout ATLAS-GEO-16-00-00.

(b) Thickness in terms of radiation lengths for the muon spectrometer detector layout MuonSpectrometer-R.05.01.02 related to detector layout ATLAS-GEO-18-00-00.

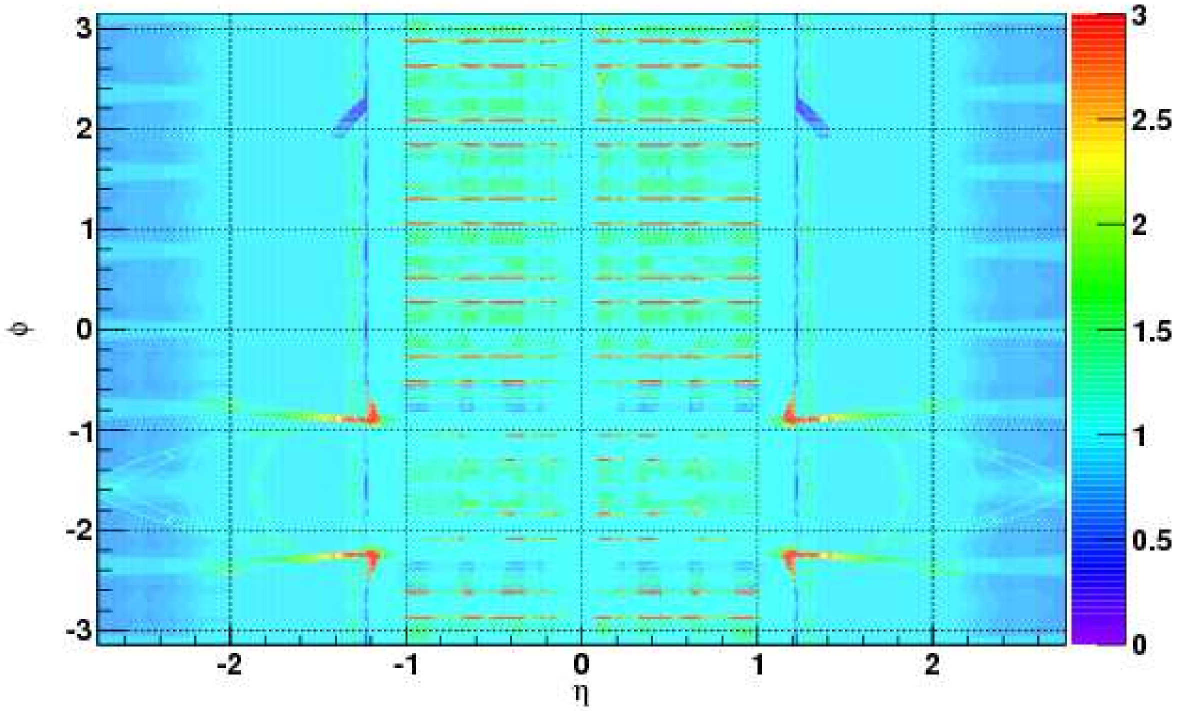

(c) Ratio of the subfigures (b) devided by subfigure (a). Especially in the barrel region for $|\eta| < 1.0$ the thickness in terms of radiation lengths for MuonSpectrometer-R.05.01.02 is increased. This is indicated by values greater than one for many areas in this region and caused by additional structures, namely RPC trigger boxes, which were inserted.

Figure 4.5.: Validation plots which display the absolute value of the thickness in terms of radiation length of the muon spectrometer or the ratio.

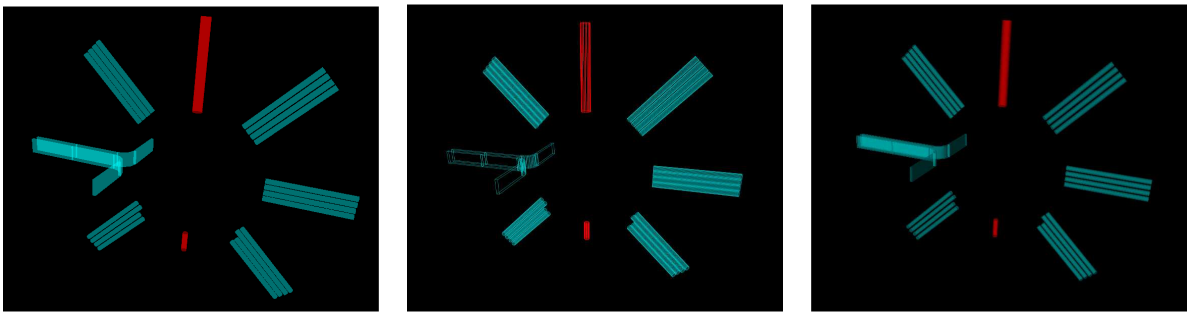

(a) Visual interpretation by *VP1* after parsing the `XML` description to `GeoModel` using `AGDD2Geo`.

(b) Visual interpretation by *PERSINT* and the internal parser.

(c) Visual interpretation by the Geant4 internal visualization method after parsing the `XML` using `AGDD2G4`.

Figure 4.6.: Visual interpretation by various visitor programs of the service structures placed at $\eta \approx 0$ in the muon spectrometer description implemented in `XML`.

4.3. Emulation of sensitive detectors

During the so called digitization, the physics processes taking place in the sensitive detectors are applied on the bare positions and deposited energy stored in the output file of the simulation step. For each of the various detector technologies used in the ATLAS experiment a separate algorithm is implemented [91] to take care of the proper treatment according to the measurement process explained in sections 3.3.1, 3.3.2 and 3.3.3. To approach more realistic simulated data a great achievement reached during the past years is that this step no longer relies on simulation and design response properties only, but is actively using information from the “conditions database”. As the name of the database implies, it holds the full set of information on the ATLAS detector conditions recorded alongside the physics stream. In particular, the knowledge of dead or disabled single channels or tubes, non-functional modules or chambers and the detector efficiencies derived from data taking are interposed by using the database in digitization.

Besides these general properties appropriate for all detector technologies, very specific conditions information is considered as well. For example in case of the MDT chambers, the drift radius obtained from Geant4 may be converted to the drift time using the r-t-relations stored in the conditions database. After that a Gaussian smearing is applied on the drift time according to the uncertainty also available as conditions data. Finally the parametrized response of the analog-to-digital converter (ADC) enters without being recalculated. However, currently the r-t-relations are hard coded and the ADC response is calculated separately for each hit which ends up to be very CPU time consuming. The algorithm which uses conditions data therefore would increase the speed while being closer to the real detector response at the same time. For this reason there are efforts in the validation of the new approach to enable it as default.

To have more realistic simulated data, the digitization may not use frequently updated conditions data only. There are also corrections applied to compensate too optimistic assumptions in the simulation, as-built parameters of the detectors or effects caused by the installation. For the example of the MDT chambers these are effects like misaligned chambers, chamber deformations or wire sagging. The accurate treatment of these kind of issues in simulation is a technically very challenging task, so that for the moment an adjustment on digitization level was considered to be sufficient. The misalignment is even too complicated to be applied in the digitization and is therefore accounted for in the reconstruction of the Monte Carlo data explicitly.

Last, the digitization is utilized to account for effects like pile-up, i.e. more than one interaction per bunch crossing, or cavern background [92], i.e. detector signals caused by the natural radiation of the cavern or remaining activation caused by previous interactions. The method of choice is to read in the hits file based on the hard scattering process, plus additional files of minimum bias events, cavern noise, beam halo or beam gas and overlay them by digitizing them all together to produce a unified output.

The general output of the digitization can have different flavors, amongst them the raw bytestream like that delivered by the detector. Other outputs are the prepared raw data (PRD), the raw data objects (RDO) and finally the simulated data objects (SDO). The latter three formats are intended to be used for validation tests, since the additionally applied transformations give an interpretation of the raw data in terms of positions which are written out. This gives the possibility to check what previously was a hit against what now is a digit.

4.4. Object reconstruction in ATLAS

Although, to perform a matching afterwards, some information of the initial hard scattering process and the simulation are kept in the output of the digitization step, this process ends the production chain of Monte Carlo data in the sense that the following operations do basically not apply any random methods to manipulate the data. The digitization output has the same format as the output of the detector so that the reconstruction of physics objects and subsequent steps in principle act similarly on real data and Monte Carlo data aside from some very specific treatments of the latter to make it more realistic.

The electronic signals are transformed to quantities like number of hits in a detector module or deposited energy, while the conditions data is used to apply for example noise corrections in the calorimeters or in very recent software versions to correct for too-optimistic alignment of the muon chambers in case of Monte Carlo data. The full event information used for reconstruction is stored in the so called event summary data (ESD) or analysis object data (AOD) accompanied already with the results of the reconstruction algorithms which built physics object out of the detector signals. For later chapters the most important reconstruction algorithms and physics objects respectively are:

- **Electrons** create hits in the inner detector due to their charge before they enter the calorimeter where they deposit their full energy in an electromagnetic shower. The sliding window algorithm [93] gathers calorimeter cells to clusters under the condition that the sum of the measured energies in a window of cells exceeds a certain threshold. Subsequently showers are formed and their shape is determined which enter the electron identification. To the hits in the inner detector a track is fitted with a charged pion particle hypothesis. For the final electron object [94] a matching of the shower and the inner detector track is performed seeded by either of them depending on the specific algorithm. Once an electron is identified the inner detector track is refitted [95] taking into account noise and energy losses due to bremsstrahlung for example. The Kalman filter is generalized in a non linear way by a Gaussian Sum Filter (GSF). For high pseudorapidities outside the inner detector acceptance electrons are identified only by their shower in the calorimeters.

- **Muons** traverse all detectors of the ATLAS experiment and produce signals in all of them due to interactions based on the fact that they are charged and minimum ionizing particles. The most reliable signals to reconstruct a full track are left in the inner detector and the muon spectrometer. Nevertheless the muon reconstruction algorithms [96] combine the data of all detectors to identify the muon and to create its trajectory. The track building in the inner detector is basically the same as for the start of electron track reconstruction, i.e. assuming a charged pion particle. Before the tracking in the muon spectrometer, hits in the tubes and (multi-)layers respectively are gathered together in so called segments on which a pattern recognition system works. These segments are used to build the muon spectrometer track. Due to differences in the geometrical acceptance of the inner detector and the muon spectrometer and the energy loss in the calorimeters, it is possible that in some of the detectors there is only a partial reconstruction. Therefore the following different types of muons are defined:

- stand alone (SA): The trajectory for this type of muons is reconstructed in the muon spectrometer only. Therefore a reliable momentum measurement requires a three station track, i.e. hits in all of the three station layers should enter the track building. To get the momentum at the IP, the measured momentum is corrected for the energy loss in the calorimeter using a parametrization. Due to the absence of an ID track the direction of flight and the impact parameter at the IP are determined by a backward extrapolation of the spectrometer track to the beam line.

- combined (CB): The trajectory reconstructed in the muon spectrometer can be matched to a track in the inner detector. Depending on the reconstruction chain the two momentum measurements are either combined statistically (for STACO [97]) or a refit is performed considering both the ID and spectrometer hits (for MUID [98]). The two approaches also differ slightly in their pattern recognition systems. For both, though, the ID track is used to get information about specific quantities closely related to the interaction point like the impact parameter with respect to the primary vertex.

- segment tagged (ST): If straight track segments in the precision muon chambers match an extrapolated trajectory of the inner detector to the muon spectrometer, this is identified as a muon. As a matter of principle all track parameters are obtained from the inner detector track.

- calorimeter tagged (CT): A trajectory in the inner detector is identified as a muon in case it can be associated to energy depositions in the calorimeters which are compatible with the hypothesis of a minimum ionizing particle. Most information of these object are derived from the inner detector track.

▷ **Jets** can be considered as any kind of shower emerging from objects produced by the hard scattering process. There is no unique definition of jets independent of the algorithm that collects and groups the constituents. The inputs are calorimeter energy depositions or tracks in the inner detector. In ATLAS the “anti-k_T” algorithm [99], based on the k_T algorithm [100], is the most common one used for jet reconstruction. Its output is quite stable against replacing any constituent by two objects with the same momentum direction and half the original's energy. This is so called “co-linear stability”. Very soft radiation between two jets that are produced nearby does not result in the merging of the jets. This feature is known as “infra-red stability”. Compared to other jet algorithms, the “anti-k_T” algorithm performs a splitting and merging of jets by itself during the jet finding so that no additional operation is needed. It is also favored because the reconstructed jets for most cases approximate well the momentum of the original parton. The two most important quantities defined in the algorithm are

$$k_{\mathrm{T},i}{}^2 = p_{\mathrm{T},i}{}^{-2} \tag{4.1}$$

$$k_{\mathrm{T},(i,j)}{}^2 = \min\left(p_{\mathrm{T},i}{}^{-2}, p_{\mathrm{T},j}{}^{-2}\right) \times \frac{\Delta R_{i,j}{}^2}{D^2} \tag{4.2}$$

where p_T is the transverse momentum, $\Delta R_{i,j}$ is the opening angle between the constituents i and j and D is a fundamental parameter of the jet algorithm related to the size of the final jets. The most common choice in ATLAS is $D = 0.4$. The momenta of two constituents are combined in a new single constituent in case $k_{\mathrm{T},(i,j)}{}^2$ of the pair is the smallest of all $k_{\mathrm{T},i}{}^2$ and $k_{\mathrm{T},(i,j)}{}^2$. The constituent i is called jet, if instead $k_{\mathrm{T},i}{}^2$ for this single constituent is the smallest of all the $k_{\mathrm{T},i}{}^2$ and $k_{\mathrm{T},(i,j)}{}^2$. This iteration is performed until all constituents have been combined into jets.

Besides these objects and algorithms, there is also dedicated software to reconstruct photons and τ leptons. Though they are more specific applications that resemble a physics analysis in some point, the tagging of jets originating from B-hadron decays (b-tagging) and the calculation of the missing transverse momentum are also considered as part of the reconstruction. All the information on the actual detector records and the derived results of reconstruction algorithms stored in the ESDs and AODs make these formats rather inconvenient for fast processing and therefore further transformations are required.

4.5. Derived data formats

During the Monte Carlo simulation, the amount of information stored in the output is increased by each of the steps. For a typical $t\bar{t}$ event the generator file measures $\sim$ 40 kB/event, while after simulation it is $\sim$ 2 MB/event and after digitization including pile up it is $\sim$ 2.8 MB/event. Due to the absence of truth information and any information regarding the simulation, the size of a corresponding real data event is much smaller. Calibration tasks or some physics analysis that rely on very specific information process on the level of ESDs/AODs which hold all information. Other analysis operate on D3PDs which is the acronym for Derived Physics Datasets. The value "3" indicates that they are the third instance of the initial detector output.

Usually each physics group produces one set of this output format with reduced information and adjusted to its needs. The advantages of this format are the possibility of accessing and processing it with the Root software [101] outside the Athena framework and the reduced file size. With about 140 kB for a typical $t\bar{t}$ event in the Standard Model D3PDs, the needed disk space is tremendously reduced. Frequently the ATLAS physics performance groups develop and update tools which work with D3PD outputs and consequently for Root based analysis. Besides calibration updates and methods to estimate systematic and statistical uncertainties, these tools also correct once more for mis-modeling or too optimistic conditions during the simulation and digitization step.

Chapter 5

Muon Performance Aspects

The final states of many interesting processes in the Standard Model or of processes predicted by theories beyond include muons. However, to be able to look for such interesting signatures, it is mandatory to first understand the objects which may eventually be reconstructed as muons and to get an idea of the related performance aspects. A study of basic muon objects is presented in section 5.1 which gives an estimate for the heavy flavor fraction in the muon inclusive spectrum. Some parts of the analysis are documented in reference [102] while the final results are not reported there. In section 5.2 a specific performance issue is addressed, namely the multiple scattering contribution to the muon momentum resolution as it is measured with the muon spectrometer. Various regions of the detector are analyzed separately and the improvement due to the more realistic detector description reported in section 4.2.1 is highlighted. Finally all relevant performance aspects regarding muons with high pseudorapidity are examined in section 5.3 like it also done in reference [55]. The detailed knowledge regarding muons with high pseudorapidity is used in the next chapter to measure an interesting process and to search for the Standard Model Higgs boson.

5.1. Muon inclusive spectrum

Many processes described by the Standard Model or by theories beyond end up with muons in the final state. Therefore it is important to understand the objects identified as muons by the reconstruction algorithms. Furthermore the production rates should be well known, because they are an important input to the muon trigger tuning. A useful approach to get a first estimate is to study the muon inclusive spectrum, i.e. to examine all reconstructed muon objects and to disentangle them by their origin. For the most dominant production processes figure 5.1 shows the differential cross section $\mathrm{d}\sigma/\mathrm{d}p_{\mathrm{T}}$ as predicted by the Pythia generator version 5.7 [103].

Light hadron decays, like the pion or kaon decay, are the main source for muons with low transverse momentum while for the intermediate transverse momentum region heavy flavor decays are the major origin. In these two cases, the muons and their predecessors respectively are usually produced together with additional hadrons and are therefore not isolated, i.e. they are produced inside or surrounded by a shower. For high transverse momenta there is an increased fraction of isolated muons without any jet nearby. The main production of these muons is via the decay of gauge bosons. A detailed study on muon isolation and isolated muons will follow in sections 5.3.5, 6.3.1 and 6.5, while muons associated to jets are addressed in this section and a rough estimate for the fraction of muons produced by heavy flavor decays will be given.

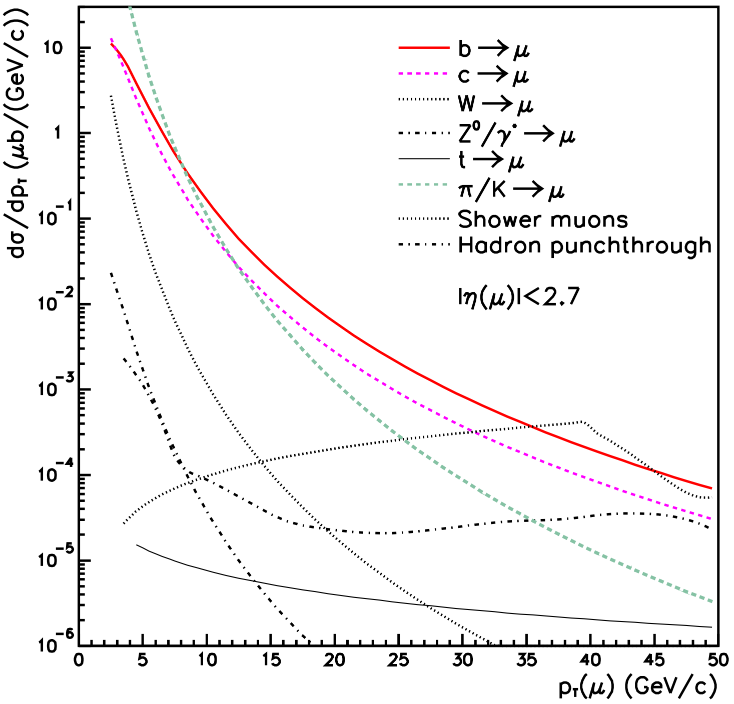

Figure 5.1.: Pythia 5.7 prediction for the differential muon production cross section $\mathrm{d}\sigma/\mathrm{d}p_\mathrm{T}$ [104]. Besides the most dominant sources ascribed to decays of particles produced by the hard scattering, two sources of fakes are given as well. In case of high energetic hadronic jets it is possible that the shower escapes the calorimeters and hadrons cause signals in the muon spectrometer. This phenomenon is called hadron punchthrough. Shower muons though are real muons that do not emerge from prompt products of the hard scattering, but from particle decays taking place in subsequent showers.

5.1.1. Discriminator variables for muons from hadron decays

Low transverse momentum muons found inside jets are mainly produced by light meson decays like pion or kaon decays in flight. For higher transverse momenta bottom quark decays and B-meson decays respectively are the dominant source. The decay of charm quarks as constituent of J/ψ-mesons or D-mesons contributes to both transverse momentum regions. For the disentanglement according to the various sources there are several useful features of the reconstructed muon object. The ones introduced below, are the momentum imbalance of the inner detector and muon spectrometer track, the determination of a secondary vertex as source for the muon and the relative transverse muon momentum with respect to a jet. Since all of them chiefly rely on a well measured inner detector track, only combined muons are considered for the following studies.

To separate the light contribution, there are three suitable quantities that are based on the fact that the lifetime of charged light mesons decaying into muons is of the order of $\sim 10^{-8}$ s, while heavy mesons already decay before about $\sim 10^{-12}$ s. Due to the longer lifetime, the inner detector track of the combined muon object is mainly caused by the meson, which decays in flight. The track in the muon spectrometer though is produced by the muon itself. In principle, the muon emission is isotropic in the rest frame of the light meson, but due to the Lorentz boost and the small mass difference there is only a very small angle in the lab system, and the two tracks may be matched to a combined muon. Because of the two distinct underlying objects there is a difference in the reconstructed momentum of the inner detector track p_{ID} and the momentum reconstructed in the muon spectrometer p_{MS} corrected for the parametrized energy loss p_{loss} in the calorimeters between the two devices [105]:

$$\frac{\Delta p}{p_{\mathrm{ID}}} = \frac{p_{\mathrm{ID}} - p_{\mathrm{MS}} - p_{\mathrm{loss}}}{p_{\mathrm{ID}}} \tag{5.1}$$

Figure 5.2(a) shows the residual $\frac{\Delta p}{p_{\mathrm{ID}}}$ for the different flavors as it is derived from a minimum bias Monte Carlo sample. In figure 5.2(b) the differential distribution with respect to the muon transverse momentum is present with early ATLAS data superimposed.

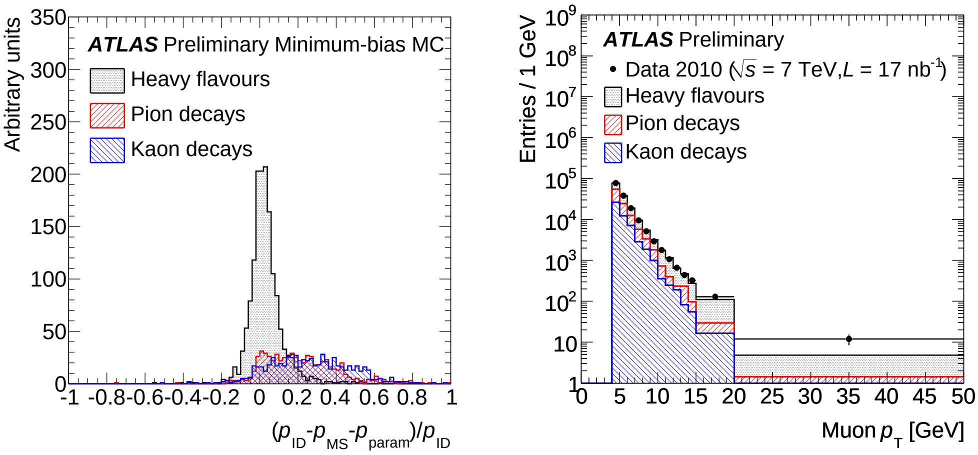

(a) Residual of the ratio $\Delta p/p_{\mathrm{ID}}$ for reconstructed muons with $p_T > 6$ GeV and the different flavor components disentangled as predicted by a minimum bias simulation.

(b) Transverse momentum spectrum from minimum bias simulation split up in various sources and rescaled to the number of entries of the observed data which is overlaid.

Figure 5.2.: Momentum imbalance for various flavor components derived from Monte Carlo simulation and transverse momentum spectrum superimposed with measured data [105].

The second very related quantity to disentangle the light flavor contribution is the matching χ^2 of the two tracks forming the combined muon. In this case, the reconstructed directions enter in addition to the difference in the momentum. As contrasted with $\frac{\Delta p}{p_{\mathrm{ID}}}$ which is a generic quantity, the matching χ^2 is dependent on the reconstruction algorithm, and no uniform statements for both, STACO and MUID (see section 4.4), can be defined. Therefore $\frac{\Delta p}{p_{\mathrm{ID}}}$ is the more convenient and the more common discriminator variable.

The third quantity based on the lifetime of the mesons is the transverse impact parameter d_0, which is the perpendicular distance of closest approach of the track with respect to the vertex in the transverse plane. As for long-lived resonances the impact parameter increases, it is rather small for short lived ones. Therefore it can be used to disentangle light and heavier flavor origins. Due to the high resolution the impact parameter is a very sensitive quantity. Although the resolution depends on the pseudorapidity and number of hits in the B-layer of the pixel detector, it is at least about 260 µm [106]. It can even be used to separate muons originating from B-meson decays with a decay length of $c\tau \approx 450$ µm and muons emerging from gauge boson decays with a negligible decay length. For this reason the impact parameter is one of the basic quantities for b-tagging [107] and secondary vertex detection [108] respectively.

Last but not least there is the soft lepton tagging as an additional technique to disentangle the different flavor sources [109]. Apart from the already introduced quantities, the lifetime is not exploited, but the kinematic properties rising from the different origins are. Due to the about one order of magnitude bigger mass of the charm quark with respect to the up, down and strange quarks and the about 3 times bigger bottom quark mass with respect to the charm quark mass, there is a different kinematic setup for the emerging muons. As mentioned before, muons originating from light sources are emitted rather in line with the trajectory of the initial particle due to the Lorentz boost and small mass difference. For the heavier sources especially, the mass difference is much bigger and therefore the direction of flight of the occurring muon is no longer an approximately straight extension of the initial trajectory or strongly collimated with the jet it is produced in. To quantify this phenomenon there is the so called relative transverse muon momentum $p_{\mathrm{T}}^{\mathrm{rel}}$:

$$p_{\mathrm{T}}^{\mathrm{rel}} = p_{\mu} \times \sin\theta_{(\mathrm{jet},\mu)} \tag{5.2}$$

The muon momentum is denoted by p_{μ} while $\theta_{(\mathrm{jet},\mu)}$ is the angle between muon momentum and jet axis. In simple words the relative transverse momentum is the muon momentum component perpendicular to the jet axis like it is illustrated in figure 5.3. In principle it is possible to separate all three sources of the muons, namely bottom, charm and light flavor sources with this quantity. Though one disadvantage is that for high jet energies, i.e. increased Lorentz boosts, objects produced by heavy flavor decays are in general more collimated and therefore also the muon is closer to the jet axis. In consequence the discrimination power of $p_{\mathrm{T}}^{\mathrm{rel}}$ is reduced for large jet energies. Besides the impact parameter also the relative transverse momentum is one of the basic variables used for b-tagging and b-tagging calibration [109, 110].

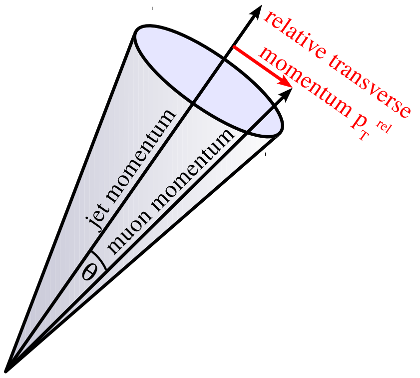

Figure 5.3.: Schematic sketch of the relative transverse muon momentum definition.

5.1.2. Data and object selection

The data used for the estimation of the heavy flavor fraction was taken in early 2010 and produced with proton-proton collisions at a center of mass energy of $\sqrt{s} = 7$ TeV. A first subset of an integrated luminosity of $331.1\,\mathrm{nb}^{-1}$ is used to verify the understanding of the leptons [102] while the full sample is extended to $1.4\,\mathrm{pb}^{-1}$ for the final estimation. All the data was collected with the whole detector in good state, i.e. all subdetectors have been fully functional. It is taken care that the events are associated to an actual bunch crossing, which especially for the early data taking phase is important to reduce background from cosmic muons. While for the first

subset a level 1 single muon trigger without any transverse momentum threshold (`L1mu0`) was required, the complete data sample of $1.4\,\mathrm{pb}^{-1}$ was analyzed with an event filter trigger for single muons with a transverse momentum of at least 4 GeV reconstructed in the muon spectrometer (`EF_mu4_MSonly_MB2_noL2_EFFS`). In both cases only events with a primary vertex with at least three tracks associated are considered to further reduce non-collision background.
For the reconstructed muon objects basic quality requirements on the inner detector track were demanded, where a hit refers to a measurement that is associated to the track:

- ▷ at least one hit in the pixel detector
- ▷ at least one hit in the B-layer
- ▷ more than 5 hits in the silicon central tracker
- ▷ in case the pseudorapidity of the track is below 1.9 there have to be more than 10 hits in the transition radiation tracker

The match of the inner detector track to the track in the muon spectrometer has to be the best match and the resulting muon has to be combined. In addition more than one hit in the trigger chambers of the muon system is required to be associated to the trajectory to have a reliable measurement for the ϕ-coordinate performed in the muon spectrometer. Finally only muons with a transverse momentum greater than 4 GeV and with a pseudorapidity less than 2.5 are considered. There is no exclusive choice of the reconstruction algorithm, but the study is done for MUID and STACO.
The anti-k_T jet algorithm is used to reconstruct jet objects (see section 4.4). The input for the algorithm is the energy measured in the calorimeter clusters. Like explained before muons as well deposit energy in the calorimeters, for which in principle one should corrected. Since this study ends up with a rough estimate only and due to the anyhow small energy deposition of the muons compared to the full jet energy, this complication is not incorporated in this analysis. In addition the quality criteria used for the jet objects are rather loose compared to later requirements which are established with a better knowledge on jets in ATLAS.
Besides a general acceptance cut for the jets to be reconstructed with a pseudorapidity below 2.5 the following requirements are demanded [111]:

- ▷ less than 80% of the measured jet energy in the hadronic end-cap calorimeter
- ▷ jet energy measured only in the electromagnetic calorimeter has to be less than 95%
- ▷ not more than 80% of the energy fraction measured by bad-quality cells of the electromagnetic calorimeter
- ▷ energy-squared-weighted cell time within two beam bunch crossings, i.e. $t_\mathrm{cells} < 50$ ns
- ▷ number of energy-ordered cells accounting for at least 90% of the jet energy is asked to be greater than 5

After the full object selection muons are associated to jets if their angular distance which is defined as $\Delta R = \sqrt{(\phi_\mathrm{jet} - \phi_\mathrm{muon})^2 + (\eta_\mathrm{jet} - \eta_\mathrm{muon})}$ is less than 0.5. Figure 5.4(a) shows the number of muons reconstructed in the $331.1\,\mathrm{nb}^{-1}$ data sample with the MUID algorithm after various cuts versus the coordinates η and ϕ and versus the transverse momentum p_T of the muon. In figure 5.4(b) control plots for the understanding of the muon objects are summarized, again for the MUID algorithm. The Monte Carlo sample which is superimposed for comparison is a minimum bias sample initially generated with Pythia 6.4 [112]. MRST LO* parton distribution functions [113] are used. Due to a less well modeled level 1 trigger and therefore a dramatic reduction by requiring the muon trigger without threshold for the minimum bias Monte Carlo sample this demand was skipped. In appendix B.1 the equivalent plots for the STACO algorithm are available.

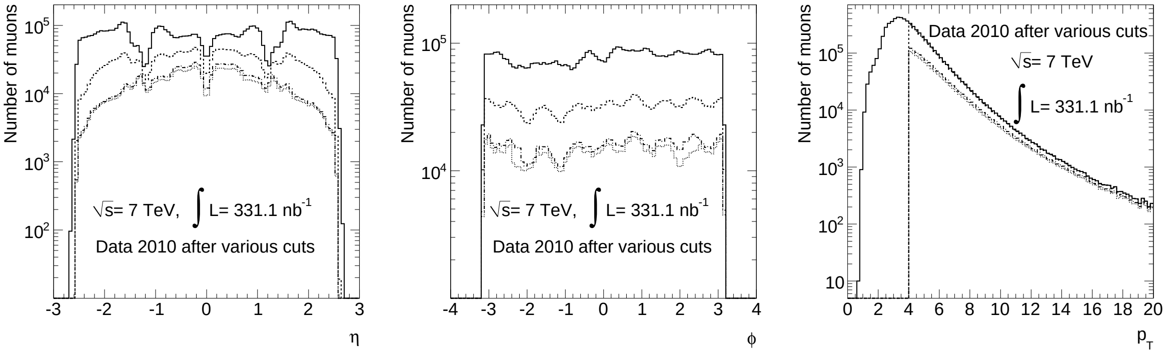

(a) Number of combined muons in data reconstructed with the MUID algorithm after various cuts versus η (left), ϕ (middle) and p_T (right). The solid line corresponds to the number of combined muons in events which pass the event selection criteria. Requiring $p_T > 4$ GeV, SCT Hits > 5, Pixel Hits > 0 leads to the dashed line. Associating the muons to a jets results in the dashed dotted line. Eventually the dotted line includes the quality criteria: ϕ-Hits > 1, B-layer > 0 and TRT Hits > 10.

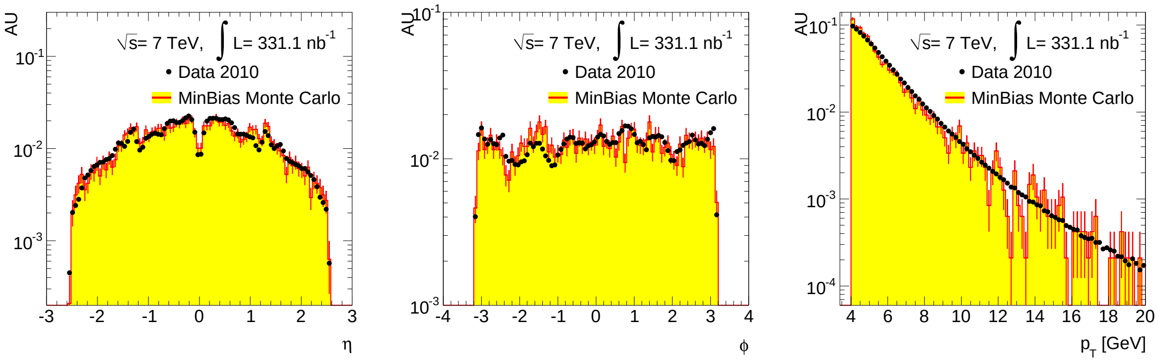

(b) Minimum bias Monte Carlo overlaid with data both scaled to the same area. In both samples the mouns fulfill all quality criteria, are associated to jets and are reconstructed by the MUID algorithm. While for the data sample a level 1 single muon trigger without threshold is demanded there is no such requirement on the Monte Carlo sample.

Figure 5.4.: Control plots to demonstrate the understanding of the reconstructed muon objects. The underlying muon reconstruction algorithm for these plots is MUID. The variations of the number of muons as function of η and ϕ are mainly caused by the geometry of the detector.

5.1.3. Template technique to extract the flavor composition

In figure 5.5 the relative transverse momentum of the muon is presented for the different flavors disentangled in Monte Carlo data and with the 331.1 nb^{-1} data sample superimposed. A reasonable agreement can be verified although the spectrum obtained form data seems to be slightly harder. For Monte Carlo data the minimum bias sample without a trigger requirement is used and the MUID reconstruction algorithm is chosen. The corresponding plots for the

STACO algorithm are shown in appendix B.2. Like it is described before the relative transverse momentum spectrum for muons originating from heavy flavors is harder than the one for muons emerging from light flavor decays. One technique, the so called template method, is utilizing this difference to disentangle the flavors in a full spectrum, i.e. for a distribution which unifies all flavors.

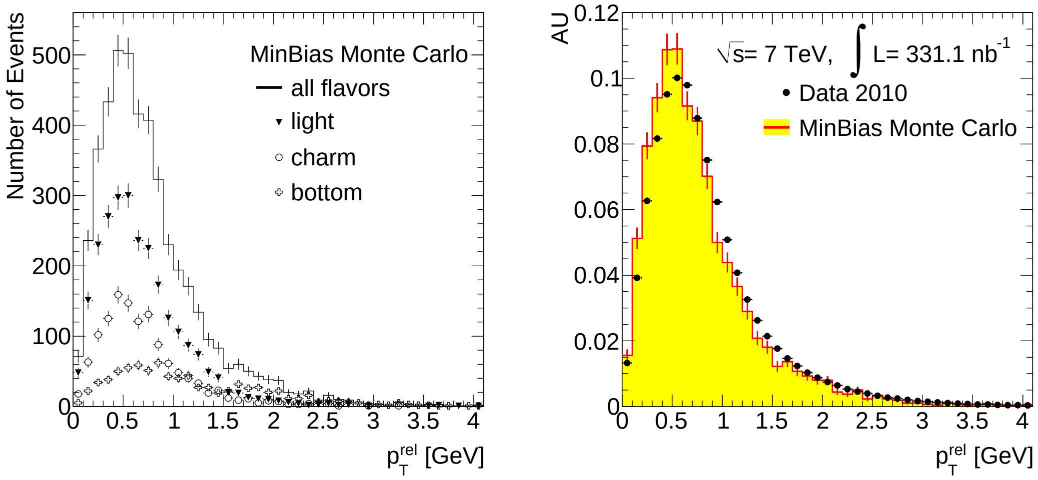

(a) Relative transverse muon momentum for muons reconstructed with the MUID algorithm contained in the minimum bias Monte Carlo in complete and split up in the different flavors.

(b) Complete relative transverse muon momentum distribution for muons reconstructed in minimum bias Monte Carlo and data reconstructed with the MUID algorithm. The distributions are scaled to the same area.

Figure 5.5.: Relative transverse muon momentum for different flavor sources obtained from simulation with data superimposed.

The idea is to derive for each of the origins, light, charm and bottom, one template distribution and perform a combined fit with the sum of the distributions to the unified spectrum. In the final fit the fractions of the three input distributions and muon sources respectively are the free parameters and therefore determined. The final step of this method is rather straight forward while for the initial part there are several options. Basically there are two approaches to get a pure sample of the different origins to derive the individual distributions and templates. Firstly this can be done in a data driven way, which of course implies sufficient high statistic in data and a very good understanding of the same. One could for example use the difference of the inner detector momentum compared to the momentum measured in the muon spectrometer to construct a sample enriched with muons from light flavor decays. For a heavy flavor enriched sample it is possible to use only jets which are present in events with another jet tagged as b-jet by the b-tagging algorithms. The only selection which cannot be derived from data such simple is for muons originating from charm quark decays.
An alternative to get pure samples is to use Monte Carlo data, which usually can be produced with sufficient high statistics. Because the generator truth is still available for the reconstructed objects, it is a comparative simple attempt to construct pure selections. A disadvantage of this approach is that one relies on a well modeled Monte Carlo simulation and generation, which one initially wants to check with the analysis. However due to the available truth information this is still possible by for example extracting the fraction of bottom quarks which are produced via gluon splitting and modeling this fraction by hand in the underlying selection of the tem-

plate distribution. Since in the early data taking the available statistics was limited and the understanding was less good than it is nowadays, the template distributions for this study are derived from Monte Carlo data. On the one hand the minimum bias sample is used for the light flavor distributions with muon transverse momenta up to 14 GeV and a set of dijet samples on the other hand, combined according to their simulated luminosity, is used for the remaining distributions. The specific properties are summarized in table 5.1.

MCID	Process	events	ϵ_{filter}	cross section [pb]	jet p_{T} (in GeV)
105001	min-bias	20×10^6	1.00	4.84×10^{10}	inclusive
108067	dijet	0.2×10^6	8.55×10^{-3}	6.78×10^8	$17 - 35$
108068	dijet	0.5×10^6	1.80×10^{-2}	4.10×10^7	$35 - 70$
108069	dijet	0.5×10^6	2.95×10^{-2}	2.19×10^6	$70 - 140$
108070	dijet	0.2×10^6	4.09×10^{-2}	8.77×10^4	$140 - 280$

Table 5.1.: Specific information on the Monte Carlo sample used. All samples are generated with the Pythia Monte Carlo generator version 6.2 and MRST LO* parton distribution functions are used. MCID denotes the Monte Carlo sample identifier and ϵ_{filter} is the filter efficiency on generator level.

For templates fitted to the distributions there are basically two options as well: They can be either a histogram or a function if the underlying data is binned or, in case of the function, data can even be unbinned. For b-tagging calibration in ATLAS which also uses $p_{\mathrm{T}}^{\mathrm{rel}}$ as a discriminator variable, histogram templates are applied since they can be adjusted rather easy to the various distributions. For this analysis though functions are fitted to binned data to evince that this approach produces reasonable results, too. In theory the $p_{\mathrm{T}}^{\mathrm{rel}}$ differential distribution could be computed exactly for the different sources of the muon although such an analytically calculated function would be rather complicated. Besides it would be unfeasible to do an unfolding of all the detector effects to get the theoretically determined spectra. Therefore the functions used in this study are chosen by taking into account aspects like the minimization of free parameters and the best fit to the distribution in terms of the shape.

For this analysis the range of the relative transverse muon momentum distributions is chosen to be between zero and 4 GeV, while the muon transverse momentum is in the range $p_{\mathrm{T}} = [4, 20]$ GeV. The final results are given in 5 bins of the muon transverse momentum, and therefore the fits are performed in each of these bins without changing any of the fit properties. To perform the fits the RooFit framework [114] within Root was used. The range of the fitting parameters given below are determined by pseudo-experiments. For each distribution of $p_{\mathrm{T}}^{\mathrm{rel}}$, there are 1000 pseudo-experiments performed and fitted. The resulting distribution of each fitted parameter is analyzed and the range is chosen as a slight extension of the width. This procedure is repeated until the found ranges remain approximately the same. For the heavy template function a scaled β-distribution is used according to the formula

$$f_b(x; p, q, a) = \frac{\Gamma(p+q)}{\Gamma(p)\Gamma(q)} (\tfrac{x}{a})^{p-1} (1 - \tfrac{x}{a})^{q-1} \tag{5.3}$$

where the scale parameter a has to be within the interval $[4., 9.]$ while the starting point of the fit is set to 4.001. The scale parameter has to be introduced because the β-distribution is ordinarily used in probability theory as continuous probability function and therefore it is only defined within 0 and 1. The fit is started with the value 2 for the parameter $p \in [1.;3.]$ while for $q \in [2.,14.]$ the starting point is set to 3. The shape of the function fits well to the $p_{\mathrm{T}}^{\mathrm{rel}}$ distribution for muons emerging from bottom quark decays including the cascade decay $b \to c \to \mu\nu X$ and especially models well the broad maximum. An example for muons with a transverse momentum between 10 and 14 GeV is given in figure 5.6(a).

To fit the $p_{\mathrm{T}}^{\mathrm{rel}}$ distribution of the muons originating from charm quark decays, a Landau distribution times an exponential function is chosen which reads in total

$$f_c(x;\mu,\sigma,b) = \tfrac{1}{\pi}\int_0^{\infty} e^{-t\ln(t)-\frac{x-\mu}{\sigma}t}\sin(\pi t)dt \cdot e^{x/b} \tag{5.4}$$

where the three parameters, namely the mean $\mu \in [0;3]$ and width $\sigma \in [0.00001;10]$ of the Landau and the exponential factor $b \in [-10;10]$, are all set to 1 at the beginning of the fit. Although the distribution looks rather close to a pure Landau, the exponential factor is needed to model the non zero value in the first $p_{\mathrm{T}}^{\mathrm{rel}}$ bin. In figure 5.6(b) an example is given for muons with a transverse momentum $p_{\mathrm{T}} \in [10;14]$ GeV.

In case of muons emerging from light flavor decays a Lognormal distribution is chosen. If a variable $y = \ln(x)$ is normally distributed, the variable x is known in common parlance to be lognormally distributed. In terms of function it reads:

$$f_l(x;\sigma,\theta,m) = \frac{e^{-((ln((x-\theta)/m))^2/(2\sigma^2))}}{(x-\theta)\sigma\sqrt{2\pi}} \tag{5.5}$$

For the fit the starting value for the shape parameter $\sigma \in [0.00001;1.]$ is set to 0.1, the location parameter $\theta \in [-10;0.]$ it is set to -2 and the scale parameter $m \in [0.00001,10.]$ finally starts at the value 2. With this function it was possible to model properly the non zero value in the first $p_{\mathrm{T}}^{\mathrm{rel}}$ bin and the rather broad maximum at the same time. Figure 5.6(c) demonstrates the fit for muons with transverse momentum of $p_{\mathrm{T}} \in [10;14]$ GeV. To examine the stability of the fit against variations of the underlying distribution, 1000 pseudo-experiments had been performed for each of the distributions in all 5 muon transverse momentum bins and the template functions are found to be reasonably stable. Appendix B.3 gives all finally derived templates that are used for the following proceeding.

Finally the template function fitted to the complete spectrum including all muon sources is a weighted sum of the three introduced functions. The parameter values found for the individual templates in the flavor-by-flavor fits enter as fixed quantities without any error. The global functions reads

$$f_g(x;\alpha,\beta) = \alpha \cdot f_b(x) + (1-\alpha)\cdot(\beta \cdot f_c(x) + (1-\beta)\cdot f_l(x)) \tag{5.6}$$

while the two parameters α and β give accordingly the fraction of the muons emerging from heavy flavor decays and the relative fraction of muons originating from charm and light decays respectively. For the fit both parameters are free within zero and 1, while the starting value is 0.2 for both. With the statistics and samples available at the time of the analysis, the found shapes of the template functions for muons emerging from charm and light flavors are quite similar. Therefore this study does not disentangle all three sources but bottom and the combination of charm and light only, i.e. the fraction reflected by the parameter α. Detailed investigations utilizing pseudo-experiments had been performed to verify that the derived fractions are stable against changes in the underlying distributions. The results of this check are presented in appendix B.4.

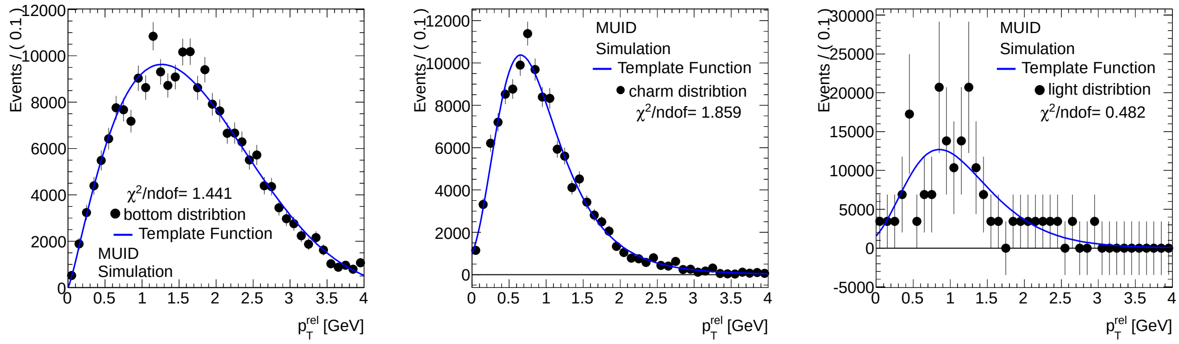

(a) Template function for muons emerging from bottom flavor decays and reconstructed with the MUID algorithm. The dijet Monte Carlo sample is used.

(b) Template function for muons emerging from charm flavor decays and reconstructed with the MUID algorithm. The dijet Monte Carlo sample is used.

(c) Template function for muons emerging from light flavor decays and reconstructed with the MUID algorithm. The minimum bias Monte Carlo sample is used.

Figure 5.6.: Example template distributions for muons emerging from the various sources and with a transverse momentum in the range $p_\mathrm{T} = [10; 14]$ GeV. All samples are scaled to an integrated luminosity of $1.4\,\mathrm{pb}^{-1}$ while for empty bins an error of one simulated event is assumed.

5.1.4. Heavy flavor estimation in the muon inclusive spectrum

Besides the stability of the fit examined in the previous section, which is focusing on the more technical issues, it is even more important that the found fractions reflect the real fractions of the underlying data. Therefore the fitting procedure is applied to two different Monte Carlo data samples, namely the combined dijet sample and the minimum bias sample. Though both samples are used to obtain the template functions it is a sensible test of the approach. The systematic uncertainty due to the method can be roughly estimated by the difference of the found and underlying fractions which is known for the Monte Carlo data. In addition the findings of the pseudo-experiments in appendix B.4 can be consulted for a systematics estimate. In figure 5.7 the final results for both Monte Carlo samples as well as for real data are presented as function of the muon transverse momentum. For figure 5.7(a) muons reconstructed with the MUID algorithm are used while for figure 5.7(b) STACO is the underlying muon reconstruction algorithm. The plotted errors for the fitted fractions correspond to the statistical error of the fraction parameter α only and do not include any systematic uncertainties like for the method or statistic uncertainties like for the fitted flavor template functions. The errors of the true fraction are the statistical errors of the underlying sample.

While for the combined dijet sample the found and real fractions are in rather good agreement, they are in less good agreement for the minimum bias sample. The major reason for this behavior is the limited statistics and therefore the increased freedom for the fit in the minimum bias sample, especially in the higher transverse momentum bins. For real data the statistics in all bins is sufficient to perform a reliable fit. In appendix B.5 the detailed global fit results are available which stress this fact as well.

To estimate the systematic uncertainties of the method, the distributions of the flavor fractions resulting from the pseudo-experiments and presented in appendix B.4, are fitted with Gaussian distributions. The maximum width reflecting the statistical uncertainty of the underlying Monte Carlo samples is approximately 8%. It enters the analysis as an estimation for the systematic uncertainty of the method. Additional systematic uncertainties are the muon momentum scale

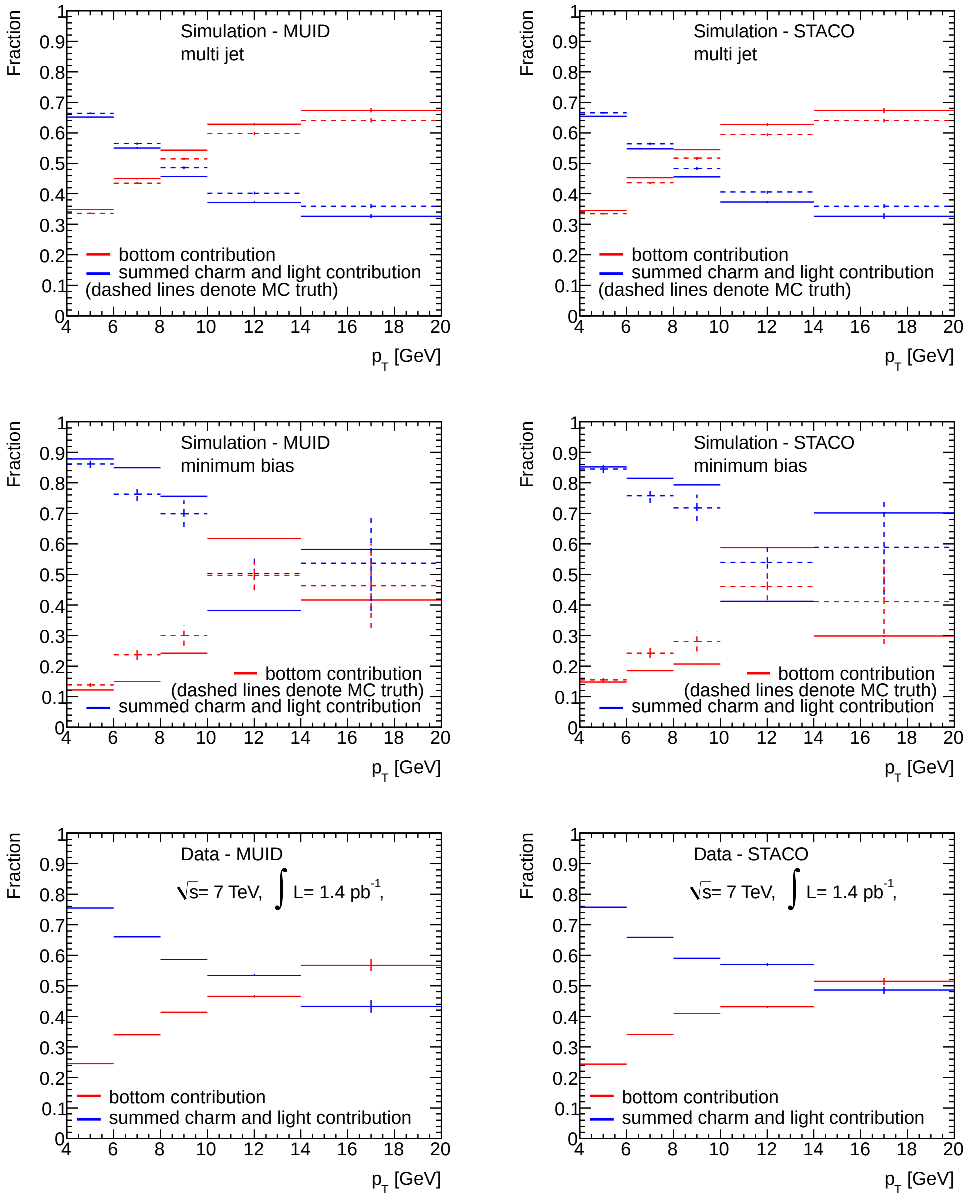

(a) Results for muons reconstructed with the MUID algorithm.

(b) Results for muons reconstructed with the STACO algorithm.

Figure 5.7.: Final results for the template approach applied on dijet (top) and minimum bias Monte Carlo (middle) as well as on data (bottom) for both muon reconstruction algorithms. The fraction is given in the following bins of the muon transverse momentum: [4; 6] GeV, [6; 8] GeV, [8; 10] GeV, [10; 14] GeV and [14; 20] GeV. The dashed lines indicate the true fraction as produced by the generator of the Monte Carlo sample while the error denotes the statistical uncertainty. The given errors for the fitted fractions and full lines respectively is the statistical uncertainty on the final fitting parameters only. No systematic uncertainties are shown. The agreement between true and fitted fraction is rather poor in case of the minimum bias Monte Carlo due to low statistics and the in consequence increased freedom of the fit.

contributing with about 3% [96] and the jet energy scale contributing with about 5% [115]. Systematic uncertainties due to the jet and muon direction resolution and the reconstruction efficiencies are not explicitly considered. The results of the pseudo-experiments already give a hint for the size of these effects and therefore partially included them. To be conservative an extra uncertainty of about 2% is applied nevertheless. Assuming these errors to be uncorrelated, the total systematic uncertainty is approximately 10%.

In conclusion the final fractions determined by the fit to data agree within the errors for the two reconstruction algorithms and are also in agreement with the true fractions suggested by the minimum bias Monte Carlo, which should be close to real data. Further investigations regarding the modeling of the bottom production and fragmentations are not performed with this early data of 2010 because of the high systematic uncertainties, in parts caused by the low statistics of the samples used to obtain the flavor template functions. With the full statistics of data taken in 2011, the additional knowledge of the detector and therefore better estimates for systematic uncertainties and finally data driven approaches to obtain samples dominated by the different flavors, the presented approach should give reliable results for the muon production fractions from the various contributions. However due to the increase of the trigger threshold of the lowest unprescaled muon trigger from 4 GeV used in early 2010 data taking periods to 18 GeV for 2011 data, studies of the kinematic region presented here become more difficult. Furthermore cross checks to results obtained by the flavor tagging group should be done. In a second iteration of this analysis most of the suggested improvements are considered [116].

5.2. Resolution estimation of the ATLAS muon spectrometer through sagitta studies

Beside a good understanding of the muon spectrum and the related production processes another important issue is to measure the muon momentum as precise as possible. For combined muons there are two independent and in some sense complementary measurements done. In the inner detector charged particles are bent in the Rϕ-plane due to the solenoid field along the z-axis. Therefore it is possible to measure very precisely the transverse component of a particle's momentum p_{T}. The muon spectrometer though is embedded in a toroid field along the ϕ-coordinate and in consequence charged particles are bent in the RZ-plane. Hence the precision measurement in the muon spectrometer is the particle's momentum projected on the RZ-plane while the full momentum is reconstructed including the less precise measurement of the θ and the ϕ-coordinate.

In spite of the weaker toroid field of ~ 0.5 T (~ 0.4 to 0.7 T) in the muon spectrometer barrel (end-cap) compared to the 2 T solenoid field in the inner detector it is possible to perform a more accurate measurement with the spectrometer for muons with high transverse momentum. The lever arm measured in the muon spectrometer can be much larger due to its enormous dimensions and a high resolution in the bending plane at the same time. In figure 5.8 the corresponding uncertainties of the transverse momentum measurement performed with the inner detector and the muon spectrometer are presented. At about $p_{\mathrm{T}} \approx 80$ GeV the relative uncertainty of muon transverse momentum measurement in the inner detector begins to grow linearly while the increase is stronger than for the muon spectrometer.

Besides the actual measured resolution figure 5.8 also shows the resolution for simulated data produced during the 2011 production campaign. Due to idealized and optimistic conditions in the simulation, the resolution is better than for real data. There are many efforts ongoing to adjust the resolution extracted from Monte Carlo simulation to the one obtained from real data. One aspect of the endeavors in the muon spectrometer software is explained in more detail

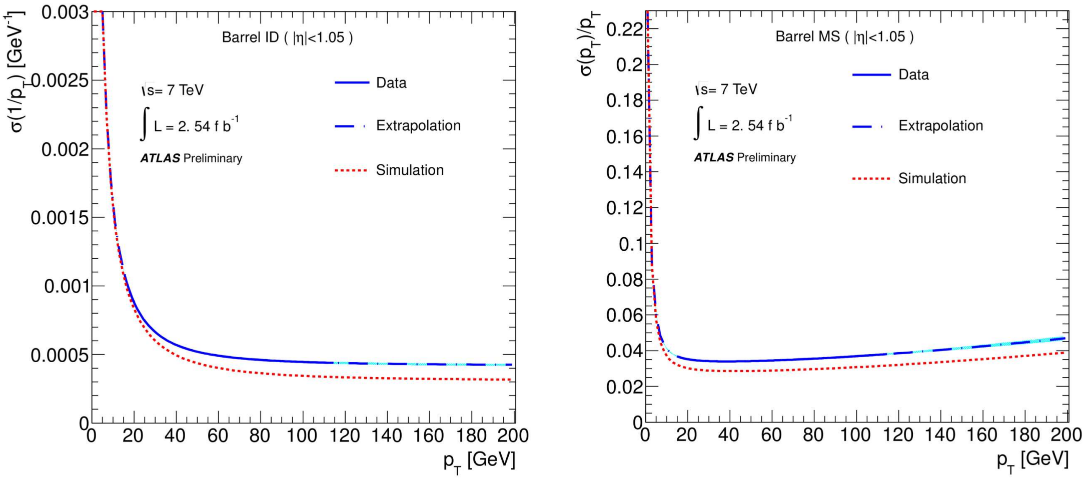

(a) Muon momentum resolution in the barrel region of the inner detector. The applied resolution function accounts for multiple scattering and intrinsic resolution.

(b) Muon momentum resolution in the barrel region of the muon spectrometer. The applied resolution function accounts for the energy loss in the calorimeters, multiple scattering and intrinsic resolution.

Figure 5.8.: Muon momentum resolution for the inner detector and muon spectrometer measurement [117]. For data the solid line indicates the fit region while the dashed line the fit extrapolation. The light blue band denotes the uncertainty, taking into account statistical and systematic errors and the correlation of the parameters. The red line corresponds to the resolution in the Monte Carlo simulation extracted from the 2011 production campaign. The presented results are derived from muons reconstructed with the MUID algorithm.

hereafter. Therefore it is necessary to understand at the first glance the precision measurement of the muon spectrometer and the various contributions to the resolution. Figure 5.9 shows the relative uncertainty on the transverse momentum measurement in the spectrometer as function of the p_{T}, but with the different contributions split up. For a wide range from about 20 GeV to 200 GeV of transverse momentum the dominant fraction of the uncertainty is caused by multiple scattering.

The precise measurement of the momentum projected on the RZ-plane in the spectrometer is amongst others based on an accurate determination of the sagitta Δ, i.e. the depth of the arc of the muon trajectory like it is defined in figure 5.10. The correlation can be obtained easily by estimating the momentum with the Centrifugal force and the Lorentz force [14, 118]

$$p_{\mathrm{RZ}}\,[\ \mathrm{GeV}] \approx 0.3 \times B_{\phi}\,[\mathrm{T}] \times R\,[\mathrm{m}] \sim \frac{1}{\Delta} \tag{5.7}$$

where B_{ϕ} is the magnetic field along ϕ and R is the radius of the bending. The sagitta enters inversely via the determination of R. For high momenta the radius increases while the sagitta gets smaller. A good knowledge of the magnetic field and the positions of the chambers is mandatory as well, but not discussed here. For medium transverse muon momenta the main contributions to the sagitta resolution σ_{Δ} are the intrinsic resolution σ_{int} due to single tube resolution and chamber-to-chamber alignment and the uncertainty introduced by multiple scatter σ_{ms} which is addressed in detail in this study. In complete the resolution is calculated as

$$\sigma_{\Delta} = \sqrt{\sigma_{\mathrm{int}}^2 + \sigma_{\mathrm{ms}}^2} \tag{5.8}$$

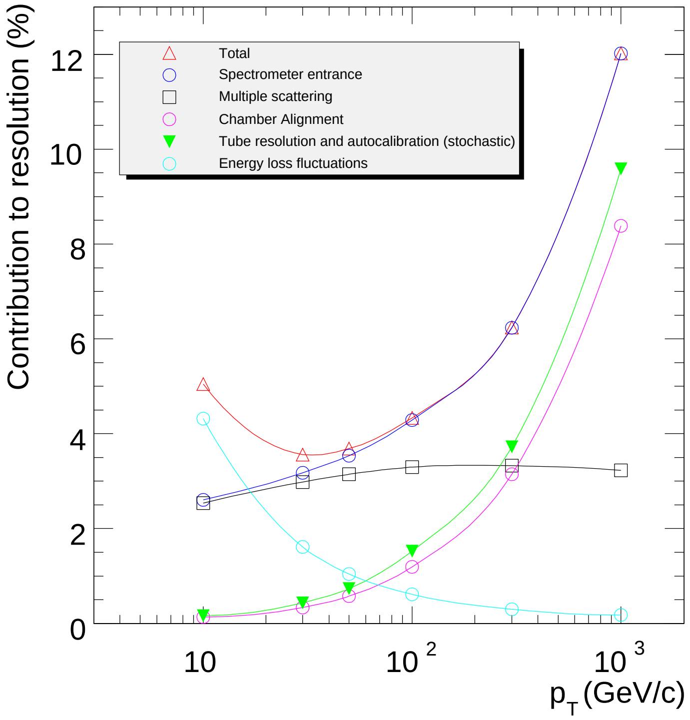

Figure 5.9.: Contributions to the momentum resolution for muons reconstructed in the muon spectrometer as a function of the transverse momentum for $|\eta| < 1.5$ [119]. The alignment curve is for an uncertainty of 30 µm in the chamber position.

Since the focus is on multiple scattering effects, muons above $p_{\mathrm{T}} = 100$ GeV are not considered and it is possible to fix the intrinsic resolution to a constant value $\sigma_{\mathrm{int}} = K0 = 100$ µm which is a good approximation to the design value [118, 53]. For a more detailed treatment of the intrinsic resolution, the Glückstern formulas [120] can be used. To get an estimate of the contribution due to multiple scattering and relate it to the material, a first step is to express σ_{ms} in terms of other quantities defined in figure 5.10. By applying the intercept theorem and the small-angle approximation one ends up with [118, 121]

$$\sigma_{\mathrm{ms}} = \frac{(b_M - b_I)(b_O - b_M)}{(b_O - b_I)} \cdot \sigma_{\theta_0} \tag{5.9}$$

In case of charged particles, like muons, most of the deflection is caused by Coulomb scattering from nuclei [14]. The theory of Molière [122] gives a good representation of the scattering distribution for small angles using roughly a Gaussian. Though for angles a few times larger than the width of the Gaussian the scattering behaves like Rutherford scattering because the tails are larger. Since for most applications the use of the Gaussian is sufficient for the central 98% of the angular distribution it is also applied in this analysis with a width given by [123]

$$\begin{aligned} \sigma_{\theta_0} &= \frac{13.6\text{ MeV}}{\beta c p} z \sqrt{x/X_0}\,[1 + 0.038\ln(x/X_0)] \\ &\approx 13.6\text{ MeV}\sqrt{\langle x/X_0\rangle}\ \cdot\ p^{-1} \end{aligned} \tag{5.10}$$

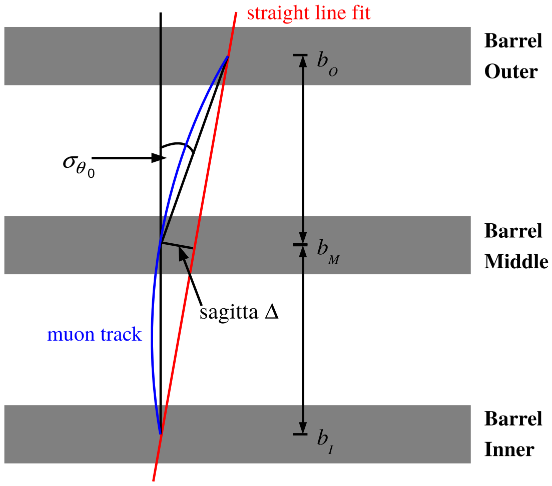

Figure 5.10.: Definition of sagitta Δ for the barrel region and declaration of the quantities b_O, b_M, b_I and the uncertainty in the angle σ_{θ_0}.

where p is the momentum, βc is the velocity and z is the charge of the incident particle. The thickness x/X_0 of the scattering medium is given in terms of radiation lengths. In equation (5.10) natural units are used while the velocity is approximated with the speed of light and the charge is set to $z = 1$. Also the logarithmic term is neglected. This is a valid approximation since from figures 4.5(a) and 4.5(b) the thickness in terms of radiation lengths can be estimated to be $\sim 12 - 13$ in small barrel sectors, $\sim 3 - 4$ in large barrel sectors, $\sim 18 - 20$ in small end-cap sectors and $\sim 30 - 34$ in large end-cap sectors. In any case the logarithmic term would not contribute more than about 20% for regular sectors. Inserting equation (5.10) in equation (5.9) gives

$$\sigma_{\mathrm{ms}} = \frac{(b_M - b_I)(b_O - b_M)}{(b_O - b_I)} \cdot 13.6\ \mathrm{MeV}\sqrt{\langle x/X_0\rangle}\ \cdot\ p^{-1} \tag{5.11}$$

$$\approx \sqrt{\langle x/X_0\rangle}\frac{K1'}{p} \approx \frac{K1}{p} \tag{5.12}$$

where $K1'$ and $K1$ are assumed to be constant values and valid for all muons. In fact, the distances b_O, b_M and b_I between the barrel chambers are only the same for muons which pass the spectrometer in the same angle. The difference in the relative spacing is up to tens of centimeters for muons hitting the spectrometer perpendicular compared to those passing in the maximum angle. In consequence the value of $K1'$ is about $4 - 5\%$ increased which should be considered as a systemic uncertainty. For the final approximation and the constant $K1$ respectively, it is presumed that the average thickness in terms of radiation lengths is the same for all muons. At least for common sectors this is indeed mostly valid, but for example not in the feet region which therefore is excluded. Eventually the sagitta resolution can be written as a function only depending on the momentum. In the setup of the barrel the momentum can even be replaced by the transverse momentum since in this case the sagitta is understood as the depth of the arc along in the RZ-plane where the bending is assumed to perfectly take place. The final dependency reads [118, 121, 124]

$$\sigma_\Delta = f(p_\mathrm{T}) = \sqrt{(K1/p_\mathrm{T})^2 + K0^2} \tag{5.13}$$

By fitting this function, the sagitta resolution can be measured in Monte Carlo data and real data to check if the material budget and in consequence the multiple scattering in the simulation is in agreement to the one extracted from data. To separate effects like a possibly insufficiently well known magnetic field, the sagitta resolution is studied during runs with the toroid field turned off. During this dedicated detector condition the muons' trajectory is bent in the solenoid field of the inner detector to measure the momentum while in the muon spectrometer it is a straight line. Besides sagitta studies the actual purpose for data taken without toroid field is to align the chambers. During 2008 and 2009 these kind of analyses had been performed with cosmic muon data [124, 125] while in 2010 and 2011 ATLAS also recorded a small amount of collision data with the toroid field disabled.

In this study about 4.9 pb^{-1} recorded in 2011 are analyzed and compared to dedicated Monte Carlo simulation. In contrast to collision data though the simulated data does not include the full inclusive production spectrum, but consist of single muon events. These positive and negative charged single muons are shot without any underlying physics process isotropically in ϕ and $|\eta| < 2.7$ and flat distributed within the transverse momentum range $p_\mathrm{T} \in [5; 60]$. In data though the transverse momentum distribution is exponentially decreasing, but it is assumed that the impact on the results is negligible because in the transverse momentum bins introduced later the yields are roughly flat for data as well. While one sample was simulated with the software version and configuration of the production campaign of 2010, the other one was produced with an individual setup close to 2011 production. In table 5.2 a full summary of the real data and Monte Carlo simulation is given.

type	run number	muon spectrometer layout	number of events	luminosity in nb^{-1}
data	177986	R.04.06	2999736	2439
data	178020	R.04.06	517016	587
data	178021	R.04.06	1819624	1389
data	178026	R.04.06	467943	474
	MCID		number of single muons	software release
MC	107370	R.04.05	499977	16.0.2.6
MC	107370	R.05.01.02	199000	16.6.2.3

Table 5.2.: Used real data recorded in 2011 and Monte Carlo simulation with solenoid field enabled, but toroid field disabled. In the 3rd column the prefix "MuonSpectrometer-" is skipped for all the entries. The referred software releases are of the type "AtlasProduction". The MCID is the Monte Carlo sample identifier.

Due to the limited statistics in data there is no requirement on the event selection including no special trigger demand besides a signal of any muon trigger. The sagitta is calculated from segments found in the calibration stream data by the Moore algorithm [126] which is part of MUID. These segments have to be matched to a combined muon track though none of the track parameters are used for the sagitta calculation. The following critera have to be fulfilled by the segments:

- ▷ number of segment hits:
  more than 4 in inner barrel stations, more than 3 in middle and outer barrel stations
- ▷ matching χ^2 divided by the degrees of freedom less than 10

There are neither additional quality requirements on the inner detector track nor on calorimetric or track isolation applied. Therefore the real data sample is diluted by muons of pion and kaon decays in flight or even heavy flavor decays. The energy loss in the calorimeters was accounted by subtracting 2.8 GeV from the transverse momentum measured in the inner detector for all muons though the energy loss actually increases with the pseudorapidity. Nevertheless this is still a good approximation, especially for the barrel region. Because of the ATLAS feet structure and the associated very inhomogeneous material distribution any segments found in the sectors 11/12 ($\sim -104°$ to $-149°$) and 14/15 ($\sim -31°$ to $-76°$) are not considered. In figure 5.11 the obtained distributions and fitting results are presented. Table 5.3 gives the rounded differences in the $K1$ parameter and the derived approximation for the suggested missing thickness in terms of radiation length as well as the conversion to aluminum for the two geometrical layouts used in simulation.

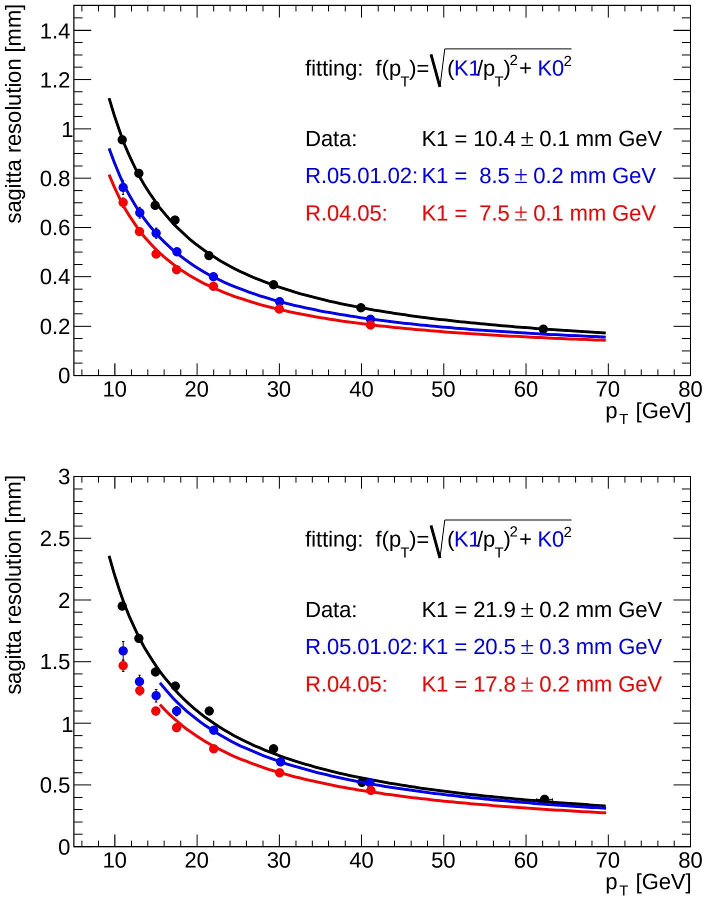

Figure 5.11.: Fit of equation (5.13) to real data and simulation introduced in table 5.2 while only the barrel large (top) and small (bottom) sectors are considered. The found segments and resulting sagitta values are binned according to the reconstructed transverse momentum of the matched inner detector track. The transverse momentum bins applied are: [10.; 12.] GeV, [12.; 14.] GeV, [14.; 16.] GeV, [16.; 19.] GeV, [19.; 25.] GeV, [25.; 35.] GeV, [35.; 50.] GeV and [50.; 100.] GeV. The relative difference between data and simulation is summarized in table 5.3 and further conclusions are given in the text. The quoted errors do not include any systematic uncertainties, but are purely resulting from the fit itself. The fundamental disagreement between large and small sectors originates from the material distribution. While in large barrel sectors there is a comparably little amount of material between the three chamber layers there are the barrel toroid coils installed in the small barrel sectors. This is also visible in figure 4.5.

sectors	muon spectrometer layout	$1 - \frac{K1_{MC}}{K1_{Data}}$	suggested missing x/X_0	corresponding thickness in terms of Al (in cm)
small	R.05.01.02	6%	12%	12.8 - 13.9
	R.04.05	19%	34%	36.3 - 39.3
large	R.05.01.02	18%	33%	8.8 - 11.7
	R.04.05	28%	48%	12.8 - 17.1

Table 5.3.: Summary table of the relative differences in the $K1$ fitting parameter obtained from various detector layouts in simulation compared to data. The values for the corresponding suggested missing thickness in terms of radition lengths is given as well as the conversion to the thickness in terms of aluminium ($X_0^{\mathrm{Al}} = 8.9$ cm) while the estimation of the average radition length per sector quoted in the text is used. All calculations are done with the central values. The relative difference in the small sectors is lower compared to the large sectors since the magnet coils installed in the small barrel sectors reflect a sizable amount of radiation lengths.

Like it is described in section 4.2.2 and figure 4.5 respectively there are new structures added in the layout called MuonSpectrometer-R.05.01.02 with respect to MuonSpectrometer-R.04.05. One example for the additional material are the trigger boxes of the RPC chambers which cause approximately 0.2 radiation lengths of additional thickness for the large barrel sectors. As indicated by the figure, for the end-cap there are no sizable difference expect for additional structures in the feet region, i.e. in the sectors 11/12 and 14/15, which are anyway not considered in this study. Therefore, in the end-cap region data is only compared to the simulated sample including layout MuonSpectrometer-R.05.01.02.

However, the definition of the sagitta needs to be modified for the end-cap region. The reason is that the material distribution is not roughly equivalent between the inner and middle chambers and the middle and outer chambers as it is true for the barrel, but material is primarily located between the inner and middle chambers because of the end-cap toroid installation. There is pretty much nothing other than air between the middle and outer chamber layers in the end-cap region and therefore the majority of multiple scattering takes place because of the end-cap toroid. In consequence the definition of the sagitta Δ given in figure 5.10 has to be modified to the one presented in figure 5.12 which accounts for the changed environment properly. The track sagitta eventually can be estimated as

$$\Delta = \frac{1}{4}\Lambda \tag{5.14}$$

where Λ is illustrated in figure 5.12 as well. For the selection of the segments the same quality criteria like for the barrel are applied while the number of segment hits are adopted for end-cap stations.

Because of the different setup of the chambers in the end-cap the muon transverse momentum is no longer perpendicular to the three station layers. Hence the approximation of the muon momentum p with the muon transverse momentum p_{T} considered in equation (5.13) is not valid any more. The functional dependence and fitting function respectively reads in consequence:

$$\sigma_\Delta = f(p) = \sqrt{(K1/p)^2 + K0^2} \tag{5.15}$$

The results are presented in figure 5.13 and table 5.4. In conclusion, in the barrel, there is indeed a better agreement of real data and simulated data achieved with the more recent version of the

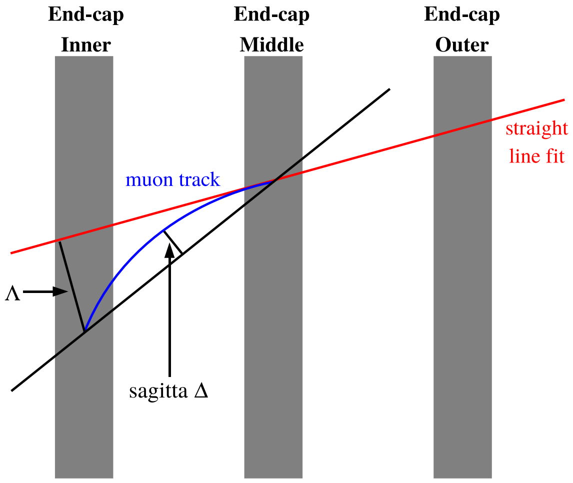

Figure 5.12.: Definition of sagitta Δ for the end-cap region. The quantity Λ is the distance between the segment found in the inner end-cap chamber and the straight line extrapolation of the segments reconstructed in the middle and outer chambers.

detector description. Though the difference is still non negligible, but there are no more single candidate structures left to explain this mismatch. This pertains to the end-cap region as well, even though the agreement of data compared to simulation is worse there. Nevertheless it is still reasonable for the time being. In order to understand additional contributions to the difference, it is necessary to elaborate about the method, systematic uncertainties and other sources which affect the sagitta resolution.

sectors	muon spectrometer layout	$1 - \frac{K1_{MC}}{K1_{Data}}$	suggested missing x/X_0	corresponding thickness in terms of Al (in cm)
small	R.05.01.02	28%	48%	109 - 124
large	R.05.01.02	23%	41%	77 - 85

Table 5.4.: Summary table of the relative differences in the $K1$ fitting parameter obtained from detector layout MuonSpectrometer-R.05.01.02 in simulation compared to data. The values for the corresponding suggested missing thickness in terms of radition lengths is given as well as the conversion to the thickness in terms of aluminium ($X_0^{\mathrm{Al}} = 8.9$ cm) while the estimations of the average radition length per sector quoted in the text are used. All calculations are done with the central values. The relative difference in the large sectors is lower compared to the small sectors since the magnet coils installed in the large end-cap sectors reflect a sizable amount of radiation lengths.

Although the fitting functions given in the equation (5.13) and (5.15) were derived by applying several rough approximations, this is ruled out to be a leading contribution for the difference since the finally obtained results are derived by the same formula for data and simulation. Therefore both are affected by the approximations in the same way. A good candidate however is the dilution of the data sample by charged pion and kaon decays in flight. As pointed out in section 5.1 these are sources for real muons and the inner detector track can be matched quite convenient to the track in the muon spectrometer while there is a difference in the momentum. In

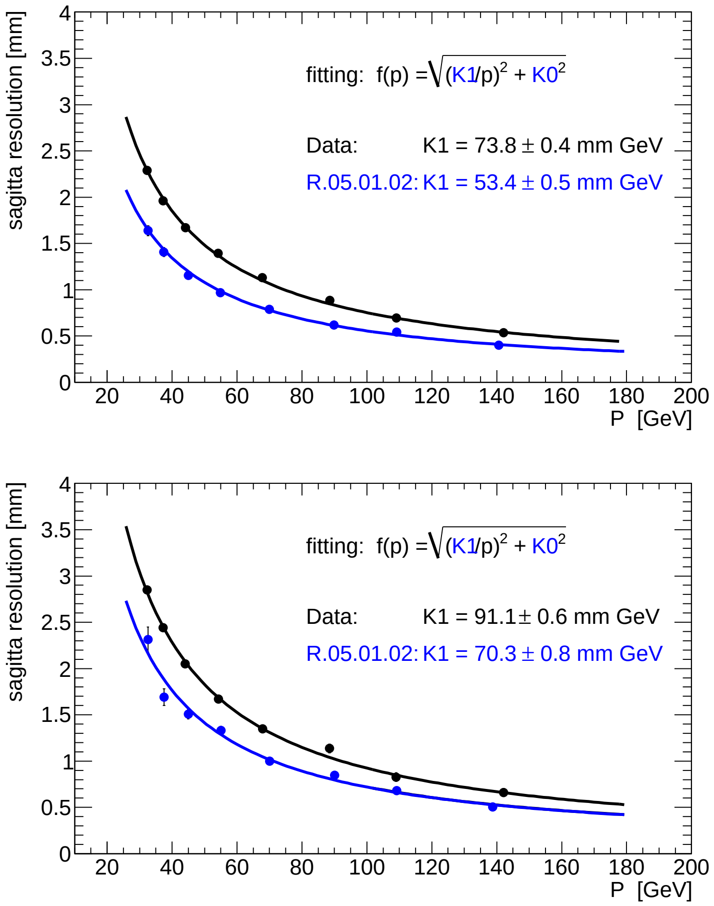

Figure 5.13.: Fit of equation (5.15) to real data and Monte Carlo simulation introduced in table 5.2 while only the end-cap large (top) and small (bottom) sectors were considered. The found segments and resulting sagitta values are binned according to the reconstructed momentum of the matched inner detector track. The momentum bins applied are: $[30.;35.]$ GeV, $[35.;40.]$ GeV, $[40.;50.]$ GeV, $[50.;60.]$ GeV, $[60.;80.]$ GeV, $[80.;100.]$ GeV, $[100.;120.]$ GeV and $[120.;160.]$ GeV The relative difference between data and simulation is summarized in table 5.4 and further conclusions are given in the text. The quoted errors do not include any systematic uncertainties, but are purely resulting from the fit itself. The fundamental disagreement between large and small sectors originates from the material distribution. While in small end-cap sectors there is a comparably little amount of material between the inner and middle chamber layers there are the end-cap toroid coils in the large end-cap sectors. This is also visible in figure 4.5.

the dedicated data sample without toroid field and the calorimeters not functional all the time, it is not possible to reject these objects consistently. In consequence the transverse momentum spectrum in data is assumed to be harder than it really is. The extracted data distribution is shifted to the right so that the derived $K1$ value is increased and therefore the difference to simulated data grows. Due to the rather complicated software setup needed to produced Monte Carlo data without toroid field, studies on the fraction of QCD events in the muon selection and their impact are still outstanding. In particular for the end-cap region the effect of wire sagging might have a deeper impact because the chambers with the longest tubes and therefore the largest sagging of the wires are installed there. Also the applied correction of 2.8 GeV for the energy loss in the calorimeters is underestimating the actual loss of energy because the amount of material increases with the pseudorapidity.

Besides there is another, probably less important, but nevertheless perhaps partially contributing source for the discrepancy of real data and simulated data, namely the used scattering model. For the 2010 production campaign including the simulation with the detector layout MuonSpectrometer-R.04.05, the Geant4 version 9.2 is used which simulates muon scattering with the Urban model [127] based on the scattering theory of Lewis [128] and related to the introduced theory of Molière. The agreement between real data and simulation with this configuration is convenient. The simulation with layout MuonSpectrometer-R.05.01.02 though is performed with Geant4 version 9.4. This version is modeling the muon scattering according to the theory of Wentzel [129] combined with a separated model for coulomb scattering [130]. This setup is also applied during the production campaign of 2011, but a detailed study reveals that the scattering is slightly underestimated. Therefore it is possible that another Monte Carlo simulation with toroid field disabled and the Urban scattering model fits even better to data.

Even if this study suggests to add more material in the simulation it can be concluded that the detector layout MuonSpectrometer-R.05.01.02 already gives a very good agreement within the chosen setup and the expounded systematic uncertainties. Nevertheless there are ongoing efforts and more recent versions of the detector layout in preparation which achieve an improvement. Moreover the amount of material is not the only contribution to the resolution, but issues like chamber alignment and deformations, the mentioned wire sagging and the r-t-relations have an impact, too. Recent studies exposed that with a proper treatment of the chamber alignment in simulation, the extracted width of the reconstructed Z boson mass agrees very well with the one obtained from real data (see figure 5.14). Once the sagitta resolution is analyzed again with all possible contributions the agreement of simulation and real data is most likely striking.

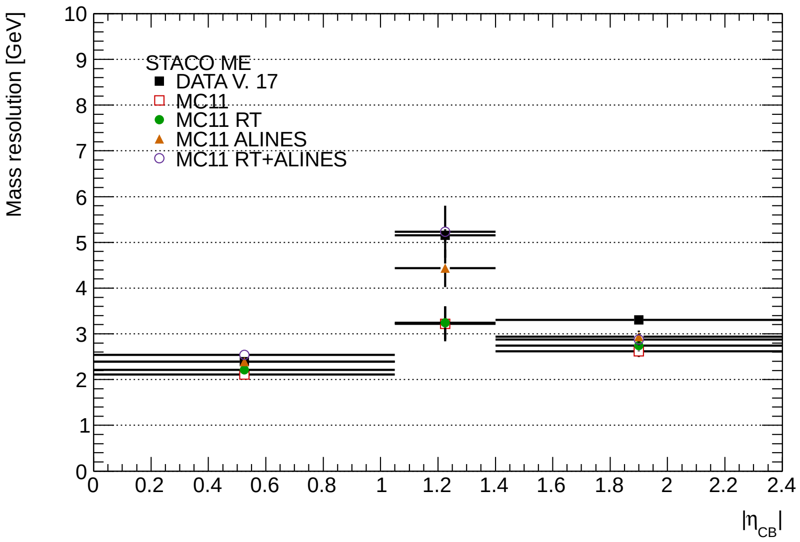

Figure 5.14.: Resolution of the Z boson mass in data (filled squares) and simulation with various configurations. While the Monte Carlo simulation of the production campaign in 2011 (open squares) and only applying proper r-t-relations on top (filled circles) show remaining discrepancies compared to data, there is rather small difference once alignment effects are considered for simulation as well (triangles). Once alignment and r-t-relations are taken into account for simulation (filled circles) the agreement is even more improved.

5.3. Extension of the muon spectrometer acceptance toward high pseudorapidities

In section 3.3.1 it is mentioned that the inner detector acceptance ends at $|\eta| \approx 2.5$ while the muon spectrometer is capable to reconstruct tracks up to $|\eta| \approx 2.7$. By including these additional muons in physics analyses with especially multi-lepton final states, the specific signal yield can be increased by a non negligible amount like it is shown in section 6.4 of the following chapter. In searches the sensitivity is also increased due to a corresponding gain in acceptance. Before muons reconstructed beyond $|\eta| = 2.5$ can be considered and judged reliable, their performance has to be studied in detail, which is the topic of this section and available in [55].
In figure 3.9 a schematic view of the RZ-plane of the ATLAS detector elements is presented. The ATLAS muon spectrometer in the high pseudorapidity region $2.5 < |\eta| < 2.7$ is equipped with precision chambers of the CSC technology at the innermost station layer and end-cap MDTs at the middle (EM) and outer (EO) layers as well as trigger chambers of the TGC technology. The full acceptance of the inner detector is not given for this region, but there are tracks at the boundary which transverse layers of the SCT and pixel detectors like it is shown in figure 5.15.

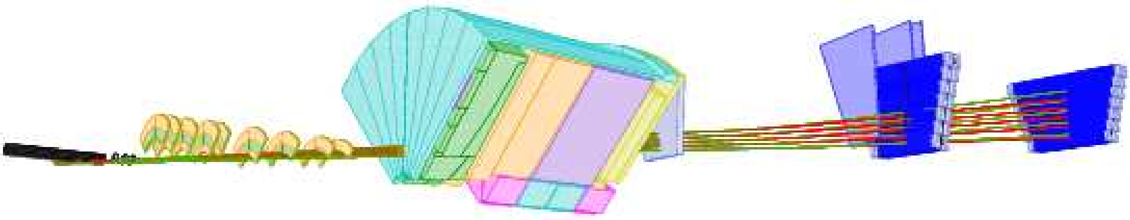

Figure 5.15.: Schematic view of the ATLAS detector elements passed by muons with transverse momenta of 10 GeV (green) and 15 GeV (red) when they are bended in the toroid magnetic field. The pseudorapidity of the tracks is in the range [2.5; 2.7] in steps of 0.05.

A common approach to study the performance of objects and to characterize them is the so called "tag and probe method". Usually this method is applied on an event or object selection of a well understood underlying physics process with at least two characteristic signatures, like two particles in the final state, while the performance of one of them is known already. There are rather tight requirements on this well-known object which tags the event. For the probe object, i.e. the one targeted in the performance analysis, the selection criteria are typically rather loose and just enough to assign it to the physics process. Especially the quantities which are subject of the analysis must not be included in the selection criteria. In case of muons with high pseudorapidity the process of choice is the Z boson decay into a muon pair. The tagging muon is required to be reconstructed in the central region with full inner detector coverage while the probe muon is in the region $|\eta| > 2.5$. Due to the fact that the muon trigger acceptance ends at $|\eta| = 2.4$ only the central muon is able to trigger the event. Therefore any trigger bias is ruled out in the following studies as a matter of principle.
The analysis is based on data from proton-proton collisions at a center of mass energy of 7 TeV recorded between March and June 2011. After selecting data of good quality which is suitable for proper muon reconstruction, the total integrated luminosity used is $1.2\,\mathrm{fb}^{-1}$ and $740\,\mathrm{pb}^{-1}$ respectively. For comparison with simulation dedicated Monte Carlo samples are used. The

$Z \to \mu\mu$ signal is generated with MC@NLO [67] and with Pythia version 6.4 [112]. Additionally several background processes have been considered. Pythia was used to generate the decay of a Z boson to a pair of τ leptons ($Z \to \tau\tau$) and the decay of a W boson to a muon and a neutrino ($W \to \mu\nu$). The sample of $b\bar{b}$ decays with jets in the final state which include two muons was produced with PythiaB [131]. To model $Z+$ jets Alpgen [68] was used while the $t\bar{t}$ background was generated with MC@NLO. Both Alpgen and MC@NLO generators are interfaced with Herwig [132] for parton shower hadronization and Jimmy [75] for simulation of the underlying event. In appendix C.1 the full set of Monte Carlo samples is given.

5.3.1. Selection of muon pairs

The events are required to possess a signal of a single muon high transverse momentum event filter trigger with a threshold of 18 GeV. To reject non-collision background at least one primary vertex with more than 2 tracks associated has to be reconstructed in the event. The relative z position of the primary vertex with respect to the nominal interaction point must not be more than 2 cm.

The tag muon, i.e. the one reconstructed in the central region of the detector, has to be combined. The inner detector track has to satisfy a set of quality criteria listed in table 5.5, where related definitions are given, too. A minimum number of hits in the silicon detectors are demanded for the tracks to be considered, while dead or missing sensors crossed are counted as hits. If the muon trajectory is reconstructed within the geometrical acceptance of the transition radiation tracker, it has to be successfully extended into that detector. This is enforced by dedicated requirements on the number of associated good hits and outliers in the TRT. These quality cuts are applied to suppress fake tracks and discriminate against muons from hadron decays.

muon spectrometer track requirements	
silicon hit requirement	• at least one hit in the B-layer or none expected • sum of pixel hits and crossed dead pixel sensors greater than 1 • sum of SCT hits and crossed dead SCT sensors greater than 5 • sum of pixel holes and SCT holes less than 3
TRT hit requirements	• $\lvert\eta\rvert \leq 1.9$: sum of hits and outliers greater than 5 and $\frac{\text{outliers}}{\text{hits+outliers}}$ less than 90% • $\lvert\eta\rvert > 1.9$: in case the sum of hits and outliers is greater than 5 the ratio $\frac{\text{outliers}}{\text{hits+outliers}}$ has to be less than 90%

Table 5.5.: A hit is defined as a measurement which is associated to the given track while a hole is an expected measurement which has not been assigned to the track. Material interactions, silicon inefficiencies or problems with the pattern recognition can result in such holes, but inactive modules are excluded from the definition. For the transition radiation tracker there are two types of outliers: Firstly these are straw tubes with a signal but not crossed by the near-by track or secondly a set of TRT measurements in the prolongation of the trajectory which, however, failed to form a smooth track in combination with the pixel and SCT hits. The requirements given in this table are determined by the ATLAS muon combined performance group and are recommended for any physics analysis of data taken in 2011.

To ensure that tracks are reconstructed with at least three muon stations there is an additional set of requirements on the hit quality of the track measured in the muon spectrometer. These demands are summarized in table 5.6 and include a veto on stations which are poorly aligned.

Central muons are rejected if their track in the inner detector or the muon spectrometer fails any of the requirements. To minimize the dilution of the selection by QCD processes, the scalar sum of the transverse momenta of other tracks inside a cone of $\Delta R = 0.4$ around the central muon track has to be less than 20% of the muon transverse momentum, i.e. the relative track isolation has to be less than 20%.

inner detector track requirements	
for regions without CSC	at least 6 hits in the inner, 4 hits in the middle and 4 hits in the outer chamber layer of either the barrel or the end-cap
for regions with CSC ($\|\eta\| > 2.0$)	at least 2 hits measured by CSC η-strips, 4 hits in the end-cap middle and 4 hits in the end-cap outer chamber layer
general	tracks with hits in BEE, BIS7/8 or EE chambers are rejected, at least 2 ϕ hits associated to the track

Table 5.6.: The given quality criteria are used to ensure that tracks are reconstructed with three stations while poorly aligned stations are excluded.

Following the idea of tag and probe, there are no quality requirements on the track quantities of the muon reconstructed above $|\eta| = 2.5$. Though to assign it to a Z boson decay it is only considered if its charge differs from the charge of the central muon. In addition the invariant mass of the muon pair $m_{\mu\mu}$ has to be within a window around the Z boson mass. The type of the muon with high pseudorapidity can either be combined or stand alone. Due to low statistics in data, there are no calorimetric muons or segment tagged muons examined in this study, but these might be issue for further investigations. All results are obtained for both muon reconstruction algorithms, namely STACO and MUID.

5.3.2. Resolution of muons with high pseudorapidity

To study the Z mass resolution both muons are required to have a transverse momentum greater than 20 GeV and the invariant mass of the pair has to fulfill 70 GeV $< m_{\mu\mu} <$ 120 GeV. One of the muons is always reconstructed in the high pseudorapidity region. Motivated by the different instrumentation, the sample is subdivided in several non exclusive collections depending on the pseudorapidity of the central muon. The region $|\eta| < 2.5$ is chosen in order to examine the full detector acceptance where coverage from the inner detector is guaranteed. The barrel is checked by requiring $|\eta| < 1.05$, the end-cap without CSC chambers is covered by the region $1.3 < |\eta| < 2.0$, and the end-cap with CSC chambers falls in the region $2.0 < |\eta| < 2.5$ like it is mentioned in section 3.3.3.

The dimuon invariant mass is fitted by a convolution of the Z line-shape and two Gaussian functions modeling the detector resolution effects with the constraint that one Gaussian contains 85% of the dimuon pairs. The value reflects the fraction of muons included in the core Gaussian in simulation, for which the fit was applied free of any constraints. The function describing the Z line-shape includes the natural width of the Z boson, a term accounting for photon radiation and one for interference [133]

$$f(x) = A\frac{1}{x^2} + B\left(\frac{x^2 - \bar{x}^2}{(x^2 - \bar{x}^2)^2 + \sigma_x^2\bar{x}^2}\right) + C\left(\frac{x^2}{(x^2 - \bar{x}^2)^2 + \sigma_x^2\bar{x}^2}\right) \tag{5.16}$$

where x denotes the reconstructed invariant mass of the muon pair $m_{\mu\mu}$ and $\bar{x}$ and σ_x are free parameters of the fit. The values of A, B and C are fixed and determined from truth information in simulation. The quality of the fit function's description of the true Z boson line-shape in simulation is tested to validate the approach.

For both reconstruction algorithms the results obtained from data and $Z \to \mu\mu$ Monte Carlo are summarized in table 5.7 while the fit on the invariant dimuon mass distributions is presented in detail in appendix C.2. The findings are compatible with results of previous studies on the Z mass resolution using muons in the high pseudorapidity region collected during 2010 data taking [134].

STACO reconstruction algorithm					
pseudorapidity of the central muon	$\lvert\eta\rvert<2.5$	$\lvert\eta\rvert<1.05$	$1.3<\lvert\eta\rvert<2$	$1.3<\lvert\eta\rvert<2.5$	$2<\lvert\eta\rvert<2.5$
data	2.68±0.02	2.28±0.04	2.84±0.04	2.90±0.03	2.99±0.05
simulation	2.24±0.03	1.98±0.05	2.35±0.05	2.40±0.04	2.49±0.06

MUID reconstruction algorithm					
pseudorapidity of the central muon	$\lvert\eta\rvert<2.5$	$\lvert\eta\rvert<1.05$	$1.3<\lvert\eta\rvert<2$	$1.3<\lvert\eta\rvert<2.5$	$2<\lvert\eta\rvert<2.5$
data	2.54±0.02	2.14±0.03	2.76±0.04	2.76±0.03	2.77±0.05
simulation	2.11±0.03	1.82±0.04	2.23±0.05	2.28±0.04	2.36±0.06

Table 5.7.: Invariant dimuon mass resolution obtained from data and simulation for both muon reconstruction algorithms. The results are given for various pseudorapidity selections of the central muon while the other muon is always required to be reconstructed in the high pseudorapidity region. The resolution and corresponding statistical error is given in units of GeV. There is no separation depending on the category of the muon reconstructed in the high pseudorapidity region.

In addition the presented values are consistent with published results which are available in appendix C.2 as well. There, the mass resolution is given in various pseudorapidity bins for the case if both muons are either combined or stand alone. It varies between 1.8(1.6) GeV and 2.6(2.0) GeV in data (simulation) for two combined muons, while for two muons reconstructed in the muon spectrometer only it lies between 3.4(2.8) GeV and 4.6(3.8) GeV. Since in this study one muon is always combined while the other one is reconstructed in the high pseudorapidity region and therefore mainly stand alone, the obtained results in table 5.7 are in between the quoted values. To adjust the resolution in simulation to the one observed in data the same transverse momentum smearing as used for muons in the end-cap region can in consequence be applied to muons reconstructed in the high pseudorapidity region. The corresponding implementation is provided in the package `MuonMomentumCorrections` used for general ATLAS offline data analyses.

5.3.3. Scale factor determation for muons in the extended region

In addition to the resolution the simulation is too optimistic regarding the reconstruction efficiency as well. For a proper use of muons with high pseudorapidity in physics analyses, and for comparisons of data and Monte Carlo it is needed to determine scale factors for the reconstruction efficiency. In order to extract these factors for muons above $|\eta| = 2.5$ outside the inner detector acceptance, it is not possible to apply the same tag and probe method like it is used in the barrel region [135]. If there was an inner detector track present it could serve in the identification of the probe track in the spectrometer, but in most cases this is not valid for muons with high pseudorapidity. For this reason the normalization to the Z boson yield is used. The efficiency scale factor is calculated by the double ratio

$$SF = \frac{N_{\text{Data}}^{Z \text{ bosons with } 1\mu \text{ in } |\eta|>2.5}}{N_{\text{MonteCarlo}}^{Z \text{ bosons with } 1\mu \text{ in } |\eta|>2.5}} \Bigg/ \frac{N_{\text{Data}}^{Z \text{ bosons with } 1\mu \text{ in } 2.2<|\eta|<2.5}}{N_{\text{MonteCarlo}}^{Z \text{ bosons with } 1\mu \text{ in } 2.2<|\eta|<2.5}} \tag{5.17}$$

where the numerator is the ratio of the number of Z boson candidates with one muon in the high pseudorapidity region found in data divided by the ones found in Monte Carlo. The denominator is the ratio of the number of Z boson candidates with one muon in the region $2.2 < |\eta| < 2.5$ found in data divided by the ones found in Monte Carlo. The second muon to form the Z boson candidate is central for both regions. With this approach the systematic uncertainty is kept small since there is no need to normalize the Monte Carlo yield to the integrated luminosity of the data.

The used Z boson candidates are formed by muon pairs with an invariant mass which differs at the most 12 GeV to the world best fit value of the Z boson mass, i.e. $|m_{\mu\mu} - m_Z| < 12$ GeV. The minimum transverse momentum of the central, tagging muon is required to be at least 20 GeV. Figure 5.16 shows the transverse momentum distribution of muons reconstructed above $|\eta| = 2.5$ in data and in signal as well as background Monte Carlo once requiring only track quality criteria plus two opposite charged muons and once after the full set of selection criteria. In the final selection the agreement of the transverse momentum distributions in data compared to Monte Carlo is very good and especially above 7 GeV the background is negligible. For both reconstruction algorithms figure 5.17 presents the derived reconstruction efficiency scale factors in 6 bins of the p_{T} of the muon in the high pseudorapidity region while the given errors correspond to the statistical uncertainty.

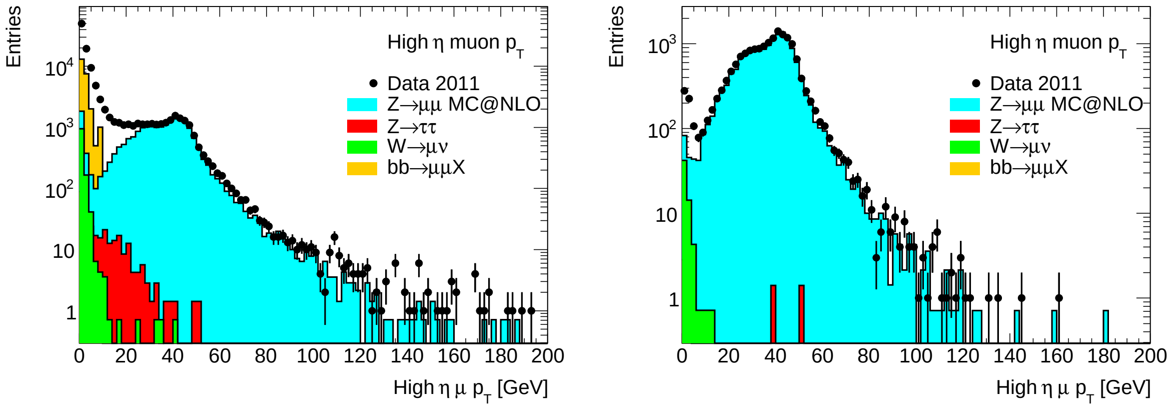

Figure 5.16.: Transverse momentum distribution of muons reconstructed in the high pseudorapidity region once with only basic selection criteria on the central muon (left) and once with the complete set of requirements to obtain Z boson candidates (right) applied. Points correspond to data and are given with statistical uncertainty. Solid lines indicate Monte Carlo simulation of the signal process $Z \to \mu\mu$ and various background processes scaled to the data luminosity of $1.2\,\text{fb}^{-1}$.

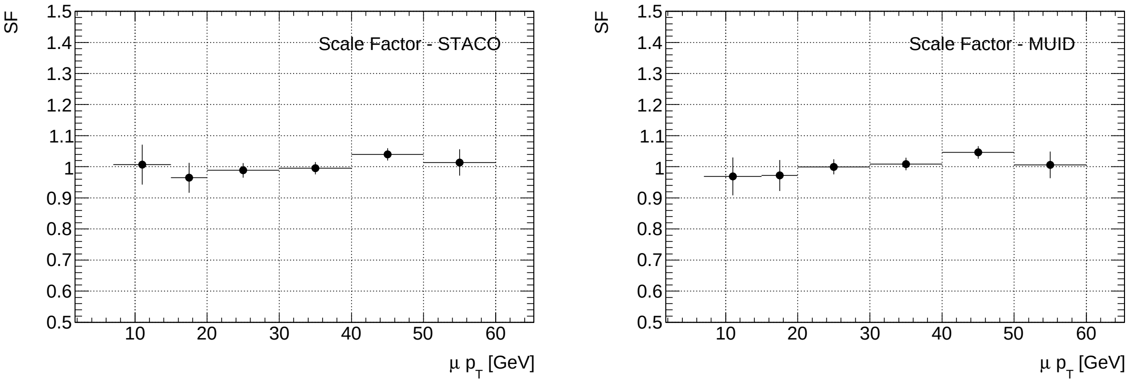

Figure 5.17.: Efficiency scale factors as a function of the transverse momentum of the muon found in the high pseudorapidity region by the STACO (left) and MUID (right) reconstruction algorithm. The given errors correspond to statistical uncertainties only.

Since above $p_{\mathrm{T}} = 7$ GeV the dilution of the selection by background processes is negligible the major uncertainty arises due to the finite resolution of the detector. This is considered as systematic uncertainty. The main contribution, namely the kinematics of the Z boson decay, is addressed by varying the transverse momentum, the isolation and the invariant mass requirements. The relative track isolation of the central muon is varied from 20% to 18% and the selection criteria on the transverse momentum of the central muon as well as on the mass window around the Z boson mass are each varied within approximately their resolution. In detail $|m_{\mu\mu} - m_Z|$ is reduced from 12 GeV to 10 GeV whereas the transverse momentum requirement on the central muon is increased from 20 GeV to 22 GeV. The latter two variations have the largest contribution to the systematic uncertainty. To obtain the total systematic uncertainty the individual systematic uncertainties are added in quadrature because they are considered to be uncorrelated. Table 5.8 summarizes the efficiency scale factors together with their systematic uncertainties. Like for the resolution these results are available in the package `MuonMomentumCorrections` used for general ATLAS offline data analyses.

STACO reconstruction algorithm						
p_{T}-Range [GeV]	7-15	15-20	20-30	30-40	40-50	50-60
scale factor	1.007	0.965	0.989	0.996	1.040	1.014
statistical uncertainty	0.064	0.048	0.024	0.020	0.020	0.042
systematic uncertainty	0.031	0.034	0.006	0.006	0.003	0.003

MUID reconstruction algorithm						
p_{T}-Range [GeV])	7-15	15-20	20-30	30-40	40-50	50-60
scale factor	0.970	0.972	0.999	1.009	1.046	1.006
statistical uncertainty	0.061	0.050	0.024	0.020	0.020	0.043
systematic uncertainty	0.032	0.041	0.006	0.006	0.003	0.001

Table 5.8.: Efficiency scale factors calculated with equation (5.17) and corresponding statistical as well as systematic uncertainty given in various ranges of the transverse momentum of the muon above $|\eta| = 2.5$ The results are given for the STACO and MUID reconstruction algorithm and presented in figure 5.17, too.

5.3.4. Hit quality of muon tracks with high pseudorapidity

To reduce the number of fake objects and poorly measured tracks it is mandatory to inspect the hit quality of muons reconstructed in the high pseudorapidity region and give recommendations for selection criteria. To accomplish this the tag and probe method introduced at the beginning is used, i.e. a central muon passing all basic quality criteria on the inner detector track and the track in the muon spectrometer is used to tag the event and the probe is selected in the region that is subject of the study. In order to perform a comparison to already well understood muon objects a control sample is defined as follows: The tagging muon is reconstructed within $|\eta| < 2.2$ and fulfills all quality criteria, while the probe muon is reconstructed in the region $2.2 < |\eta| < 2.5$. In case of the sample including muons with high pseudorapidity the central muon is reconstructed within $|\eta| < 2.5$ while the probe muon is found beyond. For both samples the introduced pairing is applied, i.e. the invariant mass has to be in the window $|m_{\mu\mu} - m_Z| < 12$ GeV and the muons have to differ in charge. In addition the central muon has to be relatively isolated regarding other tracks and has to have a transverse momentum above 20 GeV.

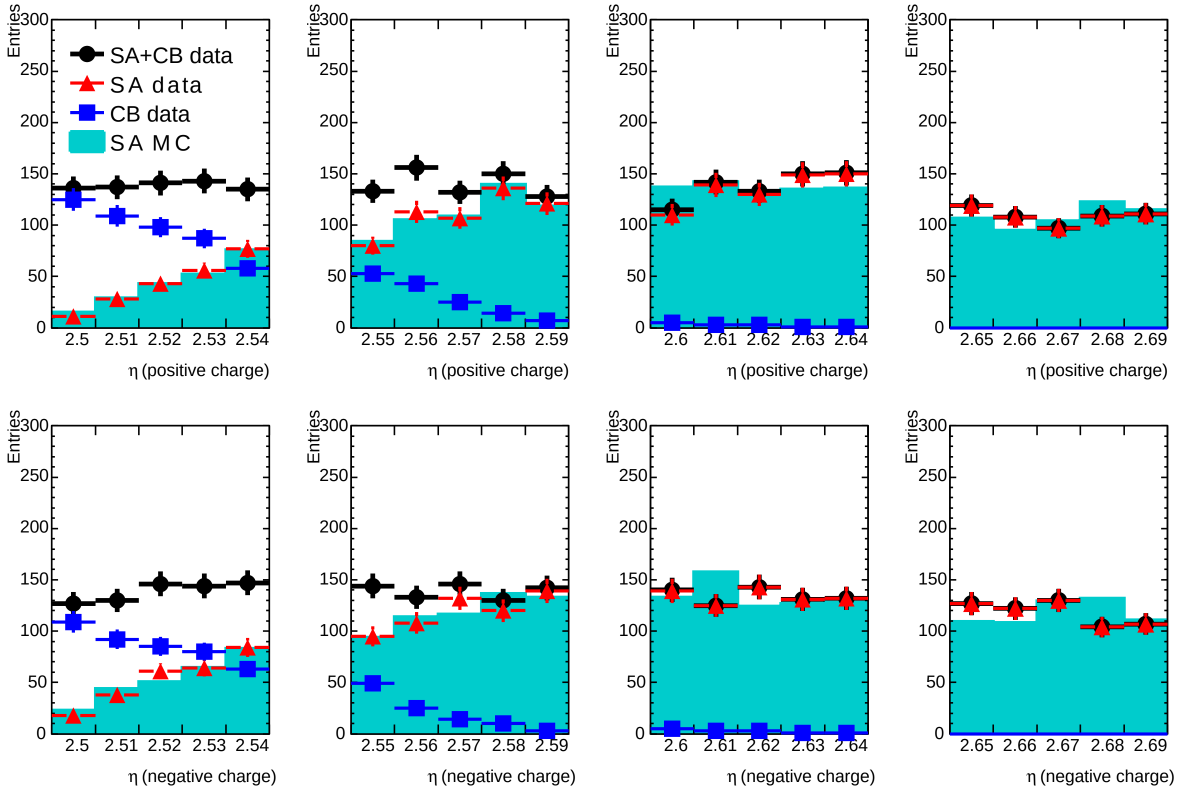

Figure 5.18.: Pseudorapidity distributions of the number of muons above $|\eta| = 2.5$ in data split up in the different reconstruction categories as well as in positive (top) and negative (bottom) charge. All quality and pairing criteria are applied. Red markers indicate stand alone muons while blue markers denote combined muons. Black markers represent the sum of both. The stand alone muons found in the $Z \to \mu\mu$ Monte Carlo are scaled to the data luminosity and superimposed as histogram. The results presented here are obtained from the STACO reconstruction algorithm while corresponding plots for the MUID algorithm can be found in figure C.4 of appendix C.3.

In the high pseudorapidity region there are still about 20% of combined muons, i.e. amongst others they are traversing parts of the inner detector before entering the muon spectrometer. The majority though are stand alone muons, i.e. they are reconstructed by the muon spectrometer exclusively. Therefore the sample is split up into these two categories. For both, the muon spectrometer quantities are examined, while for the combined muons the inner detector track properties are explored in addition. In figure 5.18 the category is plotted as a function of the pseudorapidity. As expected the number of combined muons decreases with the pseudorapidity until it vanishes above $|\eta| \approx 2.65$ as a matter of the detector geometry.

The basic inner detector track quality criteria as there are the number of hits in the B-layer, the sum of pixel detector hits and dead pixel sensors, the sum of holes in the pixel and SCT detector and the sum of SCT hits and SCT dead sensors are presented in figure 5.19. Similar looking distributions for muons reconstructed in the high pseudorapidity region and in the control region can be observed except for the sum of SCT hits and SCT dead sensors and for the sum of pixel hits and pixel dead sensors. The transition radiation tracker is not considered since its acceptance ends at about $|\eta| \approx 2.0$.

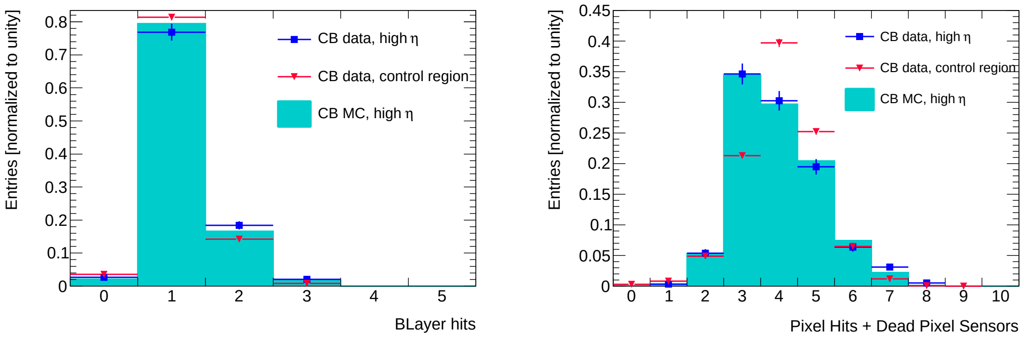

(a) Number of hits in the B-layer.

(b) Sum of hits in the pixel detector and crossed dead pixel sensors.

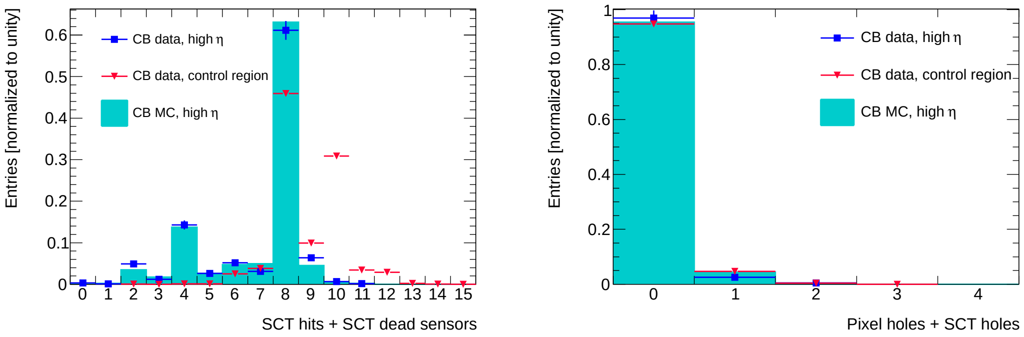

(c) Sum of hits in the SCT and crossed dead SCT sensors.

(d) Sum of the number of holes in the pixel detector and SCT.

Figure 5.19.: Distributions of various quantities measured in the inner detector for combined muons reconstructed in the high pseudorapidity region. The applied selection includes the complete set of requirements for Z boson candidates. Blue markers indicate combined muons in data found above $|\eta| = 2.5$ while red markers represent those in the control region. Combined muons with high pseudorapidity in the $Z \to \mu\mu$ Monte Carlo are superimposed as histogram. All distributions are normalized to unity and produced with muons reconstructed by the STACO algorithm. Corresponding results for the MUID algorithm are available in figure C.5 of appendix C.3.

To further investigate the difference found in the high pseudorapidity region compared to the control region the efficiency of reconstructed Z boson candidates after applying all selection criteria is shown in figure 5.20 as function of the sum of SCT hits and SCT dead sensors. By requiring the sum to be greater than 6, as is recommended for central muons, there is a drop in the signal of roughly 25%. Therefore this quality requirement should be relaxed to 3 for combined muons reconstructed above $|\eta| = 2.5$ to achieve efficiencies close to 100%. The reason for the difference is the detector geometry and is conspicuous in figure 5.15: The chance for muons with high pseudorapidity to hit the same amount of SCT disks is reduced. Further investigations correlating the muon η or z position of the vertex to the sum of SCT hits and SCT dead sensors might strengthen this argument. An equivalent geometrical argument explains the difference in the sum of pixel hits and pixel dead sensors distribution. However, since the recommended requirement for this quantity is a value greater than 1, there is no dramatically changed efficiency expected and further investigations are skipped. For muons with high pseudorapidity and muons found in the barrel this criteria is fulfilled for the majority although the actual shape of the distributions look different.

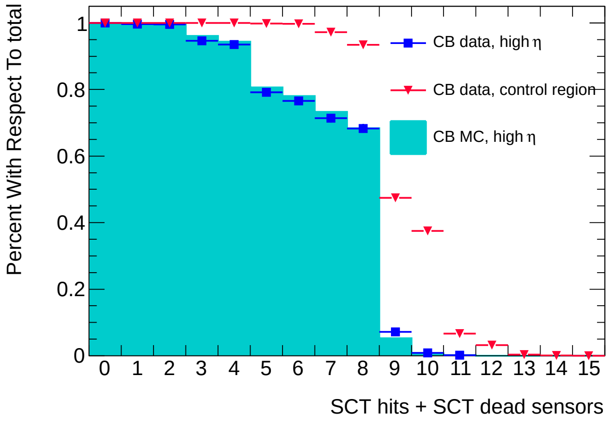

Figure 5.20.: Efficiency of reconstructed Z boson candidates and muons in the high pseudorapidity region respectively as function of the sum of SCT hits and SCT dead sensors. Blue markers indicate the efficiency for muons in data found above $|\eta| = 2.5$ while red markers represent the same for the control region. The corresponding efficiency for the high pseudorapidity region in the $Z \to \mu\mu$ Monte Carlo are superimposed as histogram. The shown results are based on the STACO reconstruction algorithm while those based on MUID are presented in figure C.6 of appendix C.3.

In case of muons reconstructed in the high pseudorapidity region exclusively by the muon spectrometer and therefore of the stand alone category, only information regarding hits in the muon spectrometer is available. In figure 5.21 the number of hits in the middle and outer MDT end-cap station layer as well as the number of CSC hits in the η and the ϕ-coordinate is presented for combined and stand alone muons reconstructed above $|\eta| = 2.5$. There is no noticeable difference in the distributions obtained for the two muon categories. Since a reliable momentum measurement in the muon spectrometer requires hits in all three station layers this should be satisfied by all muons with high pseudorapidity, especially by stand alone muons which are lacking any inner detector measurement. Figure 5.22 shows the percentage of muons versus the number of station layers in which they caused hits. About 98% of both muon categories fulfill the requirement of causing hits in all three station layers so that it should be used as a common selection criteria.

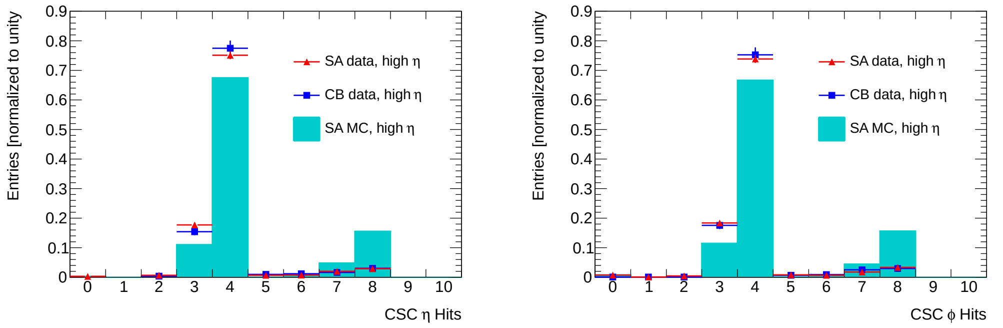

(a) Number of hits in η stripes of the CSC chambers. (b) Number of hits in ϕ stripes of the CSC chambers.

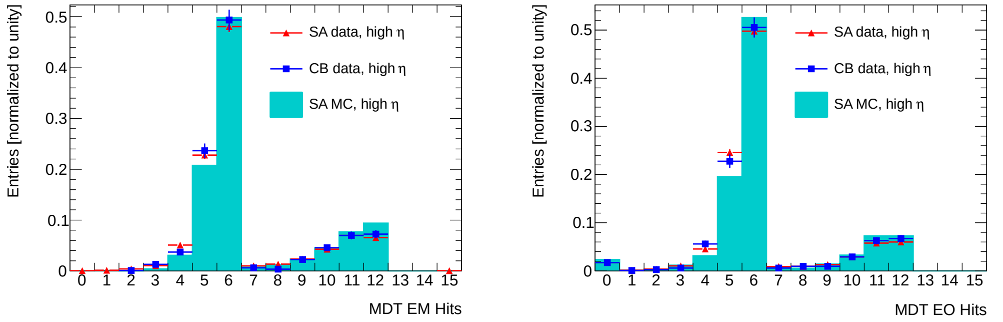

(c) Number of hits in the middle MDT end-cap station layer. (d) Number of hits in the outer MDT end-cap station layer.

Figure 5.21.: Distributions of the number of hits in various end-cap muon station layers for muon tracks above $|\eta| = 2.5$ found in data by the inner detector and muon spectrometer (blue) or the muon spectrometer exclusively (red). Stand alone muon tracks found in the $Z \to \mu\mu$ Monte Carlo are superimposed as histogram. The applied selection includes the complete set of requirements for Z boson candidates and the distributions are normalized to unity. The results presented here are based on tracks found by the STACO reconstruction algorithm while corresponding results for the MUID algorithm are shown in figure C.7 of appendix C.3.

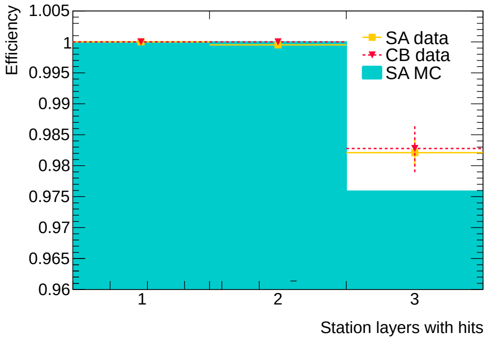

Figure 5.22.: Efficiency for stand alone muons (yellow) and combined muons (red) in data as function of the number of muon station layers which contribute to the track. The applied selection includes the complete set of requirements for Z boson candidates and the according results for stand alone muons obtained from $Z \to \mu\mu$ Monte Carlo are superimposed as histogram. While the efficiency presented here is based on the STACO reconstruction algorithm, the corresponding result obtained with the MUID algorithm is available in figure C.8 of appendix C.3.

In conclusion the suggested quality recommendations for muons reconstructed in the high pseudorapidity region are in case of the associated inner detector track of combined muons the same as for central muons introduced in table 5.5, but with a relaxed requirement from 6 to 3 on the sum of SCT hits and SCT dead sensors. The track in the muon spectrometer should be reconstructed from hits in all three station layers for both combined and stand alone muons. Since the inner detector acceptance does not sharply end at $|\eta| = 2.5$ but some detector components extend further, there is still potential for future studies to include possible hits in these components in the track reconstruction. This could be done by constructing track fragments in the inner detector which do not satisfy common requirements of inner detector tracks but give in combination with muon spectrometer signals a more precise measurement by for example a combined refit of the track.

5.3.5. Calorimeter isolation under pile-up conditions

Muons originating from hadron decays like they are studied in section 5.1 are usually accompanied by additional activity. This can be supplementary tracks in the inner detector or further energy deposition in the calorimeters, both nearby the reconstructed muon trajectory. The quantity called isolation gives a measure for the occupancy. It is defined as the scalar sum either of the transverse momenta of other tracks around the muon track and called track isolation or of the energy depositions in the calorimeter cells around the muon track and called calorimetric isolation. Typically track and calorimetric isolation are considered for cones of $\Delta R < 0.2$, 0.3 and 0.4 where the cone radius $\Delta R = \sqrt{\Delta\eta^2 + \Delta\phi^2}$ is the spacial distance in the η and ϕ-coordinate of the tracks and cell positions respectively compared to the muon track coordinates.

The tracks which enter the calculation in case of track isolation are not only required to be within the cone, but have to have at least 1 GeV transverse momentum and 4 hits in the silicon detector. Their longitudinal impact parameter z_0 as well as $|z_0 \cdot \sin\theta|$ and the impact parameter in the transverse plane d_0 have to be less than 10 mm with respect to the primary vertex. Especially the latter three requirements make the track isolation rather robust against pile-up effects since only tracks emerging most likely from the same interaction in the bunch-crossing are taken into account. Those tracks of extra interactions are rejected. Therefore the dependence of the efficiency of the track isolation on the number of vertices in the event is negligible [136], at least for pile-up scenarios with 2010 and 2011 run condiditions. It is also shown that there is a good agreement of data and simulation for the track isolation.

Comparable to track isolation there is also a quality requirement on the calorimeter cells which enter the calculation of the calorimetric isolation. The deposited energy has to be at least 2 standard deviations above the noise threshold of the cell. Those with energy depositions below this level are not considered in the sum. In a second step the calorimetric isolation is corrected for the muon, i.e. cells inside a predefined region, noted as $E_{\mathrm{T}}^{\mathrm{core}}$, close to the points where the muon track is crossing the different layers of the calorimeter are subtracted. In particular this subtraction could lead to negative values of the isolation if the energy associated to the muon is bigger than the energy in the remaining cells. There is a pile-up dependence since in contrast to the track isolation it is not possible to assign the energy deposition to a specific interaction in the bunch-crossing. With an increased number of interactions and vertices respectively there is an increase of the energy measured by the cells. This is called in-time pile-up. Because the full response time of the calorimeter cells is about 600 ns while the time spacing between two bunch-crossings is about 25 to 75 ns there is in addition so called out-of-time pile-up. This means the actual event is affected by events of previous bunch-crossings. During the 2010 and 2011 run conditions though this effect is small.

In the barrel region it is possible to set requirements on both isolation quantities since the relevant detectors provide full coverage. For muons in the high pseudorapidity region track isolation is not trustworthy because parts of the cone could extend outside the acceptance of the inner detector. Therefore the number of tracks in the cone would be reduced as matter of principle. In addition there are not any measurements from the inner detector in case of stand alone muons, which are the dominant category in this region. In consequence the cone position for track isolation would always rely on the back extrapolation of the muon spectrometer track to the inner detector. Since both aspects introduce biases on track isolation, it is not reliable for muons above $|\eta| = 2.5$ and calorimetric isolation is the only handle to reduce backgrounds originating from hadronic decays. Therefore this quantity has to be well understood and in particular corrections for the pile-up dependence have to be determined.

The muon selection for this study follows the tag and probe approach introduced before. The tagging muon has to be central, its transverse momentum has to be at least 20 GeV and the track isolation relative to its transverse momentum has to be less than 20%. The charge of the probe muon is required to differ from the charge of the tagging muon and the invariant mass of the pair has to be in the window $|m_{\mu\mu} - m_Z| < 12$ GeV around the Z boson mass. Former studies of the calorimetric isolation in cosmic data [137] and 2010 collision data [138] with only very little pile-up show a good agreement between data and the implemented calorimetric isolation [139] in simulation. Though the calorimetric isolation is most relevant in the high pseudorapidity region this study addresses the central region, too.

As a first attempt the dependence on pile-up and the number of vertices respectively can be assumed to scale linearly, and a first order correction can be considered to follow the relation:

$$E_{\mathrm{T}}^{\mathrm{coneXX}}{}_{\mathrm{corrected}} = E_{\mathrm{T}}^{\mathrm{coneXX}} - a_{E_{\mathrm{T}}^{\mathrm{coneXX}}}(\eta)\ [\ \mathrm{MeV}] \cdot n_{\mathrm{VX}} \tag{5.18}$$

The gradient of the line is denoted as $a_{E_{\mathrm{T}}^{\mathrm{coneXX}}}$ and n_{VX} represents the number of vertices. The resulting $E_{\mathrm{T}}^{\mathrm{coneXX}}{}_{\mathrm{corrected}}$ is the initial value $E_{\mathrm{T}}^{\mathrm{coneXX}}$ extrapolated to one vertex while coneXX corresponds to the three different cone sizes 0.2, 0.3 and 0.4. Due to differences in the calorimeter segmentation and the instrumentation there are 4 bins in η for the probe muon and calorimeter isolation respectively. The final values of the gradient in case of the various cone sizes are derived from the $Z \to \mu\mu$ Monte Carlo sample and summarized in table 5.9 while the detailed distributions are presented in appendix C.4. Once the correction is applied there is almost no dependence on the number of vertices. For general ATLAS offline data analyses the package `MuonIsolationCorrection` provides an implementation of the corrections.

In figure 5.23 a comparison of $Z \to \mu\mu$ Monte Carlo and a subset of $740\,\mathrm{pb}^{-1}$ of data, both corrected for pile-up according to equation (5.18), is presented for the example of a cone size of 0.2 and the STACO reconstruction algorithm. The full comparison is available in appendix C.5. For a comprehensive verification of the reliability of the correction there is an additional binning in the number of vertices per bunch-crossing performed. In conclusion the agreement of data and simulation is very good.

Though the presented approximation of the pile-up dependence gives already reasonable results which are useful for physics analysis, there are some improvements which should be respected in a second iteration of the study. Instead of fitting a line on the common mean value of the calorimetric isolation like it was done here a two step fit should be performed. Firstly a function, for example a crystal ball function, should be fitted to the distribution of the calorimetric isolation for each number of vertices. In the following step the expectation value of the used function should be fitted by a line. In scenarios with increased pile-up the linear dependence does not hold any longer due to a saturation of the calorimeter cells and therefore another

STACO						
Bin ($\|\eta\|$)	$a(\eta)_{\mathrm{etCone20}}$	error (stat.)	$a(\eta)_{\mathrm{etCone30}}$	error (stat.)	$a(\eta)_{\mathrm{etCone40}}$	error (stat.)
[0.; 1.05]	44.5	0.3	103.6	0.5	187.0	0.7
[1.05; 2.]	37.9	0.4	88.5	0.6	159.1	0.8
[2.; 2.5]	33.5	0.5	77.7	0.8	140.1	1.1
[2.5; 2.7]	30.5	1.1	66.6	1.5	117.5	1.9

MUID						
Bin ($\|\eta\|$)	$a(\eta)_{\mathrm{etCone20}}$	error (stat.)	$a(\eta)_{\mathrm{etCone30}}$	error (stat.)	$a(\eta)_{\mathrm{etCone40}}$	error (stat.)
[0.; 1.05]	44.2	0.3	103.1	0.5	186.6	0.7
[1.05; 2.]	38.1	0.4	88.5	0.6	159.1	0.8
[2.; 2.5]	33.6	0.5	77.9	0.8	140.3	1.1
[2.5; 2.7]	27.9	1.3	63.5	1.7	113.8	2.1

Table 5.9.: Pile-up correction factors determined using equation (5.18), together with their statistical uncertainties for both reconstruction chains. The unit of the correction factor and its error is MeV.

relation becomes more reasonable. With increased statistics samples one might also choose a finer binning in η. In this context it becomes sensible to switch from a simulation based approach to a data driven attempt to acquire the underlying distributions. For dedicated cone sizes some of these improvements are already realized in the `MuonIsolationCorrection` package. Eventually out-of-time pile-up effects have to be studied, especially if the LHC provides collisions with a small bunch-spacing of only 25 ns. A relation to describe this effect probably becomes more complicated though because corresponding corrections are going to rely on much more information than in case of in-time pile-up.

The presented studies on muons reconstructed in the high pseudorapidity region give a very good overview of the properties of these objects and confirm that they are well understood. Therefore these muons should be considered in physics analyses, because they will increase either the sensitivity in searches for new physics or the event yield for known processes. Since calorimetric isolation is the only handle to suppress muons origination from hadronic decays, the requirement on this quantity should be different for central muons and those above $|\eta| = 2.5$. Since the determination of related efficiencies and rejection factors respectively is dependent on the full object selection, such studies have to be performed for each analysis and an example is given in section 6.3.1 of the following chapter.

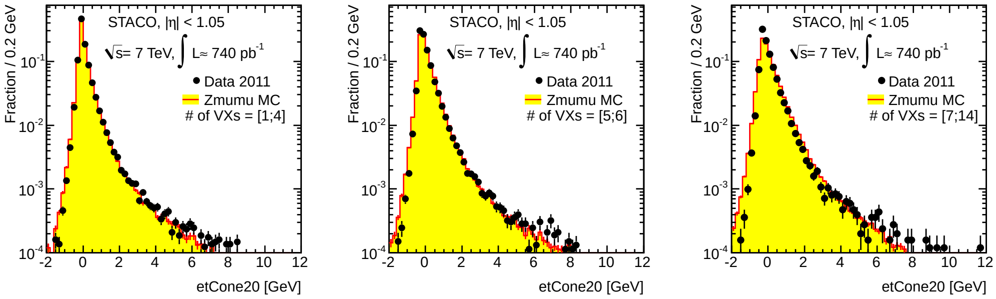

(a) calorimetric isolation after pile-up correction for the probe muon in $|\eta| < 1.05$

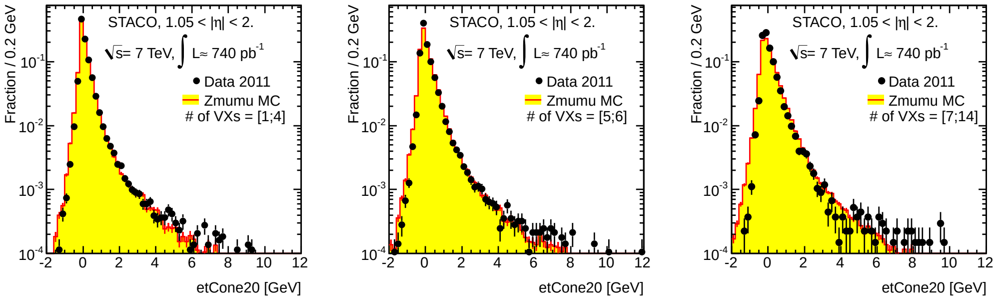

(b) calorimetric isolation after pile-up correction for the probe muon in $1.05 < |\eta| < 2.0$

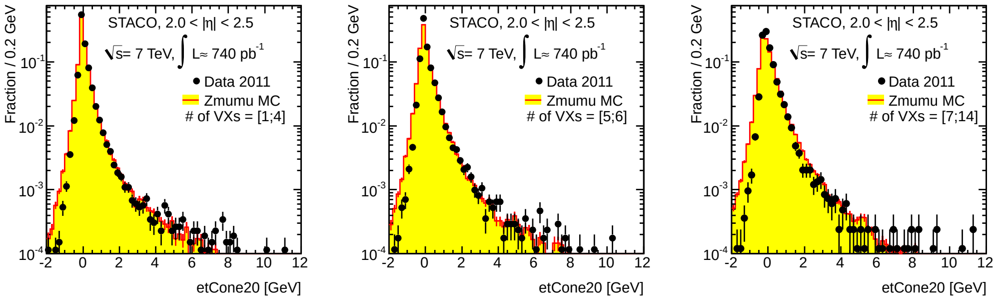

(c) calorimetric isolation after pile-up correction for the probe muon in $2.0 < |\eta| < 2.5$

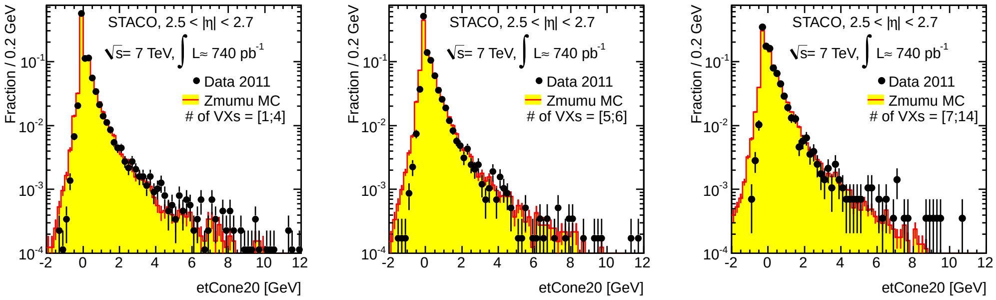

(d) calorimetric isolation after pile-up correction for the probe muon in $2.5 < |\eta| < 2.7$

Figure 5.23.: The calorimetric isolation in a cone of 0.2 after correcting for pile-up according to equation (5.18). For the muon pair the full set of selection criteria to obtain Z boson candidates is applied while the probe muons are considered in four pseudorapidity regions. There is an additional division depending on the number of vertices in the bunch-crossing. The results presented here are based on the STACO reconstruction algorithm and the black points refer to data while $Z \to \mu\mu$ Monte Carlo is superimposed as histogram. The given uncertainties are statistical. Corresponding findings for other cone radii and the MUID reconstruction algorithm are available in appendix C.5.

Chapter 6

Measurement of the inclusive ZZ production cross section

The inclusive production cross section of two Z bosons measured through the four lepton final state is the result of this chapter and given in section 6.6 as well as in reference [40]. After a brief introduction to the relevant aspects of the Standard Model and theories beyond in section 6.1, the event and object selection is explained in detail in the sections 6.2 and 6.3. In particular analysis aspects regarding muons found in the high pseudorapidity region are highlighted in the object selection as well as in section 6.4 which explains the strategy of the analysis. An alternative method to estimate the background for the analyzed four charged lepton final state is reported in section 6.5. The presentation of the measured cross section is followed by section 6.7 where further implications of the results are pointed out. Besides derived limits on anomalous triple gauge couplings, the intersection with the search for the Standard Model Higgs boson available in reference [140] is pointed out.

6.1. Physics scope of the measurement

The complete Standard Model Lagrangian evinced in chapter 4 and introduced in equation (2.33) allows the production of a Z boson pairs in hadron collisions due to the term $\boxed{q\bar{q}Z}$. The dominant production mechanism at the LHC is based on a quark-anti-quark initial state with the anti-quark present from a sea quark. To a smaller extent gluon-gluon initial states contribute as well and have to be considered. Emphazised by figure 3.4 this becomes more important at the LHC than it was at the Tevatron. The corresponding Feynman diagrams at lowest order are illustrated in figure 6.1. The Born-only cross section for $pp \to ZZ$ is calculated to be 4.17 pb at $\sqrt{s} = 7$ TeV while the theory prediction for the cross section based on the CT10 PDF set, considering the natural width of the Z bosons and including one loop corrections as well as corrections regarding the two gluon initial state is $5.89^{+0.22}_{-0.18}$ pb [141].

Moreover the presence of a Standard Model Higgs boson gives rise to another production channel of a Z boson pair because of the term $\boxed{ZZH}$ and the Higgs boson decay $H \to ZZ$ respectively. Especially in case of $2m_Z \lesssim m_H$ this decay is one of the most important search channels for the Higgs as it is shown in figure 2.3. In addition to the Feynman diagram of the Higgs decay, there is a supplementary diagram in figure 6.2 which illustrates the Z boson pair production on tree-level based on anomalous triple gauge couplings (aTGCs).

Due to the absence of terms like $\boxed{ZZZ}$ and $\boxed{ZZA}$ in the Standard Model Lagrangian, the predicted neutral anomalous triple gauge couplings are zero on tree-level and completely fixed to this value by the electroweak gauge structure. On one-loop level though they can be generated through fermion triangles and are of the order of $\mathcal{O}(10^{-4})$ [142]. However, they have not yet been determined with the same precision as other aspects of the electroweak sector like vector

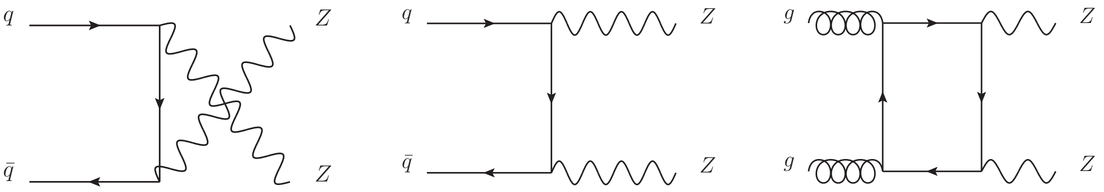

Figure 6.1.: Lowest order Feynman diagrams for ZZ production in hadron collisions as allowed in the Standard Model. While there are t-channel and u-channel tree-level Feynman diagrams in case of $q\bar{q}$ in the initial state, there are higher order box diagrams for gg like the given example.

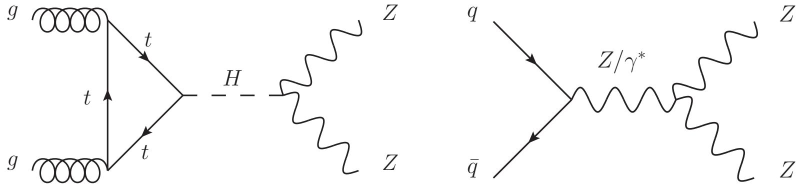

Figure 6.2.: Possible Z boson pair production in hadron collisions through a s-channel Feynman diagram which either includes a Higgs boson (left) or a Z/γ^* coupling anomalously, i.e. not allowed in the Standard Model (right).

boson masses and their couplings to fermions as it was pointed out in chapter 2. The analysis of diboson production at the LHC is therefore essential to test the high energy behavior of electroweak interactions and to probe for possible new physics in the bosonic sector. Particularly at high diboson invariant masses and high transverse momenta of the produced bosons, the production cross section will be significantly enhanced if there are aTGCs. Hence, the Z boson pair production not only has huge impact on the search for the Higgs because it is irreducible background there, but it is also important for physics beyond the Standard Model.

The following study focuses on the subsequent decay of each of the Z bosons of the pair into two charged leptons ($ZZ \to \ell^+\ell^-\ell'^+\ell'^-$) while the leptons are considered to be either electrons or muons ($\ell,\ \ell' = e,\ \mu$). Although the final production cross section measurement will only be provided for both Z bosons on-shell (ZZ), some measurements are performed with the consideration of an off-shell Z boson, i.e. Z/γ^*. The expression ZZ^* indicates that one Z boson is possibly off-shell. The shortcut $ZZ^{(*)}$ refers explicitly to both cases. Finally the results are combined with the findings if of one of the Z bosons decays into two neutrinos and two charged leptons emerge from the other Z boson decay ($ZZ \to \ell^+\ell^-\nu\bar{\nu}$), again with the charged leptons as either electrons or muons. For this channel the branching fraction is increased by a factor of six, but one suffers from larger background. Both Z bosons are assumed to be on-shell in this scenario. Details regarding the analysis including the two neutrinos in the final state can be found in reference [40, 143].

Examples for the lowest order Feynman diagrams for both final states are given in figure 6.3. On top of the Higgs decay and aTGCs, there are additional non Standard Model processes including the pair production of doubly-charged Higgs bosons $H^{++/--}$ [144] which have four charged leptons in the final state, too. Furthermore the yield of events with $\ell^+\ell^-\ell'^+\ell'^-$ and $\ell^+\ell^-\nu\bar{\nu}$ in the final state including ZZ production can be enhanced by non Standard Model processes based on radion resonances [145] or supersymmetry [146].

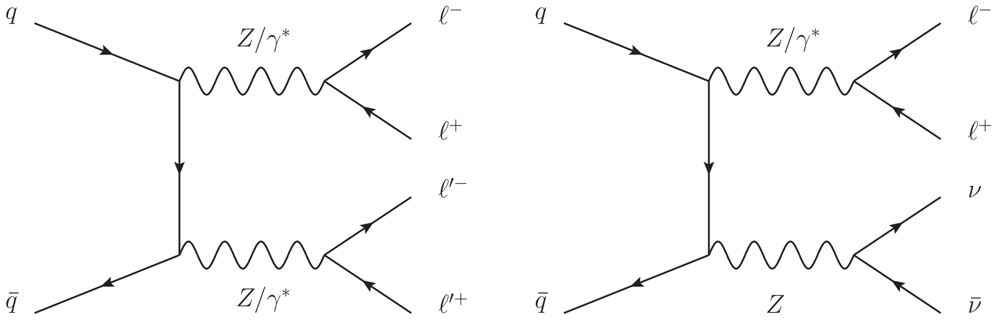

Figure 6.3.: Extension of the Feynman diagrams presented in figure 6.1 to the four charged lepton as well as the two charged lepton and two neutrino final state.

At LEP, Z boson pair production was studied by the L3 [147], OPAL [148], ALEPH [149] and DELPHI [150] collaborations in multiple final states including $e^+e^- \to \ell^+\ell^-\ell'^+\ell'^-$. There is also a combination of all LEP measurements available, which includes, beside the combined cross section, limits on anomalous ZZZ and $ZZ\gamma$ couplings [151] and the Higgs mass [152]. The experiments at the Tevatron collider looked for double Z boson production as well. The analysis of the $\ell^+\ell^-\ell'^+\ell'^-$ and $\ell^+\ell^-\nu\bar{\nu}$ final state with $1.9\,\text{fb}^{-1}$ of data by the D0 collaboration yielded a measurement of 1.60 ± 0.63 (stat.)$^{+0.16}_{-0.17}$ (sys.) pb on the ZZ production cross section [153]. In a more recent paper submitted for publication the cross section was found to be $1.40^{+0.43}_{-0.37}$ (stat.) $\pm$ 0.14 (sys.) pb based on $6.4\,\text{fb}^{-1}$ of analyzed data [38]. Furthermore derived limits on anomalous TGCs [154] are provided. In the study of $1.9\,\text{fb}^{-1}$ of data the CDF experiment observed a significance of 4.4 standard deviations [39] for the Standard Model ZZ production in combination of the $\ell^+\ell^-\ell'^+\ell'^-$ and $\ell^+\ell^-\nu\bar{\nu}$ channel while the measured cross section is $1.4^{+0.7}_{-0.6}$ (stat. + sys.) pb. Results on the Standard Model Higgs search by efforts before the LHC era are summarized in figure 2.2 of section 2.3.

In 2011 results on the Z boson pair production were released from ATLAS [155] and CMS [156], both based on a the first $1\,\text{fb}^{-1}$ of data collected in 2011. In the four charged lepton channel ATLAS observed 12 events corresponding to a significance of 5.6σ for the ZZ observation and a measured cross section of $8.5^{+2.7}_{-2.3}$ (stat)$^{+0.4}_{-0.3}$ (syst) $\pm$ 0.3 (lumi.) pb which is consistent with the theoretical expectations. Limits on the anomalous triple gauge coupling based on this measurement were provided as well.

In the following sections the measurement of the Z boson pair production cross section is presented in detail for the subsequent decay of each Z boson into a pair of muons or electrons. The analysis is based on the complete dataset of $4.64\,\text{fb}^{-1}$ collected by ATLAS during 2011 from proton-proton collisions with a center of mass energy of $\sqrt{s} = 7$ TeV. With a branching fraction of 0.03366 per channel for $Z \to \ell^+\ell^-$ [14], the predicted cross section for $pp \to ZZ \to \ell^+\ell^-\ell'^+\ell'^-$ is 6.67 fb for the $eeee$ and $\mu\mu\mu\mu$ channels, while it is 13.35 fb for the $ee\mu\mu$ channel. For the sum of the three channels it is 26.69 fb, and therefore approximately 124 events are expected to be produced within the integrated luminosity of $4.64\,\text{fb}^{-1}$. The measurement strategy is a cut-based approach with a simple set of requirements. The eventual measurement relies on the number of observed events, an estimate for the background to be subtracted to obtain the original signal yield, a determination of the signal acceptance to extrapolate the observed signal yield to the actual produced signal yield and finally the luminosity to convert the produced signal yield to a production cross section.

Due to limited geometric as well as kinematic acceptance and lepton selection criteria only a fraction of the stated number of events is anticipated to be detected. The reduced phase space volume in which the actual measurement is done is called fiducial volume. Monte Carlo simulation is used to calculate the signal acceptance and efficiency by comparing reconstructed information to the generator level. At this stage measurements from the trigger and combined performance groups regarding the agreement of data with respect to simulation and concerning any corrections needed for the Monte Carlo enter. There are adjustments of the reconstructed objects in simulation to address mis-modeling of the lepton identification, reconstruction efficiency, and the resolution of the energy in case of electrons or of the momentum in case of muons. For muons reconstructed in the region $|\eta| > 2.5$ the corresponding performance studies are presented in section 5.3. Due to a difference in the amount of pile-up in data and simulation, a re-weighting of the simulated events is applied to achieve a similar distribution of Monte Carlo events as a fraction of interactions per bunch-crossing as observed in data.

The number of processes with four charged leptons in the final state is limited in the Standard Model and therefore the expected background contamination is small. The most significant contributions are jets which are misidentified as electrons or muons and produced in combination with a leptonically decaying Z boson ($Z \to \ell^+\ell^- +$ jets). Because of a smaller cross section compared to such processes and therefore less substantial, there are background events originating from other diboson production WZ and WW. Also single top and $t\bar{t}$ production have to be considered due to the decay $t \to Wb$ with a subsequent leptonic W decay and semileptonic bottom quark decay. The applied selection of four isolated charged leptons with high transverse momenta keeps the background on a manageable level.

6.2. Definition of the data sample

The data for this analysis was recorded by ATLAS during proton-proton collision at a center of mass energy of $\sqrt{s} = 7$ TeV between April and November 2011. Data-quality flags are available per luminosity block and indicating if all relevant subdetectors are in operational state. They are used to perform a pre-selection of the events. The basic selection holds $4.64\,\text{fb}^{-1}$ of integrated luminosity as reported by the ATLAS luminosity calculation tool, with an estimated uncertainty of 3.9% [60]. Moreover all events are required to satisfy the unprescaled event filter trigger with the lowest threshold on single leptons transverse energy E_T (for electrons) or transverse momentum p_{T} (for muons). For electrons the threshold was $E_T = 20$ GeV (`e20_medium`) until end of June and increased to 22 GeV afterwards (`e22_medium` until end of August and `e22vh_medium1` subsequently). In case of the single muon trigger the threshold always was 18 GeV (`mu18_MG` until June and `mu18_MG_medium` subsequently) although the initial seeding changed slightly.

To account for mis-modeling of the single lepton trigger efficiency in simulation compared to data, an according scale factor has to be applied on the Monte Carlo events. In order to do this, the events have to possess at least one finally selected lepton within $\Delta R < 0.1$ of a triggered object. To be in the geometrical acceptance of the trigger only electrons reconstructed below $|\eta| = 2.47$ and muons found in the region $|\eta| < 2.4$ can be matched. In addition the transverse momentum has to be above 25 GeV for electrons and 20 GeV for muons to be at the trigger plateau.

The scale factors are derived by a tag and probe method using $Z \to \ell^+\ell^-$ events and dependent on the flavor as well as the transverse momentum of the individual lepton. If N_l is the number of leptons matching a triggered object and $\epsilon_{Data(MC),l_n}$ is the trigger efficiency determined with tag and probe from data (Monte Carlo) for a single lepton flavor of the lepton l_n, the scale factor calculates as:

$$SF = \frac{1 - \prod_{n=1}^{N_l} (1 - \epsilon_{Data,l_n})}{1 - \prod_{n=1}^{N_l} (1 - \epsilon_{MC,l_n})} \tag{6.1}$$

Statistical uncertainties on the trigger efficiency are obtained from Monte Carlo and the systematic uncertainty associated with the scale factors for muon triggers is 0.2% while for electron triggers it is 1% as reported by the corresponding performance groups. Table 6.1 summarizes the trigger efficiencies determined with the ZZ Monte Carlo sample after all selection criteria listed below expect for the trigger object-lepton matching. The values never drop below 98%.

Channel	Trigger Efficiency [%]	
	ZZ Selection	ZZ^* Selection
$eeee$	$100.0^{+0.0}_{-0.4}$	$99.6^{+0.2}_{-0.5}$
$\mu\mu\mu\mu$	$98.7^{+0.4}_{-0.6}$	$98.2^{+0.4}_{-0.5}$
$ee\mu\mu$	$99.6^{+0.2}_{-0.3}$	$98.8^{+0.3}_{-0.4}$
$\ell\ell\ell\ell$	$99.4^{+0.2}_{-0.2}$	$98.8^{+0.2}_{-0.2}$

Table 6.1.: Trigger efficiency for $ZZ^{(*)}$ events with four charged leptons passing all selection criteria, but without any requirement on the trigger or of a trigger matched lepton. To reproduce the trigger efficiency measured in data and Monte Carlo, the scale-factors are applied per object.

Care was taken that the fraction of events with certain detector conditions and corresponding configurations is equivalent in Monte Carlo compared to data. In detail the share of simulated events assigned to data taking periods is adjusted to the actual amount of data in the periods. The according allocation is performed by the `PileupReweighting` software tool. Therefore the quota of events with the different trigger thresholds is reflected appropriately by the Monte Carlo. The main purpose of the package though is to provide event weights based on the number of interactions per bunch crossing to eventually describe the right amount of pile-up in Monte Carlo as it is present in data. Furthermore parts of the calorimeter corresponding to 6 Front-End boards were absent from data taking for about one and a half months, from May to June 2011, which led to a reduced acceptance. In Monte Carlo a corresponding scaling is applied.

The signal Monte Carlo used in the study is based on events generated by PowhegBox [157] and interfaced to Pythia [73]. They are calculated on next-to-leading order, but considering only $q\bar{q}$ in the initial state. In the final state there is up to one additional parton on top of the ZZ system and the CT10 PDF set [66] is used to acquire the parton distribution functions. The events are filtered to have three leptons with a transverse momentum above 5 GeV each and a dilepton invariant mass above 4 GeV. The production due to gluon-gluon initial state is expected to be $\sim$ 6%. Therefore a comparison of $q\bar{q} \to ZZ$ and $gg \to ZZ$ is performed to spot possible differences in acceptance and efficiency. The gg2zz generator [158] interfaced to Herwig [74, 132] and Jimmy [75] for hadronization and multiple parton scattering is used to produce the sample which will be denoted as gg2zz in the following. For this sample a similar three lepton filter is applied while there is no demand on the dilepton invariant mass. The leptons are required to be present in $|\eta| < 10$. The MC@NLO [67] generator version 3 only provides calculations for both Z bosons on-shell. Therefore it does not model appropriately the fiducial phase-space with one Z boson off-shell. Finally also the leading order generators Pythia [73] and SHERPA [69] are used for comparisons. The filters applied on the PYTHIA sample are the same as for GG2ZZ. For SHERPA there is a dilepton invariant mass of at least 12 GeV required while leptons have to have $p_\mathrm{T} > 1$ GeV. The next-to-leading order MCFM prediction is used to determine the scale to next-to-leading order for the leading-order samples. The scale factor is commonly known as k-factor. In table 6.2 all samples are summarized. Interference of Z/γ^* is implemented appropriately in all the used generators.

MCID	Process	Generator	events	fiducial k-factor (ZZ; ZZ^*)	ϵ_filter	cross section [pb]
126159	$ZZ \to e^+e^-e^+e^-$	POWHEGBOX	100000	1.00 ; 1.00	0.70	0.0657
126160	$ZZ \to \mu^+\mu^-\mu^+\mu^-$	POWHEGBOX	100000	1.00 ; 1.00	0.71	0.0657
126861	$ZZ \to e^+e^-\mu^+\mu^-$	POWHEGBOX	200000	1.00 ; 1.00	0.63	0.1516
126862	$ZZ \to \mu^+\mu^-\tau^+\tau^-$	POWHEGBOX	200000	1.00 ; 1.00	0.13	0.1517
126863	$ZZ \to e^+e^-\tau^+\tau^-$	POWHEGBOX	200000	1.00 ; 1.00	0.13	0.1515
126864	$ZZ \to \tau^+\tau^-\tau^+\tau^-$	POWHEGBOX	100000	1.00 ; 1.00	0.013	0.06597
116600	$gg \to ZZ \to \ell^+\ell^-\ell^+\ell^-$	GG2ZZ	65000	1.00 ; 1.00	0.60339	0.00279
116601	$gg \to ZZ \to e^+e^-e^+e^-$	GG2ZZ	65000	1.00 ; 1.00	0.99319	0.00279
116602	$gg \to ZZ \to \mu^+\mu^-\mu^+\mu^-$	GG2ZZ	65000	1.00 ; 1.00	0.99475	0.00279
116603	$gg \to ZZ \to e^+e^-\mu^+\mu^-$	GG2ZZ	65000	1.00 ; 1.00	0.99411	0.00558
126148	$ZZ \to \ell^+\ell^-\ell^+\ell^-$	SHERPA	459998	1.68 ; 1.60	1.0	0.26622
109292	$ZZ \to \ell^+\ell^-\ell^+\ell^-$	PYTHIA	149969	1.36 ; 1.33	0.6235	0.07494

Table 6.2.: A list of all used signal Monte Carlo samples including information on the production process, the Monte Carlo sample identifier (MCID), the underlying generator, the cross section, the number of fully simulated events and the corresponding k-factors. The different event selection filters applied on generator level can be found in the text while the resulting efficiency ϵ_filter is given in the table.

For background studies a variety of Monte Carlo samples is used which in general correspond to $\sim 1-10\,\mathrm{fb}^{-1}$ integrated luminosity each. A detailed list including cross-sections for the simulated processes, generator names, generator level filter efficiencies and total number of events is given in appendix D.1. The k-factors derived from matrix element calculations [159] and used to scale samples produced by leading-order generators to next-to-leading order or even next-to-next-to-leading order are given as well. To simulate Z or W boson production including up to five additional partons and jets respectively in the final state, the ALPGEN [68] generator is used. Also dilepton events from Drell-Yan production with $10 < m_{\ell^+\ell^-} < 40$ GeV and W/γ are simulated with this generator. Any top-quark production, i.e. $t\bar{t}$, Wt and single top, is modeled with MC@NLO. For WW background simulation MC@NLO and HERWIG are used. The WZ sample is generated by HERWIG as well while $W/Z+\gamma$ is modeled with MADGRAPH [160]. Heavy flavor dijets in the final state are generated with PYTHIAB [131] which is very accurate in describing heavy flavor processes.

In summary the pre-selected events have to pass the following requirements: The relevant detectors of the ATLAS experiment have to be fully functional during data taking. The event has to be pass the appropriate high level trigger. There have to be at least three tracks associated to the primary vertex. And finally the noise warning flag of the liquid argon detector must not be set. All events that pass these basic requirements are processed further and the lepton selection as described in the following section is performed.

6.3. Selection criteria for considered physics objects

To identify events with two Z bosons which subsequently decay into four charged leptons, it is mandatory to reconstructed these leptons. This section gives an overview on the selection criteria of the leptons but starts with a brief introduction of the measurement of transverse missing energy ($E_{\mathrm{T}}^{\mathrm{miss}}$). In background studies, there are dedicated requirements on this quantity for the event selection. The used algorithm `MET_RefFinal` [161] determines the missing transverse energy for both the electron and muon channels. The calorimeter energy depositions are classified by the algorithm corresponding to their identification with physics objects, e.g. electrons, hard jets, remaining soft jets and further unclustered objects. The performance of the latter contribution is optimized using the tracker information, e.g. for tracks with low transverse momentum, and avoids double counting of tracks and calorimeter energies. Moreover measurements of different classes of isolated and non-isolated muons are considered. Amongst the usual and previously used definitions of the transverse missing energy in ATLAS the `MET_RefFinal` algorithm gives the best resolution and lowest bias for the measurement of $E_{\mathrm{T}}^{\mathrm{miss}}$.

6.3.1. Prescripton for reconstructed muons

The muon objects considered in this analysis are combined, segment tagged or stand alone muons reconstructed by the STACO algorithm and calorimeter tagged muons reconstructed by the CaloTrkMuID algorithm. A first basic requirement on all muons found by STACO is their classification as `loose`, i.e. they have essentially to be recognized as a candidate and there has to be one tagging segment if they are reconstructed in the end-cap above $|\eta| = 1.05$. The segment does not necessarily have to contain a TGC measurement for the ϕ-coordinate. In the pseudorapidity region $|\eta| < 2.5$ combined and segment tagged muons are considered, if their transverse momentum is above 7 GeV. For both, the matched inner detector track has to fulfill the requirements listed in table 5.5 in section 5.3. To be matched to a triggered object, the muons must be reconstructed in the central region, have to be combined and pass an increased cut of $p_{\mathrm{T}} > 20$ GeV. In the high pseudorapidity region $2.5 < |\eta| < 2.7$ reconstructed muons are taken into account if they are of the category combined or stand alone and exhibit $p_{\mathrm{T}} > 10$ GeV. In addition the quality criteria for muons with high pseudorapidity formulated in section 5.3 have to be fulfilled. For combined muons the requirements on the sum of SCT hits and crossed SCT dead sensors is slightly loosened compared to the central region. The track in the muon spectrometer of muons with high pseudorapidity has to possess hits in all station layers of the spectrometer.

In the pseudorapidity region $|\eta| < 0.1$ also calorimeter tagged muons are considered if their transverse momentum is above 20 GeV and if they do not overlap within $\Delta R < 0.1$ with combined or segment tagged muons already found by the STACO algorithm. The CaloTrkMuID algorithm [162] is used to reconstruct these additional muons which help to recover efficiency in the gap of the muon spectrometer located around $\eta \approx 0$. The calorimeter is used to tag inner detector tracks as originating form muons. A muon with sufficient momentum will traverse all layers of the calorimeter leaving a signal according to minimal ionization. The reconstruction algorithm is based on this behavior and performs a cut based quality selection as well as a likelihood ratio based quality selection. Thereby it is possible to reject hadron and electron backgrounds since low momentum hadrons deposit most of their energy in first layers and leave no signal in the last layers while high momentum hadrons will deposit much energy in the core cells of the shower. The majority of an electron's energy is deposited in the electromagnetic calorimeter. The requirements on the inner detector track of a calorimeter tagged muon follow table 5.5, too. On top of this, either they have to pass tight pre-selection criteria and leave signals in all calorimeter layers or the likelihood ratio testing the muon hypothesis has to be more than 90%

For all muon candidates comprising an inner detector track, it is ensured that they emerge from the primary vertex, i.e. the vertex for which the sum of the transverse momenta of the associated tracks is the largest. This is done by requiring the absolute value of the longitudinal impact parameter with respect to the primary vertex $|z_0|$ to be less than 2 mm and the significance of the impact parameter in the transverse plan to be less than 3.5. In order to suppress background of secondary muons originating from hadronic jets and heavy quark decays there are requirements on relative track and calorimetric isolation applied. The calorimeter isolation is corrected for in time pile-up effects according to section 5.3.5.

To stress the relevance to make use of both isolation quantities and to motivate the eventually applied cut values, a dedicated investigation is performed using a tag and probe method. The event and muon object selection follows the criteria described before, except that no calorimeter tagged muons are considered and the requirement on $|z_0|$ is relaxed to 10 mm. The tagging muon has to be reconstructed in the pseudorapidity region up to $|\eta| = 2.5$ and its transverse momentum has to be above 20 GeV. In addition a track isolation relative to the transverse momentum of less than 20% in a cone of $\Delta R = 0.4$ is required. Probe muons have to satisfy all track quality criteria, but there is no isolation applied.

To measure the efficiency on signal muons, a high statistics Monte Carlo sample of Z boson production with the subsequent decay into a pair of muons is used. The dimuon invariant mass is required to be within a window of 12 GeV around the Z boson mass pole. The efficiency of the relative track and calorimetric isolation is studied for a cone size of $\Delta R = 0.2$. The rejection of background muons, denoted as fake rejection and defined as

$$\text{fake rejection} = 1 - \text{fake efficiency} = 1 - \frac{N_{\text{selected}}}{N_{\text{all fakes}}}, \tag{6.2}$$

is studied on a dedicated sample derived from data and enriched with background muons. To construct the sample, the trigger requirement for data taken after June was modified. The single muon event filter trigger was replaced by an event filter trigger which gets activated by a single muon with $p_{\mathrm{T}} > 18$ GeV and a jet with $E_T > 10$ GeV. The trigger settings before June are kept unchanged since for this period no comparable unprescaled single muon plus jet trigger was available. Subsequently the events have to comprise two muons with an invariant mass below 50 GeV, i.e. they are in the low mass side band of the Z boson peak. Therefore the amount of background muons in the sample is enhanced additionally. Nevertheless a dilution by signal muons remains in the sample. This contamination is estimated from $Z \to \mu\mu +$ jets and $W \to \mu\nu +$ jets simulation and eventually subtracted.

Figure 6.4 shows the fake rejection relative to the signal efficiency for various values of the relative calorimetric isolation in a cone of $\Delta R < 0.2$ in case of probe muons found in the region $|\eta| < 2.5$. The final cut value of 0.30 for the analysis is more than 99% efficient on signal muons while approximately 35% of background is rejected. A corresponding graph for the relative track isolation in a cone of $\Delta R < 0.2$ is presented in figure 6.5. Again the finally applied cut value of 0.15 is more than 99% efficient on signal muons while the fake rejection amounts to 65%. The combination of relative track and calorimetric isolation in a cone of $\Delta R < 0.2$ is presented in figure 6.6. For this graph the relative track isolation of the probe muons is already required to be less than 0.15 and the fake rejection related to the efficiency is shown for various values of the relative calorimetric isolation. An additional rejection of about 10% can be achieved requiring the relative calorimetric isolation to be less than 0.30. Therefore it is reasonable to put demands on both isolation quantities. Assuming them uncorrelated, which in reality is not the case, the resulting rejection of their combination would be the product of the separate rejections and would amount to approximately 77%.

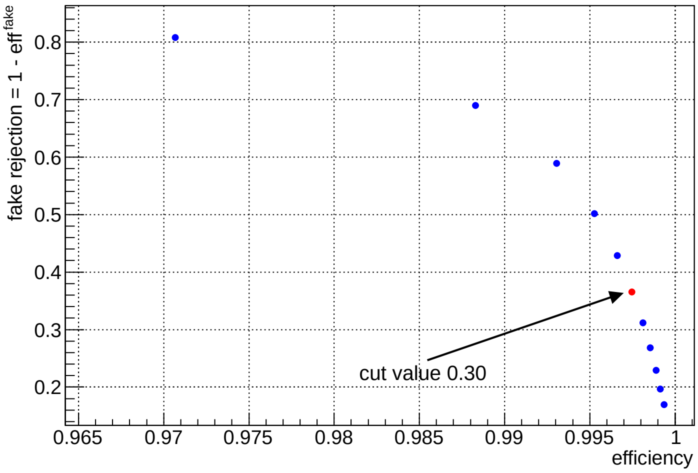

Figure 6.4.: Selection efficiency of muons in $Z \to \mu\mu$ simulation versus the corresponding rejection in a background enriched data sample for various cut values on the relative calorimeter isolation in a cone of $\Delta R < 0.2$. All muons are required to be found in the region $|\eta| < 2.5$. The cut value starts at 0.05 and increases up to 0.55 in steps of 0.05. The red point indicates the finally considered relative calorimeter isolation of 0.30.

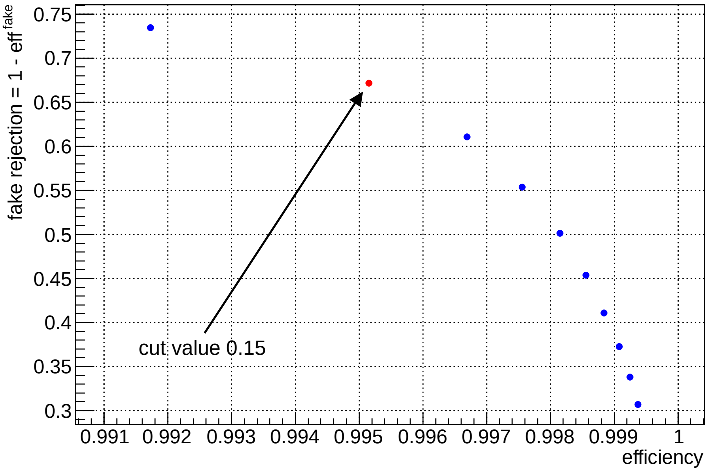

Figure 6.5.: Selection efficiency of muons in $Z \to \mu\mu$ simulation versus the corresponding rejection in a background enriched data sample for various cut values on the relative track isolation in a cone of $\Delta R < 0.2$. All muons are required to be found in the region $|\eta| < 2.5$. The cut value starts at 0.10 and increases up to 0.55 in steps of 0.05. The red point indicates the finally considered relative track isolation of 0.15.

Like described in section 5.3.5 the situation is different for muons reconstructed in the region above $|\eta| = 2.5$, where most muons are not matched to an inner detector track and where the track isolation is not reliable any longer. In consequence the calorimetric isolation is the only instrument to suppress background from hadronic jets or heavy flavor decays. Therefore the cut value has to be tighter since no pre-selection is performed. In figure 6.7 the fake rejection related to the efficiency is shown for various values of the relative calorimetric isolation in a cone

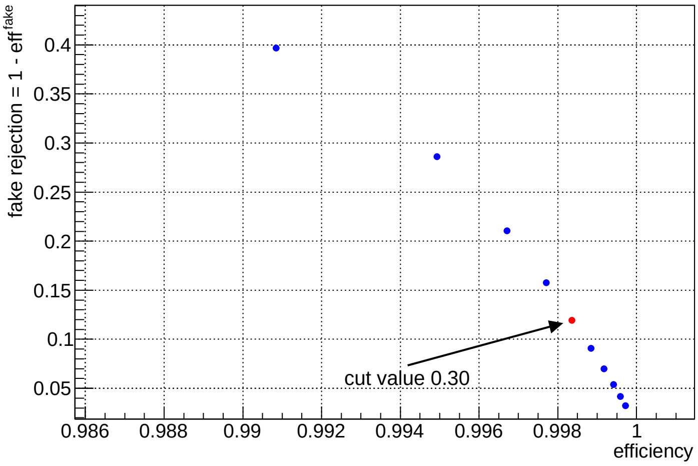

Figure 6.6.: Muon selection efficiency in $Z \to \mu\mu$ simulation versus the corresponding rejection in a background enriched data sample for different requirements on the relative calorimeter isolation while track isolation of 0.15 is pre-applied. Both isolations are considered in a cone of $\Delta R < 0.2$ and the muons have to be found in the region $|\eta| < 2.5$. The finally chosen cut relative calorimeter isolation of 0.30 is indicated by the red marker. The cut value is increased up to 0.55 by steps 0.05 and starts at 0.10.

of $\Delta R < 0.2$. To obtain a fake rejection close to the one for $|\eta| < 2.5$ while preserving a high number of signal muons, the relative calorimeter isolation of 0.15 is a good compromise. With this cut about 98% of the signal remain while approximately 50% of the background muons are rejected. In summary all muons reconstructed in the region $|\eta| < 2.5$ are required to have a relative track isolation less than 0.15 in a cone of $\Delta R < 0.2$. The relative calorimetric isolation in the same cone and corrected for pile-up has to be less than 0.30 for $|\eta| < 2.5$ and 0.15 above. Too optimistic modeling and deficits in the simulation give rise to some disagreement of the measured reconstruction efficiency and resolution for muon objects in Monte Carlo compared to data. To determine the differences and compensate for them, section 5.3 gives instructions in case of muons found above $|\eta| = 2.5$. For the muon spectrometer region $|\eta| < 2.5$, the muon combined performance group studied $W$and Z boson candidates in 2011 data [163]. The results in terms of scaling factors, momentum scaling and momentum smearing for the full muon spectrometer acceptance are summarized and provided for ATLAS offline analysis in the packages `MuonEfficiencyCorrections` and `MuonMomentumCorrections`. Corresponding systematic uncertainties are included in these packages as well. In the further analysis, simulated objects and events are treated and weighted accordingly.

6.3.2. Prescripton for reconstructed electrons

The reconstruction of electrons is performed as introduced in section 4.4. In the central pseudorapidity region $|\eta| < 2.47$, including the calorimeter crack $1.37 < |\eta_{\text{cluster}}| < 1.52$, the considered electrons have to be reconstructed at least by a cluster based algorithm or in combination with a track based algorithm if possible. By the time electrons have left the SCT, they lose up to 50% of their initial energy and have lower momentum as they travel towards the calorimeter. The main cause is bremsstrahlung emission and in consequence a constant track curvature as assumed by the standard track reconstruction is no longer valid. A non-Gaussian contribution to event-by-event fluctuations of the calorimetry and tracking measurement are induced by the

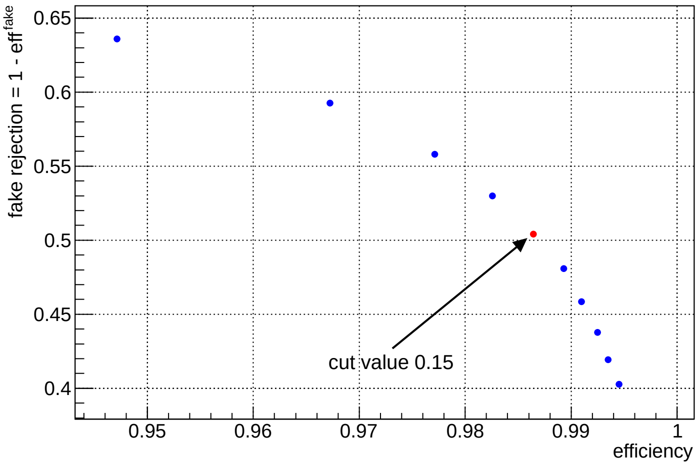

Figure 6.7.: Selection efficiency of muons in $Z \to \mu\mu$ simulation versus the corresponding rejection in a background enriched data sample for various cut values on the relative calorimeter isolation in a cone of $\Delta R < 0.2$. All muons are required to be reconstructed in the region $2.5 < |\eta| < 2.7$ where the track isolation is not reliable. The cut value starts at 0.05 and increases up to 0.275 in steps of 0.025. The red marker labels the finally considered relative calorimeter isolation of 0.15.

bremsstrahlung emission. The reconstructed track parameters can therefore be improved by allowing a proper modeling of the energy loss due to bremsstrahlung during the fitting. In practice this is done by refitting the tracks using a Gaussian-sum filter (GSF) [95]. A non-linear generalization of the Kalman filter taking into account non-Gaussian noise is applied. It is modeled as a weighted sum of Gaussian components and therefore acting like a weighted sum of Kalman filters operating in parallel. Subsequently electron and photon calorimeter clusters are tried to match with the refitted tracks.

Electrons found in the central region have to be classified as “`loose++`” [94] as a first basic requirement. This quality is granted electrons which satisfy simple identification criteria based on the hadronic leakage and on the lateral shape as well as the width of the shower, both derived from only the middle layers of the electromagnetic calorimeter. Also rather loose requirements on the quality have to be fulfilled by the associated track. This pre-selection provides excellent identification efficiency though low background rejection. In order to avoid data quality issues like problems with the front-end boards of the liquid argon calorimeter, all electron candidates have to pass an additional object quality cut, namely “`OQ&1446 == 0`”. The criteria indicates if the electron cluster is affected by the presence of a dead front-end board in the first or second sampling layer, of a dead region affecting the three samplings, of a masked cell in the core or any combination of these features. In data and simulation, a special scaling is applied on the energy of electrons found in the calorimeter crack region $1.37 < |\eta_{\mathrm{cluster}}| < 1.52$ using the dedicated tool for ATLAS offline analysis, namely `egammaAnalysisUtils`, provided by the e/γ performance group.

If the track associated to an electron candidate comprises in total at least 4 hits in the silicon detectors, i.e. SCT and pixel detector, the energy measurement of the clusters is used while the η and ϕ-coordinates are taken from the track. All electron parameters are taken directly form the clusters in case of fewer than 4 silicon hits. The transverse energy defined in this way has to be at least 7 GeV for all candidates. The cluster η and ϕ is in both cases used for the pseudorapidity requirement and overlap removal.

Similar to the muon selection, also electrons are ensured to originate from the primary vertex by requiring the absolute value of the longitudinal impact parameter of the associated track with respect to the primary vertex $|z_0|$ to be less than 2 mm. The significance of the impact parameter in the transverse plane has to be less than 6. To reduce background from hadronic jets the relative track isolation has to be less than 15% and the relative calorimetric isolation has to be less than 30%, both in a cone of $\Delta R < 0.2$. Analogously to muons, the calorimetric isolation is corrected for the energy deposited by the electron itself and corrected for pile-up like it is endorsed by the e/γ performance group.
In the forward pseudorapidity region $2.47 < |\eta| < 3.16$, it is also possible to reconstruct electrons with a specialized algorithm. However, due to the lack of tracking, these objects have no track associated to them and are based on measurements in the calorimeters only. Consequently it is impossible to determine their charge and no track isolation criteria or requirements on track parameters can be applied. Therefore electrons found in this region have to be classified as "`tight`" to be considered for the cross section measurement. All information in the calorimeters are analyzed to form this quality flag and discriminate against hadronic and photonic background. In addition the same object quality cuts like for electrons in the central region has to be passed. A minimal transverse momentum of 20 GeV is required for the forward electons.
Finally an overlap removal procedure is performed: If electrons are found closer than $\Delta R = 0.1$ to a reconstructed muon which passes all selection criteria of section 6.3.1, they are rejected. In case of two electrons within a cone of $\Delta R < 0.1$, the one with the lower transverse momentum is removed. However, if in the boundary region, around $|\eta| \approx 2.47$, there is an overlap between a central and a forward electron, the central one is kept. In Monte Carlo simulation the direction of electrons is kept constant while their energy is smeared to match the resolution observed for electrons forming $W$and Z candidates in 2011 data [94]. The corresponding studies are performed by the e/γ performance group. According methods provided by the `egammaAnalysisUtils` package for ATLAS offline data analysis are applied for following measurement. Scale corrections to the actual electron energy scale are applied during the data reconstruction.

6.4. Analysis strategy and event classification

The final result of this analysis is the total ZZ production cross sections σ_{ZZ}^{tot} which calculate as

$$\sigma_{ZZ}^{\text{tot}} = \frac{N_{\ell\ell\ell'\ell'}^{\text{obs, ZZ}} - N_{\ell\ell\ell'\ell'}^{\text{bkg}}}{\mathcal{L} \times BR(ZZ \to \ell\ell\ell'\ell') \times C_{ZZ} \times A_{ZZ}} \tag{6.3}$$

where $N_{\ell\ell\ell'\ell'}^{\text{obs}}$ is the number of observed events, $N_{\ell\ell\ell'\ell'}^{\text{bkg}}$ is the number of estimated background events, $\mathcal{L}$ is the integrated luminosity, C_{ZZ} is reconstruction correction factor and A_{ZZ} is the acceptance correction factor. In a first step the fiducial cross section $\sigma_{ZZ^{(*)}}^{\text{fiducial}}$ is measured, i.e. the full phase space is reduced to a fiducial volume defined such that it matches fairly well to the experimental selection criteria. This is done to minimize any systematic uncertainties due to the extrapolation from the region accessible with the detector to the full phase space. Like indicated, the measurement in the fiducial volume is also done for the case of one Z boson allowed to be off-shell. The fiducial cross section is given by:

$$\sigma_{ZZ^{(*)}}^{\text{fiducial}} = \frac{N_{\ell\ell\ell'\ell'}^{\text{obs, ZZ}^{(*)}} - N_{\ell\ell\ell'\ell'}^{\text{bkg}}}{\mathcal{L} \times C_{ZZ^{(*)}}} \tag{6.4}$$

There are several requirements to be passed by an event to be included in the number of observed events $N^{\mathrm{obs},\,\mathrm{ZZ}^{(*)}}_{\ell\ell\ell'\ell'}$ with $\ell,\ \ell' = e,\ \mu$. Firstly it has to comprise four and only four leptons which fulfill all selection criteria introduced in section 6.3. This strict requirement on the number of leptons is applied to simplify the background estimate, although it essentially is possible that additional leptons are produced and reconstructed besides the signal process $ZZ^{(*)} \to \ell^+\ell^-\ell'^+\ell'^-$. According to Monte Carlo predictions this is accomplished by 1.3% of the signal events, but in data no event with five leptons and fulfilling all selection requirements is observed. As second criteria there has to be at least one electron (muon) with transverse momentum above 20 GeV (25 GeV) which is matched to a triggered object for reasons elucidated in section 6.3. If the selected leptons are not well separated, i.e. if $\Delta R\,(\ell,\ell) > 0.2$ is not valid for all possible combinations, the event is rejected.

Subsequently a pairing is performed by asking two pairs of same flavor and oppositely charged leptons. However, in order to minimize backgrounds, calorimetric muons, muons with high pseudorapidity and forward electrons are only supposed to be paired with central leptons and allowed to occur once in an event. In the case of forward electrons, the paired central electron has to have a transverse momentum above 20 GeV in addition. This procedure still does not give unique results for events exhibiting four same flavor leptons with two of each charge. The finally chosen configuration is the one minimizing the quantity $|m_{12} - m_Z| + |m_{34} - m_Z|$, with the Z pole mass m_Z and the invariant masses m_{12}, m_{34} of two lepton pairs of a certain pairing of the lepton quadruple consisting of leptons 1, 2, 3 and 4. In any case the lepton pair forming the Z candidate closest to the Z pole mass has to be inside the mass window $66 < m_{12} < 116$ GeV and is called the primary Z candidate. If the other one, called secondary Z candidate, satisfies $66 < m_{34} < 116$ GeV the event is classified as ZZ event, i.e. with both Z bosons considered to be onshell. If the secondary Z candidate fulfills 20 GeV $< m_{34}$ the event enters the category ZZ^*. The two selections are not exclusive and the latter one includes all events of the first one. An additional nomenclature classifies the Z candidates according to their transverse momentum and denotes the higher p_T candidate as leading while lower p_T candidate is called subleading.

Due to corrections on Monte Carlo events, like mentioned in section 6.2, and on leptons, introduced in section 6.3, overall event-level scale factors are obtained. In table 6.3 these factors are summarized and contain all relevant weights to adjust the pile-up in simulation and to model trigger as well as reconstruction efficiencies correctly. The number of signal events, as predicted by fully corrected simulation and normalized to $\mathcal{L} = 4.64\,\mathrm{fb}^{-1}$, is reported in table 6.4 after each selection requirement.

Channel	Overall Average Scale Factor	
	ZZ	ZZ^*
$\ell^-\ell^+\ell^-\ell^+$	0.9672	0.9653
$e^+e^-e^+e^-$	0.9523	0.9475
$\mu^+\mu^-\mu^+\mu^-$	0.9807	0.9804
$e^+e^-\mu^+\mu^-$	0.9646	0.9629

Table 6.3.: Overall event level scale factors for simulated events listed for each channel separated as well as for their combination. The values result from applying the appropriate scale factors to all relevant objects and account for e.g. the various efficiencies. The Sherpa sample with one additional parton in the final state is used for the calculation, but due to similar kinematics the results for PowhegBox do not differ by much.

N_{ZZ}(normalized to 4.6 fb^{-1})	$\ell^-\ell^+\ell^-\ell^+$	$e^+e^-e^+e^-$	$\mu^+\mu^-\mu^+\mu^-$	$e^+e^-\mu^+\mu^-$
Four leptons	82.27 ± 0.43	15.23 ± 0.17	25.49 ± 0.23	41.55 ± 0.31
Trigger Match	80.66 ± 0.41	15.01 ± 0.17	24.93 ± 0.23	40.69 ± 0.31
Quadruplet	79.41 ± 0.41	14.51 ± 0.17	24.92 ± 0.23	39.98 ± 0.29
Primary Z mass	69.21 ± 0.38	12.92 ± 0.16	21.6 ± 0.22	34.67 ± 0.28
Secondary Z mass, ZZ^*	65.37 ± 0.37	12.51 ± 0.15	20.35 ± 0.21	32.50 ± 0.27
Secondary Z mass, ZZ	53.41 ± 0.34	10.28 ± 0.14	16.45 ± 0.19	26.67 ± 0.24

Table 6.4.: Expected number of events for $\mathcal{L} = 4.6\,\text{fb}^{-1}$ as predicted by Monte Carlo. The yield is given on the different stages of the event selection. Contributions from $ZZ \to \tau + X$ with a subsequent decay of the τ lepton into an electron or a muon are included while additional details for this are given in table 6.6. The quoted uncertainties are statistical.

The fiducial volume is used to acquire the reconstruction correction factor $C_{ZZ^{(*)}}$ by comparing the finally reconstructed events with the initally generated ones. It is defined as:

- exactly four lepton final state $(Z/\gamma^*)(Z/\gamma^*) \to \ell^+\ell^-\ell'^+\ell'^-$ with $\ell, \ell' = e, \mu$ and for which each Z boson decayed to a particle-antiparticle pair of a given lepton flavor, i.e. $Z \to e^+e^-$ or $Z \to \mu^+\mu^-$
- $66 < m_{12}(Z/\gamma^*) < 116$ GeV with $m_{12}(Z/\gamma^*)$ resulting form the pairing introduced before
- $66 < m_{34}(Z/\gamma^*) < 116$ GeV in case of both Z bosons on-shell or 20 GeV $< m_{34}(Z/\gamma^*)$ for the fiducial volume with one Z boson allowed to be off-shell
- transverse momentum of the leptons p_{T}^{ℓ} above 7 GeV with an absolute pseudorapidity $|\eta^{\ell}|$ less than 3.16
- leptons have to be well separated, i.e. the distance $\Delta R(\ell, \ell)$ has to be above 0.2

Photons within a distance of $\Delta R < 0.1$ around a lepton are accounted to the lepton four-momentum in the calculation of the invariant masses of the lepton pairs from generator information. A detailed comparison of the fiducial and the reconstruction phase space propounds that the fiducial one is slightly bigger than the actual phase space of the measurement. While a trigger matched lepton with an increased transverse momentum threshold is always required for the measurement, the lower limit for the transverse momentum in the fiducial volume is fixed at 7 GeV. Also the non common leptons, namely electrons above $|\eta| > 2.47$, muons above $|\eta| > 2.5$ and calorimeter tagged muons, have a modified lower bound for the transverse momentum which is not adapted by the fiducial volume. Finally the reconstruction of muon objects ends at $|\eta| = 2.7$ while the fiducial volume extends further. In order to eventually report a fiducial cross section which combines all $\ell^+\ell^-\ell'^+\ell'^-$-channels, the fiducial volume is unified. In consequence the reconstruction correction factor $C_{ZZ^{(*)}}$ is not completely free of theoretical systematic uncertainties emerging from the extrapolation.

Table 6.5 summarizes various cross sections for $ZZ \to e^+e^-\mu^+\mu^-$ predicted by the MCFM [141] generator version 6.2. The values have to be multiplied by a factor of two to obtain cross sections for $ZZ \to \ell^+\ell^-\ell'^+\ell'^-$ where $\ell, \ell' = e, \mu$. There are results for both, the ZZ and ZZ^* mass requirement, presented while in the calculation of some cross sections the γ^* diagrams are excluded. The choice of the renormalization and factorization scale as well as the PDF set introduces uncertainties. They are estimated by the comparison of the nominal calculation using $\mu_R = \mu_F = m_{ZZ}$ and iterations with $\mu_R = \mu_F = m_{ZZ}/2$ as well as $\mu_R = \mu_F = 2 \cdot m_{ZZ}$. For the PDF uncertainties the 52 error sets of the CT10 PDF set are used. The gluon-gluon contribution to the ZZ production is included in the used version of MCFM, and thus the cross section increases compared to predictions from earlier versions [159]. The total cross section is enhanced by 5.8% due to this contribution. Singly-resonant diagrams are considered in the MCFM version. In case of both Z bosons on-shell they are not negligible. The NLO prediction for the total ZZ production with both Z bosons on-shell (zero-width) is $6.18^{+0.25}_{-0.18}$ pb using the CT10 PDF set [66] and setting the renormalization and factorization scale to $\mu_R = \mu_F = m_Z$.

	$\sigma(ee\mu\mu)$ (fb)	Value shift (%)	
	CT10	CT10 error set	Scale variation
On-shell	13.991±0.009	$^{+2.4}_{-2.5}$	$^{+3.8}_{-2.7}$
On-shell (no γ^*)	13.972±0.009	$^{+2.4}_{-2.5}$	$^{+3.8}_{-2.7}$
$66 < m_{12} < 116$ GeV $66 < m_{34} < 116$ GeV	13.329±0.011	$^{+2.4}_{-2.5}$	$^{+3.7}_{-2.7}$
$66 < m_{12} < 116$ GeV $66 < m_{34} < 116$ GeV (no γ^*)	13.068±0.010	$^{+2.4}_{-2.5}$	$^{+3.7}_{-2.7}$
$66 < m_{12} < 116$ GeV $66 < m_{34} < 116$ GeV $p_T^\ell > 7$ GeV, $\lvert\eta^\ell\rvert < 3.16$, $\Delta R_{\min} > 0.2$	10.596±0.013	$^{+3.0}_{-3.1}$	$^{+3.7}_{-2.7}$
($66 < m_{12} < 116$ GeV, $m_{34} > 20$ GeV) or ($66 < m_{34} < 116$ GeV, $m_{12} > 20$ GeV)	16.699±0.044	$^{+2.5}_{-2.5}$	$^{+3.5}_{-2.6}$
($66 < m_{12} < 116$ GeV, $m_{34} > 20$ GeV) or ($66 < m_{34} < 116$ GeV, $m_{12} > 20$ GeV) $p_T^\ell > 7$ GeV, $\lvert\eta^\ell\rvert < 3.16$, $\Delta R_{\min} > 0.2$	12.616±0.037	$^{+2.5}_{-2.6}$	$^{+3.7}_{-2.5}$

Table 6.5.: Cross section for $pp \to ZZ^{(*)} \to ee\mu\mu$ under various assumptions regarding the mass of the occurring Z bosons. The values are calculated with MCFM version 6.2 at NLO in QCD using the CT10 PDF set for the central values. The uncertainties obtained from the 52 CT10 error sets and the difference with MSTW2008NLO are listed in the column labeled "CT10 error set". Changing the factorization and renormalization scale by a factor of two from the default value of m_Z gives the uncertainties in the column labeled "Scale variation". In addition the cross sections excluding the γ^* diagrams are given in case of both Z bosons in a window around the Z mass pole. To obtain the corresponding cross sections for the 4ℓ final state, the quoted numbers for the $ee\mu\mu$ final state have to be multiplied by two.

An additional uncertainty on the predicted cross sections, which is neither addressed in detail nor propagated to the final result, arises from higher order electroweak corrections. A possible attempt to obtain an estimation is changing the electroweak scheme considered in the MCFM generator. This scheme determines which sub-set of the electroweak quantities G_F, m_W, m_Z, $\sin^2(\theta_W)$ and $\alpha_{\text{em}}(m_Z)$ is used as input parameters and which are calculated. Chapter 2 gives a rough idea how the parameters are linked. To get a more complete understanding especially on the impact of higher order electroweak effects the reader is referred to the corresponding review in reference [14]. The MCFM default scheme, applied in this analysis as well, is the so called G_μ scheme. The parameters G_F, m_W and m_Z are used as input while $\sin^2(\theta_W)$ and $\alpha_{\text{em}}(m_Z)$ are calculated. Switching to the coupling and the Weinberg angle as input parameters and calculating the gauge boson masses, results in a ZZ production cross section differing by approximately 4%. Since this uncertainty is of the order of the uncertainties introduced by the scale variation and the PDF, its consideration in future studies might be reasonable. Beforehand though, more detailed investigations have to be performed, to understand if the approach of changing the scheme is appropriate.

Finally the ratio of the number of reconstructed signal events in simulation passing all the criteria listed before and the number of $ZZ \to \ell^+\ell^-\ell'^+\ell'^-$ events generated inside the fiducial volume gives the reconstruction correction factor $C_{ZZ^{(*)}}$. The obtained values are presented in table 6.6. Since the reconstruction efficiency factor for muons is higher than for electrons the expected yield in the four muon channel is enhanced compared to the four electron channel. Events from $ZZ \to \tau + X$ with a subsequent decay of the τ lepton into an electron or muon contribute to the reconstructed event count equivalent to $0.24 \pm 0.01\%$ for ZZ and $1.73 \pm 0.04\%$ for ZZ^* events. The probability of a τ lepton being reconstructed as an electron or muon is assigned a conservative 100% uncertainty on the number of such events derived from signal Monte Carlo sample. It is considered as a systematic uncertainty since there is no explicit τ subtraction performed. Four lepton events which are outside the fiducial volume at generator level due to mis-reconstructed kinematics contribute to 0.89% (0.82%) in case of ZZ (ZZ^*). This effect is largely dominated by mis-pairing.

	$eeee$		$\mu\mu\mu\mu$		$ee\mu\mu$		$llll$	
	ZZ	ZZ^*	ZZ	ZZ^*	ZZ	ZZ^*	ZZ	ZZ^*
Contamination (%) from $ZZ \to \tau$+X	0.37 ± 0.04	2.16 ± 0.09	0.25 ± 0.03	1.53 ± 0.06	0.18 ± 0.02	1.70 ± 0.05	0.24 ± 0.01	1.73 ± 0.04
Contamination (%) from events outside fiducial region	1.04 ± 0.14	1.08 ± 0.13	0.62 ± 0.09	0.53 ± 0.07	0.81 ± 0.08	0.76 ± 0.07	0.80 ± 0.06	0.75 ± 0.05
Reconstruction factor C_{ZZ}	0.428 ± 0.005	0.410 ± 0.004	0.687 ± 0.004	0.679 ± 0.004	0.546 ± 0.003	0.540 ± 0.003	0.552 ± 0.002	0.542 ± 0.002
True Reconstruction Efficiency	0.422 ± 0.005	0.398 ± 0.004	0.681 ± 0.004	0.665 ± 0.004	0.541 ± 0.003	0.527 ± 0.003	0.546 ± 0.002	0.529 ± 0.002

Table 6.6.: Information on the selection efficiency and contaminations in the signal Monte Carlo generated with PowhegBox. The quoted uncertainties are statistical. The first row lists the percentage contamination due to $ZZ \to \tau + X$ events passing the full selection. The contamination caused by events falling outside of the fiducial region at generator level, but passing the selection due to mis-reconstruction of the energy, momentum or track direction, is shown in the following row. The third and fourth row show the reconstruction correction factor $C_{ZZ^{(*)}}$ which is defined as the ratio of the number of events passing the selection to the number of generated events in the fiducial. While for the third row contributions from $ZZ \to \tau + X$ and events outside the fiducial region are included in the numerator, they are excluded for in fourth row which therefore shows the “true” reconstruction efficiency.

In conclusion the $C_{ZZ^{(*)}}$ factor also corrects for the events from τ decays and those outside the fiducial region. Table 6.6 reports besides the values used to extract the signal production cross section later on also the true reconstruction factors including contributions removed from the numerator. To account for quark-antiquark and gluon-gluon initial states appropriately,

$C_{ZZ^{(*)}}$ is calculated as the weighted average of results from the PowhegBox (for $q\bar{q} \rightarrow ZZ$) and gg2zz (for $gg \rightarrow ZZ$) while the gg2zz contribution is taken as 5.75% at the M_{ZZ} scale for the ZZ selection.

The consideration of the non common lepton categories, namely calorimetric muons in the region $|\eta| < 0.1$, muons found in the region $2.5 < |\eta| < 2.7$ and electrons in the region $2.47 < |\eta| < 3.16$ increases the signal yield by a decent amount. In case of the ZZ selection the background contamination remained unchanged while for the ZZ^* selection an increase of 22% was observed. Table 6.7 holds the expected increase of the signal yield derived form the PowhegBox ZZ signal simulation and the actual increase observed in data split up in the various channels. These values are also a valid estimation of the increase in the expected signal yield for other analysis with rather similar object and event selections. One example is the search for the Higgs boson in the $H \rightarrow ZZ^* \rightarrow \ell^+\ell^-\ell'^+\ell'^-$ channel which considers muons in the high pseudorapidity region and calorimetric muons as well. Some more details about the compatibility of the measurement of the inclusive ZZ production cross section and the search for the Standard Model Higgs boson via the $H \rightarrow ZZ^*$ decay channel can be found in section 6.7.3.

	ZZ			
lepton type	$e^+e^-e^+e^-$	$\mu^+\mu^-\mu^+\mu^-$	$e^+e^-\mu^+\mu^-$	$\ell^-\ell^+\ell^-\ell^+$
forward electrons	14.3% (12.2%)	-	0.0% (6.9%)	3.4% (5.9%)
high-η muons	-	5.0% (6.8%)	4.0% (5.0%)	3.4% (4.6%)
calorimetric muons	-	10.0% (10.7%)	0.0% (3.9%)	3.4% (5.2%)
all extended leptons	14.3% (12.2%)	15.0% (17.7%)	8.0% (16.6%)	11.8% (16.1%)

	ZZ^*			
lepton type	$e^+e^-e^+e^-$	$\mu^+\mu^-\mu^+\mu^-$	$e^+e^-\mu^+\mu^-$	$\ell^-\ell^+\ell^-\ell^+$
forward electrons	16.7% (11.9%)	-	0.0% (6.9%)	4.0% (5.7%)
high-η muons	-	3.7% (6.5%)	6.7% (5.0%)	4.0% (4.5%)
calorimetric muons	-	7.4% (10.4%)	0.0% (3.8%)	2.7% (5.1%)
all extended leptons	16.7% (11.9%)	11.1% (17.1%)	10.0% (16.4%)	12.0% (15.7%)

Table 6.7.: The percentage increase of the signal event count observed in data for extending the muon η coverage from $|\eta| < 2.5$ to $|\eta| < 2.7$ (“high-η muons”), for including calorimeter-tagged muons in the region $|\eta| < 0.1$ and for extending the electron η coverage from $|\eta| < 2.47$ to $|\eta| < 3.16$ (“forward electrons”) split up into the various channels. The corresponding predictions derived from the PowhegBox signal Monte Carlo are reported in brackets. The values are given relative to the event yield derived with common leptons only. While the rows labeled with the extended lepton type list the increased yield due to this specific type only, the rows labeled with “all extend leptons” include in addition events comprising more than one type of additional leptons.

6.5. Data-driven background estimation

In the Standard Model $ZZ \rightarrow 4\ell$ is the most common process with four isolated, prompt leptons in the final state. All background processes contain at least one fake lepton, i.e. an object which is identified as isolated and prompt lepton though it is not. Examples are muons from in-flight decays of pions and kaons, electrons from prompt photons, leptons from heavy-flavor quark decays or jets with a leading charged hadron misidentified as electron or muon. The main properties of these objects, considered as background in this study, are already discussed in section 5.1 for the muon case. While the fake objects tend to be spatially correlated with jets and in consequence mostly fail the isolation requirement, leptons from the decay of a Z boson are primarily isolated. Nevertheless there may be electrons and muons in the tails of the jet distributions which satisfy the identification and isolation requirements. However, the tails of the jet fragmentation may not be modeled well in the simulation, and thus data based techniques are applied to estimate the background. An indication, that an estimation purely based on simulation is probably not reliable enough, is given in figure 6.8. With the previously introduced selection criteria there is a rather good agreement of data and Monte Carlo below the Z peak while it is fairly poor outside. Anyhow, the statistics of the Monte Carlo is in principle sufficient to determine the background and it is eventually used to estimate the systematic uncertainty.

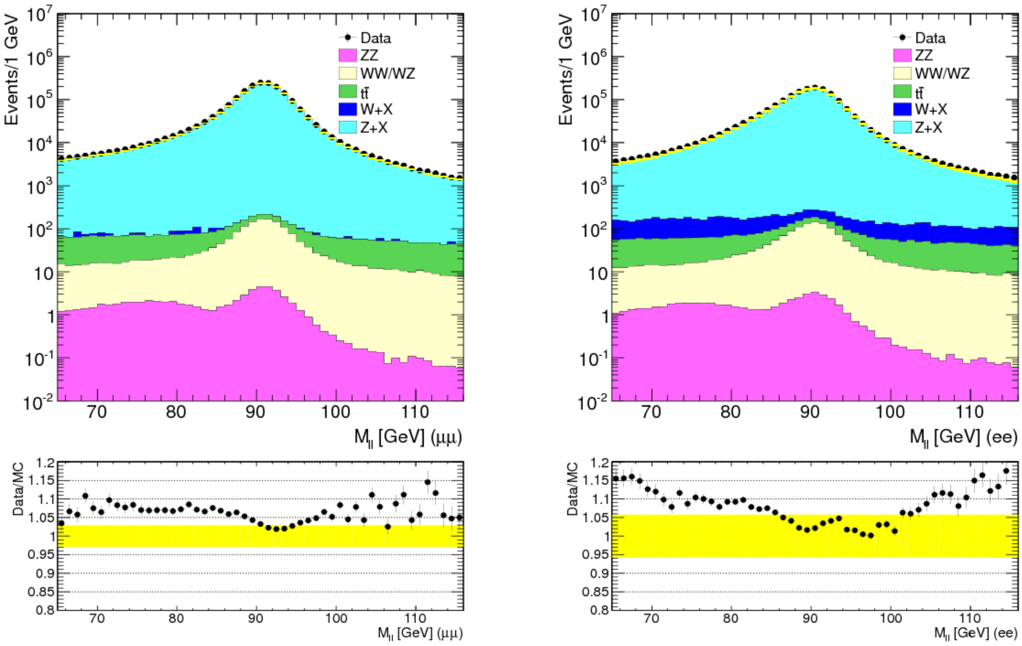

Figure 6.8.: Comparison of data and simulation for dimuon events (left) and dielectron events (right), both with oppositely charged leptons in the mass window $66 < m_{\ell\ell} < 116$ GeV. The lepton selection follows the criteria for $ZZ \rightarrow 4\ell$ events introduced before while the transverse momentum requirement is increased to 20 GeV to suppress background poorly modeled in Monte Carlo. In the lower part of each plot the ratio of data and simulation is shown with statistical plus systematic uncertainties indicated by a yellow band.

A specific list of dominant backgrounds is given in table 6.8 which reports the processes and emerging amount of true, prompt leptons (T) and possible fake leptons (F). All of the processes contain directly or subsequently produced electroweak gauge bosons which are assumed to decay into prompt leptons. The case of a lepton emerging from a τ lepton decay are included as well. Main contributors to the background are $Z+$ jets, $Z+b\bar{b}$, $Z+\gamma+$ jets and single top as well as $t\bar{t}$ production. The production of two W bosons or of a W and Z boson associated with jets is an additional share of the background.

signature	N_{TTTF}	N_{TTFF}	N_{TFFF}	N_{TTTFF}	N_{TTFFF}	N_{TFFFF}
process	$WZ + 1$ jet	$Z + 2$ jets, $t\bar{t}$, $tW + 1$ jet, $WW + 2$ jets,	$W + 3$ jets, single $t + 2$ jets	$WZ + 2$ jets	$Z + 3$ jets	$W + 4$ jets

Table 6.8.: Potential Standard Model background for a four charged lepton final state. The processes are classified regarding the amount of true leptons (T) and possible fake leptons (F) in their final state, i.e. signature respectively.

The basic idea to estimate the number of background events $N^{\text{bkg}}_{\ell\ell\ell'\ell'}$ included in the final selection, starts with a sample derived from data. It is chosen to be close to the signal region, but exhibits at least one lepton origination from another source than a Z boson decay. To ensure that the sample is dominated by such events, some of the lepton identification criteria are inverted. Afterwards an extrapolation to the signal region is performed. The so called fake factor FF is used as extrapolation factor and is calculated as follows: Objects are identified as "pre-leptons" if they essentially pass all lepton selection criteria, except a few requirements which are reserved for a second stage. These criteria are different for the various lepton objects. Depending on whether a pre-lepton fulfills the remaining requirements or fails some of them at the second selection stage, it is classified as "selected lepton" or as "lepton-like jet". The collection of selected leptons is denoted by "L" while the lepton-like jets are labeled with "J". Finally the fake factor is the ratio of the probability that a pre-lepton is classified as a selected lepton divided by the probability that it is found to be a lepton-like jet. The average fake factor in a sample of selected leptons L plus lepton-like jets J is related to the probability f of a fake lepton F to be identified as a selected lepton:

$$FF = \frac{L}{J} \quad \text{and} \quad f = \frac{L}{L+J} \qquad \Longrightarrow \qquad FF = \frac{f}{1-f} \quad \text{and} \quad f = \frac{FF}{1+FF} \tag{6.5}$$

As a matter of principle for data, it is not possible to distinguish the different background sources given in table 6.8. The probability f can be used to calculate the expected number of events with a certain number of selected leptons and lepton-like jets emerging from events with a certain number of true and fake leptons. In general true leptons are assumed to be always identified as selected leptons. Nevertheless N^{ZZ}_{LLLJ} denotes the number of $ZZ \to \ell\ell\ell'\ell'$ events with one true lepton misidentified as lepton-like jet and N^{ZZ}_{LLLJJ} is the equivalent for the process $ZZ \to \ell\ell\ell'\ell' +$ jet. The following equations hold:

$$N_{LLLJ} = N_{TTTF} \cdot (1-f) + N_{TTFF} \cdot 2 \cdot f \cdot (1-f) + N_{TFFF} \cdot 3 \cdot f^2 \cdot (1-f) + N^{ZZ}_{LLLJ} \tag{6.6}$$

$$N_{LLJJ} = N_{TTFF} \cdot (1-f)^2 + N_{TFFF} \cdot 3 \cdot f \cdot (1-f)^2 \tag{6.7}$$

$$N_{LJJJ} = N_{TFFF} \cdot (1-f)^3 \tag{6.8}$$

$$N_{LLLJJ} = N_{TTTFF} \cdot (1-f)^2 + N_{TTFFF} \cdot 3 \cdot f \cdot (1-f)^2 + N_{TFFFF} \cdot 6 \cdot f^2 \cdot (1-f)^2 + N^{ZZ}_{LLLJJ} \tag{6.9}$$

$$N_{LLJJJ} = N_{TTFFF} \cdot (1-f)^3 + N_{TFFFF} \cdot 4 \cdot (1-f)^3 \tag{6.10}$$

$$N_{LJJJJ} = N_{TFFFF} \cdot (1-f)^4 \tag{6.11}$$

For the following calculations the event classes N_{LJJJJ} and N_{LJJJ} are not considered. They are rather far away from the signal region and in both cases, for ZZ and ZZ^*, the corresponding actual event counts in data are at least one order of magnitude smaller than for the other classes. Since both contributions contain higher powers of the term $(1-f)$ which will convert to the fake factor, it is also certain that their impact will be minor. In consequence of this approximation the background processes summarized in the classes N_{TFFFF} and N_{TFFF} are dropped since they have only very little influence on the terms N_{LLLJJ} and N_{LLJJ}. Their cross section and therefore the expected number of events is smaller than for the other processes which are able to produce these signatures. With the remaining terms the equations are reduced to:

$$\begin{aligned} N_{LLLJ} &= N_{TTTF} \cdot (1-f) + N_{TTFF} \cdot 2 \cdot f \cdot (1-f) + N^{ZZ}_{LLLJ} \\ N_{LLJJ} &= N_{TTFF} \cdot (1-f)^2 \end{aligned} \tag{6.12}$$

$$\begin{aligned} N_{LLLJJ} &= N_{TTTFF} \cdot (1-f)^2 + N_{TTFFF} \cdot 3 \cdot f \cdot (1-f)^2 + N^{ZZ}_{LLLJJ} \\ N_{LLJJJ} &= N_{TTFFF} \cdot (1-f)^3 \end{aligned} \tag{6.13}$$

If the knowledge of the true underlying signature would be given, the background of produced Z boson pairs which decay to four charged lepton final states would be calculated as

$$N^{\mathrm{bkg}}_{\ell\ell\ell'\ell'} = N_{TTTF} \cdot f + N_{TTFF} \cdot f^2 + N_{TTTFF} \cdot 2 \cdot f \cdot (1-f) + N_{TTFFF} \cdot 3 \cdot f^2 \cdot (1-f). \tag{6.14}$$

This relation can be formulated in terms of measurable event counts by using the equations (6.12) and (6.13). After some simplifications the final equation for the number of background is given by

$$N^{\mathrm{bkg}}_{\ell\ell\ell'\ell'} = (N_{LLLJ} + 2 \cdot N_{LLLJJ} - N^{ZZ}_{LLLJ} - 2 \cdot N^{ZZ}_{LLLJJ}) \cdot FF - (3 \cdot N_{LLJJJ} + N_{LLJJ}) \cdot FF^2 \tag{6.15}$$

Studies on Monte Carlo and data have shown that the actual number of events, which comprise in the final state five objects passing the first stage quality criteria, is rather small. In consequence the resulting contribution to the background is very low as well. Therefore these event classes can be neglected. In good approximation it is sufficient to consider just the classes given in equation (6.12). The relation to estimate the background reduces to

$$\begin{aligned} N^{\mathrm{bkg}}_{\ell\ell\ell'\ell'} &= N_{TTFF} \cdot f^2 + N_{TTTF} \cdot f && (6.16) \\ &= (N_{LLLJ} - N^{ZZ}_{LLLJ}) \cdot FF - N_{LLJJ} \cdot FF^2. && (6.17) \end{aligned}$$

For the further analysis this equation is used to assess the background contamination in the final selection. The central quantity, not yet determined though, is the fake factor $FF = L/J$. To continue the data driven attempt, FF should be derived from data as well. The required sample has to be as unbiased as possible and enriched with fake leptons, i.e. with leptons which do not result from gauge boson decays. The two selections used in this analysis are the so called "Z-tagged" sample for the final result and the "inclusive" sample for cross check purposes. For the Z-tagged sample the basic event selection criteria, especially the trigger settings remain the same as for the analysis. An event is required to possess either two electrons or muons which pass the full lepton selection requirements introduced in section 6.3. They have to be oppositely charged and their invariant mass has to fulfill $|m_{\ell\ell} - m_Z| < 20$ GeV. In addition one of the leptons is required to be matched with a triggering object. The missing transverse momentum of the event has to be less than 25 GeV. Events passing the selection are searched for an additional lepton which either satisfies the selected lepton or lepton-like jet requirements. The extra lepton originates primarily from $Z+$ jets events, although there is also a contribution of leptons emerging from ZZ and $W^{\pm}Z$ decays. This contamination of signal like leptons is estimated from simulation and subtracted, so that the fake factor finally calculates as:

$$FF = \frac{N^{\mathrm{data}}_{\mathrm{selected\ lepton}} - N^{\mathrm{signal\ contribution\ from\ MC}}_{\mathrm{selected\ lepton}}}{N^{\mathrm{data}}_{\mathrm{lepton-like\ jet}} - N^{\mathrm{signal\ contribution\ from\ MC}}_{\mathrm{lepton-like\ jet}}} \tag{6.18}$$

Below it is shown that the subtracted signal contribution derived from Monte Carlo is rather minor and commonly at least one order of magnitude smaller than the event yield obtained from data. The fake factor is derived depending on the object's transverse momentum $FF(p_{\mathrm{T}})$ and pseudorapidity $FF(\eta)$. The at the end applied value is an averaged factor calculated by the following equation:

$$FF(p_{\mathrm{T}},\eta) = \frac{FF(p_{\mathrm{T}}) \times FF(\eta)}{\langle FF(p_{\mathrm{T}},\eta)\rangle} \tag{6.19}$$

The quantity $\langle FF(p_{\mathrm{T}},\eta)\rangle$ denotes the average fake factor in the sample, i.e. the ratio L/J. There is no correlation assumed to be present between the p_{T} and η dependence. The fake objects comprised in the Z-tagged sample are close to the fake objects expected in the analysis itself, which is an advantage. The second benefit is caused by the fact that the triggering object is used to form the Z boson. Therefore the fake object can be examined down to low transverse momenta without introducing a bias due to the trigger threshold. Actually there is no bias caused by the trigger at all. A downside though is the need of reasonable statistics of events with a Z boson. Since this was not given for the first measurement of the ZZ production cross section in $1\,\mathrm{fb}^{-1}$ of data [155] with the ATLAS experiment, the background estimate was based on fake factors derived from the inclusive sample. The lepton transverse momentum cut applied in this preceding analysis was set to 15 GeV and no extended leptons had been considered at all. Also the definition of selected and jet-like leptons differed. The estimate using the inclusive sample will be addressed in more detail in the following although for the final result, it is used as a cross-check only.

To enter the inclusive sample the default event selection requirements have to be fulfilled. However, to enrich the sample with fake leptons, the trigger settings are changed for data taken after June 2011 by replacing the single muon trigger with an event filter trigger which gets activated by a single muon with $p_{\mathrm{T}} > 18$ GeV plus a jet with $E_T > 10$ GeV. Subsequently the event has to contain either one or two objects that pass the first stage object selection criteria for electrons or muons. In case of one pre-lepton the transverse mass, calculated by including missing energy, has to be less than 50 GeV. If there are two pre-leptons, they have to be of the same flavor, but not necessarily opposite charge and their invariant mass is required to be less than 50 GeV. This selection aims to collect events from multi-jet and $b\bar{b}$ production. Finally the equations (6.18) and (6.19) are used to extract the fake factor from this sample. Although the selection is located in the low mass sideband region of the $W^{\pm}$and Z boson decay, so signal contamination arises from these processes. Analogously to the Z-tagged sample, the contribution is estimated from Monte Carlo and subtracted.

The objects used to extract the fake factor for electrons have to pass in the first stage all selection criteria up to track and calorimetric isolation and identification, i.e. `loose++` or `tight`. Due to the absence of any isolation requirement for forward electrons the only cut saved for the second stage is the identification. To be considered as selected electron and enter the collection L the pre-electron has to pass all the remaining requirements. To enter the J collection, i.e. to be classified as electron-like jet, the pre-selected object has to fail the identification or both isolation criteria if available. If the isolation is available and both the identification and the isolation criteria are failed the object is completely rejected since it is too far away from signal electrons. In addition objects failing both requirements are badly modeled in simulation as further studies have shown. The described classification for electrons is summarized in table 6.9 and illustrated in figure 6.9. Because the electron trigger is based to a certain extent on the shapes of the calorimeter shower, all pre-electrons matching a triggered object are rejected in the inclusive sample to avoid any trigger bias. In consequence the majority remaining in the sample are two electron events with one of them excluded. Figure 6.10 presents the distributions parametrized in p_{T} and η for selected electrons, electron-like jets and the resulting fake factors as they are obtained from the inclusive sample. Corresponding distributions from the Z-tagged sample are gathered in appendix D.2 and show reasonable agreement.

	selected electron	electron-like jets
electrons	track isolation < 0.15 and calorimetric iso < 0.30 and `loose++`	(`!loose++` and track isolation < 0.15 and calorimetric isolation < 0.30) or (`loose++` and track isolation > 0.15 and calorimetric isoloation > 0.30)
forward electrons	`tight`	`!tight`

Table 6.9.: Second stage selection criteria used to categorize a pre-selected electron either as selected electron or electron-like jet. Forward electrons, i.e. those found in the region $2.47 < |\eta| < 3.16$ are only classified by their identification due to the absence of calorimetric isolation in the selection requirements and no track isolation at all.

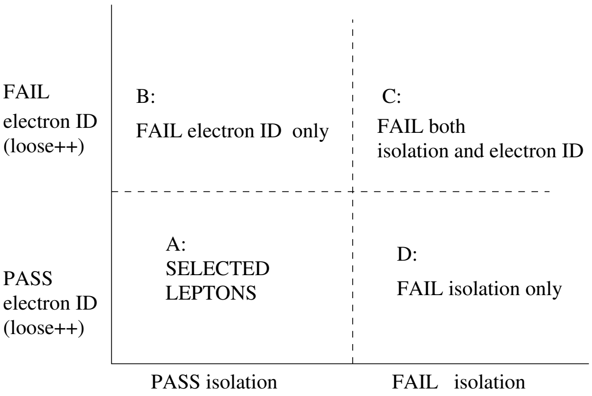

Figure 6.9.: Visual illustration of the row labeled "electrons" in table 6.9. Objects assigned to the square "C" are rejected while those in squares "B" and "D" are considered as electron-like jets.

For muons a similar classification is applied to get the fake factor. To be considered as a pre-muon all selection criteria but the calorimetric isolation and, if available, the track isolation as well as the requirement on the significance of the impact parameter in the transverse plane d_0, have to be passed. For muons with high pseudorapidity $|\eta| > 2.5$, there is no reliable track isolation and the d_0 is only measured if it is a combined muon. The selected muons which form the L collection, are those passing the full set of requirements. The J collection of muon-like jets contains all objects passing either or both of the isolation requirements or if available the d_0 significance cut. In case all second stage cuts are failed the object is rejected. In contrast to the electron trigger, there are only very loose requirements on the object quality for the muon trigger. In consequence pre-muons matched to a triggered object are not excluded and the trigger bias is estimated to be small. The introduced categories of muons and muon-like objects are reported in table 6.10 and figure 6.11. The number of objects in the L and J collection obtained from the inclusive sample and in dependence of p_{T} and η are shown in figure 6.12. The

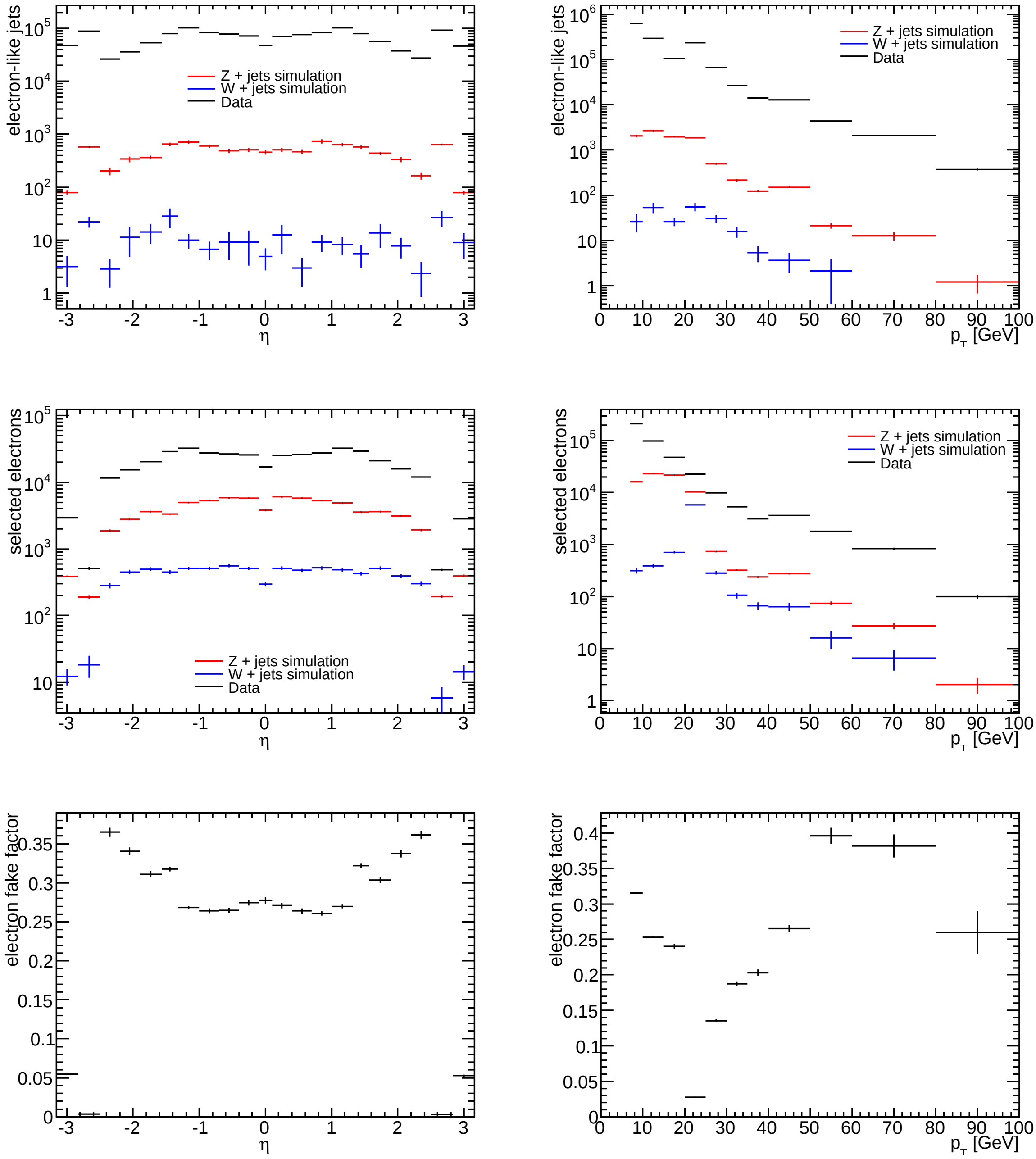

Figure 6.10.: The first row shows the number of electron-like jets found in data (black) as well as in $Z+$ jets (red) and $W+$ jets (blue) simulation which estimates the contribution of signal like electrons in the sample. In the second row the equivalent is shown for selected electrons. The last row shows the fake factors FF which are calculated as the ratio of row one and two after revising for the signal contamination. On the left the object counts are shown as a function of the pseudorapidity while on the right they are present as a function of the transverse momentum. These displayed distributions are based on the inclusive sample. The corresponding plots produced with the Z-tagged sample are available in appendix D.2.

resulting fake factor is presented in this figure as well. Appendix D.2 holds related figures for the Z-tagged sample which correspond rather well.

	selected muons	muon-like jets
central/ calorimetric muons	track isolation < 0.15 and calorimetric isolation < 0.30 and d_0-significance < 3.5	(d_0-significance > 3.5 and track isolation < 0.15 and calorimetric isolation < 0.30) or (d_0-significance < 3.5 and (track isolation > 0.15 or calorimetric isolation > 0.30)
high-η muons (stand alone)	calometric isolation < 0.15	calometric isolation > 0.15
high-η muons (combined)	calometric isolation < 0.15 and d_0-significance < 3.5	calometric isolation > 0.15 or d_0-significance > 3.5

Table 6.10.: Second stage selection criteria used to categorize a pre-selected muon either as selected muon or muon-like jet. Muons with high pseudorapidity, i.e. those found in the region $2.5 < |\eta| < 2.7$ are classified by their relative calorimetric isolation and, if available the d_0 significance. Due to a not reliable track isolation, this requirement is not used for them. For common, central muons and calorimeter tagged muons the same categorization requirements are applied.

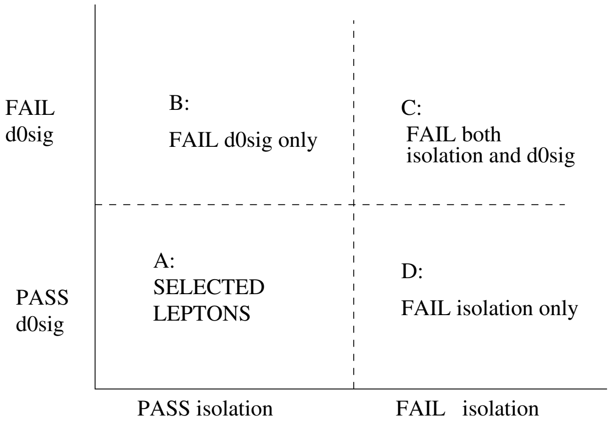

Figure 6.11.: Visual illustration of the row labeled “central/calorimetric muons” in table 6.10. Objects assigned to the square “C” are rejected while those in squares “B” and “D” are considered as muon-like jets.

With the event counts for N_{LLLJ} and N_{LLJJ} in data and N^{ZZ}_{LLLJ} from simulation, the background can be estimated by using equation (6.17). The inserted fake factors are calculated accordingly to equation (6.19) and derived from the inclusive sample. The expected background, splitted up into the different channels for $ZZ \to \ell\ell\ell'\ell'$ with both Z bosons on-shell, is presented in table 6.11 while for the case of one Z boson allowed to be off-shell it is table 6.12. The statistical uncertainty is the relative error on the number of events measured in the channels, transfered to the number of events with the fake factors applied. For the overall estimate of background events the statistical errors of the individual contributions are assumed to be fully correlated. If

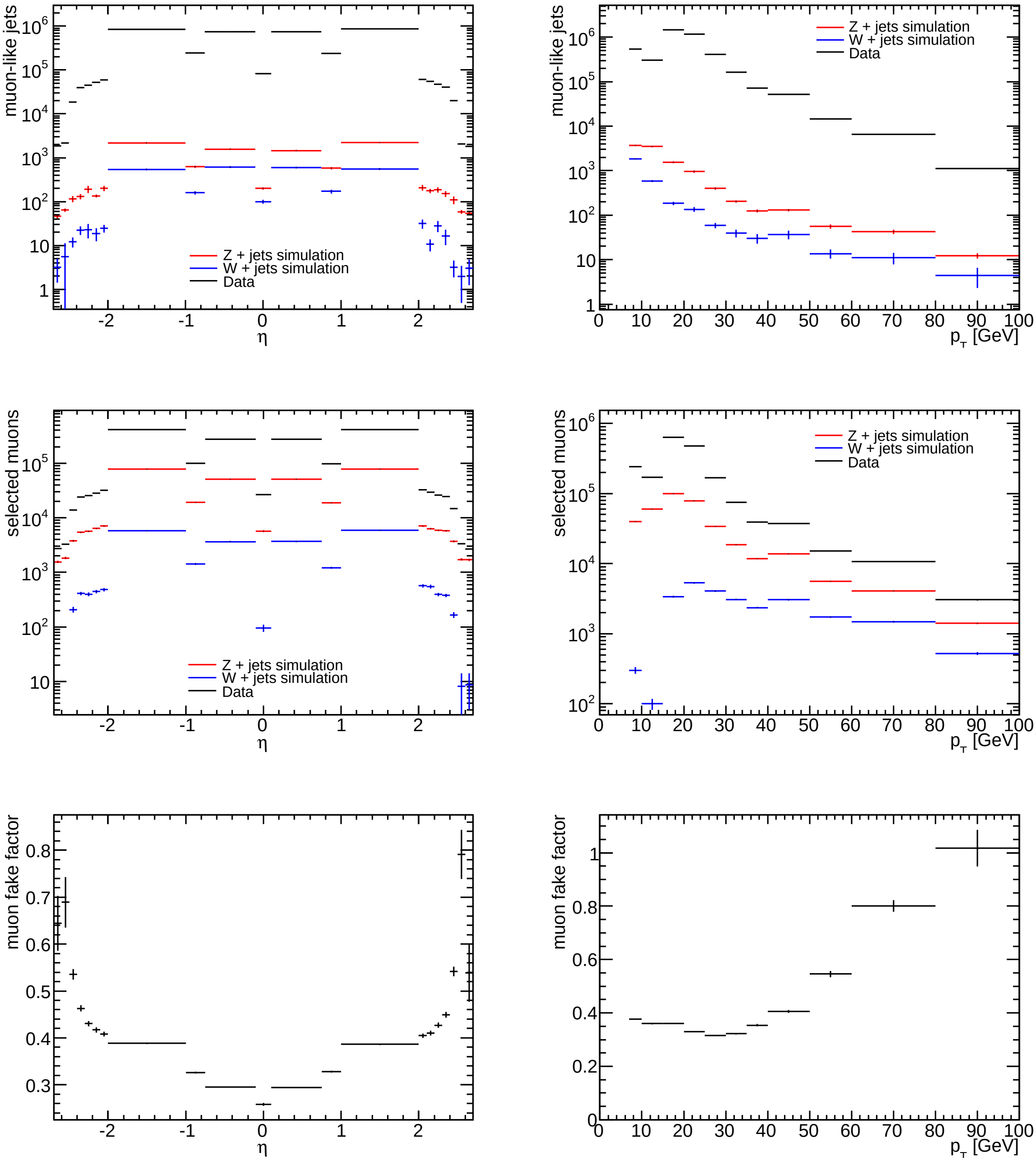

Figure 6.12.: The first row shows the number of muon-like jets found in data (black) as well as in $Z+$ jets (red) and $W+$ jets (blue) simulation which estimates the contribution of signal like muons in the sample. In the second row the equivalent is shown for selected muons. The last row shows the fake factors FF which are calculated as the ratio of row one and two after revising for the signal contamination. On the left the object counts are shown as a function of the pseudorapidity while on the right they are present as a function of the transverse momentum. These displayed distributions are based on the inclusive sample. The corresponding plots produced with the Z-tagged sample are available in appendix D.2.

the estimate turns out to be negative, an upper limit is set by assuming a truncated Gaussian with mean at zero and sigma equal to the statistical uncertainty. Compared to quoting a sigma equal to the estimated uncertainties minus the negative estimate for the mean background value, the applied approach is conservative.

Ingredients in eq. (6.17)	$eeee$	$\mu\mu\mu\mu$	$2e2\mu$	Combined ($\ell\ell\ell\ell$)
(+) N_{LLLJ} (unweight)	19.00	1.00	13.00	33.00
(+) $N_{LLLJ} \times FF$	2.75 ± 0.63	0.32 ± 0.32	2.35 ± 0.65	5.42 ± 0.96
(−) N^{ZZ}_{LLLJ} (unweight)	2.58	0.65	3.86	7.09
(−) $N^{ZZ}_{LLLJ} \times FF$	0.54 ± 0.33	$0.28^{+0.35}_{-0.28}$	0.90 ± 0.46	1.71 ± 0.66
(−) N_{LLJJ} (unweight)	72.00	4.00	60.00	136.00
(−) $N_{LLJJ} \times FF^2$	2.10 ± 0.25	1.13 ± 0.56	1.14 ± 0.15	4.38 ± 0.63
$N^{\mathrm{bkg}}_{\ell\ell\ell'\ell'}$	0.11 ± 1.21	-1.09 ± 1.23	0.31 ± 1.26	-0.67 ± 2.26
$N^{\mathrm{bkg}}_{\ell\ell\ell'\ell'}$ (final)	$0.11^{+1.21}_{-0.11}$	< 1.23	$0.31^{+1.26}_{-0.31}$	< 2.26

Table 6.11.: Background estimate for $ZZ \to \ell^+\ell^-\ell'^+\ell'^-$ events in $4.6\,\mathrm{fb}^{-1}$ based on fake factors derived from the inclusive sample. The first three columns hold the values for the individual channels while the last column is the combination. The event counts found in data and signal Monte Carlo respectively are presented before and after reweighting with the fake factors. The sign at the beginning of each row indicates how the numbers enter in equation (6.17) for the actual background calculation. In case the central value of the estimate turns out to be negative the upper bound is determined as explained in the text. The corresponding results obtained with the Z-tagged sample are available in table 6.13.

Ingredients in eq. (6.17)	$eeee$	$\mu\mu\mu\mu$	$2e2\mu$	Combined ($\ell\ell\ell\ell$)
(+) N_{LLLJ} (unweight)	58.00	2.00	68.00	128.00
(+) $N_{LLLJ} \times FF$	11.80 ± 1.55	0.58 ± 0.41	13.24 ± 1.61	25.62 ± 2.27
(−) N^{ZZ}_{LLLJ} (unweight)	3.24	1.00	4.93	9.16
(−) $N^{ZZ}_{LLLJ} \times FF$	0.67 ± 0.37	0.42 ± 0.42	1.16 ± 0.52	2.24 ± 0.76
(−) N_{LLJJ} (unweight)	246.00	11.00	235.00	492.00
(−) $N_{LLJJ} \times FF^2$	8.65 ± 0.55	2.17 ± 0.66	6.90 ± 0.45	17.73 ± 0.97
$N^{\mathrm{bkg}}_{\ell\ell\ell'\ell'}$	2.48 ± 2.48	-2.01 ± 1.48	5.18 ± 2.58	5.65 ± 4.00
$N^{\mathrm{bkg}}_{\ell\ell\ell'\ell'}$ (final)	2.48 ± 2.48	< 1.48	5.18 ± 2.58	5.65 ± 4.00

Table 6.12.: Background estimate for $ZZ^* \to \ell^+\ell^-\ell'^+\ell'^-$ events in $4.6\,\mathrm{fb}^{-1}$ based on fake factors derived from the inclusive sample. The first three columns hold the values for the individual channels while the last column is the combination. The event counts found in data and signal Monte Carlo respectively are presented before and after reweighting with the fake factors. The sign at the beginning of each row indicates how the numbers enter in equation (6.17) for the actual background calculation. In case the central value of the estimate turns out to be negative the upper bound is determined as explained in the text. The corresponding results obtained with the Z-tagged sample are available in table 6.14.

Tables 6.13 and 6.14 quote the corresponding background estimates for $ZZ \to \ell\ell\ell'\ell'$ with both Z bosons on-shell and one Z boson allowed to be off-shell respectively as obtained with fake factors from the Z-tagged sample. The statistical uncertainties are calculated like for the inclusive sample. The fake factors determined with the Z-tagged sample are in addition to data once again extracted from Monte Carlo and a reasonable agreement is found. The systematic uncertainty is estimated by taking the difference between the fake factors received from the two sources. A similar study using two sets of inclusive samples is not possible due to missing high statistics simulation of inclusive jet production and heavy quark production with sufficiently low momentum filters on generator level. The quoted upper bounds in case of negative background estimates derived from the Z-tagged sample are the statistical and systematic uncertainties summed in quadrature instead of the statistical uncertainty only like for the inclusive sample.

Ingredients in eq. (6.17)	$eeee$	$\mu\mu\mu\mu$	$2e2\mu$	Combined ($\ell\ell\ell\ell$)
(+) $N_{LLLJ} \times FF$	1.63 ± 0.34	0.21 ± 0.21	1.84 ± 0.40	3.67 ± 0.57
(−) $N^{ZZ}_{LLLJ} \times FF$	0.17 ± 0.13	$0.12^{+0.20}_{-0.12}$	0.34 ± 0.21	0.63 ± 0.32
(−) $N_{LLJJ} \times FF^2$	0.96 ± 0.10	0.33 ± 0.16	0.83 ± 0.09	2.12 ± 0.21
$N^{\text{bkg}}_{\ell\ell\ell'\ell'}$	0.50	< 0.64	0.66	0.92
	$^{+0.57}_{-0.50}$(stat)	$[0^{+0.57}_{-0}$(stat)	$^{+0.70}_{-0.66}$(stat)	$^{+1.10}_{-0.92}$(stat)
	± 0.26(syst)	$^{+0.30}_{-0}$(syst)]	± 0.55(syst)	$^{+0.71}_{-0.74}$(syst)

Table 6.13.: Background estimate for $ZZ \rightarrow \ell^+\ell^-\ell'^+\ell'^-$ events in $4.6\,\text{fb}^{-1}$ based on fake factors derived from the Z-tagged sample. The first three columns hold the values for the individual channels while the last column is the combination. The event counts found in data and signal Monte Carlo respectively are presented after reweighting with the fake factors. The sign at the beginning of each row indicates how the numbers enter in equation (6.17) for the actual background calculation. In case the central value of the estimate turns out to be negative the upper bound is determined as explained in the text.

Ingredients in eq. (6.17)	$eeee$	$\mu\mu\mu\mu$	$2e2\mu$	Combined ($\ell\ell\ell\ell$)
(+) $N_{LLLJ} \times FF$	8.85 ± 0.98	0.21 ± 0.21	10.63 ± 1.06	19.70 ± 1.46
(−) $N^{ZZ}_{LLLJ} \times FF$	0.29 ± 0.18	$0.20^{+0.25}_{-0.20}$	0.56 ± 0.28	1.05 ± 0.42
(−) $N_{LLJJ} \times FF^2$	4.24 ± 0.23	1.10 ± 0.31	4.24 ± 0.23	9.58 ± 0.45
$N^{\text{bkg}}_{\ell\ell\ell'\ell'}$	4.33	< 0.91	5.84	9.07
	± 1.39(stat)	$[0^{+0.77}_{-0}$(stat)	± 1.57(stat)	± 2.32(stat)
	± 0.62(syst)	$^{+0.49}_{-0}$(syst)]	± 0.93(syst)	± 1.29(syst)

Table 6.14.: Background estimate for $ZZ^* \rightarrow \ell^+\ell^-\ell'^+\ell'^-$ events in $4.6\,\text{fb}^{-1}$ based on fake factors derived from the Z-tagged sample. The first three columns hold the values for the individual channels while the last column is the combination. The event counts found in data and signal Monte Carlo respectively are presented after reweighting with the fake factors. The sign at the beginning of each row indicates how the numbers enter in equation (6.17) for the actual background calculation. In case the central value of the estimate turns out to be negative the upper bound is determined as explained in the text.

The Monte Carlo prediction for the number of events passing the various stages of the selection requirements are shown in tables 6.15 to 6.17 for the different channels with contributions from $Z+$ jets, WZ/WW and top-quark production separated. The dominant source for all channels is $Z+$ jets. The total background combined for all channels and as predicted from simulation is presented in table 6.18. All corrections and scale-factors are applied and the results are scaled to the data luminosity of $4.64\,\text{fb}^{-1}$. The Monte Carlo is only used as an additional cross-check for the data-driven method like mentioned before because it relies on a good modeling of leptons in jets and has rather high statistical uncertainties.

requirement	Z+jets	WZ/WW	top
four leptons	12.22 ± 1.82	0.78 ± 0.39	0.16 ± 0.16
trigger match	11.90 ± 1.80	0.78 ± 0.39	0.16 ± 0.16
two opposite charge, same flavor pairs	6.99 ± 1.46	0.58 ± 0.22	0.16 ± 0.16
$66 < M_{Z1} < 116$ GeV	5.09 ± 1.24	0.54 ± 0.21	0.00 ± 0.00
$M_{Z2} > 20$ GeV	3.48 ± 0.92	0.32 ± 0.09	0.00 ± 0.00
$66 < M_{Z2} < 116$ GeV	0.56 ± 0.24	0.13 ± 0.06	0.00 ± 0.00

Table 6.15.: The number of background events in the $eeee$ channel passing the various levels of the event selection as predicted by Monte Carlo. The expected yields are given for $Z+$ jets background including contributions from light and heavy flavors, for WZ/WW and for $t\bar{t}$ and single top which are comprised in the column labeled "top". All event counts are normalized to the integrated data luminosity.

requirement	Z+jets	WZ/WW	top
four leptons	0.26 ± 0.26	0.06 ± 0.05	0.00 ± 0.00
trigger match	0.26 ± 0.26	0.06 ± 0.05	0.00 ± 0.00
two opposite charge, same flavor pairs	0.26 ± 0.26	0.06 ± 0.05	0.00 ± 0.00
$66 < M_{Z1} < 116$ GeV	0.00 ± 0.00	0.06 ± 0.05	0.00 ± 0.00
$M_{Z2} > 20$ GeV	0.00 ± 0.00	0.06 ± 0.05	0.00 ± 0.00
$66 < M_{Z2} < 116$ GeV	0.00 ± 0.00	0.01 ± 0.01	0.00 ± 0.00

Table 6.16.: The number of background events in the $\mu\mu\mu\mu$ channel passing the various levels of the event selection as predicted by Monte Carlo. The expected yields are given for $Z+$ jets background including contributions from light and heavy flavors, for WZ/WW and for $t\bar{t}$ and single top which are comprised in the column labeled "top". All event counts are normalized to the integrated data luminosity.

The background for $\ell^+\ell^-\ell'^+\ell'^-$ estimated by the two data-driven approaches and the Monte Carlo prediction agree quite well. For the ZZ selection the background estimated with fake factors from the Z-tagged sample comprises $0.92^{+1.10}_{-0.92}(\text{stat})^{+0.71}_{-0.74}(\text{syst})$ events, for fake factors derived from the inclusive sample it is less than 2.26 events and Monte Carlo predicts 1.46 ± 0.37 events. In case of one Z boson allowed to be off-shell the corresponding values are $9.07 \pm 2.32(\text{stat}) \pm 1.29(\text{syst})$ events for the Z-tagged approach, $5.65 \pm 4.00(\text{stat})$ events for the inclusive one and $8.26 \pm 1.30(\text{stat})$ events extracted from simulation. For the following analysis the values determined by the data-driven approach using the Z-tagged sample are used.

In order to extract limits on neutral anomalous triple gauge couplings, like they are reported in section 6.7.2, it is necessary to study differential distributions of kinematic variables of ZZ events. However, it is not possible to estimate the background to these distributions applying the full lepton object selection since there is a lack of statistics in the simulated samples as well as in the control regions of the data-driven one. Therefore the lepton object requirements are loosened and the demand on oppositely charged leptons forming the secondary Z candidate is

requirement	Z+jets	WZ/WW	top
four leptons	21.98 ± 2.86	1.18 ± 0.20	0.10 ± 0.13
trigger match	20.81 ± 2.79	1.18 ± 0.20	0.10 ± 0.13
two opposite charge, same flavor pairs	7.04 ± 1.21	0.65 ± 0.16	0.03 ± 0.11
$66 < M_{Z1} < 116$ GeV	4.93 ± 0.96	0.56 ± 0.15	0.00 ± 0.00
$M_{Z2} > 20$ GeV	3.95 ± 0.91	0.46 ± 0.14	0.00 ± 0.00
$66 < M_{Z2} < 116$ GeV	0.68 ± 0.28	0.11 ± 0.05	0.00 ± 0.00

Table 6.17.: The number of background events in the $ee\mu\mu$ channel passing the various levels of the event selection as predicted by Monte Carlo. The expected yields are given for $Z+$ jets background including contributions from light and heavy flavors, for WZ/WW and for $t\bar{t}$ and single top which are comprised in the column labeled "top". All event counts are normalized to the integrated data luminosity.

requirement	Z+jets	WZ/WW	top
four leptons	34.46 ± 3.40	2.03 ± 0.44	0.27 ± 0.21
trigger match	32.96 ± 3.33	2.02 ± 0.44	0.27 ± 0.21
two opposite charge, same flavor pairs	14.29 ± 1.91	1.28 ± 0.27	0.19 ± 0.20
$66 < M_{Z1} < 116$ GeV	10.03 ± 1.57	1.16 ± 0.26	0.00 ± 0.00
$M_{Z2} > 20$ GeV	7.43 ± 1.29	0.83 ± 0.17	0.00 ± 0.00
$66 < M_{Z2} < 116$ GeV	1.24 ± 0.36	0.25 ± 0.08	0.00 ± 0.00

Table 6.18.: The number of background events in the combination of all four charged lepton channels passing the various levels of the event selection as predicted by Monte Carlo. The expected yields are given for $Z+$ jets background including contributions from light and heavy flavors, for WZ/WW and for $t\bar{t}$ and single top which are comprised in the column labeled "top". All event counts are normalized to the integrated data luminosity.

dropped. To enter the looser sample the event has to contain one Z candidate with two opposite charged leptons of the same flavor, passing all nominal lepton selection criteria and with an invariant mass in the nominal Z mass window. For both, electrons and muons, the two leptons forming the secondary Z candidate have to pass the nominal lepton selection criteria except the calorimeter isolation, the track isolation and the requirement on the impact parameter in the transversal plane. The demand on the invariant mass of the second pair remains the same as for the full event selection of ZZ events.

The differential distributions are extracted from Monte Carlo while the changed efficiencies due to the loosened selection criteria are accounted by scaling the corresponding events with the ratio of the number of events passing the tight selection to the number of events passing the loosened requirements. The invariant mass of the two lepton pairs was not restricted for the calculation of the ratio. An efficiency of 0.051 was found for a electron pair with loosened requirements while the determined efficiency for muons passing the relaxed criteria is 0.012. To respect any difference in shape occurring in events with the different "loose" Z candidate types this scaling is used. In a second step the distributions were scaled to the data-driven background estimates for $ZZ^{(*)}$ after the shape was determined. The statistical error per bin is a combination of the statistical error on the histogram and the one of the full data-driven estimate propagated accordingly. For the systematic uncertainty per bin, only the corresponding error of data-driven estimate is used.

6.6. ZZ cross section determination through the four charged lepton final state

The data selection introduced in section 6.2 is analyzed in order to find events with a four charged lepton final state originating from a pair of Z bosons with both on-shell or one allowed to be off-shell. It is searched for muons and electrons that pass all the object selection criteria listed in section 6.3. Subsequently the strategy explained in section 6.4 is used to isolate the relevant events while the background is estimated by a data-driven method elucidated in section 6.5. The resulting observed candidate events for ZZ and ZZ^* decays into four charged leptons and the corresponding background estimates are summarized in table 6.19.

	$e^+e^-e^+e^-$	$\mu^+\mu^-\mu^+\mu^-$	$e^+e^-\mu^+\mu^-$	$\ell^-\ell^+\ell^-\ell^+$
Observed ZZ	16	23	27	66
Observed ZZ^*	21	30	33	84
Expected ZZ signal	$10.3 \pm 0.1 \pm 1.0$	$16.5 \pm 0.2 \pm 0.9$	$26.7 \pm 0.2 \pm 1.7$	$53.4 \pm 0.3 \pm 3.2$
Expected ZZ^* signal	$12.3 \pm 0.2 \pm 1.2$	$20.5 \pm 0.2 \pm 1.1$	$31.6 \pm 0.3 \pm 2.0$	$64.4 \pm 0.4 \pm 4.0$
Expected ZZ background	$0.5 \pm 0.6 \pm 0.3$	< 0.6	$0.7 \pm 0.7 \pm 0.6$	$0.9 \pm 1.1 \pm 0.7$
Expected ZZ^* background	$4.3 \pm 1.4 \pm 0.6$	< 0.9	$5.8 \pm 1.6 \pm 0.9$	$9.1 \pm 2.3 \pm 1.3$

Table 6.19.: Summary of observed $ZZ^{(*)} \rightarrow \ell^+\ell^-\ell'^+\ell'^-$ candidate events in data and the estimated background as well as the expected signal yield as predicted from simulation. The corresponding numbers are given split up in the individual channels and in combination. The first uncertainty quoted is statistical while the second one is systematic.

The distributions of the final candidate events with respect to the transverse momentum of the leading and subleading Z boson are presented in figure 6.13 for both Z bosons on-shell and in figure 6.14 for one Z boson allowed to be off-shell. Furthermore these figures hold the number of events as function of the mass of the diboson system and its transverse momentum. In case of ZZ^*, the event count in dependence of the leading and subleading Z boson is reported, too. In figure 6.15 the mass of the leading Z candidate is correlated to the mass of the subleading Z candidate for data and simulation. The estimated background distribution is shown in the same figure, but in a separate plot. Figure 6.16 shows for the measured and simulated $ZZ \rightarrow \ell\ell\ell'\ell'$ events the spacial distance ΔR of the two leptons forming a Z candidate with respect to the transverse momentum of the Z boson. The minimal spacial distance $\min(\Delta R)$ of two leptons forming a Z candidate is displayed as a function of the four lepton invariant mass $M^{ZZ^{(*)}}$, again for data and simulation.
To convert the counts of $ZZ^{(*)} \rightarrow \ell\ell\ell'\ell'$ events to an actual cross section the strategy pointed out in section 6.4 is applied. In a first step the fiducial cross section is calculated according to equation (6.4) which is then extrapolated to the full phase space following equation (6.3). The reconstruction correction factor is defined as

$$C_{ZZ^{(*)}} = \epsilon_{trig}\epsilon_{event}\epsilon_{lep}\alpha_{reco} \tag{6.20}$$

where ϵ_{trig} denotes the trigger efficiency, ϵ_{event} summarizes the efficiency of the event level requirements and ϵ_{lep} is the product of the individual efficiencies of the leptons to pass the selection criteria. The quantity α_{reco} accounts for differences in the reconstruction to generator-level fiducial volume and includes smearing corrections and resolutions. In practice $C_{ZZ^{(*)}}$ is calculated as the ratio of the number of events passing the reconstruction level requirements as

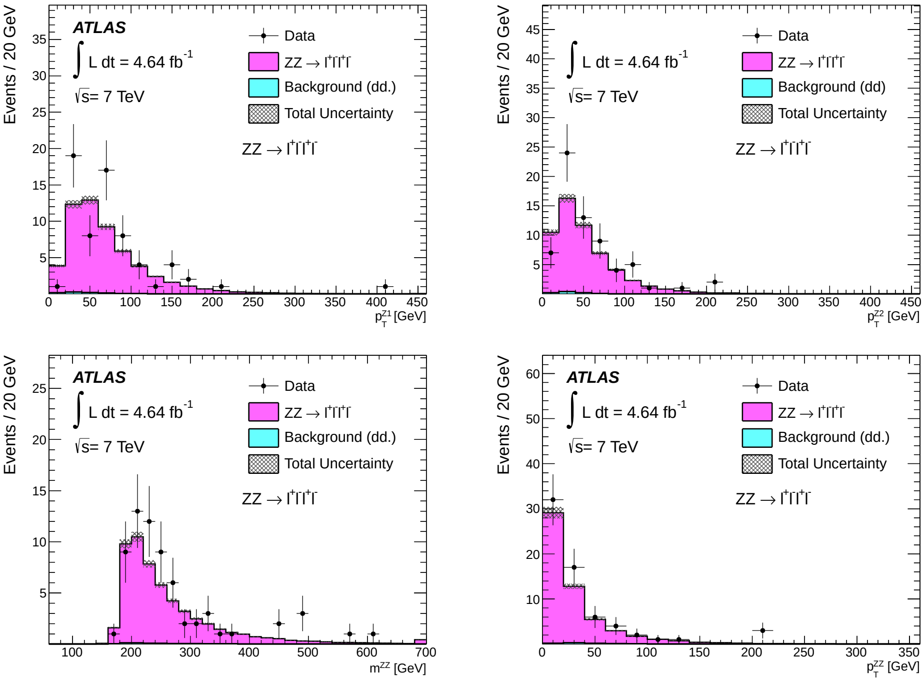

Figure 6.13.: Kinematic distributions of $ZZ \rightarrow 4\ell$ candidate events as observed in data (points) with the data-driven background estimation and expected signal predicted from Monte Carlo superimposed as stacked histograms. The combined statistical and systematic uncertainty on the signal prediction is indicated by the gray band. In the top row the distributions in dependence of the transverse momentum of the leading (left) and subleading Z boson are present. The bottom row displays the number of events distributed in the transverse momentum (left) and mass (right) of the diboson system.

they are contained in the fully simulated sample after all necessary corrections, divided by the number of events inside the fiducial volume at the generator-level. Formally it reads

$$C_{ZZ^{(*)}} = \frac{N^{\text{MC pass all cuts}}_{\text{reconstructed } ZZ^{(*)}} \times SF}{N^{\text{MC fiducidal volume}}_{\text{generated } ZZ^{(*)}}} \tag{6.21}$$

with a scale factor SF accounting for discrepancies in the trigger efficiency and reconstruction efficiency between data and Monte Carlo. The factor is applied on a event-by-event basis and is obtained according to equation (6.1). More abstractly, it is defined as

$$SF = \frac{\epsilon^{data}_{trig}}{\epsilon^{MC}_{trig}} \cdot \frac{\epsilon^{data}_{reco}}{\epsilon^{MC}_{reco}} \tag{6.22}$$

with $\epsilon_{reco} = \epsilon_{lep} \cdot \epsilon_{event}$. In summary the reconstruction correction factor essentially gives the probability of reconstructing an event in case all the objects would have been in the detector and all the selection criteria are fulfilled. It extrapolates from the reconstruction level to truth fiducial level like mentioned in section 6.4. It is less sensitive to purely theoretical uncertainties like for example the used PDF set. The resulting values calculated for each channel separately and with different generators are given in table 6.20. The comparison of the generators is performed to study the impact of different parton showering models and underlying event models. Also the gluon-gluon contribution to the ZZ production and changes of the kinematic distributions between LO/NLO calculations are examined by this comparison. To combine all channels in order to obtain a total cross section, the branching ratios have to be inserted appropriately.

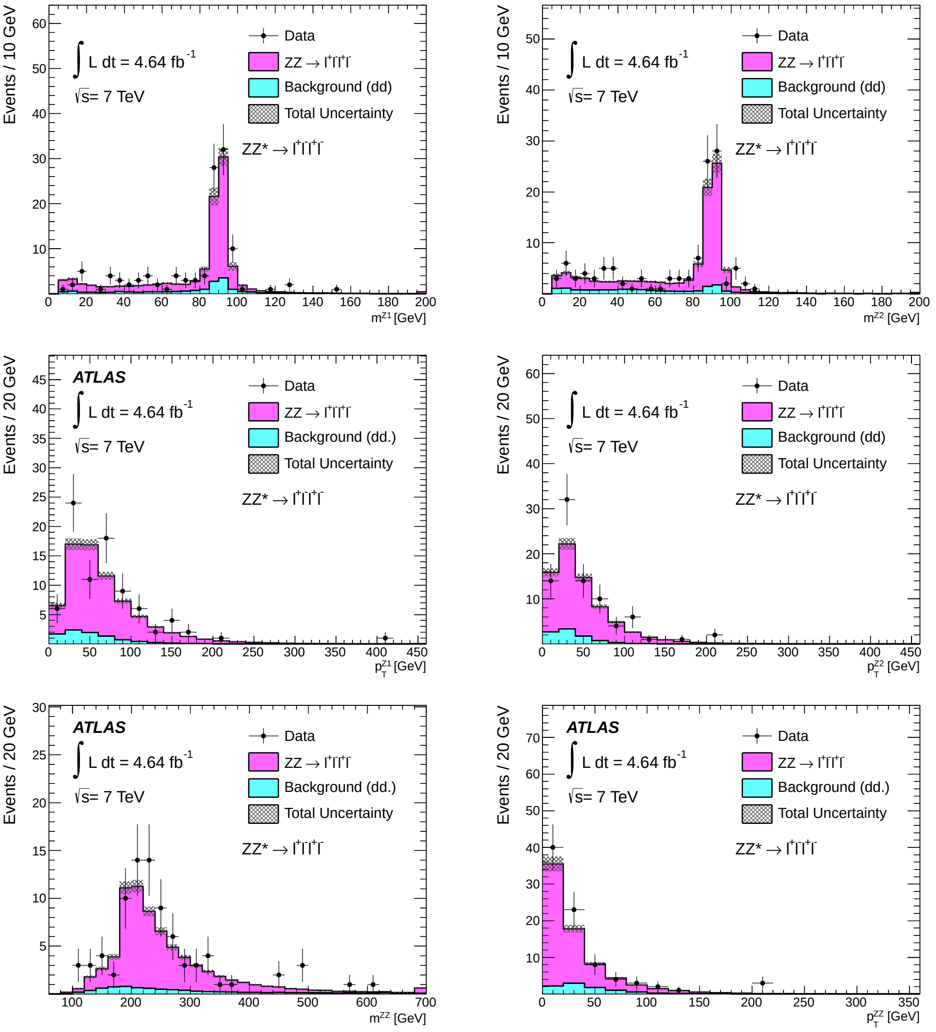

Figure 6.14.: Kinematic distributions of $ZZ^* \rightarrow 4\ell$ candidate events as observed in data (points) with the data-driven background estimation and expected signal predicted from Monte Carlo superimposed as stacked histograms. The combined statistical and systematic uncertainty on the signal prediction is indicated by the gray band. The top row shows the distribution of the events as function of the leading (left) and subleading Z boson mass (right). In the second row the distributions in dependence of the transverse momentum of the leading (left) and subleading Z boson are present. The third row displays the number of events distributed in the transverse momentum (left) and mass (right) of the diboson system.

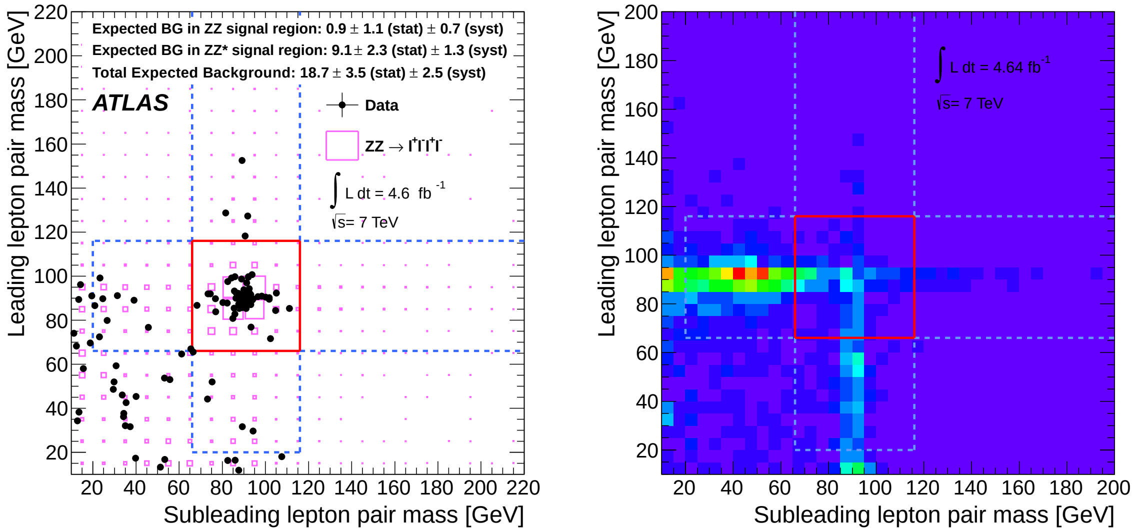

Figure 6.15.: On the left, the mass of the leading lepton pair versus the mass of the sub-leading lepton pair is presented. The $ZZ^{(*)} \rightarrow \ell^+\ell^-\ell'^+\ell'^-$ signal prediction from simulation is displayed as boxes while their size is proportional to the event count in each bin. The observed data events are superimposed as solid circles. The corresponding distribution of background events as obtained from Monte Carlo is shown on the right. In both plots the region enclosed by the solid red (dashed blue) lines indicates the region as defined by the $ZZ^{(*)}$ requirement on the lepton-pair masses.

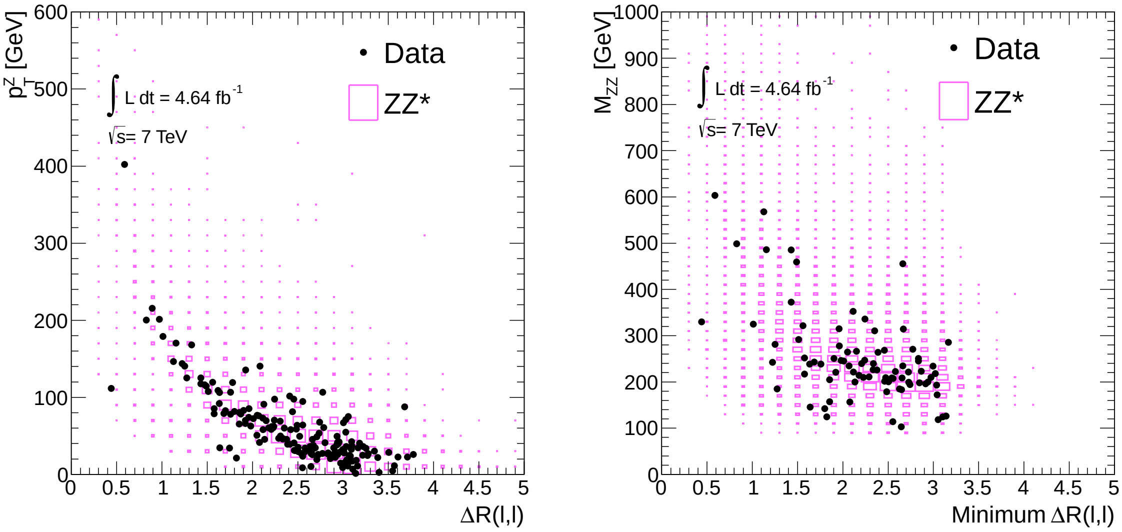

Figure 6.16.: The transverse momentum of the Z boson candidates is shown on the left as function of the angle between the leptons forming the pair. There are two entries per $ZZ^{(*)}$ event. On the right, there is the invariant mass of the diboson system M_{ZZ} versus the minimum spacial distance of the leptons forming the Z boson pairs. For both plots events observed in data are indicated by solid black circles while the corresponding signal Monte Carlo prediction is represented by boxes with a size proportional to the event count in each bin.

ZZ^* Selection

Generator	$e^+e^-e^+e^-$	$\mu^+\mu^-\mu^+\mu^-$	$e^+e^-\mu^+\mu^-$	combined
Sherpa	0.420 ± 0.004	0.682 ± 0.004	0.536 ± 0.003	0.544 ± 0.002
Pythia	0.413 ± 0.004	0.689 ± 0.004	0.543 ± 0.003	0.547 ± 0.002
PowhegBox	0.408 ± 0.004	0.674 ± 0.004	0.537 ± 0.003	0.539 ± 0.002
gg2zz	0.457 ± 0.002	0.761 ± 0.002	0.589 ± 0.002	0.600 ± 0.001
PowhegBox + gg2zz	0.410 ± 0.004	0.679 ± 0.004	0.540 ± 0.003	0.542 ± 0.002

ZZ Selection

Generator	$e^+e^-e^+e^-$	$\mu^+\mu^-\mu^+\mu^-$	$e^+e^-\mu^+\mu^-$	combined
Sherpa	0.437 ± 0.004	0.689 ± 0.004	0.550 ± 0.003	0.557 ± 0.002
Pythia	0.425 ± 0.004	0.695 ± 0.004	0.549 ± 0.003	0.555 ± 0.002
PowhegBox	0.426 ± 0.005	0.682 ± 0.004	0.543 ± 0.003	0.549 ± 0.002
gg2zz	0.466 ± 0.002	0.765 ± 0.002	0.596 ± 0.002	0.606 ± 0.001
PowhegBox + gg2zz	0.428 ± 0.005	0.687 ± 0.004	0.546 ± 0.003	0.552 ± 0.002

Table 6.20.: Comparison of the reconstruction correction factor $C_{ZZ^{(*)}}$ obtained with various generators. The upper section of the table holds the values for the ZZ^* selection while in the lower part the corresponding values for ZZ are listed. The quoted uncertainties are statistical. Finally the determined differences are reported as systematic uncertainties in table 6.21.

There are several systematic uncertainties related to the lepton reconstruction which constitute the systematic uncertainty of $C_{ZZ^{(*)}}$. For both, electrons and muons, there are uncertainties introduced by the reconstruction efficiency scale factor which is applied on the Monte Carlo. The event yield is computed while varying this scale factor. The variation around the nominal value is propagated appropriately to the systematic uncertainty of $C_{ZZ^{(*)}}$. The scale as well as the smearing of the energy and of the transverse momentum respectively applied on simulated electrons and muons cause another systematic uncertainty. Again the corrections are varied within their errors and the impact on $C_{ZZ^{(*)}}$ enters its systematic uncertainty. Due to the requirement on the impact parameters and the isolation another scale factor and systematic uncertainty arises. Here the corresponding estimates evaluated by the $H \to ZZ$ analysis [164] are applied. In detail the assigned uncertainty for muons below 15 GeV is 2%, for 15−20 GeV it is 1% and above 20 GeV it is less than 1%. In case of electrons with $p_{\mathrm{T}} < 15$ GeV the found uncertainty is 5%, for 15 − 20 GeV it is 2% and for 20 − 35 GeV it is 1% while it is less than 1% above 35 GeV. For electrons, there is an additional uncertainty related to the identification efficiency entering the uncertainty on $C_{ZZ^{(*)}}$. In table 6.21 all mentioned uncertainties are summarized including the errors assigned to the trigger efficiency and resolution of the interaction point.

Once the fiducial cross section is determined, the total cross section is calculated accroding to equation (6.3). The acceptance correction factor is defined as A_{ZZ} and performs the extrapolation from the truth fiducial volume to the full phase-space at truth level. It is calculated for each channel separately by the ratio

$$A_{ZZ} = \frac{N^{\text{MC fiducial volume}}_{\text{generated } ZZ}}{N^{\text{MC all}}_{\text{generated } ZZ}}. \tag{6.23}$$

Source %	$eeee$		$\mu\mu\mu\mu$		$ee\mu\mu$		$llll$	
Reconstruction Uncertainties	ZZ	ZZ^*	ZZ	ZZ^*	ZZ	ZZ^*	ZZ	ZZ^*
e energy resolution	< 0.1	< 0.1	-	-	< 0.1	< 0.1	< 0.1	< 0.1
e energy scale	0.5	0.6	-	-	0.1	0.1	0.1	0.2
e identification efficiency	5.5	6.0	-	-	2.7	2.8	2.4	2.5
e reconstruction	3.9	4.0	-	-	1.9	2.0	1.7	1.7
e isolation/z0/d0Sig	3.3	3.6	-	-	1.6	1.7	1.4	1.5
μ momentum resolution	-	-	< 0.1	< 0.1	< 0.1	< 0.1	< 0.1	< 0.1
μ momentum scale	-	-	< 0.1	< 0.1	< 0.1	< 0.1	< 0.1	< 0.1
μ reconstruction efficiency	-	-	1.2	1.2	0.6	0.6	0.7	0.7
μ isolation/z0/d0Sig	-	-	2.2	2.4	1.1	1.2	1.3	1.3
IP Resolution	< 0.1	< 0.1	0.4	0.4	0.3	0.3	0.3	0.3
Trigger	< 0.1	< 0.1	0.3	0.4	0.1	0.2	0.2	0.2
Total Reconstruction Uncertainty ($C_{ZZ^{(*)}}$)	7.5	8.1	2.6	2.7	3.9	4.1	3.6	3.7

Theoretical Uncertainties	ZZ	ZZ^*
MC Generator Difference ($C_{ZZ^{(*)}}$)	1.6	1.5
PDF & Scale (A_{ZZ})	0.6	2.5
MC Generator Difference (A_{ZZ})	1.1	0.2
Total (A_{ZZ})	1.3	2.5

	$eeee$		$\mu\mu\mu\mu$		$ee\mu\mu$		$llll$	
	ZZ	ZZ^*	ZZ	ZZ^*	ZZ	ZZ^*	ZZ	ZZ^*
Total ($C_{ZZ^{(*)}}$)	7.7	8.2	3.0	3.1	4.2	4.4	3.9	4.0
Luminosity	3.9							

Table 6.21.: Summary of all considered relative uncertainties (in %) assigned to the two correction factors $C_{ZZ^{(*)}}$ and A_{ZZ} as indicated by the parenthesis next to the description of the uncertainty source. For the reconstruction uncertainties the sums in quadrature of the weighted average of the three channels and a combined uncertainty is reported. More details regarding PDF and scale uncertainties can be found in table 6.5. The differences between the various generators are detailed in tables 6.20 and 6.22.

The results for different generators are given in table 6.22. Uncertainties on the correction factor arise due to the choice of the PDF set, the factorization and renormalization scale and the gluon-gluon contribution to the initial state. The PDF uncertainty is determined by using the 52 CT10 error sets, while shifting the scale up and down by a factor of two gives an estimate of the uncertainty related to the scale. In table 6.5 these contributions are already introduced, and adding them in quadrature gives a total uncertainty of 0.6%. Because of the modeling of initial state radiation, final state radiation and the underlying event, there is an additional uncertainty of 1.1% which is evaluated by comparing results of MCFM and PowhegBox. All uncertainties on $C_{ZZ^{(*)}}$ and A_{ZZ} as well as the uncertainty due to the luminosity measurement are summarized in table 6.21.

ZZ^* Selection				
Generator	$e^+e^-e^+e^-$	$\mu^+\mu^-\mu^+\mu^-$	$e^+e^-\mu^+\mu^-$	combined
MCFM			0.755 ± 0.002	0.755 ± 0.002
PowhegBox	0.745 ± 0.001	0.745 ± 0.001	0.749 ± 0.001	0.747 ± 0.001
gg2zz	0.919 ± 0.004	0.919 ± 0.004	0.919 ± 0.004	0.919 ± 0.003
PowhegBox + gg2zz	0.755 ± 0.001	0.755 ± 0.001	0.758 ± 0.001	0.757 ± 0.001

ZZ Selection				
Generator	$e^+e^-e^+e^-$	$\mu^+\mu^-\mu^+\mu^-$	$e^+e^-\mu^+\mu^-$	combined
MCFM			0.795 ± 0.001	0.795 ± 0.001
PowhegBox	0.796 ± 0.001	0.796 ± 0.001	0.796 ± 0.001	0.796 ± 0.001
gg2zz	0.932 ± 0.004	0.932 ± 0.004	0.932 ± 0.004	0.932 ± 0.004
PowhegBox + gg2zz	0.804 ± 0.001	0.804 ± 0.001	0.804 ± 0.001	0.804 ± 0.001

Table 6.22.: Comparison of the reconstruction correction factor A_{ZZ} obtained with various generators. The upper section of the table holds the values evaluated for the ZZ^* selection although they are not used subsequently. In the lower section, there are the corresponding values for the ZZ selection listed. The quoted uncertainties are statistical. Finally the determined differences are reported as systematic uncertainties in table 6.21. The MCFM calculation is performed for the $2e2\mu$ channel only. It comprises also the 5.75% contribution of the gluon-gluon initial state at the dynamic scale of $m_{ZZ}/2$ used in this analysis. This percentage share is used to calculate the weighted average of PowhegBox and gg2zz, too, which is the nominal A_{ZZ}. Replacing the nominal Pythia showering connected to PowhegBox by Herwig + Jimmy the resulting differences are 0.2% for the ZZ^* and 0.1% for the ZZ selection.

Finally all required ingredients are determined to calculate the per channel fiducial cross sections for $pp \to ZZ^{(*)} \to \ell\ell\ell'\ell'$ according to equation (6.4) and the total one for ZZ through equation (6.3). The final aim of this analysis, though, is to measure the inclusive production cross section as the combination of all channels. The uncertainties on the combined measurement are decreased. Secondly the branching fractions of the Z boson into two leptons, which are the difference to the per channel cross sections, are already precisely measured by former experiments as pointed out in section 2. In principle, the total sum over channels of observed events, the total sum over channels of expected background events and the weighted sum over channels of acceptance could be used to calculate the combined cross section. This approach though does not necessarily take into account better signal-to-background ratios in particular channels, but give the highest weight to the highest statistic channel. Another attempt is a minimum χ^2 method resulting in a covariance weighted average. Unfortunately higher statistics than currently available are needed for this combination.

Here a maximum log-likelihood approach is used to calculate the combined cross section. It respects the Poisson statistics of the underlying sample as well as the systematic uncertainties. Before the profile likelihood function L is maximized with respect to the cross section σ, the channels are combined. For the fiducial cross section the profile likelihood function is calculated as the product of a Poisson probability distribution P, a Gamma distribution function Γ for the background parameter and a Gaussian distribution function G for the remaining nuisance parameters:

$$L(\sigma, C_{ZZ^{(*)}}, b; \Delta_b, \Delta_{C_{ZZ^{(*)}}}, N) = P(\sigma, C'_{ZZ^{(*)}}, b'; N) \times G(C'_{ZZ^{(*)}}; C_{ZZ^{(*)}}, \Delta_{C_{ZZ^{(*)}}}) \times \Gamma(b'; b, \Delta_b). \quad (6.24)$$

For the total cross section, the likelihood is extended by a Gaussian function $G(A'_{ZZ}; A_{ZZ}, \Delta_{A_{ZZ}})$ to account for the uncertainty on the acceptance correction factor A_{ZZ}. The Gamma distribution is given by

$$\text{Gamma}(x; k, \theta) = \frac{1}{\theta^k}\frac{1}{\Gamma(k)}x^{k-1}e^{-x/\theta} \text{ for } x \geq 0, \text{ and } k, \theta > 0. \tag{6.25}$$

with k and θ chosen in order to achieve the point of maximum probability to be at the mean background estimate b. The variance is the same like for a truncated Gaussian with a maximum probability at the mean background estimate b and a sigma equal to the uncertainty on the nominal background uncertainty Δb. In comparison to the Gaussian though, no artificial truncation at zero background yield is need for the Gamma function since it transits to zero at this point by definition. With the total number of observed events N and the total number of signal events calculated as

$$\begin{aligned} s(\sigma^{\text{fid}}, C_{ZZ^{(*)}}) &= \sigma^{\text{fid}} \times \mathcal{L} \times C_{ZZ^{(*)}} \\ s(\sigma^{\text{tot}}, C_{ZZ}) &= \sigma^{\text{tot}} \times \mathcal{L} \times C_{ZZ} \times A_{ZZ} \times \text{BR}_{\text{comb}}(ZZ \to \ell\ell\ell'\ell'), \end{aligned} \tag{6.26}$$

the Poisson function reads

$$P(\sigma, C_{ZZ^{(*)}}, b; N) = \frac{e^{-(s(\sigma, C_{ZZ^{(*)}})+b)} \times (s(\sigma, C_{ZZ^{(*)}}) + b)^N}{N!}. \tag{6.27}$$

For computational reasons $-\ln(L)$ is minimized rather than the maximization of L. With the final cross section measurement there are a statistical and systematic uncertainty associated. The statistical uncertainty is obtained from the result of the fit when the systematic uncertainties are fixed. By the variation of the individual and total systematic uncertainties, the systematic uncertainty of the final result is retrieved. The concluding measured production cross sections for $pp \to ZZ \to \ell\ell\ell'\ell'$ are summarized in table 6.23 and the theoretical predictions are included in the caption. Within errors all measured cross sections agree with prediction. In addition the total cross section for $ZZ \to \ell^+\ell^-\ell'^+\ell'^-$ agrees with the measurement performed by the CMS experiment which is $6.24^{+0.86}_{-0.80}(\text{stat.})^{+0.41}_{-0.32}(\text{syst.}) \pm 0.14(\text{lumi.})$ pb [42]. For the CMS result there are also τ leptons considered in final state.

combined fiducial cross section	$ZZ^* \to \ell\ell\ell'\ell'$	$29.8^{+3.8}_{-3.5}(\text{stat.})^{+1.7}_{-1.5}(\text{syst.}) \pm 1.2(\text{lumi.})(\text{fb})$
	$ZZ \to \ell\ell\ell'\ell'$	$25.4^{+3.3}_{-3.0}(\text{stat.})^{+1.2}_{-1.0}(\text{syst.}) \pm 1.0(\text{lumi.})(\text{fb})$
fiducial cross section for various channels	$ZZ \to e^+e^-e^+e^-$	$7.8^{+2.2}_{-1.8}(\text{stat.})^{+0.8}_{-0.6}(\text{syst.}) \pm 0.3(\text{lumi.})(\text{fb})$
	$ZZ \to e^+e^-\mu^+\mu^-$	$10.4^{+2.2}_{-1.9}(\text{stat.})^{+0.6}_{-0.5}(\text{syst.}) \pm 0.4(\text{lumi.})(\text{fb})$
	$ZZ \to \mu^+\mu^-\mu^+\mu^-$	$7.2^{+1.6}_{-1.4}(\text{stat.})^{+0.3}_{-0.3}(\text{syst.}) \pm 0.3(\text{lumi.})(\text{fb})$
total cross section	from $ZZ \to \ell\ell\ell'\ell'$	$7.0^{+0.9}_{-0.8}(\text{stat.})^{+0.4}_{-0.3}(\text{syst.}) \pm 0.3(\text{lumi.})(\text{pb})$

Table 6.23.: Measured fiducial cross section for ZZ^* and ZZ as combination of the three decay channels. For ZZ the cross section determined in the various four charged lepton channels is reported as well. An extrapolation to the full phase space is provided for the ZZ production cross section. The fiducial cross section for ZZ^* and ZZ is predicted by the combination of PowhegBox and gg2zz to be $25.6 \pm 0.1(\text{stat.})^{+1.3}_{-1.1}(\text{theory})$ fb and $20.9 \pm 0.1(\text{stat.})^{+1.1}_{-0.9}(\text{theory})$ fb. The total cross section predicted by MCFM is $5.89^{+0.22}_{-0.18}$ pb.

6.7. Implications of the ZZ production cross section measurement

6.7.1. Combined cross section measurement including neutrinos in the final state

In addition to the production cross section measurement of two Z bosons with a subsequent decay into four charged leptons [165] ($ZZ \to \ell^+\ell^-\ell'^+\ell'^-$), there is a similar measurement with two charged and two neutral leptons, namely neutrinos, in the final state ($ZZ \to \ell^+\ell^-\nu\bar{\nu}$) performed with the ATLAS experiment [166]. With the prospect of the combination of the two measurements, the fiducial volumes are chosen to be close and the object selection for both analyses was adjusted at a certain stage. Although the study of the $ZZ \to \ell^+\ell^-\nu\bar{\nu}$ decay comprises as a matter of principle also the measurement of missing energy. Due to the observation of only three rather than four quantities in the final state, events are selected differently. For example the invariant mass of the two reconstructed leptons has to be in a more narrow window around the Z boson mass $76 < m_{\ell\ell} < 106$ GeV. A detailed description of the strategy can be found elsewhere [40, 143]. The most important auxiliary quantities used to suppress background events are the axial-$E_{\mathrm{T}}^{\mathrm{miss}}$ and fractional p_{T} difference.

Both of them reflect the fact that the Z bosons tend to be produced back-to-back. The axial-$E_{\mathrm{T}}^{\mathrm{miss}}$ is given by $-\vec{E}_{\mathrm{T}}^{\mathrm{miss}} \cdot \vec{p}^{\,Z}/p_{\mathrm{T}}^{Z}$ where $\vec{p}^{\,Z}$ $\left(p_{\mathrm{T}}^{Z}\right)$ is the (transverse) momentum of the fully reconstructed Z candidate. The quantity is required to be bigger than 75 GeV and can be understood as the projection in the transverse plane of the missing transverse energy along the opposite direction of the leptonically decaying Z candidate. The fractional p_{T} difference, defined as $\left|E_{\mathrm{T}}^{\mathrm{miss}} - p^{Z}/p_{\mathrm{T}}^{Z}\right|$, has to be less than 0.4. To reduce further backgrounds there is a veto on events with at least one jet of $p_{\mathrm{T}} > 25$ GeV in the region $|\eta| < 4.5$. Events with a third more loosen lepton are rejected as well. Finally a background to signal ratio of one can be achieved while the background estimation is more complicated than for the four lepton final state. A more complete explanation is available in reference [40, 143].

The yield and estimated background contamination of observed $ZZ \to \ell^+\ell^-\nu\bar{\nu}$ candidate events is reported in table 6.24 for the two channels with missing transverse energy and either two electrons or two muons in the final state. The resulting fiducial cross sections according to equation (6.4) and the combined $ZZ \to \ell^+\ell^-\nu\bar{\nu}$ cross section is given in table 6.25. In addition this table holds the total production cross section of a Z boson pair extrapolated from the $ZZ \to \ell^+\ell^-\nu\bar{\nu}$ channel and the ultimate combination with the measurement extrapolated from the $ZZ \to \ell\ell\ell'\ell'$. All the combinations are performed with a maximum likelihood fit like it is explained in section 6.6 while correlations of the uncertainties of the different channels are respected. Due to the not completely equivalent fiducial volumes and distinct final states, the correction factors A_{ZZ} and C_{ZZ} are different for the two channels.

	$e^+e^- E_{\mathrm{T}}^{\mathrm{miss}}$	$\mu^+\mu^- E_{\mathrm{T}}^{\mathrm{miss}}$	$\ell^+\ell^- E_{\mathrm{T}}^{\mathrm{miss}}$
Observed ZZ	35	52	87
Expected ZZ signal	$17.8 \pm 0.3 \pm 1.7$	$21.6 \pm 0.3 \pm 2.0$	$39.3 \pm 0.4 \pm 3.7$
Expected ZZ background	$20.8 \pm 2.3 \pm 1.2$	$26.1 \pm 2.8 \pm 1.4$	$46.9 \pm 4.8 \pm 1.9$

Table 6.24.: Summary of observed $ZZ \to \ell^-\ell^+\nu\bar{\nu}$ candidate events in data and the estimated background as well as the expected signal yield as predicted from simulation. The corresponding numbers are given split up in the individual channels and in combination. The first uncertainty quoted is statistical while the second one is systematic.

combined fiducial cross section	$ZZ \to \ell^-\ell^+\nu\bar{\nu}$	$12.7^{+3.1}_{-2.9}(\text{stat.})^{+1.7}_{-1.7}(\text{syst.}) \pm 0.5(\text{lumi.})(\text{fb})$
fiducial cross section for various channels	$ZZ \to e^-e^+\nu\bar{\nu}$ $ZZ \to \mu^-\mu^+\nu\bar{\nu}$	$5.0^{+2.2}_{-2.0}(\text{stat.})^{+0.9}_{-1.0}(\text{syst.}) \pm 0.2(\text{lumi.})(\text{fb})$ $7.5^{+2.2}_{-2.0}(\text{stat.})^{+0.9}_{-0.9}(\text{syst.}) \pm 0.3(\text{lumi.})(\text{fb})$
extrapolated total cross sections	$ZZ \to \ell\ell\ell'\ell'$ $ZZ \to \ell^-\ell^+\nu\bar{\nu}$	$7.0^{+0.9}_{-0.8}(\text{stat.})^{+0.4}_{-0.3}(\text{syst.}) \pm 0.3(\text{lumi.})(\text{pb})$ $5.9^{+1.4}_{-1.3}(\text{stat.})^{+0.9}_{-0.8}(\text{syst.}) \pm 0.2(\text{lumi.})(\text{pb})$
combined total cross section	ZZ (combined)	$6.7 \pm 0.7(\text{stat.})^{+0.4}_{-0.3}(\text{syst.}) \pm 0.3(\text{lumi.})(\text{pb})$

Table 6.25.: Measured fiducial cross section for $ZZ \to \ell^-\ell^+\nu\bar{\nu}$ as combination and for the two decay channels separately. The extrapolation to the full phase space for $ZZ \to \ell^-\ell^+\nu\bar{\nu}$, $ZZ \to \ell\ell\ell'\ell'$, like already reported in table 6.23, and their ultimate combination. The fiducial cross section for $ZZ \to \ell^-\ell^+\nu\bar{\nu}$ is predicted by the combination of PowhegBox and gg2zz to be $12.5 \pm 0.1(\text{stat.})^{+1.0}_{-1.1}(\text{theory})$ fb. For the ultimate combination of the $ZZ \to \ell^-\ell^+\nu\bar{\nu}$ and $ZZ \to \ell\ell\ell'\ell'$ channel the MCFM prediction is $5.89^{+0.22}_{-0.18}$ pb.

6.7.2. Extraction of limits on an anomalous triple gauge coupling

Anomalous triple gauge couplings (aTGCs), like they are mentioned in section 6.1, yield an increased observation of Z boson pairs. In the Standard Model Lagrangian terms of the structure $\boxed{ZZZ}$ and $\boxed{ZZA}$ would occur including complex couplings commonly labeled with f_4^V and f_5^V [167] with $V = Z,\ \gamma$. All of them violate charge conjugation. While f_5^Z and f_5^γ are CP conserving, it is violated by the f_4^V couplings. Due to differences in their momentum structure, f_4^V and f_5^V can be studied individually. Therefore the observed differential event counts of $ZZ \to \ell\ell\ell'\ell'$ and $ZZ \to \ell^+\ell^-\nu\bar{\nu}$ depending on the leading Z boson transverse momentum p_T^Z are compared to the expected number of events in simulation. In table 6.26 the observed yields are summarized. The Monte Carlo samples including aTGCs are generated with Sherpa [69] and subsequently reweighted by the Baur-Rainwater [168] and BHO [169] generators.

There is a form factor parameterization $f_i^V = f_{i0}^V/(1 + s/\Lambda^2)^n$ introduced in this study to cause the couplings to vanish at high parton center of mass energies $\sqrt{s}$, so that partial-wave unitarity is guaranteed. At the energy scale Λ physics beyond the Standard Model will be directly observable while f_{i0}^V are the low-energy approximations of the couplings. The power of the form factor is denoted as n and fixed at a value of 3 in this study. Once the scale Λ is set to 3 TeV which affords values of the expected limits within a range consistent with unimpaired unitarity at LHC energies [168]. On the other hand a scheme with violated unitarity is studied by not considering the form factor, i.e. with $\Lambda = \infty$. A maximum profile likelihood ratio is used to determine confidence intervals for the anomalous triple gauge couplings.

In comparison with previous limits and recent results from the CMS experiment [42], figure 6.17 presents the set limits on each coupling, assuming all of the other couplings to be zero. For data and for 10000 pseudo-experiments, generated using the expected number of events at each point in the corresponding aTGC parameter space, the profile likelihood ratio is calculated. In case of a value larger than the one observed in data, for more than 95% of the pseudo-experiments, the parameter point is rejected. Systematic uncertainties are considered as nuisance parameters. The determined two dimensional 95% confidence intervals can be found elsewhere [40].

	Expected background	Expected ZZ signal	Observed events
$ZZ \to \ell\ell\ell'\ell'$			
$0 < p_{\mathrm{T}}^{Z} < 60$ GeV	$0.6 \pm 0.8 \pm 0.5$	$27.9 \pm 0.2 \pm 2.0$	28
$60 < p_{\mathrm{T}}^{Z} < 100$ GeV	$0.2 \pm 0.2 \pm 0.2$	$14.6 \pm 0.2 \pm 1.2$	25
$100 < p_{\mathrm{T}}^{Z} < 200$ GeV	$0.1 \pm 0.1 \pm 0.1$	$9.3 \pm 0.1 \pm 0.9$	11
$p_{\mathrm{T}}^{Z} > 200$ GeV	$0.01 \pm 0.01 \pm 0.01$	$1.6 \pm 0.1 \pm 0.3$	2
$ZZ \to \ell^-\ell^+\nu\bar{\nu}$			
$50 < p_{\mathrm{T}}^{Z} < 90$ GeV	$26.0 \pm 4.5 \pm 1.1$	$13.6 \pm 0.2 \pm 1.3$	42
$90 < p_{\mathrm{T}}^{Z} < 130$ GeV	$16.0 \pm 2.8 \pm 0.7$	$15.7 \pm 0.3 \pm 1.7$	29
$p_{\mathrm{T}}^{Z} > 130$ GeV	$4.9 \pm 1.8 \pm 0.2$	$10.1 \pm 0.1 \pm 1.5$	16

Table 6.26.: Differential background estimate, expected signal yield and observed event count in intervals of the transverse momentum of the leading Z boson candidate for the $ZZ \to \ell\ell\ell'\ell'$ and $ZZ \to \ell^-\ell^+\nu\bar{\nu}$ selection. The uncertainty quoted first is statistical while the second one is systematic for both, expected background and signal.

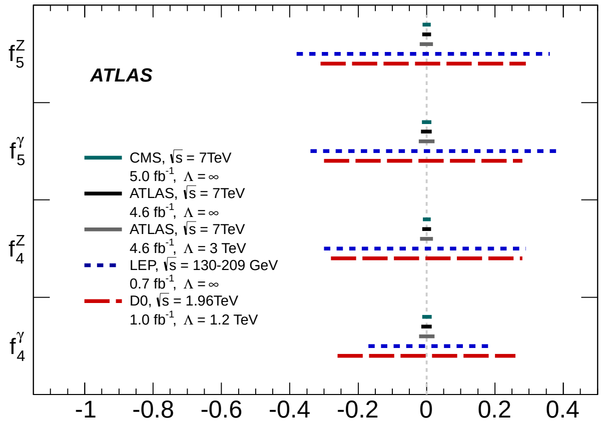

Figure 6.17.: Confidence intervals on a level of 95% for anomalous neutral triple gauge couplings as measured from ATLAS [40], CMS [42], LEP [151] and Tevatron [154] experiments. Information on luminosities, centre-of-mass energies and the cut-off scale Λ for each experiment are shown in the plot.

6.7.3. Intersection with the search for the Standard Model Higgs boson

The left Feynman diagram in figure 6.2 already indicates similar final states for the decay of a Higgs boson to a pair of Z bosons like their usual production without the presence of a Higgs. In consequence the presented procedure for the measurement of the inclusive ZZ production cross section also includes Higgs decays although it is not optimized to select them. The other way around $ZZ^{(*)}$ production is an irreducible background for the search of the Standard Model Higgs Boson which could be proven amongst others by a resonance peak in the four charged lepton invariant mass distribution. Therefore the basic object and event selection criteria of both analyses, the measurement and the search, do not differ substantially. In general the leptons considered for the search have looser selection criteria. For example the transverse momentum threshold for muons is reduced and the accepted absolute value of the impact parameter along the beam axis is larger. For electrons a special identification quality is introduced. The cuts on the isolation are more relaxed as well. The main differences though are introduced by the actual event selection while modified trigger settings do not have much of an impact. Also allowing more than 4 leptons is less crucial.

$m_{4\ell}$ [GeV]	≤ 120	130	140	150	160	165	180	$(\geq)190$	≥ 200
m_{min} [GeV]	15	20	25	30	30	35	40	50	60
m_{min} [GeV] (low mass)	17.5	22.5	-	30	30	35	40	50	-

Table 6.27.: Lower mass requirement m_{min} as function of the combined invariant mass $m_{4\ell}$, applied on the lepton pair with an invariant mass further afar from the Z mass pole. A linear interpolation is used for $m_{4\ell}$ values between the reference values. While the second row reports the values used in the analysis of winter 2011/2012 [140], the bottom row lists the values optimized for lighter Higgs masses as used in summer 2012 [170].

The first search performed with data taken during 2011 [140] asked for an invariant mass of the lepton pair closer to the Z mass pole m_{12} in the window $|m_Z - m_{12}| < 15$ GeV. This requirement is even tighter than for the $ZZ^{(*)}$ production cross section measurement. On the invariant mass of the second lepton pair m_{34} a sliding mass cut, according to $m_{\text{min}} < m_{34} < 115$ GeV, is performed. The values for m_{min} are available in table 6.27. The cross section measurement applies either a fixed window of $66 < m_{34} < 116$ GeV in case of ZZ or merely a lower limit of 20 GeV $< m_{34}$ for ZZ^*. The obtained invariant mass distribution for $m_{4\ell}$ resulting from the search for a Standard Model Higgs in the channel $H \to ZZ^{(*)} \to 4\ell$ is given in figure 6.18. This figure holds in addition an illustration of the derived 95% confidence level upper limits on a Standard Model Higgs boson as a function of its mass m_H. A zoom to the low mass range $100 < m_{4\ell} < 250$ GeV is provided in figure 6.19. Although there is nothing significant visible at this stage, the presented plot suggests an enhanced number of events for some low m_H wherefore the analysis is optimized subsequently. At this point it should be emphasized that for $m_H < 350$ GeV the resolution of a resonant peak is dominated by the experimental resolution rather than the actual width of a Higgs. Therefore studies and improvements, like they are reported in section 5.2, are of high importance.

A second search for the Standard Model Higgs boson with data taken in 2011 and 2012 is optimized for a Higgs boson with lower mass. The sliding mass cut is changed to the values reported in the bottom row of table 6.27. However, more effective is the modified mass window for the invariant mass of the lepton pair closer to the Z mass pole which becomes $50 < m_{12} < 106$ GeV. To reject background from J/ψ, any combination of leptons with the same flavor and opposite charge is required to have more than 5 GeV, otherwise the event is discarded. The expected number of events in 2011 and 2012 data in the $H \to ZZ^{(*)} \to 4\ell$ channel is estimated to be 5.28 ± 0.46 [171] while for 2011 data exclusively it is 2.37 ± 0.15 [170]. The selection criteria used to measure the fiducial ZZ^* production cross section are estimated by simulation to perform $\sim 40\%$ less efficient on the Standard Model Higgs signal. Therefore the contribution due to the presence of a Higgs impacts the observed event count for $ZZ^{(*)}$ less than 3% [40].

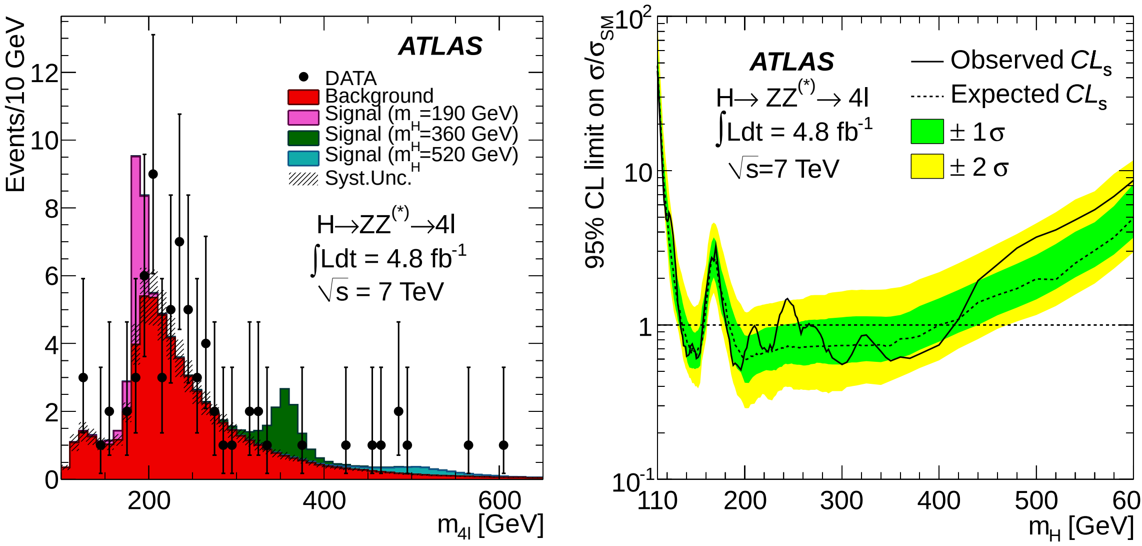

Figure 6.18.: On the left the four lepton invariant mass distribution of the candidate events selected by the search for the Standard Model Higgs in the winter 2011/2012 [140] is shown. The background expectation and the signal expectation for several Higgs masses is superimposed. The given error bars represent 68.3% central confidence intervals. A zoom for the mass range $100 < m_{4\ell} < 250$ GeV is given in figure 6.19. The underlying dataset is the same as for the measurement of the fiducial ZZ^* production cross section and therefore the plot given here is comparable with the lower left plot of figure 6.14. The plot on the right shows the derived expected (dashed) and observed (full line) 95% confidence level upper limits on the Standard Model Higgs boson production cross section as a function of m_H, divided by the expected Standard Model Higgs boson cross section. The expected limits with $\pm\sigma$ ($\pm 2\sigma$) fluctuations are indicated by the green (yellow) band.

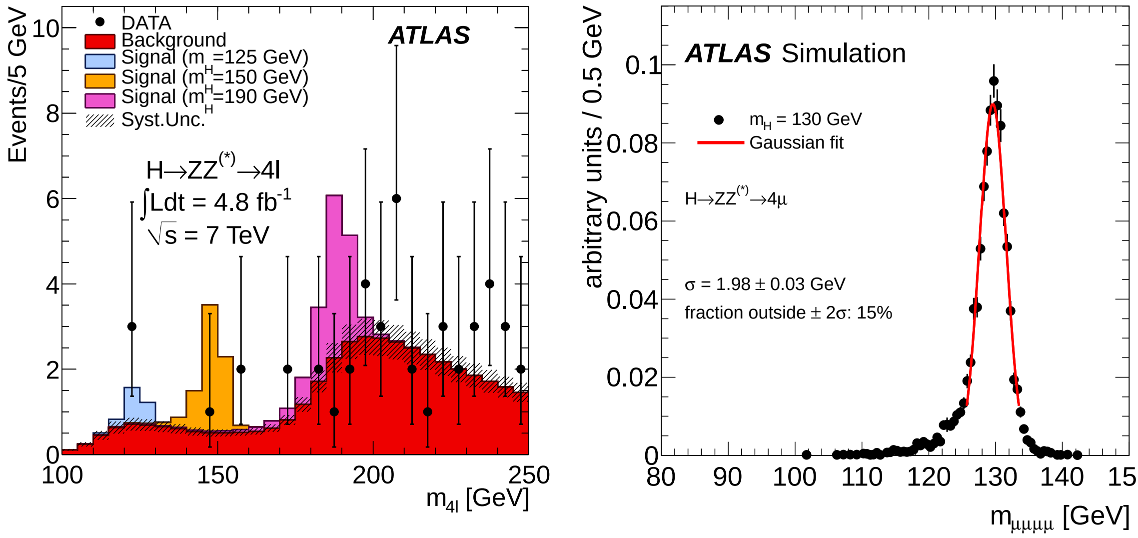

Figure 6.19.: The left plot shows a zoom of the left plot in figure 6.18 into the mass range of $100 - 250$ GeV. On the right the invariant mass distribution for simulated $H \to ZZ^* \to 4\mu$ events is presented. For the chosen Higgs mass of $m_H = 130$ GeV the width is dominated by the experimental resolution. The Gaussian is fitted in a range of $\pm 2\sigma$ while the fraction of events outside this region is found to be 15%.

A comparison of the final samples of both analyses derived from 2011 data was done one an event-by-event basis. In the $2e2\mu$ channel the search for the Higgs boson as well as the $ZZ^{(*)}$ cross section measurement collects 33 events though 5 events in the Higgs sample are not considered by the $ZZ^{(*)}$ sample due to more strict quality cuts and the modified invariant mass requirement. On the other hand 4 events in the $ZZ^{(*)}$ sample are not present in the Higgs sample due to the different invariant mass cuts. One event is only included in the $ZZ^{(*)}$ sample since it comprises an electron with $|\eta| > 2.47$, however, the Higgs search does not consider this kind of extra leptons at all. In the 4μ there are again 33 events selected by the Higgs search while for the cross section measurement there are only 30. The main reason again are the different mass requirements though one event is discarded from the $ZZ^{(*)}$ sample because of a muon with a transverse momentum below the applied threshold and one event is absent in the Higgs sample due to the J/ψ veto. In the $4e$ channel the absolute difference between the samples is one though 5 events considered in the Higgs selection are rejected by the $ZZ^{(*)}$ criteria. Albeit there are 4 additional events allowed by those criteria while three of them comprise forward electrons. The remaining reasons for the differences are once more the non identical mass and quality requirements. Although forward electrons are not taken into account in the search for the Higgs boson, calorimeteric muons and muons with high pseudorapidity are used. Due to the comparable selection criteria the gain in event yield reported in table 6.7 applies also for the Higgs search. To underline the significance of extending the detector acceptance based on studies like the one presented in section 5.3, it has to be mentioned that both data samples, 2011 and 2012, considered for the search of a Standard Model Higgs contain each three muons with high pseudorapidity.

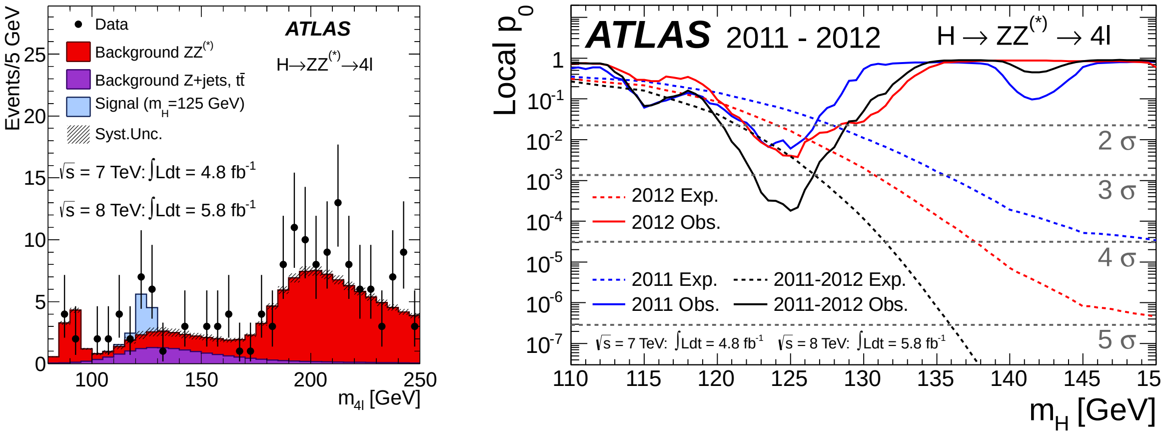

Figure 6.20.: The four lepton invariant mass distribution in the mass range of $m_H = [80; 250]$ GeV, shown on the left, is a combination of data taken with a center of mass energy of $\sqrt{s} = 7$ TeV during 2011 and $\sqrt{s} = 8$ TeV for 2012 [171]. The expected background and a signal scenario for $m_H = 125$ GeV is superimposed. The observed (solid) local probability that the background fluctuates to the observed number of events or higher (p_0) and the corresponding expectation (dashed) as function of m_H is displayed on the right. While the blue graph is derived from 2011 data only, it is the red one for 2012 data. The black graph is the combination.

Figure 6.20 presents the obtained four lepton invariant mass distribution comprising the 2011 and 2012 data selection of the Higgs search in the $H \to ZZ^{(*)} \to 4\ell$ channel. The local probability to explain the observed number of events by an upwards fluctuation of the background is reported in the figure as well. This probability is significantly low in a range around 125 GeV. Besides the $H \rightarrow ZZ^{(*)} \rightarrow 4\ell$ channel, there are also other channels expected to be sensitive for a Standard Model Higgs decay in this mass region, like it is suggested in figure 2.3. Consulting the corresponding searches for a Standard Model Higgs performed with the ATLAS detector, like through the channels $H \rightarrow \gamma\gamma$ and $H \rightarrow WW^{(*)} \rightarrow e\nu\mu\nu$ channel, and combining the results leads to figure 6.21. Indeed there is evidence for a new particle with a mass of $126.0 \pm 0.4\,(\mathrm{stat}) \pm 0.4\,(\mathrm{syst})$ GeV [171]! This observation is also confirmed by the CMS experiment [172]. At a first glance it is compatible with the Standard Model Higgs boson though detailed investigations of the observed resonance have to performed to prove this statement. Nevertheless, the allowed mass range presented in figure 2.2 becomes much more restricted by the searches of the LHC experiments and the observed particle occurs in a region not excluded by any experiment preceding the LHC era.

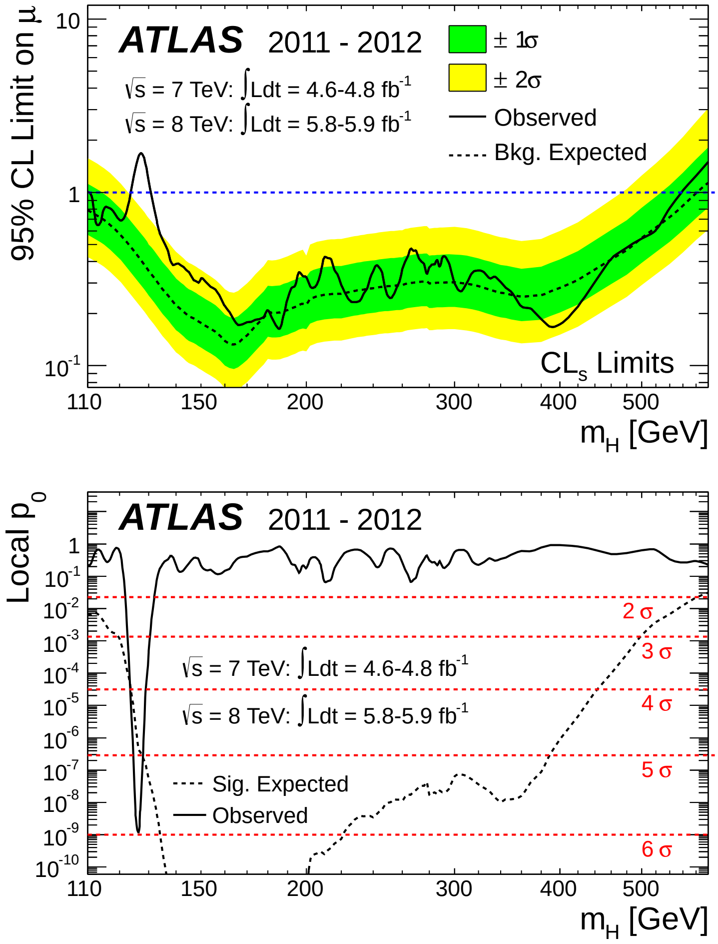

Figure 6.21.: Both plots present combined results [171] of all Standard Model Higgs search channels as a function of m_H. The left one displays the observed (solid) 95% confidence level upper limit on the signal strength and the expectation (dashed) under the background-only hypothesis. The green (yellow) bands show the $\pm\sigma$ $(\pm 2\sigma)$ uncertainties on the background-only expectation. The observed (solid) local probability that the background fluctuates to the observed number of events or higher (p_0) and the expectation (dashed) for a Standard Model Higgs boson signal hypothesis are plotted on the right.

Chapter 7

Conclusion

There is one out of the billions of events recorded by the ATLAS experiment during the data taking period in 2011 which summarizes appropriately all issues addressed in this thesis. The event is displayed in figure 7.1 [165] and comprises four reconstructed muons in the final state. Those four muons can be paired to form two Z bosons, one with a mass of 89.18 GeV and one of the mass 88.03 GeV. In consequence this event is considered by the selection of two important analyses reported in the thesis and performed with the ATLAS experiment, namely the measurement of the inclusive ZZ production cross section [40] and the search for the Standard Model Higgs boson [140]. The implications of both analyses for particle physics are extensive.

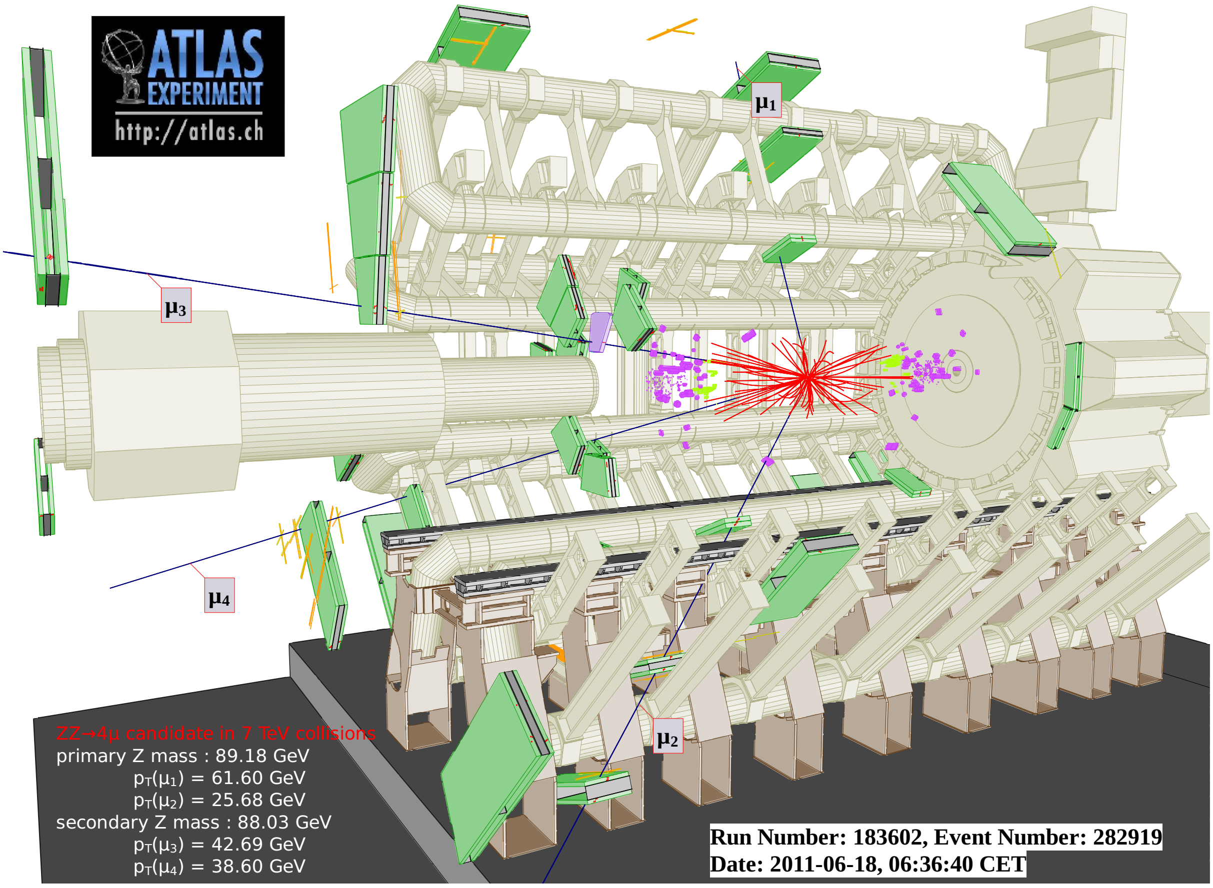

Figure 7.1.: Display of event number 282919 in run 183602 recorded on June 18 in 2011 by the ATLAS experiment. See chapter 7 for further explanations.

The first analysis tests the electroweak sector of the well-established Standard Model of particle physics at energies never reached before in a laboratory. The inclusive ZZ production cross section is measured to $6.7 \pm 0.7(\text{stat.})^{+0.4}_{-0.3}(\text{syst.}) \pm 0.3(\text{lumi.})(\text{pb})$ and agrees within errors with the theory expectation of $5.89^{+0.22}_{-0.18}$ pb. The differential distribution of the obtained result can even be used to set limits with an unprecedented accuracy on physics beyond the Standard Model scenarios predicting neutral triple gauge couplings on tree-level. The search for the Standard Model Higgs boson, which makes also use of the displayed event, finally succeeded with the combination of data recorded by the ATLAS experiment during the years 2011 and 2012 in finding a resonance peak at $126.0 \pm 0.4\,(\text{stat}) \pm 0.4\,(\text{syst})$ GeV [171] which is compatible with the Standard Model Higgs at a first glance. Albeit both analyses already achieved outstanding results, they have future prospects of the same importance. In a next step the inclusive ZZ production cross section measurement at 8 TeV [41] has to be combined with the one presented in this thesis to improve the study on neutral triple gauge couplings. On the other hand the properties of the particle observed during the search for the Standard Model Higgs boson have to be examined in detail to understand if it really is compatible with the theory prediction.

In addition to the contribution to the physics analyses, the displayed event emphasize as well the performance issues reported in this thesis. Firstly it is the only event in 2011 data with four reconstructed muons comprising a muon with high pseudorapidity and being considered by both physics analyses. Therefore the impact of the presented study regarding the performance of muons in the region $2.5 < |\eta| < 2.7$ in order to establish an extended acceptance range of the muon spectrometer can be recognized directly. However, in principle not only the two mentioned analyses, but any physics analysis looking for muons in the final state could benefit from this study. Due to the general presents of muons in the displayed event, the study on the inclusive muon spectrum enters as well. It is helpful to understand reconstructed muon objects in a common sense and to disentangle them depending on their different sources. The reported work especially aims at the contribution of muon emerging from heavy flavor decays which are background for both issued analyses.

Last, but not least the illustration itself and the shown representation of the ATLAS muon spectrometer is a fraction of this thesis. The multiple scattering contribution to the muon spectrometer momentum resolution was estimated from data and simulation. Due to observed differences, great efforts are made to get a better agreement which was indeed achieved with the displayed detector description. Besides the implementation of additional structures, also the validation within the ATLAS software framework is pointed out. However, simulation still seems be to rather optimistic and therefore further improvements and investigations have to be performed in the future. In conclusion this thesis reports on reconstructed muon objects in general and their use case in high-level physics analyses with considerable influence on particle physics.

Appendix A

Helicity projection of Dirac spinors

This appendix gives more details regarding the convention used to describe the isospin multiplets. Firstly a particle with momentum p and spin s can be represented by a Dirac spinor $u(p,s)$ while its antiparticle $v(p,s)$ is related according to the following equation

$$v(p,s) \equiv C\bar{u}^T(p,s) = i\gamma_2 u^*(p,s) \tag{A.1}$$

where C denotes the charge conjugation operator and γ_2 is the second of the Dirac γ-matrices. Basically the Dirac spinor comprises both helicity states, namely right handed (R, $+1/2$) and left handed (L, $-1/2$). Since the currents introduced in the main text act only for specific helicity states, it is a common approach to continue the calculation with Dirac spinors which only include one of the them. In order to do this the projection operators P_R and P_L are introduced. They are built out of the γ_5 matrix and read

$$P_R = \frac{1}{2}(1+\gamma_5) \qquad \text{and} \qquad P_L = \frac{1}{2}(1-\gamma_5)\ . \tag{A.2}$$

Once those operators are applied on the particle's Dirac spinor, the result is again a Dirac spinor, but only comprising one helicity state. Formally this means

$$P_{R/L}\, u = u_{R/L} \qquad \text{and} \qquad P_{R/L}\, v = v_{L/R} \tag{A.3}$$

In the next step the left handed spinors are gathered to a isospin doublet L since the carry the same isospin quantum number. The right handed spinors form an isospin singlet.

Appendix B

Additional material for the inclusive spectrum

This appendix holds further material for the analysis of the muon inclusive spectrum and the determination of the heavy flavor fraction described in chapter 5.1. On the one hand there are plots for muons reconstructed with the STACO algorithm which are shown only for the MUID reconstruction algorithm in the main body. On the other hand additional information on the approach of using pseudo-experiments to check for the stability of the template method are presented.

B.1. Data and Monte Carlo comparison

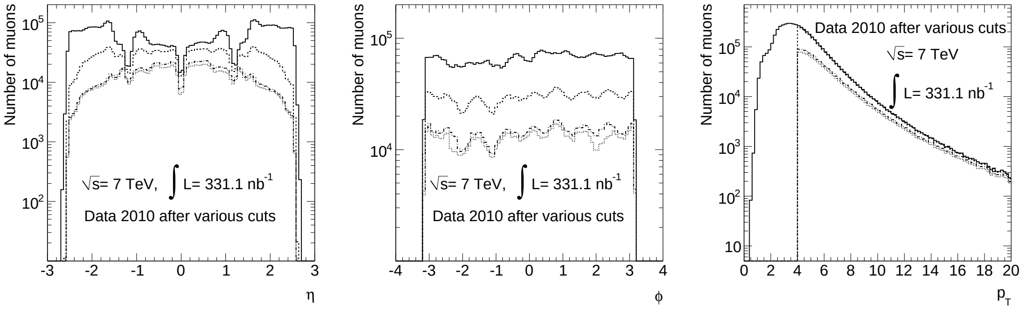

(a) Number of combined muons in data after various cuts versus η (left), ϕ (middle) and p_T (right). The solid line corresponds to the number of combined muons in events which pass the event selection criteria. Requiring $p_T > 4$ GeV, SCT Hits > 5, Pixel Hits > 0 leads to the dashed line. Associating the muons to a jets results in the dashed dotted line. Eventually the dotted line includes the quality criteria: ϕ-Hits > 1, B-layer > 0 and TRT Hits > 10.

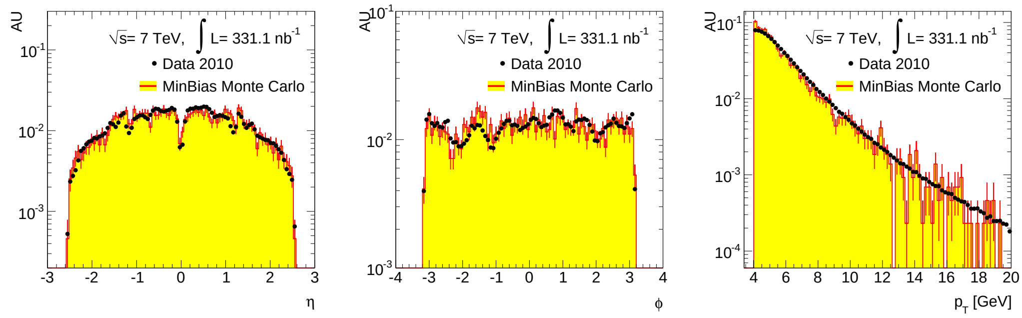

(b) Minimum bias Monte Carlo overlaid with data both scaled to the same area. In both samples the mouns fulfill all quality criteria and are associated to jets. While for the data sample a level 1 single muon trigger without threshold is demanded there is no such requirement on the Monte Carlo sample.

Figure B.1.: Control plots to demonstrate the understanding of the reconstructed muon objects. The underlying muon reconstruction algorithm for these plots is STACO.

In figure B.1(a) muons reconstructed with the STACO algorithm are shown after various cuts of the analysis. The number of events is plotted versus the η-coordinate, the ϕ-coordinate and the transverse muon momentum p_{T}. Like for the plots in the main body no unexpected features are visible. Figure B.1(b) shows the muons reconstructed with the STACO algorithm after all analysis cuts for the minimum bias Monte Carlo sample and with data superimposed. Both samples are scaled to the same area, and while for data a level 1 trigger for single muons is applied, there is no trigger requested for the Monte Carlo. In conclusion there is a reasonable agreement and the used muons can be considered as understood. For further information regarding the number of hits in the various detectors which strengthen this statement the reader is referred to [102].

B.2. Relative transverse muon momentum distributions

The plots presented in figure B.2 show once the transverse muon momentum distribution for muons reconstructed with the STACO algorithm as obtained from the minimum bias Monte Carlo sample in sum for all flavor sources and split up in light, charm and heavy flavors. Secondly the complete distribution available in the Monte Carlo sample is superimposed with the distribution found in data while both distributions are scale to the same area. There are no major differences to the plots shown in figure 5.5.

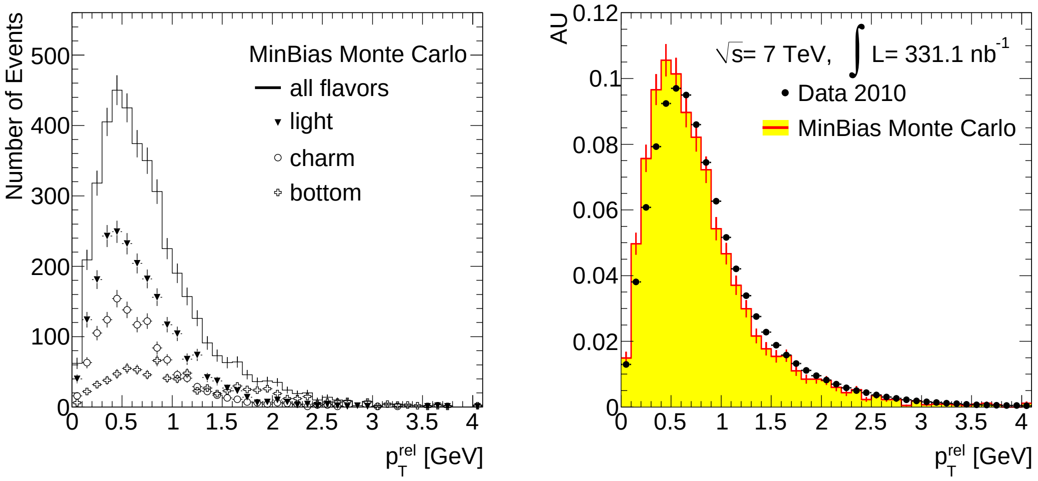

(a) Relative transverse muon momentum for muons reconstructed with the STACO algorithm contained in the minimum bias Monte Carlo in complete and split up in the different flavors.

(b) Complete relative transverse muon momentum distribution for muons reconstructed in minimum bias Monte Carlo and data reconstructed with the STACO algorithm. The distributions are scaled to the same area.

Figure B.2.: Relative transverse muon momentum for different flavor sources and data.

B.3. Detailed template determinaton per flavor

For the determination of the fraction as presented in section 5.1.4, template functions from the minimum bias Monte Carlo sample and simulated dijet sample are used without any further variation. While for muons emerging from light flavor decays and with a transverse momenta below 14 GeV the minimum bias Monte Carlo was used to extract the corresponding relative transverse momentum distribution, all the other relative transverse momentum distributions are obtained from the simulated dijet sample. The template functions for muons reconstructed with the MUID algorithm are given in figure B.3, and figure B.4 shows the results for the STACO algorithm accordingly.

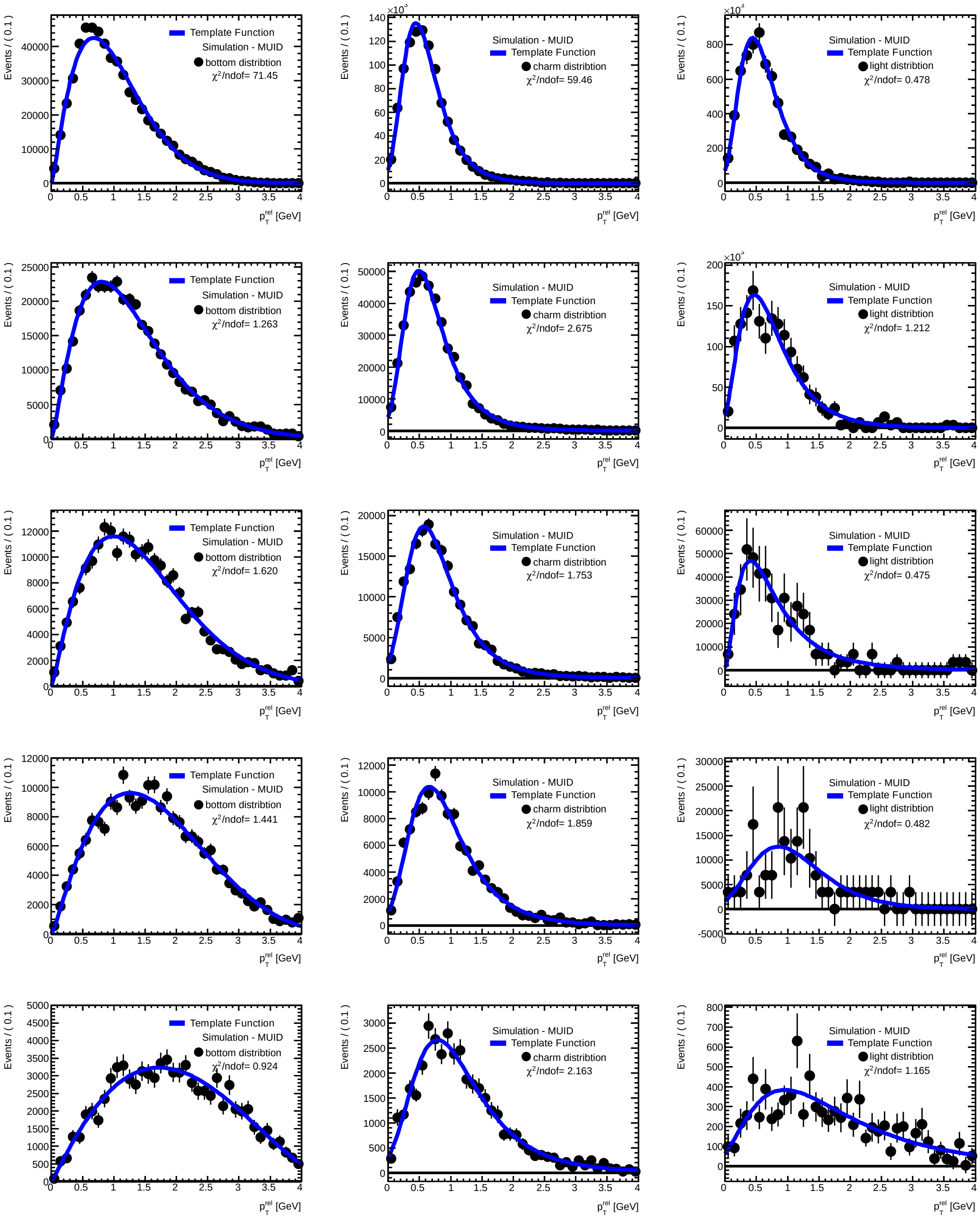

Figure B.3.: Template functions for the relative transverse muon momentum for bottom (left), charm (middle) and light (right) flavor decays. The results for the 5 muon transverse momentum bins are presented from top to bottom. The underlying muons are reconstructed by the MUID algorithm.

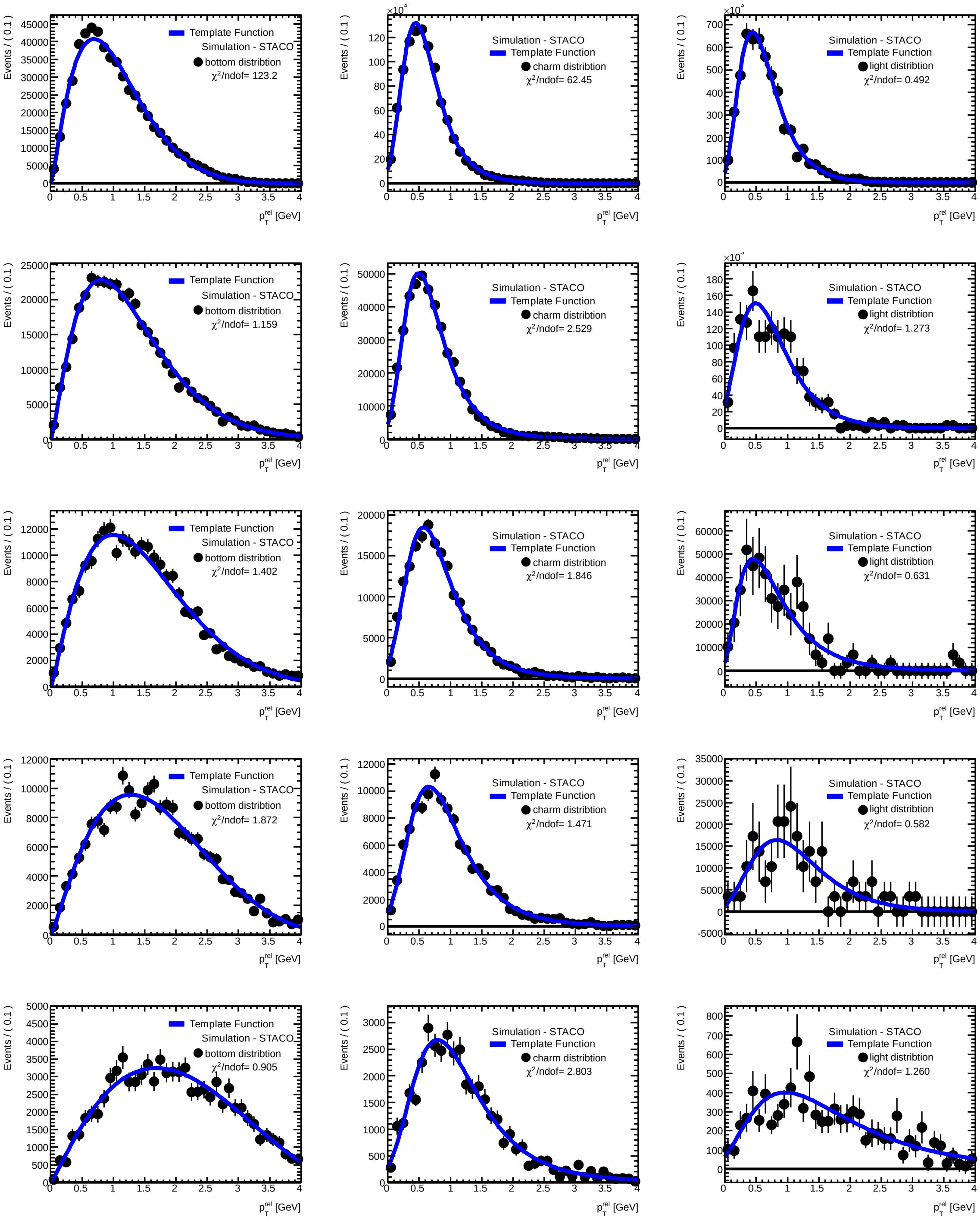

Figure B.4.: Template functions for the relative transverse muon momentum for bottom (left), charm (middle) and light (right) flavor decays. The results for the 5 muon transverse momentum bins are presented from top to bottom. The underlying muons are reconstructed by the STACO algorithm.

B.4. Stability of fraction determination

The derived parameter values and template functions respectively, found in 1000 pseudo-experiments based on variations within the statistical uncertainty of the used Monte Carlo samples are stored and used for fits on the full distribution including all flavor contributions as obtained from the dijet Monte Carlo sample without any variation. Due to the different underlying templates, the fraction α determined by the fit of the global function given in equation (5.6) varies. In figure B.5 the fitted fractions and the true fractions of the Monte Carlo sample are presented. The results are obtained for muons reconstructed with the MUID algorithm in all 5 muon transverse momentum bins though the corresponding distributions for the STACO algorithm do not show major differences. In conclusion the fit of the fraction is considered as stable. In addition the presented flavor fractions obtained by using the different template functions from the pseudo-experiments are fitted with a Gaussian distribution. The found widths vary from about 1% to once somewhat less than 8% and reflect the impact of the statistical uncertainty of the underlying Monte Carlo samples on the fitting method. In the analysis it enters as systematic uncertainty. To be conservative 8% uncertainty caused by this source are assumed in the study to also cover other effects pointed out in section 5.1.4, but not studied in detail.

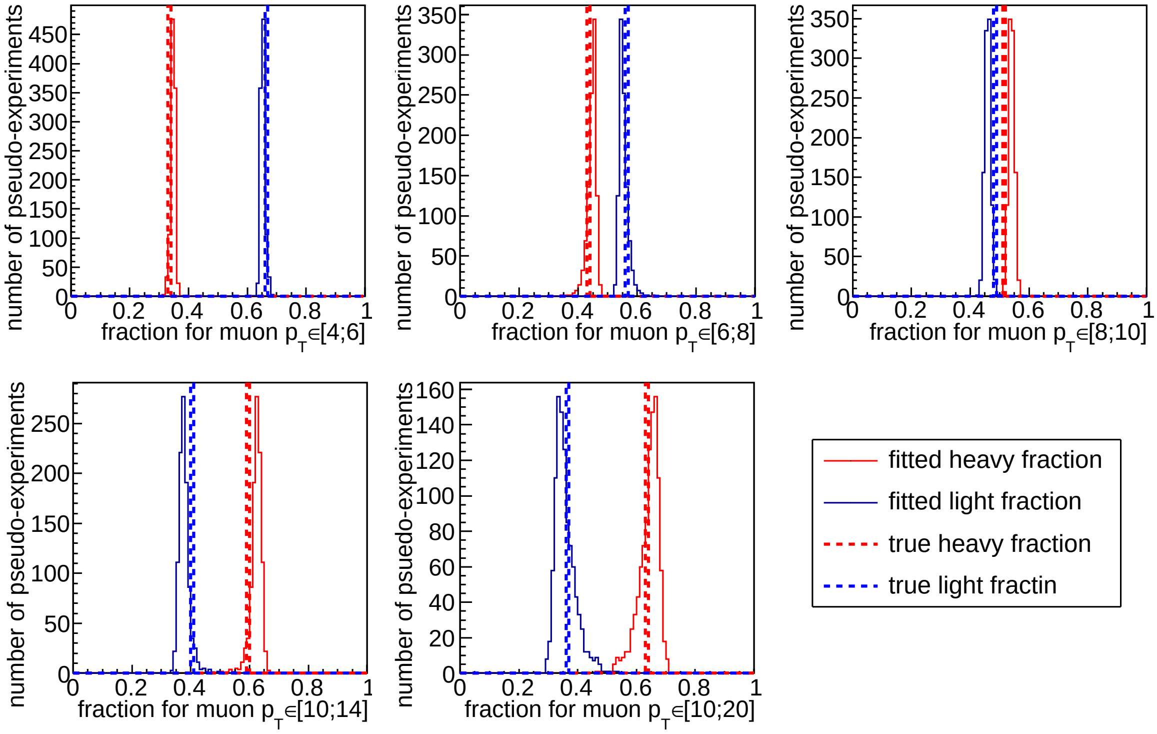

Figure B.5.: Fraction of the heavy flavor decays (red) and the combination of light and charm flavor decays (blue) as determined by template functions extracted from pseudo-experiments (solid line) and the true fraction superimposed (dashed line). The study is performed on the dijet Monte Carlo sample while muons reconstructed by the MUID algorithm are used.

B.5. Detailed results of global template fit

In this section the detailed fitting results to the full distributions for each of the 5 muon transverse momentum bins are presented. The global fits performed on the minimum bias Monte Carlo sample and the simulated dijet sample as well as on real data are given in figure B.6 for muons reconstructed with the MUID algorithm. In figure B.7 the results are shown for STACO accordingly. While for the dijet Monte Carlo and real data sample the statistics are reasonable there is a sizable decrease for the high transverse muon momentum bins in the simulated minimum bias sample which impacts the freedom of the fit.

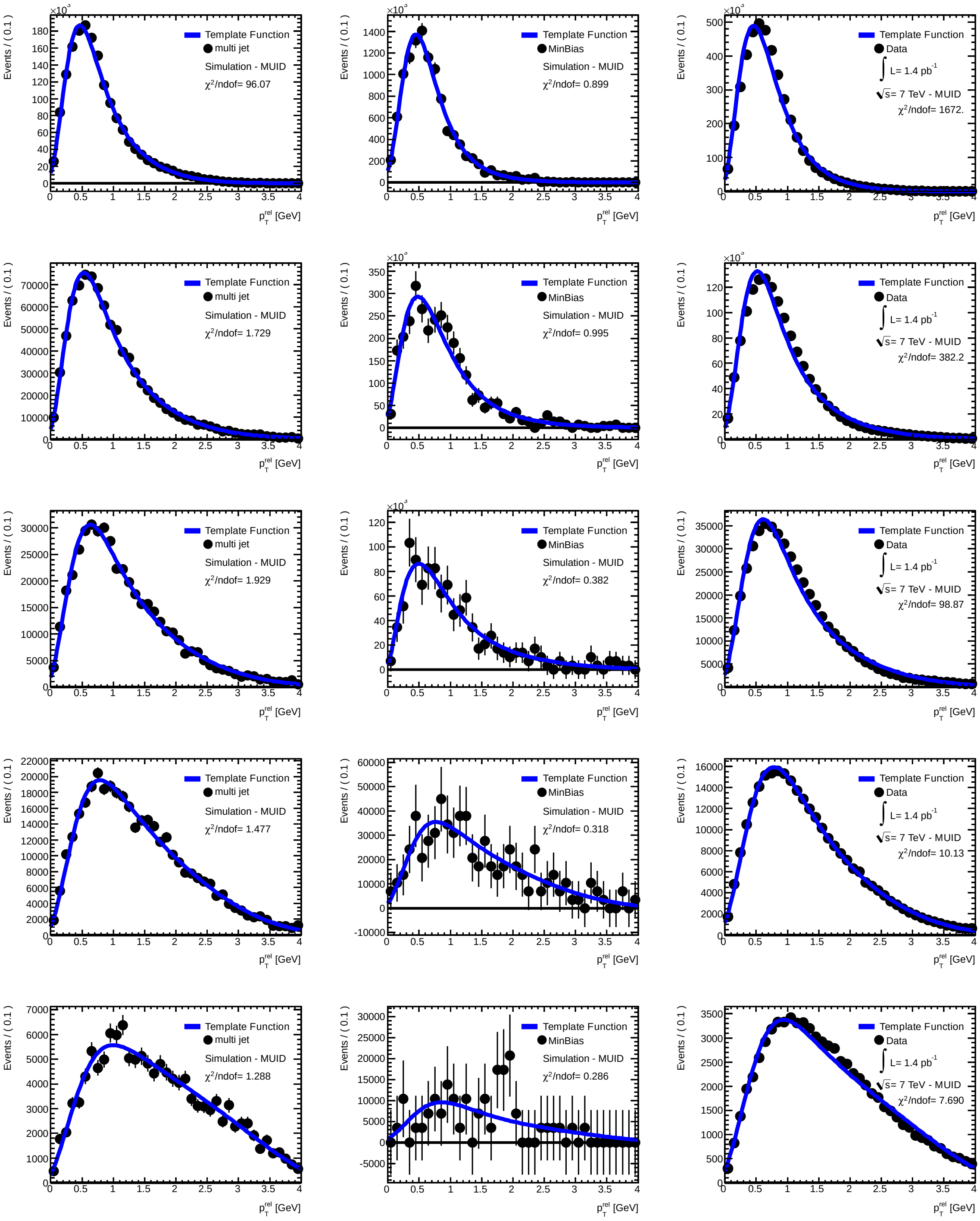

Figure B.6.: Results for the fit to the full distribution extracted from the dijet Monte Carlo sample (left), the minimum bias Monte Carlo sample (middle) and real data (right). The muons are reconstructed with the MUID algorithm and the 5 muon transverse momentum bins are given from top to bottom.

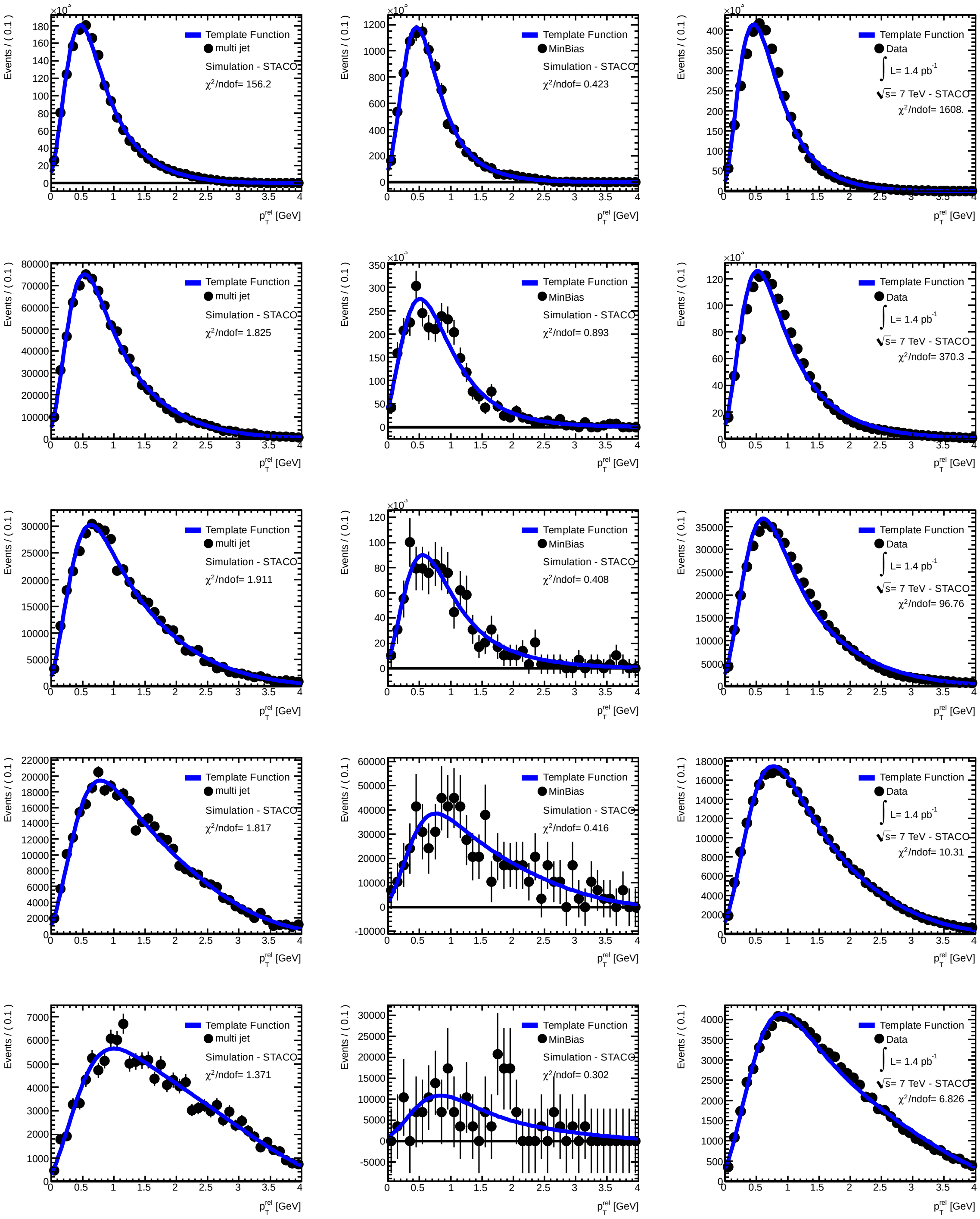

Figure B.7.: Results for the fit to the full distribution extracted from the dijet Monte Carlo sample (left), the minimum bias Monte Carlo sample (middle) and real data (right). The muons are reconstructed with the STACO algorithm and the 5 muon transverse momentum bins are given from top to bottom.

Appendix C

Auxilary material for muons with high pseudorapidity

In section 5.3 the performance of the muons with high pseudorapidity is analyzed. Though the most important results are given for both muon reconstruction algorithms some particular examples plots are presented for the STACO algorithm only. This chapter holds the corresponding distributions based on the MUID algorithm as well as additional information and plots missing in the main body.

C.1. Monte Carlo samples

For comparison of data and simulation the following samples of $t\bar{t}$, W boson, Z boson and heavy flavor jet production are used in the analysis. For all samples the Monte Carlo identifier (MCID), the actual process, the generator and the efficiency on generator level ϵ_{filter} as well as various other sample and process specific quantites are listed. All of them are created during the production campaign in 2010 and the according ATLAS simulation software setup is used with reflects best the run conditions of 2011 data on the standard of knowledge at this time.

MCID	Process	Generator	events	ϵ_{filter}	cross section [pb]
105200	$t\bar{t}$	MC@NLO	15000000	0.56	143.99
106021	$W \to \mu\nu + 1$ lepton	Pythia	1000000	0.88	878.21
106052	$Z \to \tau\tau$	Pythia	500000	1.0	854.00
106088	$Z \to \mu\mu$	MC@NLO	5000000	1.0	953.30
106047	$Z \to \mu\mu$	Pythia	5000000	1.0	855.25
108490	$bb\mu2p5\mu2p5X$	PythiaB	4000000	1.0	520.00
109305	$Z \to \mu\mu + bb + 0partons$	Alpgen/Jimmy	150000	1.0	6.5639
109306	$Z \to \mu\mu + bb + 1parton$	Alpgen/Jimmy	100000	1.0	2.4739
109307	$Z \to \mu\mu + bb + 2partons$	Alpgen/Jimmy	40000	1.0	0.88713
109308	$Z \to \mu\mu + bb + 3partons$	Alpgen/Jimmy	10000	1.0	0.39008

Table C.1.: Monte Carlo samples of Z boson signal production and important background processes.

C.2. Resolution of the invariant mass of muon pairs

In section 5.3.2 the resolution of the invariant mass of muon pairs with one muon reconstructed above $|\eta| = 2.5$ is studied. In table 5.7 the corresponding results for fitting equation (5.16) to the Z boson candidates is presented for simulation and data for several collections regarding the pseudorapidity of the combined and tagging muon respectively. In figures C.1 the related distributions including the fit are given for the STACO reconstruction algorithm while figures C.2 shows the results based on the MUID algorithm. Figure C.3 shows the official ATLAS results for the resolution of muon pairs in various pseudorapidity regions. In case of two combined muons the resolution varies between 1.8(1.6) GeV to 2.6(2.0) GeV in data (simulation) while for two stand alone muons it is 3.4(2.8) GeV to 4.6(3.8) GeV.

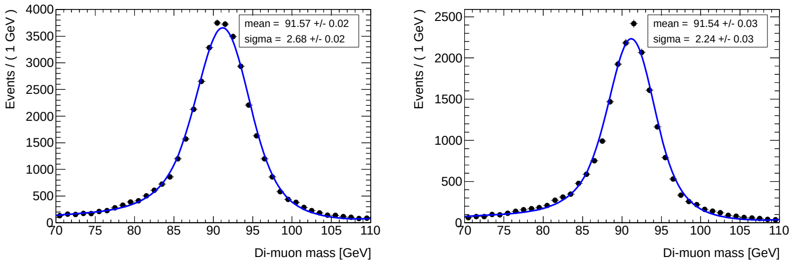

(a) resolution obtained from data (left) and simulation (right) in case of the tagging muon in $|\eta| < 2.5$

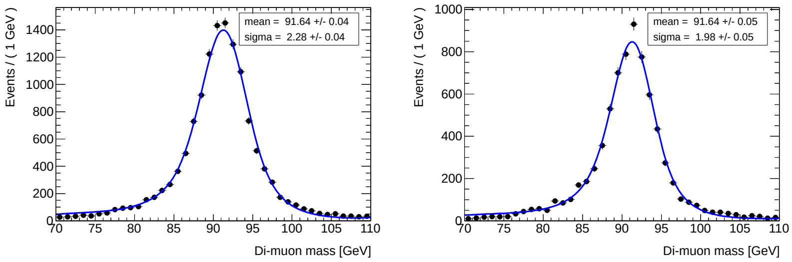

(b) resolution obtained from data (left) and simulation (right) in case of the tagging muon in $|\eta| < 1.05$

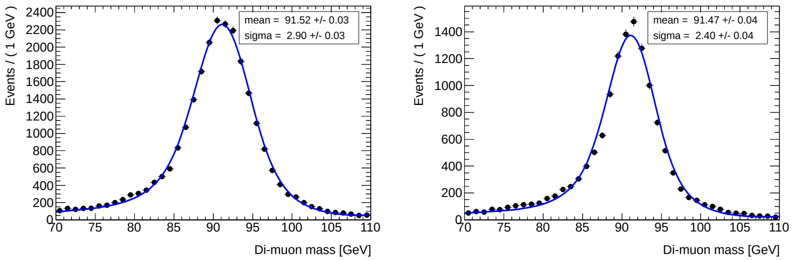

(c) resolution obtained from data (left) and simulation (right) in case of the tagging muon in $1.3 < |\eta| < 2.$

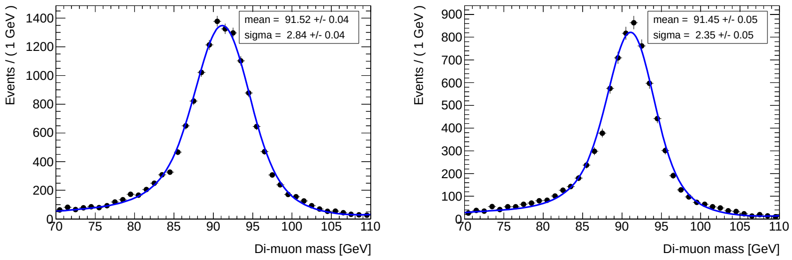

(d) resolution obtained from data (left) and simulation (right) in case of the tagging muon in $1.3 < |\eta| < 2.5$

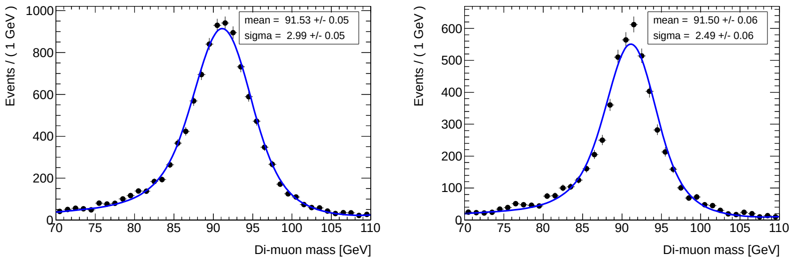

(e) resolution obtained from data (left) and simulation (right) in case of the tagging muon in $2.0 < |\eta| < 2.5$

Figure C.1.: Resolution of the invariant mass of muon pairs passing the full set of selection criteria for Z boson candidates in various ranges regarding the pseudorapidity of the tagging muon as obtained from data and $Z \to \mu\mu$ Monte Carlo. The results for the fit of equation (5.16) are superimposed. The presented results are based on the STACO reconstruction algorithm.

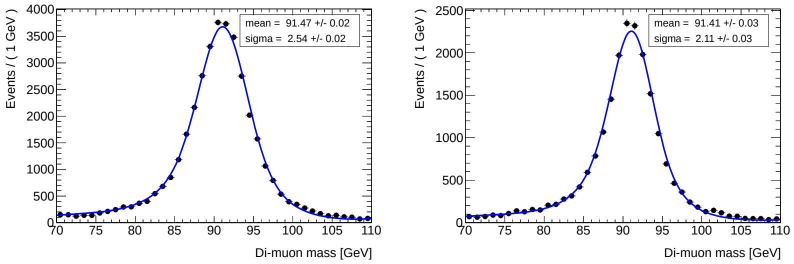

(a) resolution obtained from data (left) and simulation (right) in case of the tagging muon in $|\eta| < 2.5$

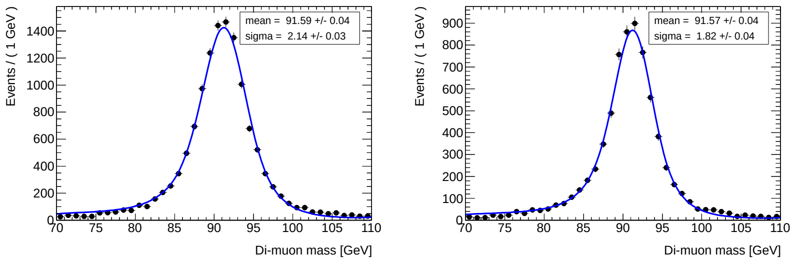

(b) resolution obtained from data (left) and simulation (right) in case of the tagging muon in $|\eta| < 1.05$

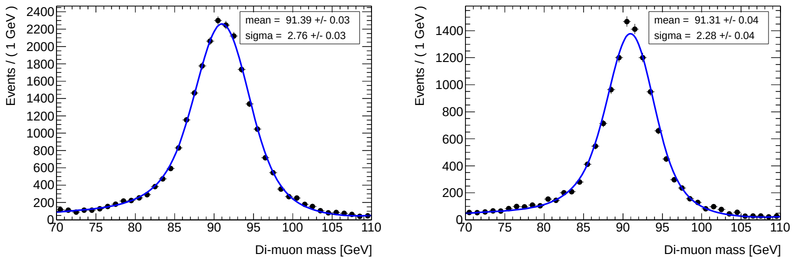

(c) resolution obtained from data (left) and simulation (right) in case of the tagging muon in $1.3 < |\eta| < 2.$

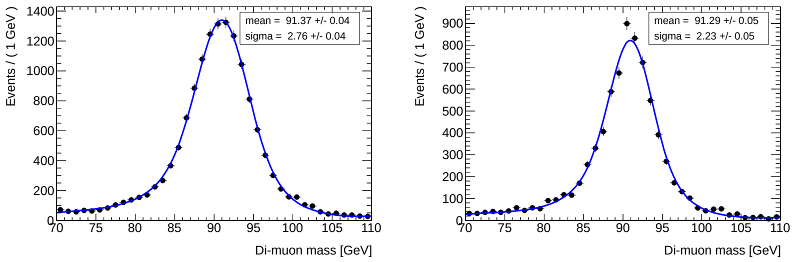

(d) resolution obtained from data (left) and simulation (right) in case of the tagging muon in $1.3 < |\eta| < 2.5$

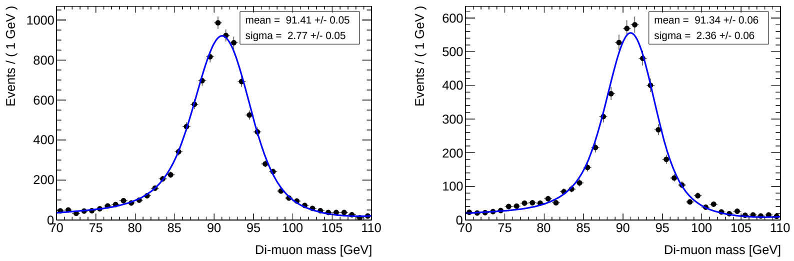

(e) resolution obtained from data (left) and simulation (right) in case of the tagging muon in $2.0 < |\eta| < 2.5$

Figure C.2.: Resolution of the invariant mass of muon pairs passing the full set of selection criteria for Z boson candidates in various ranges regarding the pseudorapidity of the tagging muon as obtained from data and $Z \to \mu\mu$ Monte Carlo. The results for the fit of equation (5.16) are superimposed. The presented results are based on the MUID reconstruction algorithm.

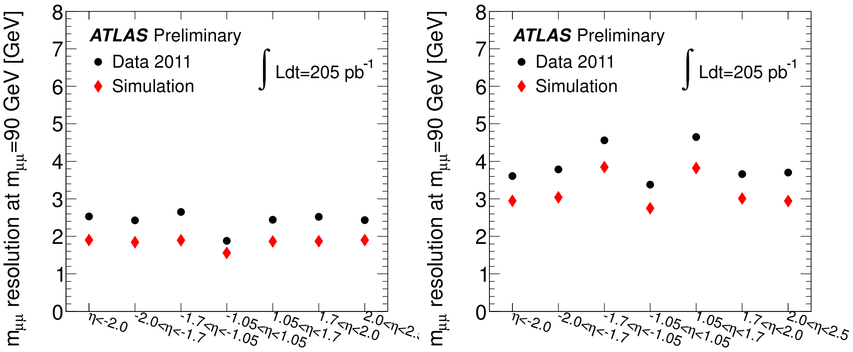

Figure C.3.: Resolution of muon pairs in different pseudorapididty regions as obtained from two combined muons (left) or two stand alone muon (right) reconstructed in data and simulation [173].

C.3. Hit quality distributions for muons with high pseudorapidity

In section 5.3.4 hit distributions of muon tracks reconstructed in the high pseudorapidity region are studied for the various detector technologies and eventually recommendations on the quality are given. The distributions presented in the main body are based on the muons reconstructed by the STACO algorithm and look rather similar to the corresponding distributions obtained with the MUID algorithm shown in this section. Figure C.4 shows the amount of muons split up in the different reconstruction categories. The hit distributions in the subdetectors of the inner detector are available in figure C.5 while the efficiency for Z boson candidates depending on the sum of SCT hits and SCT dead sensors is shown in figure C.6. The amount of hits in the various chamber of the muon spectrometer can be found in figure C.7. Eventually figure C.8 presents the efficiency of muons in the high pseudorapidity region as a function of the station layers of the muon spectrometer used for reconstruction.

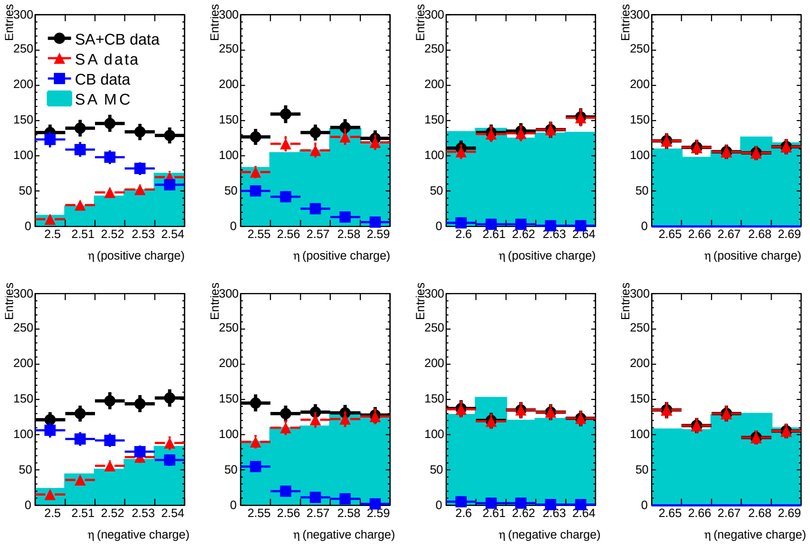

Figure C.4.: Pseudorapidity distributions of the number of muons above $|\eta| = 2.5$ in data split up in the different reconstruction categories as well as in positive (top) and negative (bottom) charge. All quality and pairing criteria are applied. Red markers indicate stand alone muons while blue markers denote combined muons. Black markers represent the sum of both. The stand alone muons found in the $Z \to \mu\mu$ Monte Carlo are scaled to the data luminosity and superimposed as histogram. The presented results are obtained from the MUID reconstruction algorithm.

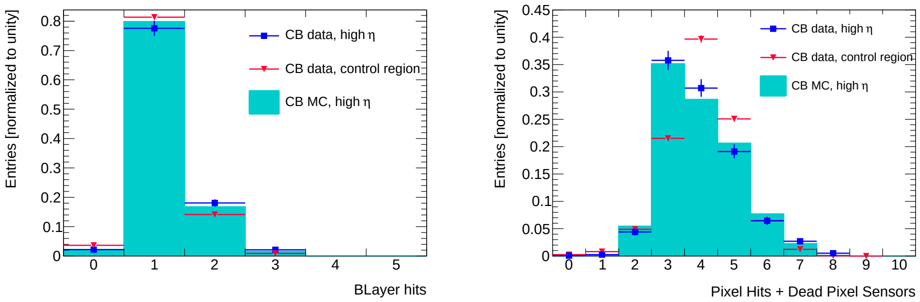

(a) Number of hits in the B-layer.

(b) Sum of hits in the pixel detector and crossed dead pixel sensors.

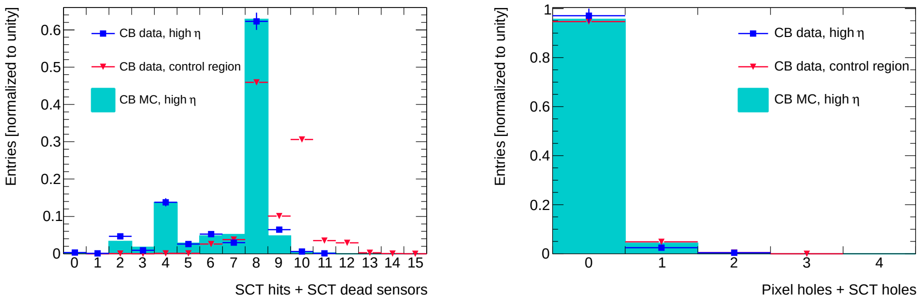

(c) Sum of hits in the SCT and crossed dead SCT sensors.

(d) Sum of the number of holes in the pixel detector and SCT.

Figure C.5.: Distributions of various quantities measured in the the inner detector for combined muons reconstructed in the high pseudorapidity region. The applied selection includes the complete set of requirements for Z boson candidates. Blue markers indicate combined muons in data found above $|\eta| = 2.5$ while red markers represent those in the control region. Combined muons with high pseudorapidity in the $Z \to \mu\mu$ Monte Carlo are superimposed as histogram. All distributions are normalized to unity and produced with muons reconstructed by the MUID algorithm.

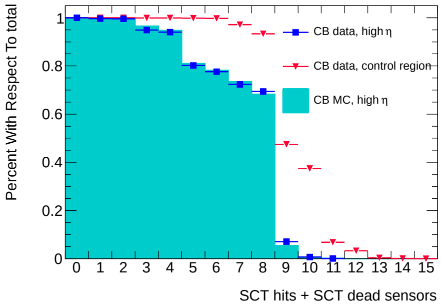

Figure C.6.: Efficiency of reconstructed Z boson candidates and muons in the high pseudorapidity region respectively as function of the sum of SCT hits and SCT dead sensors. Blue markers indicate the efficiency for muons in data found above $|\eta| = 2.5$ while red markers represent the same for the control region. The corresponding efficiency for the high pseudorapidity region in the $Z \to \mu\mu$ Monte Carlo are superimposed as histogram. The shown results are based on the MUID reconstruction algorithm.

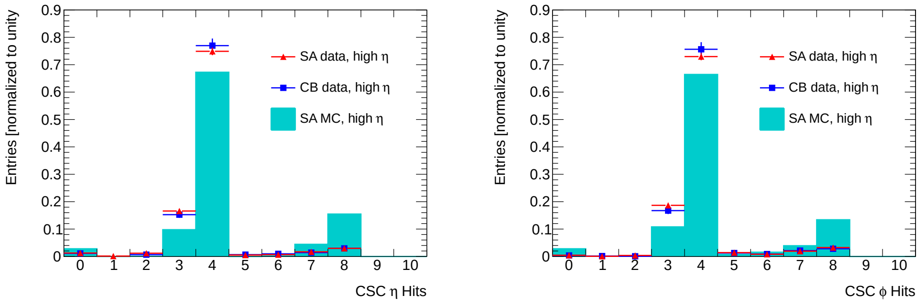

(a) Number of hits in η stripes of the CSC chambers. (b) Number of hits in ϕ stripes of the CSC chambers.

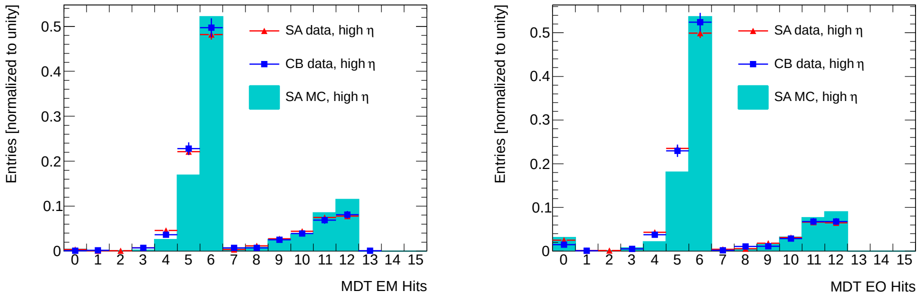

(c) Number of hits in the middle MDT end-cap station layer. (d) Number of hits in the outer MDT end-cap station layer.

Figure C.7.: Distributions of the number hits in various end-cap station layers of the muon spectrometer for muon tracks above $|\eta| = 2.5$ found in data by the inner detector and muon spectrometer (blue markers) or the muon spectrometer exclusively (red markers). Stand alone muon tracks found in the $Z \to \mu\mu$ Monte Carlo are superimposed as histogram. The applied selection includes the complete set of requirements for Z boson candidates and the distributions are normalized to unity. The results presented here are based on tracks found by the MUID reconstruction algorithm.

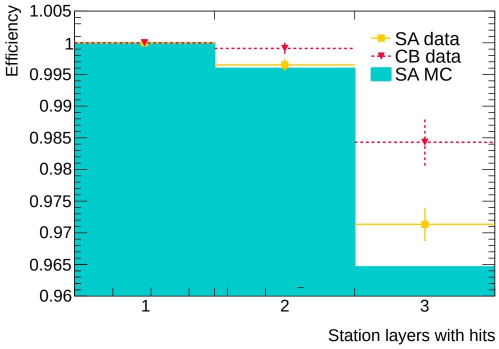

Figure C.8.: Efficiency for stand alone muons (yellow markers) and combined muons (red markers) in data as function of the number of station layers in the muon spectrometer which contribute to the track. The applied selection includes the complete set of requirements for Z boson candidates and the according results for stand alone muons obtained from $Z \to \mu\mu$ Monte Carlo are superimposed as histogram. The efficiency presented here is based on the MUID reconstruction algorithm.

C.4. Pile-up dependence of calorimeter isolation

With equation (5.18) in section 5.3.5 there is a basic function given to perform a first order correction for in-time pile-up affecting the calorimetric isolation. The final results are summarized in table 5.9 while the corresponding fits are presented in figures C.9 to figures C.12 based on the STACO and MUID reconstruction algorithm respectively. Before the correction is applied there is an approximately linear dependence of the calorimetric isolation on the number of vertices in the bunch-crossing. Once the correction is applied the distributions become close to flat.

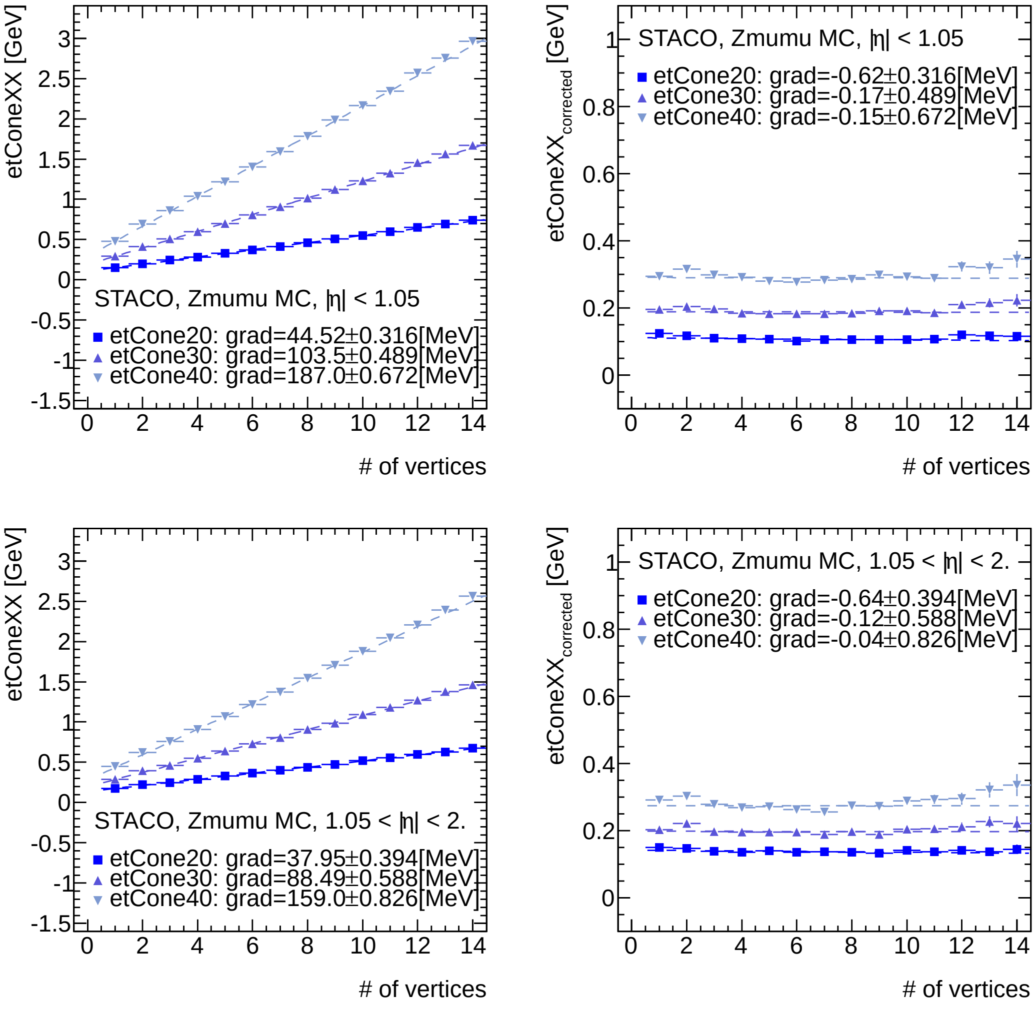

Figure C.9.: The selection follows the full set of requirements for Z boson candidates. The mean value of the calorimetric isolation in cones with radius of 0.2, 0.3 and 0.4 for probe muons reconstructed in two central pseudorapidity ranges, namely $|\eta| < 1.05$ (top) and $1.05 < |\eta| < 2.0$ (bottom), is shown as a function of the number of vertices in the bunch-crossing. Statistical uncertainties are represented by the error bars. In each of the η regions the calorimetric isolation is available before the pile-up correction (left) with a fit according to equation (5.18) applied and after the correction (right) again fitted with a straight line. The shown results are based on the STACO reconstruction algorithm.

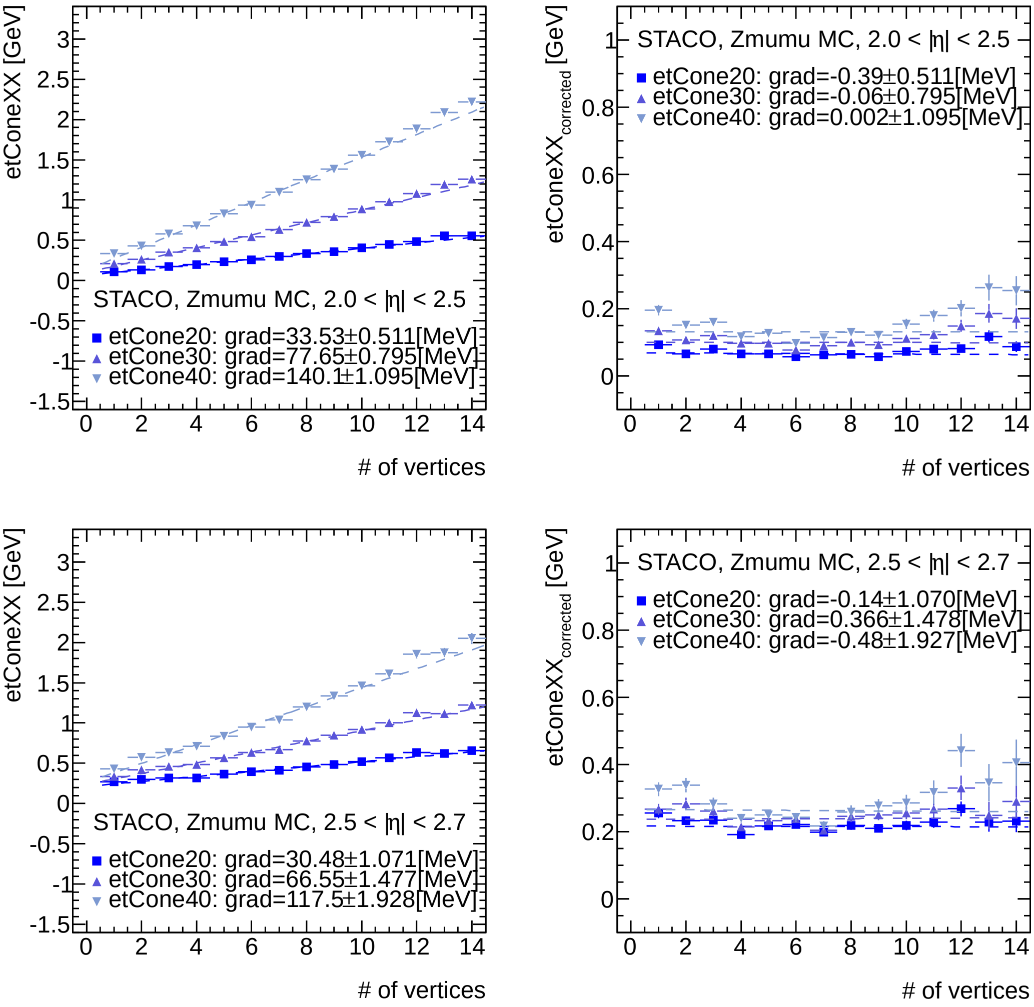

Figure C.10.: The selection follows the full set of requirements for Z boson candidates. The mean value of the calorimetric isolation in cones with radius of 0.2, 0.3 and 0.4 for probe muons reconstructed in two forward pseudorapidity ranges, namely $2.0 < |\eta| < 2.5$ (top) and $2.5 < |\eta| < 2.7$ (bottom), is shown as a function of the number of vertices in the bunch-crossing. Statistical uncertainties are represented by the error bars. In each of the η regions the calorimetric isolation is available before the pile-up correction (left) with a fit according to equation (5.18) applied and after the correction (right) again fitted with a straight line. The shown results are based on the STACO reconstruction algorithm.

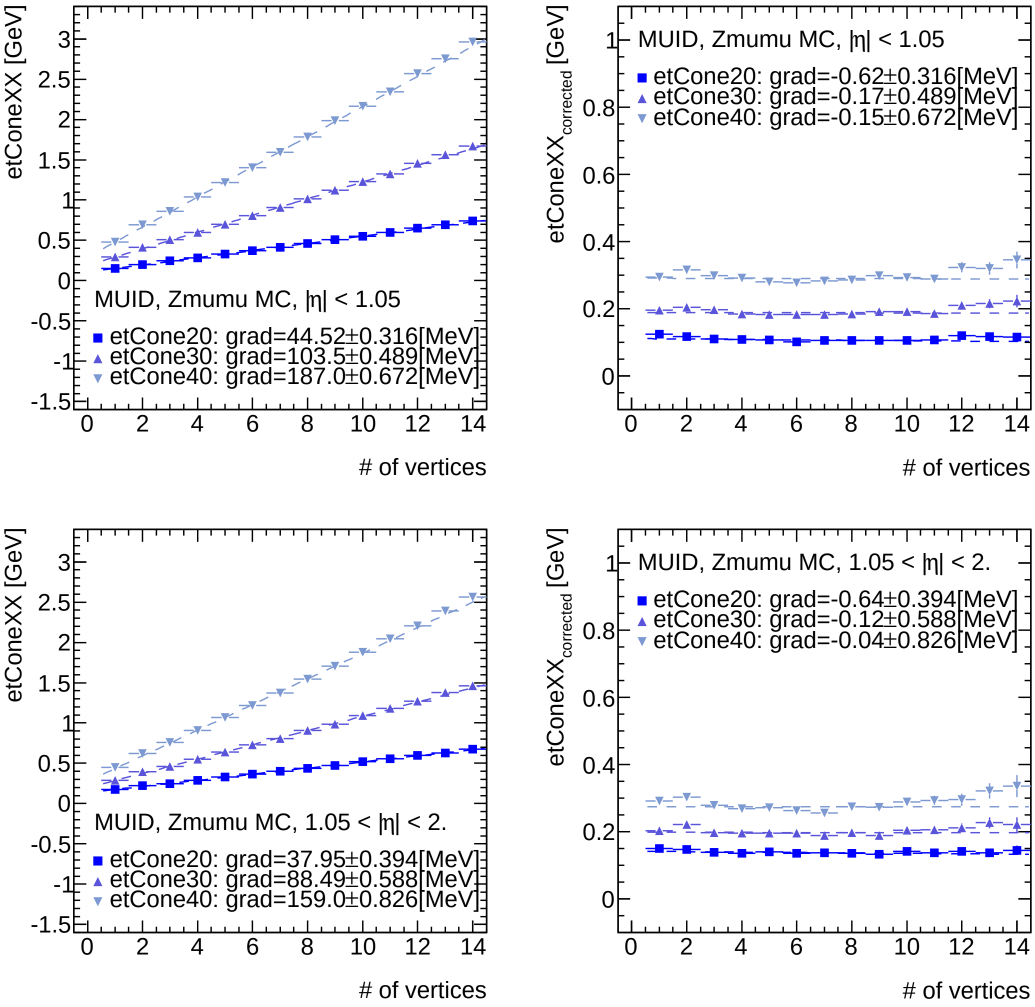

Figure C.11.: The selection follows the full set of requirements for Z boson candidates. The mean value of the calorimetric isolation in cones with radius of 0.2, 0.3 and 0.4 for probe muons reconstructed in two central pseudorapidity ranges, namely $|\eta| < 1.05$ (top) and $1.05 < |\eta| < 2.0$ (bottom), is shown as a function of the number of vertices in the bunch-crossing. Statistical uncertainties are represented by the error bars. In each of the η regions the calorimetric isolation is available before the pile-up correction (left) with a fit according to equation (5.18) applied and after the correction (right) again fitted with a straight line. The shown results are based on the MUID reconstruction algorithm.

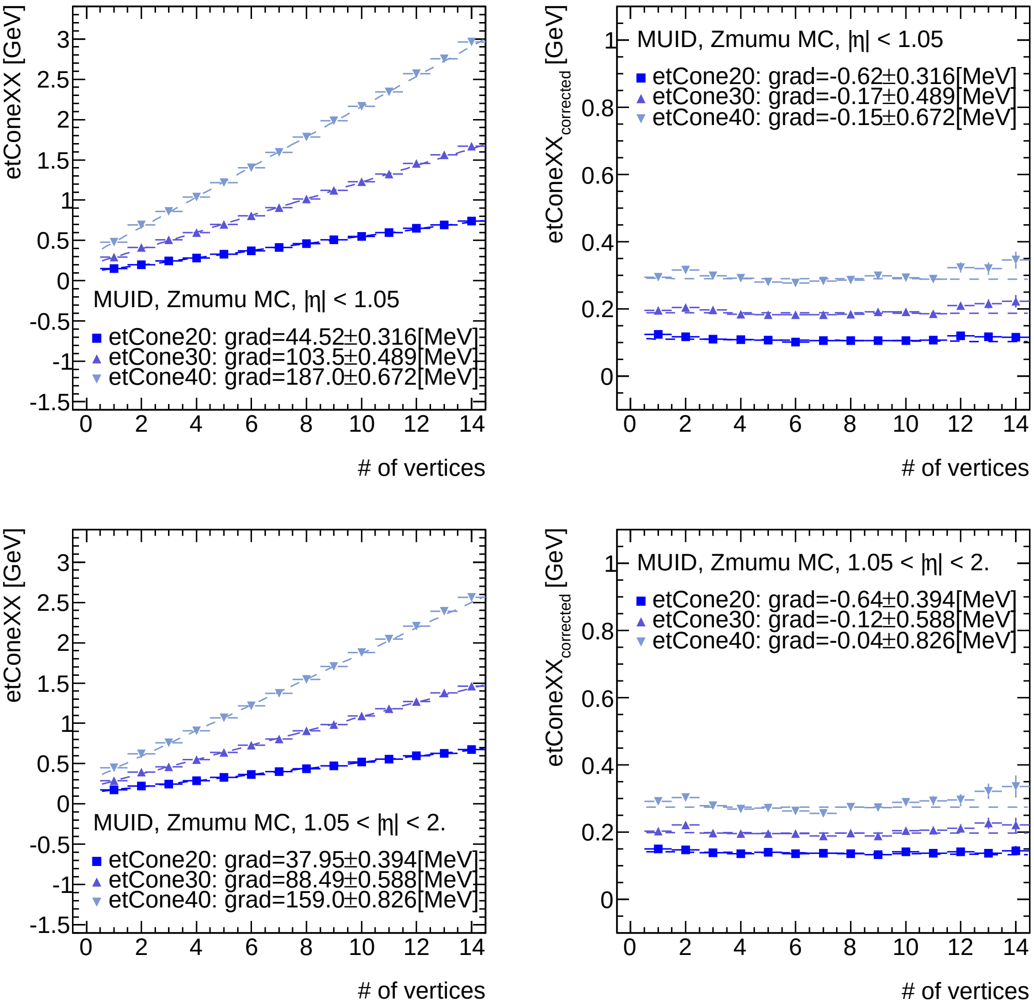

Figure C.12.: The selection follows the full set of requirements for Z boson candidates. The mean value of the calorimetric isolation in cones with radius of 0.2, 0.3 and 0.4 for probe muons reconstructed in two forward pseudorapidity ranges, namely $2.0 < |\eta| < 2.5$ (top) and $2.5 < |\eta| < 2.7$ (bottom), is shown as a function of the number of vertices in the bunch-crossing. Statistical uncertainties are represented by the error bars. In each of the η regions the calorimetric isolation is available before the pile-up correction (left) with a fit according to equation (5.18) applied and after the correction (right) again fitted with a straight line. The shown results are based on the MUID reconstruction algorithm.

C.5. Calorimetric isolation in data and simulation

For muons reconstructed with the STACO algorithm the good agreement of calorimetric isolation in data and simulation after the in-time pile-up correction is demonstrated on the example of a cone of 0.2 in section 5.3.5. In figures C.13 and C.14 it is presented for cones of 0.3 and 0.4 respectively. The corresponding results based on muons reconstructed with the MUID algorithm are shown in figures C.15 to C.17. There is no sizable difference visible and for both reconstruction algorithms the agreement of data compared to Monte Carlo is adequate.

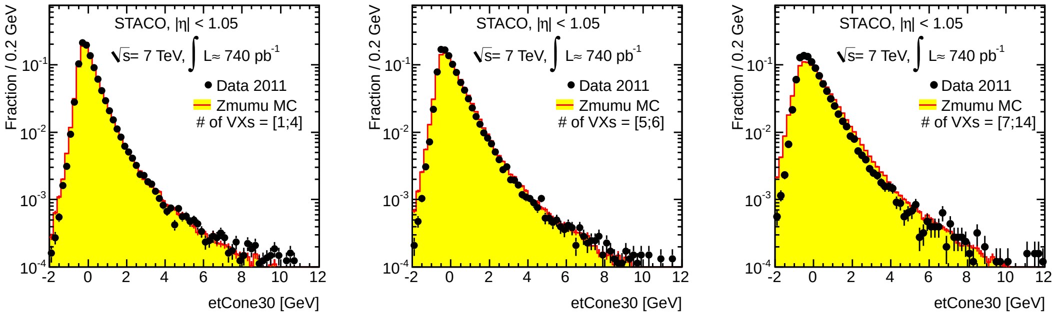

(a) calorimetric isolation after pile-up correction for the probe muon in $|\eta| < 1.05$

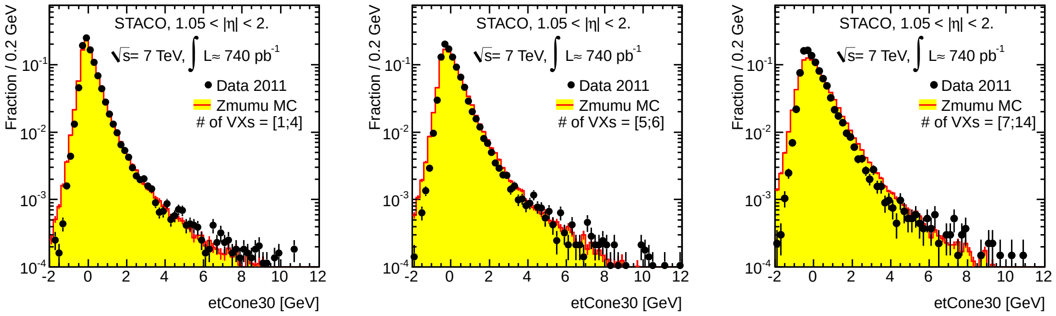

(b) calorimetric isolation after pile-up correction for the probe muon in $1.05 < |\eta| < 2.0$

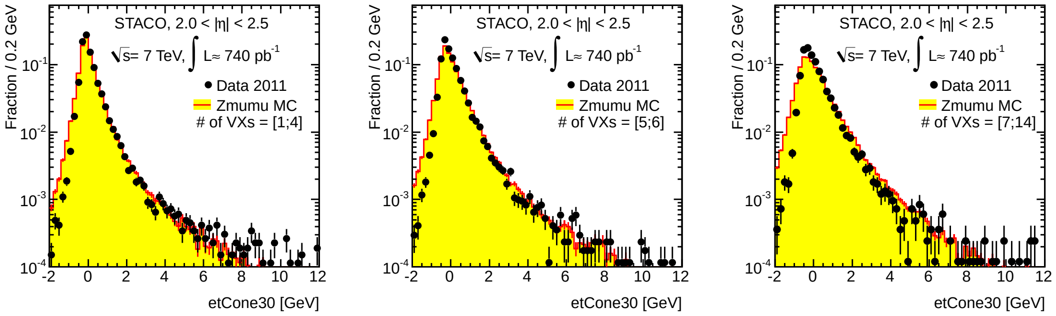

(c) calorimetric isolation after pile-up correction for the probe muon in $2.0 < |\eta| < 2.5$

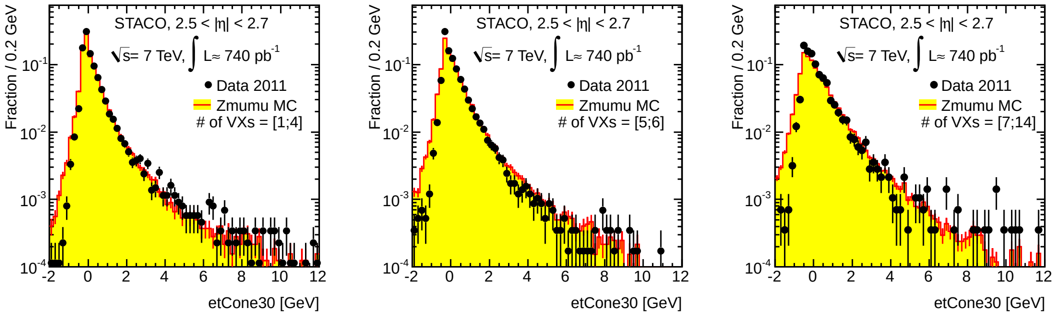

(d) calorimetric isolation after pile-up correction for the probe muon in $2.5 < |\eta| < 2.7$

Figure C.13.: The calorimetric isolation in a cone of 0.3 after correcting for pile-up according to equation (5.18). For the muon pair the full set of selection criteria to obtain Z boson candidates is applied while while the probe muons are considered in four pseudorapidity regions. There is an additional division depending on the number of vertices in the bunch-crossing. The results presented here are based on the STACO reconstruction algorithm and the black points refer to data while $Z \to \mu\mu$ Monte Carlo is superimposed as histogram. The given uncertainties are statistical.

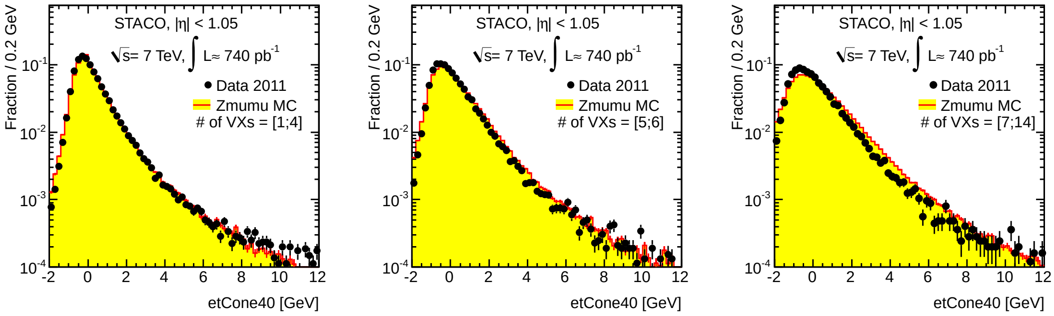

(a) calorimetric isolation after pile-up correction for the probe muon in $|\eta| < 1.05$

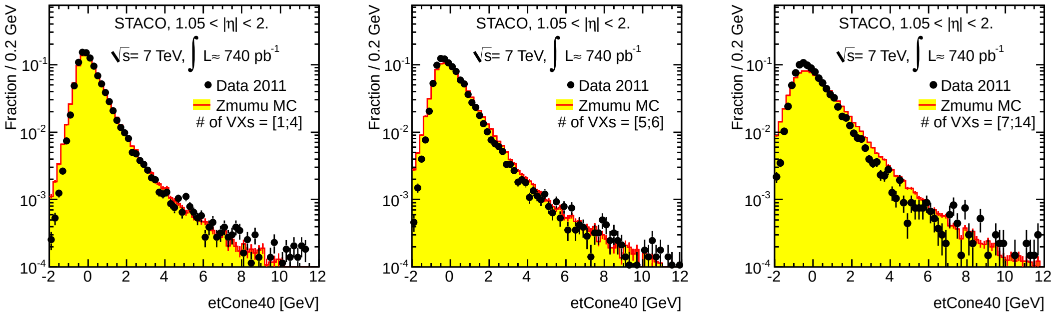

(b) calorimetric isolation after pile-up correction for the probe muon in $1.05 < |\eta| < 2.0$

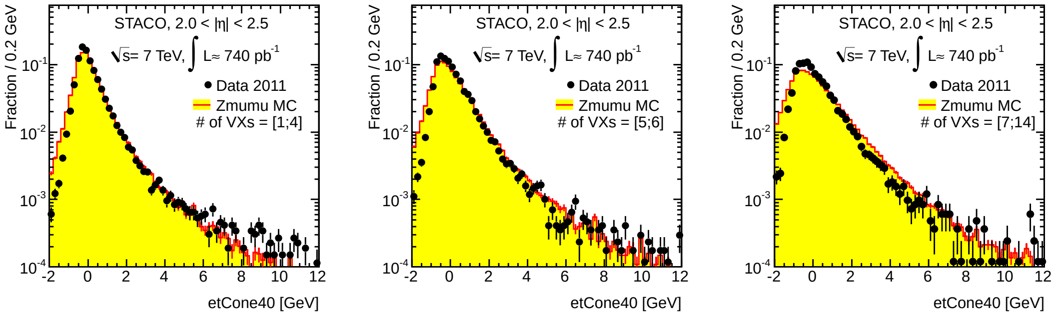

(c) calorimetric isolation after pile-up correction for the probe muon in $2.0 < |\eta| < 2.5$

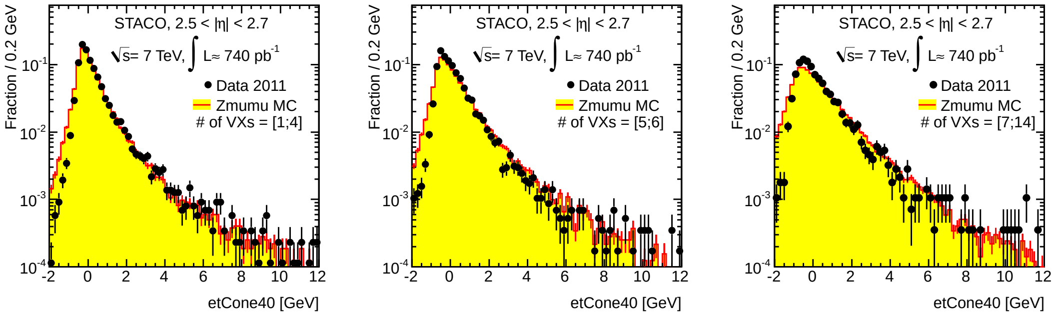

(d) calorimetric isolation after pile-up correction for the probe muon in $2.5 < |\eta| < 2.7$

Figure C.14.: The calorimetric isolation in a cone of 0.4 after correcting for pile-up according to equation (5.18). For the muon pair the full set of selection criteria to obtain Z boson candidates is applied while the probe muon with looser requirements is not only reconstructed above $|\eta| = 2.5$, but in four different pseudorapidity regions. There is an additional division depending on the number of vertices in the bunch-crossing. The results presented here are based on the STACO reconstruction algorithm and the black points refer to data while $Z \to \mu\mu$ Monte Carlo is superimposed as histogram. The given uncertainties are statistical.

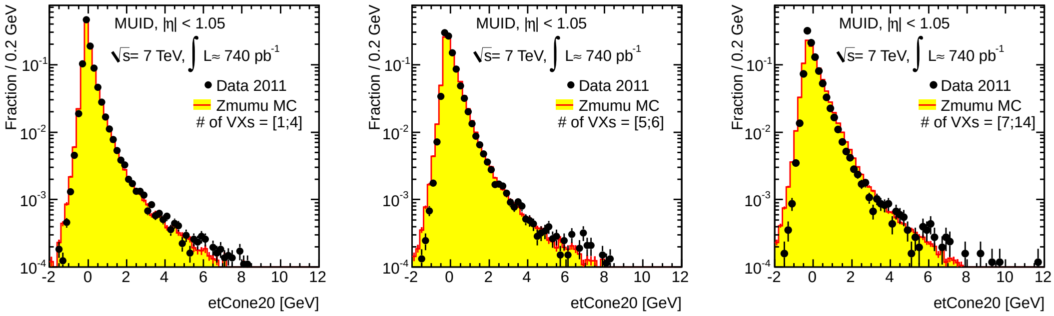

(a) calorimetric isolation after pile-up correction for the probe muon in $|\eta| < 1.05$

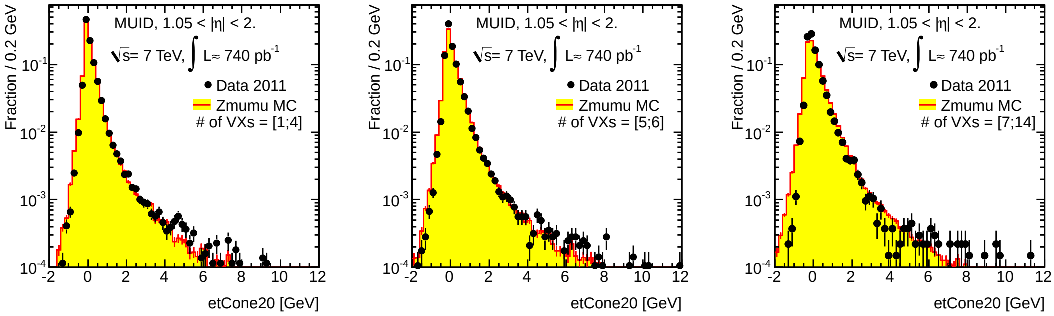

(b) calorimetric isolation after pile-up correction for the probe muon in $1.05 < |\eta| < 2.0$

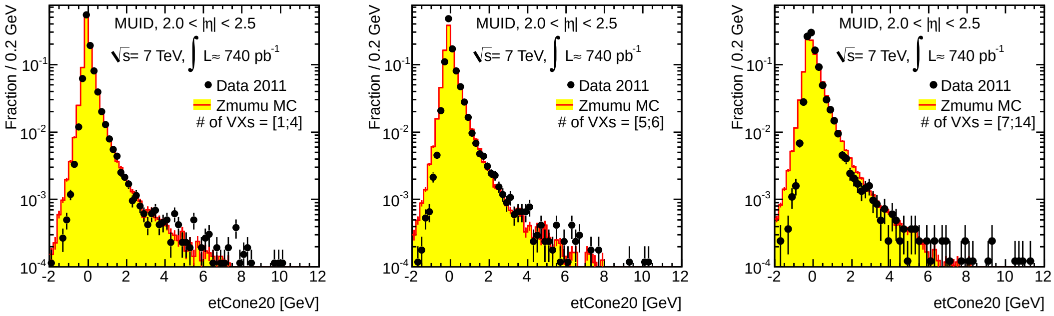

(c) calorimetric isolation after pile-up correction for the probe muon in $2.0 < |\eta| < 2.5$

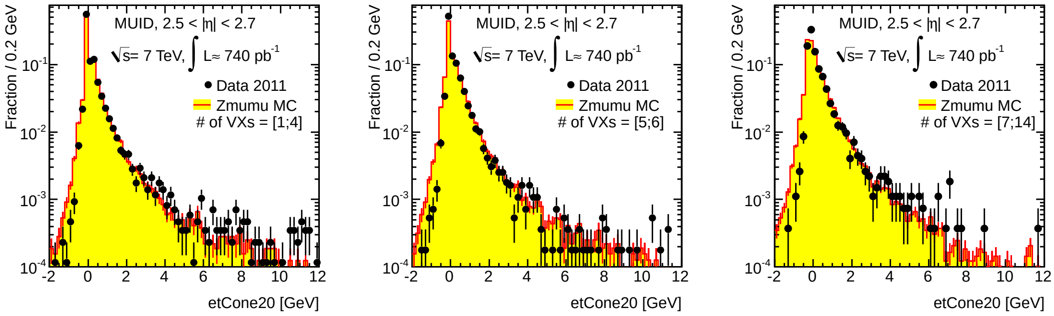

(d) calorimetric isolation after pile-up correction for the probe muon in $2.5 < |\eta| < 2.7$

Figure C.15.: The calorimetric isolation in a cone of 0.2 after correcting for pile-up according to equation (5.18). For the muon pair the full set of selection criteria to obtain Z boson candidates is applied while the probe muons are considered in four pseudorapidity regions. There is an additional division depending on the number of vertices in the bunch-crossing. The results presented here are based on the MUID reconstruction algorithm and the black points refer to data while $Z \to \mu\mu$ Monte Carlo is superimposed as histogram. The given uncertainties are statistical.

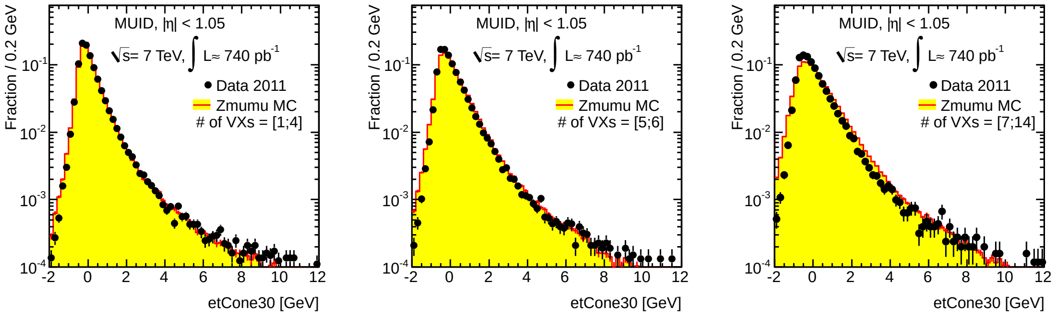

(a) calorimetric isolation after pile-up correction for the probe muon in $|\eta| < 1.05$

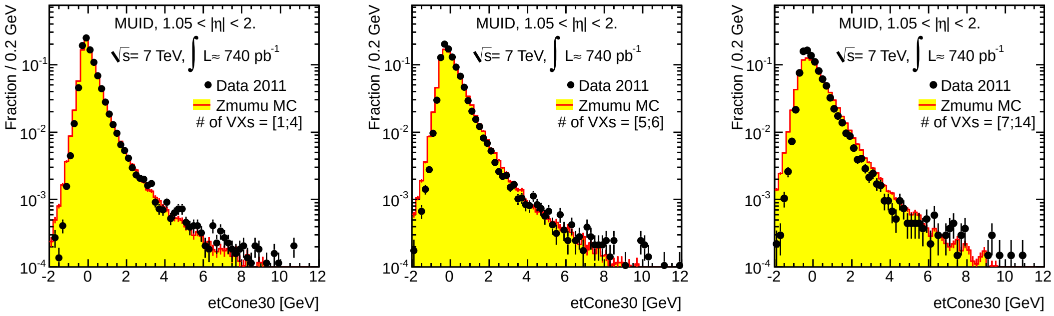

(b) calorimetric isolation after pile-up correction for the probe muon in $1.05 < |\eta| < 2.0$

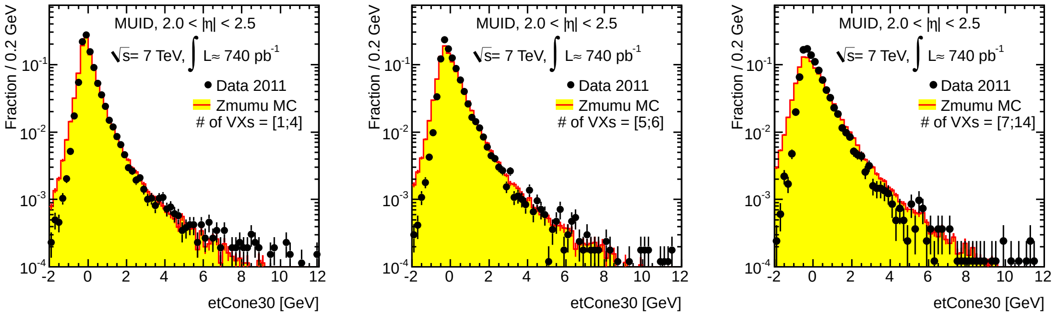

(c) calorimetric isolation after pile-up correction for the probe muon in $2.0 < |\eta| < 2.5$

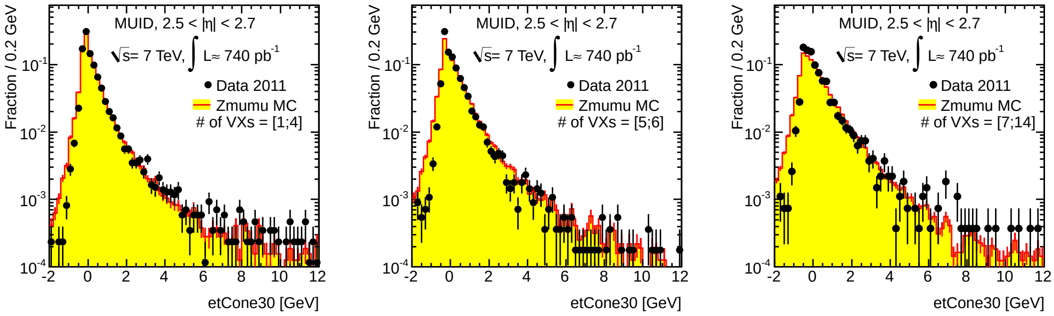

(d) calorimetric isolation after pile-up correction for the probe muon in $2.5 < |\eta| < 2.7$

Figure C.16.: The calorimetric isolation in a cone of 0.3 after correcting for pile-up according to equation (5.18). For the muon pair the full set of selection criteria to obtain Z boson candidates is applied while the probe muons are considered in four pseudorapidity regions. There is an additional division depending on the number of vertices in the bunch-crossing. The results presented here are based on the MUID reconstruction algorithm and the black points refer to data while $Z \rightarrow \mu\mu$ Monte Carlo is superimposed as histogram. The given uncertainties are statistical.

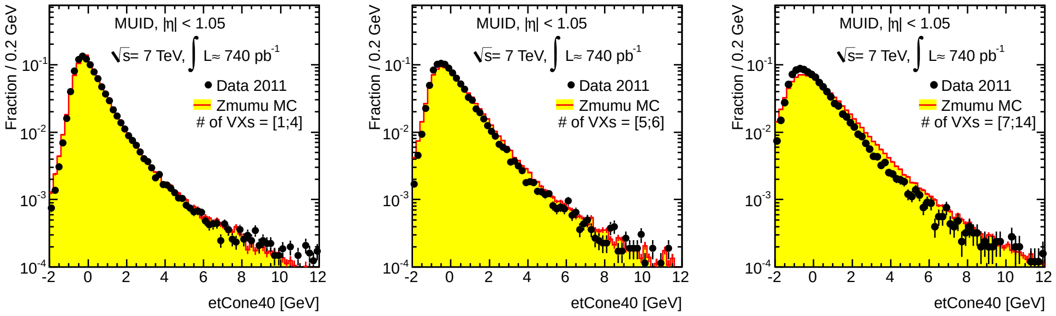

(a) calorimetric isolation after pile-up correction for the probe muon in $|\eta| < 1.05$

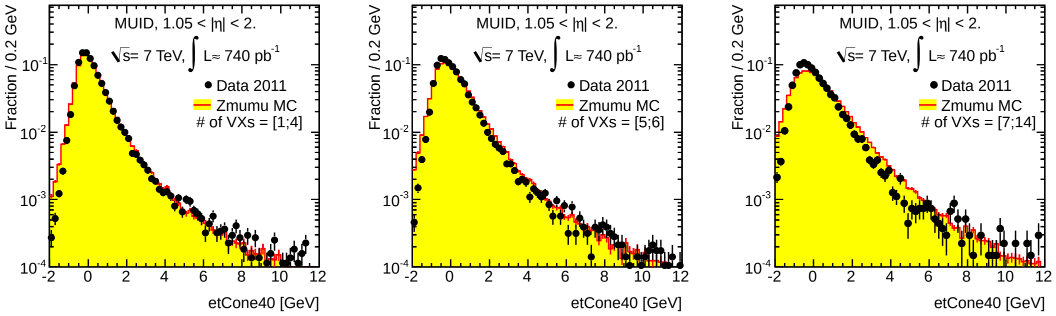

(b) calorimetric isolation after pile-up correction for the probe muon in $1.05 < |\eta| < 2.0$

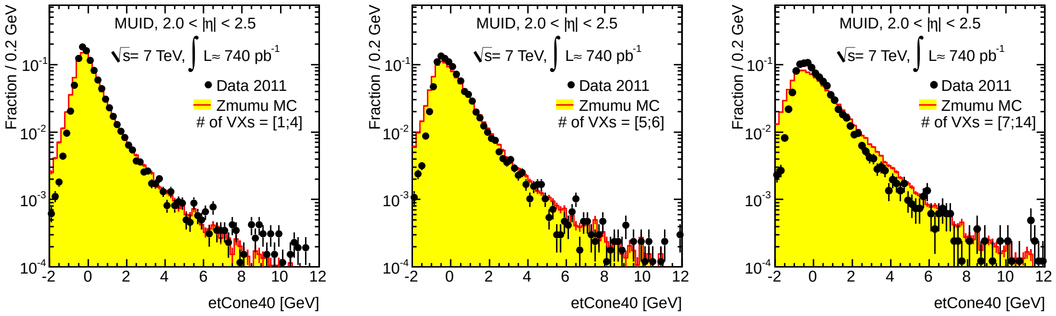

(c) calorimetric isolation after pile-up correction for the probe muon in $2.0 < |\eta| < 2.5$

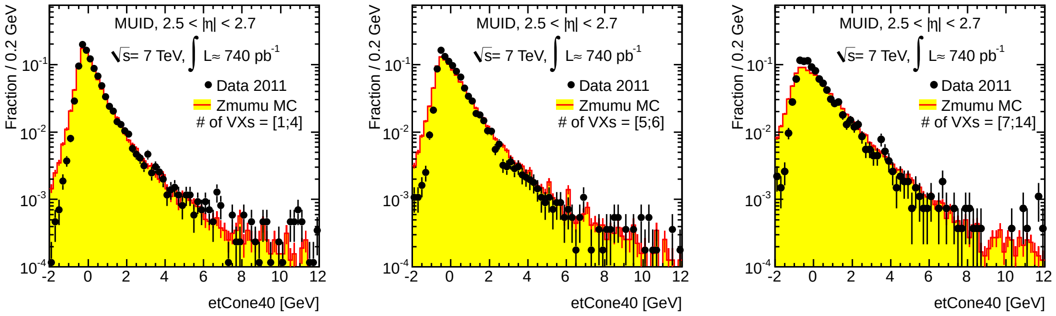

(d) calorimetric isolation after pile-up correction for the probe muon in $2.5 < |\eta| < 2.7$

Figure C.17.: The calorimetric isolation in a cone of 0.4 after correcting for pile-up according to equation (5.18). For the muon pair the full set of selection criteria to obtain Z boson candidates is applied while the probe muons are considered in four pseudorapidity regions. There is an additional division depending on the number of vertices in the bunch-crossing. The results presented here are based on the MUID reconstruction algorithm and the black points refer to data while $Z \to \mu\mu$ Monte Carlo is superimposed as histogram. The given uncertainties are statistical.

Appendix D

Supporting material for the measurement of the inclusive ZZ cross section

In chapter 6 the measurement of the inclusive ZZ production cross section is present. The used singal Monte Carlo is reported in section 6.2 while a a list of the considered simulated background is skipped. The complete list is reported in this appendix in section D.1. In addition there is supporting material for section 6.5 of chapter 6. While in the main text an alternative method to determine the fake factors and therefore the background of the signal signature is present, the details given in section D.2 of this appendix report the corresponding results obtained from the Z-tagged sample which is the approach eventually used for the cross section calculation.

D.1. List of considered background samples

The following tables report all considered background samples. The list of simulated samples including at least one top quark or a dijet final state is given in table D.1. In table D.2 the simulated samples for single Z boson production and its subsequent decay into two charged leptons plus additional partons is reported. The simulated background due to diboson production can be found in table D.3. Table D.4 finally holds the used list of Monte Carlo sample with single W boson and additional partons production followed by a leptonic decay of the W boson. All the tables report the Monte Carlo sample identifier (MCID), the simulated process and the used generator. If the used generator only provides leading-order calculation the given k-factors are used to scale the samples to next-to-leading-order. The filter efficiency on generator level and the cross section of the process are presented in the last two rows of each table.

MCID	Process	Generator	events	k-factor	ϵ_{filter}	cross section [pb]
105200	$t\bar{t}$	MC@NLO	14983835	1.0	0.55551	164.57
117360	t-channel$\rightarrow e$	MC@NLO	994897	1.0	1.0	6.94
117361	t-channel$\rightarrow \mu$	MC@NLO	999295	1.0	1.0	6.83
117362	t-channel$\rightarrow \tau$	MC@NLO	999948	1.0	1.0	7.26
117363	s-channel$\rightarrow e$	MC@NLO	199899	1.0	1.0	0.498
117364	s-channel$\rightarrow \mu$	MC@NLO	199850	1.0	1.0	0.498
117365	s-channel$\rightarrow \tau$	MC@NLO	190000	1.0	1.0	0.498
105500	Wt	MC@NLO	994897	1.0	1.0	15.74
105757	$bb/cc \rightarrow \mu10\mu10X$	PythiaB	296599	1.0	1.0	2830.3
105758	$bb/cc \rightarrow \mu10e10X$	PythiaB	795695	1.0	1.0	4017.1
105759	$bb/cc \rightarrow e10e10X$	PythiaB	2920985	1.0	1.0	1693.0

Table D.1.: Monte Carlo samples modeling top quark production (including $t\bar{t}$ and single top) and dijet backgrounds.

MCID	Process	Generator	events	k-factor	$\epsilon_{\mathrm{filter}}$	cross section [pb]
107650	$Z \rightarrow ee + 0$ partons	Alpgen/Jimmy	6368284	1.25	1.0	668.32
107651	$Z \rightarrow ee + 1$ parton	Alpgen/Jimmy	1334897	1.25	1.0	134.36
107652	$Z \rightarrow ee + 2$ partons	Alpgen/Jimmy	809999	1.25	1.0	40.54
107653	$Z \rightarrow ee + 3$ partons	Alpgen/Jimmy	220000	1.25	1.0	11.16
107654	$Z \rightarrow ee + 4$ partons	Alpgen/Jimmy	60000	1.25	1.0	2.88
107655	$Z \rightarrow ee + 5$ partons	Alpgen/Jimmy	20000	1.25	1.0	0.83
107660	$Z \rightarrow \mu\mu + 0$ partons	Alpgen/Jimmy	6615230	1.25	1.0	668.68
107661	$Z \rightarrow \mu\mu + 1$ parton	Alpgen/Jimmy	1334296	1.25	1.0	134.14
107662	$Z \rightarrow \mu\mu + 2$ partons	Alpgen/Jimmy	404947	1.25	1.0	40.33
107663	$Z \rightarrow \mu\mu + 3$ partons	Alpgen/Jimmy	110000	1.25	1.0	11.19
107664	$Z \rightarrow \mu\mu + 4$ partons	Alpgen/Jimmy	30000	1.25	1.0	2.75
107665	$Z \rightarrow \mu\mu + 5$ partons	Alpgen/Jimmy	10000	1.25	1.0	0.77
107670	$Z \rightarrow \tau\tau + 0$ partons	Alpgen/Jimmy	10613179	1.25	1.0	668.40
107671	$Z \rightarrow \tau\tau + 1$ parton	Alpgen/Jimmy	1999491	1.25	1.0	134.81
107672	$Z \rightarrow \tau\tau + 2$ partons	Alpgen/Jimmy	404950	1.25	1.0	40.36
107673	$Z \rightarrow \tau\tau + 3$ partons	Alpgen/Jimmy	509847	1.25	1.0	11.25
107674	$Z \rightarrow \tau\tau + 4$ partons	Alpgen/Jimmy	29999	1.25	1.0	2.79
107675	$Z \rightarrow \tau\tau + 5$ partons	Alpgen/Jimmy	45000	1.25	1.0	0.77

Drell-Yan samples with $10 < m_{\ell\ell} < 40$ GeV and 20 GeV $< p_{\mathrm{T}}$ for the leading lepton

MCID	Process	Generator	events	k-factor	$\epsilon_{\mathrm{filter}}$	cross section [pb]
116250	$Z \rightarrow ee + 0$ partons	Alpgen/Jimmy	994949	1.22	1.0	3051.6
116251	$Z \rightarrow ee + 1$ parton	Alpgen/Jimmy	299998	1.22	1.0	87.87
116252	$Z \rightarrow ee + 2$ partons	Alpgen/Jimmy	499997	1.22	1.0	41.40
116253	$Z \rightarrow ee + 3$ partons	Alpgen/Jimmy	149998	1.22	1.0	8.38
116254	$Z \rightarrow ee + 4$ partons	Alpgen/Jimmy	40000	1.22	1.0	1.85
116255	$Z \rightarrow ee + 5$ partons	Alpgen/Jimmy	10000	1.22	1.0	0.46
116260	$Z \rightarrow \mu\mu + 0$ partons	Alpgen/Jimmy	999849	1.22	1.0	3051.6
116261	$Z \rightarrow \mu\mu + 1$ parton	Alpgen/Jimmy	300000	1.22	1.0	84.87
116262	$Z \rightarrow \mu\mu + 2$ partons	Alpgen/Jimmy	999994	1.22	1.0	41.45
116263	$Z \rightarrow \mu\mu + 3$ partons	Alpgen/Jimmy	150000	1.22	1.0	8.38
116264	$Z \rightarrow \mu\mu + 4$ partons	Alpgen/Jimmy	39999	1.22	1.0	1.85
116265	$Z \rightarrow \mu\mu + 5$ partons	Alpgen/Jimmy	10000	1.22	1.0	0.46
116270	$Z \rightarrow \tau\tau + 0$ partons	Alpgen/Jimmy	999649	1.22	1.0	3055.1
116271	$Z \rightarrow \tau\tau + 1$ parton	Alpgen/Jimmy	299999	1.22	1.0	84.93
116272	$Z \rightarrow \tau\tau + 2$ partons	Alpgen/Jimmy	498899	1.22	1.0	41.47
116273	$Z \rightarrow \tau\tau + 3$ partons	Alpgen/Jimmy	150000	1.22	1.0	8.36
116274	$Z \rightarrow \tau\tau + 4$ partons	Alpgen/Jimmy	39999	1.22	1.0	1.85
116275	$Z \rightarrow \tau\tau + 5$ partons	Alpgen/Jimmy	10000	1.22	1.0	0.46

Table D.2.: Monte Carlo samples of single Z boson and possible additional parton production with a subsequent decay of the Z boson into charged leptons. The Drell-Yan production is listed as well.

MCID	Process	Generator	events	k-factor	ϵ_{filter}	cross section [pb]
105985	WW	Herwig	50000	1.52	0.38863	29.592
105986	ZZ	Herwig	50000	1.41	0.21152	4.6
105987	WZ	Herwig	50000	1.58	1.0	3.432
117410	$\gamma W + 0$ partons	Alpgen	210000	1.432	1.0	213.06
117411	$\gamma W + 1$ partons	Alpgen	265000	1.432	1.0	52.199
117412	$\gamma W + 2$ partons	Alpgen	175000	1.432	1.0	17.259
117413	$\gamma W + 3$ partons	Alpgen	264999	1.432	1.0	5.3361
117414	$\gamma W + 4$ partons	Alpgen	64999	1.432	1.0	1.3762
117415	$\gamma W + 5$ partons	Alpgen	20000	1.432	1.0	0.3382
128850	$\gamma^* W(\ell\nu ee)$	Pythia,MadGraph	294999	1.0	1.0	4.80130
128851	$\gamma^* W(\ell\nu\mu\mu)$	Pythia,MadGraph	149900	1.0	1.0	1.45360
128852	$\gamma^* W(\ell\nu\tau\tau)$	Pythia,MadGraph	50000	1.0	1.0	0.21330
108323	$\gamma Z(ee)$	Pythia,MadGraph	50000	1.41	1.0	9.63
108324	$\gamma Z(\mu\mu)$	Pythia,MadGraph	50000	1.41	1.0	9.63
108325	$\gamma Z(\tau\tau)$	Pythia,MadGraph	50000	1.41	0.15	9.41
105940	$W^+Z \to \ell\nu qq$	MC@NLO	25000	1.0	1.0	1.6889
105941	$W^+Z \to \ell\nu\ell\ell$	MC@NLO	25000	1.0	1.0	0.15924
105942	$W^+Z \to qq\ell\ell$	MC@NLO	24950	1.0	1.0	0.49836
106024	$W^+Z \to \tau\nu\ell\ell$	MC@NLO	25000	1.0	1.0	0.07962
106025	$W^+Z \to \ell\nu\tau\tau$	MC@NLO	25000	1.0	1.0	0.07962
106026	$W^+Z \to \tau\nu\tau\tau$	MC@NLO	24950	1.0	1.0	0.03981
106027	$W^-Z \to \tau\nu\ell\ell$	MC@NLO	25000	1.0	1.0	0.04302
106028	$W^-Z \to \ell\nu\tau\tau$	MC@NLO	25000	1.0	1.0	0.04302
106029	$W^-Z \to \tau\nu\tau\tau$	MC@NLO	25000	1.0	1.0	0.02151
105970	$W^-Z \to \ell\nu qq$	MC@NLO	25000	1.0	1.0	0.91264
105971	$W^-Z \to \ell\nu\ell\ell$	MC@NLO	100000	1.0	1.0	0.08605
105972	$W^-Z \to qq\ell\ell$	MC@NLO	100000	1.0	1.0	0.2693
113190	$W^+Z \to qq\tau\tau$	MC@NLO	25000	1.0	1.0	0.24918
113191	$W^-Z \to qq\tau\tau$	MC@NLO	25000	1.0	1.0	0.13465
105921	$qq \to W^+W^- \to ee\nu\nu$	MC@NLO	199949	1.0	1.0	0.503
105922	$qq \to W^+W^- \to e\mu\nu\nu$	MC@NLO	200000	1.0	1.0	0.503
105923	$qq \to W^+W^- \to e\tau\nu\nu$	MC@NLO	200000	1.0	1.0	0.503
105924	$qq \to W^+W^- \to \mu\mu\nu\nu$	MC@NLO	199000	1.0	1.0	0.503
105925	$qq \to W^+W^- \to \mu e\nu\nu$	MC@NLO	199949	1.0	1.0	0.503
105926	$qq \to W^+W^- \to \mu\tau\nu\nu$	MC@NLO	200000	1.0	1.0	0.503
105927	$qq \to W^+W^- \to \tau\tau\nu\nu$	MC@NLO	199678	1.0	1.0	0.503
105928	$qq \to W^+W^- \to \tau e\nu\nu$	MC@NLO	199950	1.0	1.0	0.503
105929	$qq \to W^+W^- \to \tau\mu\nu\nu$	MC@NLO	200000	1.0	1.0	0.503
106011	$gg \to W^+W^- \to ee\nu\nu$	gg2ww	10000	1.0	0.99	0.0145
106012	$gg \to W^+W^- \to e\mu\nu\nu$	gg2ww	10000	1.0	0.99	0.0145
106013	$gg \to W^+W^- \to e\tau\nu\nu$	gg2ww	10000	1.0	0.92	0.0145
106014	$gg \to W^+W^- \to \mu\mu\nu\nu$	gg2ww	9999	1.0	0.99	0.0145
106015	$gg \to W^+W^- \to \mu e\nu\nu$	gg2ww	10000	1.0	0.99	0.0145
106016	$gg \to W^+W^- \to \mu\tau\nu\nu$	gg2ww	10000	1.0	0.93	0.0145
106017	$gg \to W^+W^- \to \tau\tau\nu\nu$	gg2ww	10000	1.0	0.33	0.0145
106018	$gg \to W^+W^- \to \tau e\nu\nu$	gg2ww	10000	1.0	0.92	0.0145
106019	$gg \to W^+W^- \to \tau\mu\nu\nu$	gg2ww	10000	1.0	0.93	0.0145

Table D.3.: Simulated background from diboson production including WW, $W\gamma$ and $Z\gamma$.

MCID	Process	Generator	events	k-factor	ϵ_{filter}	cross section [pb]
107680	$W \to e\nu + 0$ partons	ALPGEN/JIMMY	3358884	1.2	1.0	6921.6
107681	$W \to e\nu + 1$ parton	ALPGEN/JIMMY	2499645	1.2	1.0	1304.3
107682	$W \to e\nu + 2$ partons	ALPGEN/JIMMY	3768632	1.2	1.0	378.29
107683	$W \to e\nu + 3$ partons	ALPGEN/JIMMY	1008947	1.2	1.0	101.43
107684	$W \to e\nu + 4$ partons	ALPGEN/JIMMY	250000	1.2	1.0	25.87
107685	$W \to e\nu + 5$ partons	ALPGEN/JIMMY	69999	1.2	1.0	7.0
107690	$W \to \mu\nu + 0$ partons	ALPGEN/JIMMY	3462942	1.2	1.0	6919.6
107691	$W \to \mu\nu + 1$ parton	ALPGEN/JIMMY	2498593	1.2	1.0	1304.2
107692	$W \to \mu\nu + 2$ partons	ALPGEN/JIMMY	3768737	1.2	1.0	377.83
107693	$W \to \mu\nu + 3$ partons	ALPGEN/JIMMY	1008446	1.2	1.0	101.88
107694	$W \to \mu\nu + 4$ partons	ALPGEN/JIMMY	254950	1.2	1.0	25.75
107695	$W \to \mu\nu + 5$ partons	ALPGEN/JIMMY	70000	1.2	1.0	6.92
107700	$W \to \tau\nu + 0$ partons	ALPGEN/JIMMY	3418296	1.2	1.0	6918.6
107701	$W \to \tau\nu + 1$ parton	ALPGEN/JIMMY	2499194	1.2	1.0	1303.2
107702	$W \to \tau\nu + 2$ partons	ALPGEN/JIMMY	3750986	1.2	1.0	378.18
107703	$W \to \tau\nu + 3$ partons	ALPGEN/JIMMY	1009946	1.2	1.0	101.51
107704	$W \to \tau\nu + 4$ partons	ALPGEN/JIMMY	249998	1.2	1.0	25.64
107705	$W \to \tau\nu + 5$ partons	ALPGEN/JIMMY	65000	1.2	1.0	7.04

Table D.4.: Monte Carlo samples of single $W^{\pm}$boson and possible additional parton production with a subsequent leptonic decay of the $W^{\pm}$boson.

D.2. Fake factors derived from the Z-tagged sample

The approach to determine the number of background events of the four charged lepton signature origination from ZZ production and subsequent decay of both Z bosons into charged leptons is reported in section 6.5 of chapter 6. The results presented in the main text are based on fake factors derived from an inclusive sample. In this section the corresponding fake factors from the Z-tagged sample are given. All important details are explained in section 6.5. The fake factors for electrons are shown in figure D.1 while the ones for muons are displayed in figure D.2. In both figures the fake factors derived from data and simulation (labeled as “Z+jets”) are presented while the signal contamination by WZ and ZZ events is already subtracted. The difference of the fake factors from data and simulation are finally used to estimate the systematic uncertainty.

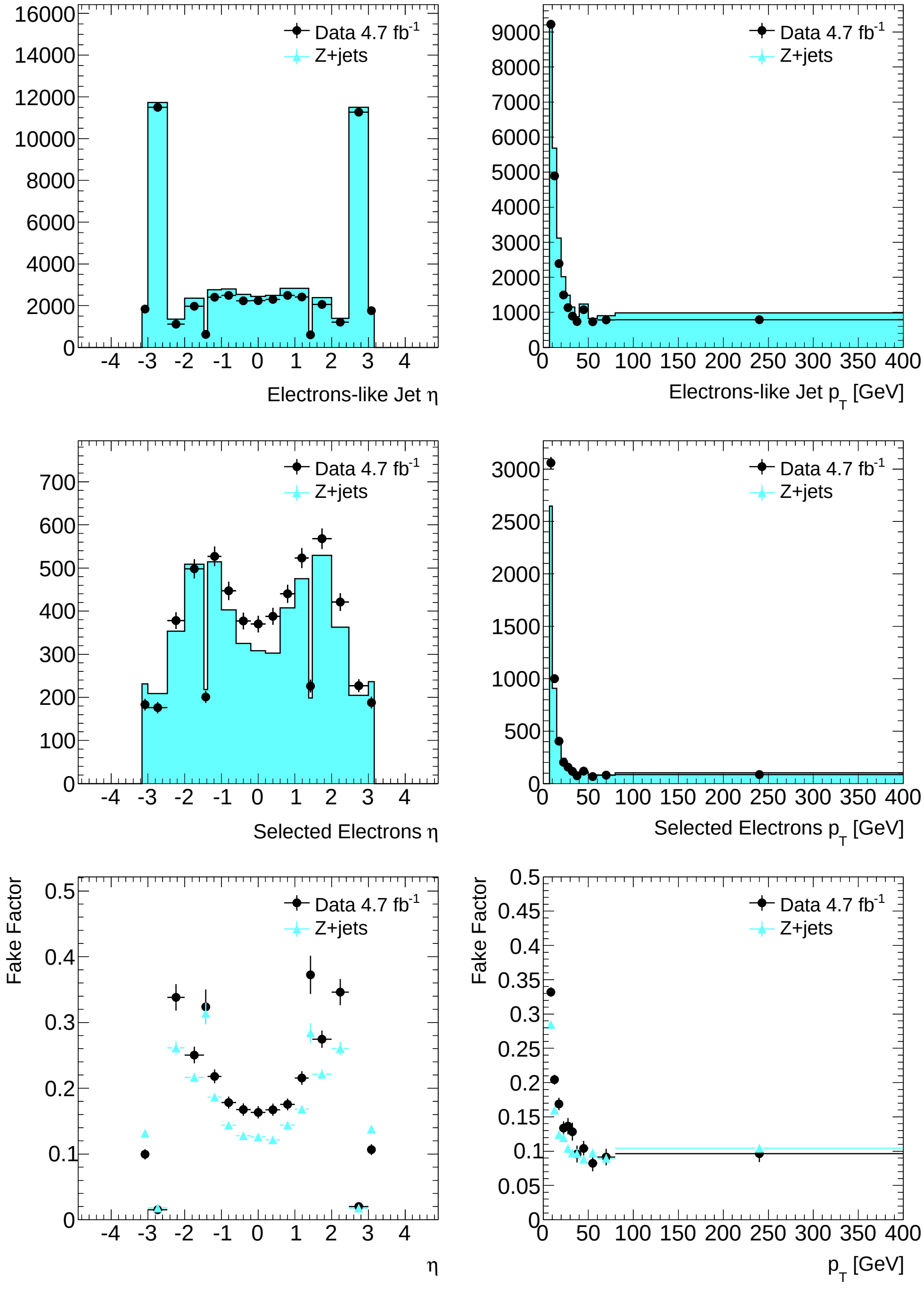

Figure D.1.: The first row shows the number of electron-like jets found in data as well as in $Z+$ jets simulation. For both the signal contamination is estimated by ZZ and WZ Monte Carlo and already subtracted. In the second row the equivalent is shown for selected electrons. The last row shows the fake factors FF which are calculated as the ratio of row one and two. On the left the object counts are shown as a function of the pseudorapidity while on the right they are present as a function of the transverse momentum. These displayed distributions are based on the Z-tagged sample. The corresponding plots produced with the inclusive sample are available in figure 6.10 of section 6.5.

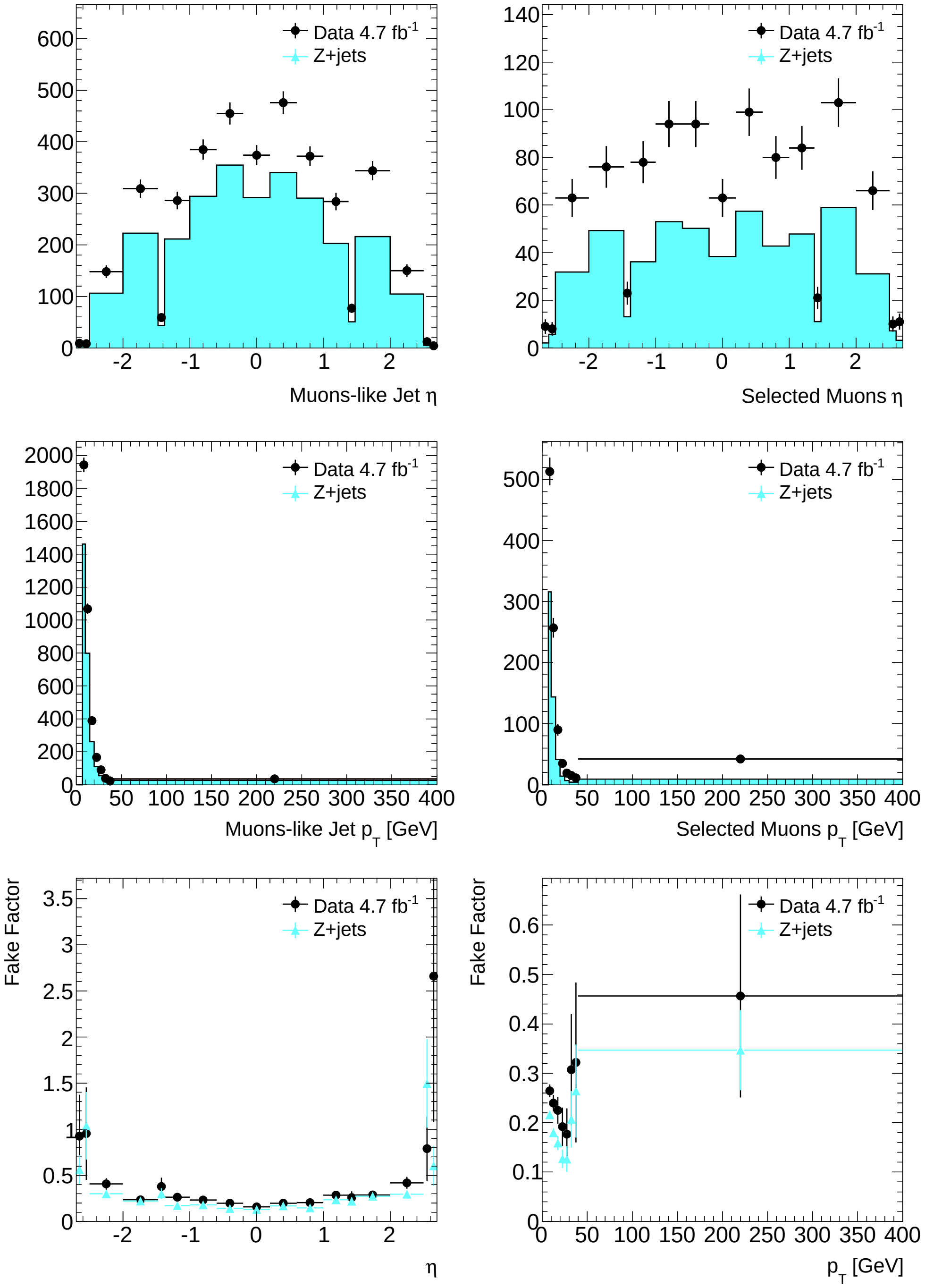

Figure D.2.: The first row shows the number of muon-like jets found in data as well as in $Z+$ jets simulation. For both the signal contamination is estimated by ZZ and WZ Monte Carlo and already subtracted. In the second row the equivalent is shown for selected muons. The last row shows the fake factors FF which are calculated as the ratio of row one and two. On the left the object counts are shown as a function of the pseudorapidity while on the right they are present as a function of the transverse momentum. These displayed distributions are based on the Z-tagged sample. The corresponding plots produced with the inclusive sample are available in figure 6.12 of section 6.5.

List of Figures

Bibliography

[1] F. Hasert, H. Faissner, W. Krenz, J. Von Krogh, D. Lanske, et al., *Search for elastic muon-neutrino electron scattering*, *Phys.Lett.* **B46** (1973) 121–124, [`doi: 10.1016/0370-2693(73)90494-2`].

Gargamelle Neutrino Collaboration, *Observation of neutrino like interactions without muon or electron in the Gargamelle neutrino experiment*, *Phys.Lett.* **B46** (1973) 138–140, [`doi: 10.1016/0370-2693(73)90499-1`].

[2] A. Benvenuti and e. al., *Observation of muonless neutrino induced inelastic interactions*, *Phys.Rev.Lett.* **32** (1974) 800–803, [`doi: 10.1103/PhysRevLett.32.800`].

[3] K. Nishijima, *Charge independence theory of V-particles*, *Prog.Theor.Phys.* **13** (1955) 285–304, [`doi: 10.1143/PTP.13.285`].

T. Nakano and K. Nishijima, *Charge independence for V-particles*, *Prog.Theor.Phys.* **10** (1953) 581–582, [`doi: 10.1103/PhysRev.108.1611`].

M. Gell-Mann, *The interpretation of the new particles as displaced charge multiplets*, *Il Nuovo Cimento (1955-1965)* **4** (1956) 848–866, [`doi: 10.1007/BF02748000`].

[4] B. Rossi and D. B. Hall, *Variation of the rate of decay of mesotrons with momentum*, *Phys.Rev.* **59** (1941) 223–228, [`doi: 10.1103/PhysRev.59.223`].

N. Nereson and B. Rossi, *Further measurements on the disintegration curve of mesotrons*, *Phys.Rev.* **64** (1943) 199–201, [`doi: 10.1103/PhysRev.64.199`].

B. Rossi and N. Nereson, *Experimental determination of the disintegration curve of mesotrons*, *Phys. Rev.* **62** (1942) 417–422, [`doi: 10.1103/PhysRev.62.417`].

B. Rossi, K. Greisen, J. C. Stearns, D. K. Froman, and P. G. Koontz, *Further measurements of the mesotron lifetime*, *Phys. Rev.* **61** (1942) 675–679, [`doi: 10.1103/PhysRev.61.675`].

[5] E. Fermi, *An attempt of a theory of beta radiation. 1.*, *Z.Phys.* **88** (1934) 161–177, [`doi: 10.1007/BF01351864`].

E. Fermi, *Trends to a theory of beta radiation*, *Nuovo Cim.* **11** (1934) 1–19, [`doi: 10.1007/BF02959820`].

[6] J. S. Schwinger, *A theory of the fundamental interactions*, *Annals Phys.* **2** (1957) 407–434, [`doi: 10.1016/0003-4916(57)90015-5`].

T. Lee and C.-N. Yang, *Possible nonlocal effects in mu decay*, *Phys.Rev.* **108** (1957) 1611–1614, [`doi: 10.1103/PhysRev.108.1611`].

[7] UA1 Collaboration, *Experimental observation of isolated large transverse energy electrons with associated missing energy at* $\sqrt{s} = 540\text{-}GeV$, *Phys.Lett.* **B122** (1983) 103–116, [`doi: 10.1016/0370-2693(83)91177-2`].

[8] UA2 Collaboration, *Observation of single isolated electrons of high transverse momentum in events with missing transverse energy at the CERN $\bar{p}p$ collider*, *Phys.Lett.* **B122** (1983) 476–485, [`doi: 10.1016/0370-2693(83)91605-2`].

[9] MuLan Collaboration, *Improved measurement of the positive muon lifetime and determination of the Fermi constant*, *Phys.Rev.Lett.* **99** (2007) 032001, [`arXiv:0704.1981`], [`doi: 10.1103/PhysRevLett.99.032001`].

[10] S. Weinberg, *A model of leptons*, *Phys.Rev.Lett.* **19** (1967) 1264–1266, [`doi: 10.1103/PhysRevLett.19.1264`].

[11] UA1 Collaboration, *Experimental observation of lepton pairs of invariant mass around 95-GeV/c^2 at the CERN SPS collider*, *Phys.Lett.* **B126** (1983) 398–410, [`doi: 10.1016/0370-2693(83)90188-0`].

[12] UA2 Collaboration, *Evidence for $Z^0 \to e^+e^-$ at the CERN $\bar{p}p$ collider*, *Phys.Lett.* **B129** (1983) 130–140, [`doi: 10.1016/0370-2693(83)90744-X`].

[13] The LEP Electroweak Working Group, *Summary results and updates*, *`http://lepewwg.web.cern.ch/LEPEWWG`*.

[14] J. Beringer et al. (Particle Data Group), *The review of particle physics*, *Phys.Rev.D* **86** (2012) 010001.

[15] B. Pontecorvo, *Mesonium and anti-mesonium*, *Sov.Phys.JETP* **6** (1957) 429.

Z. Maki, M. Nakagawa, and S. Sakata, *Remarks on the unified model of elementary particles*, *Prog.Theor.Phys.* **28** (1962) 870–880, [`doi: 10.1143/PTP.28.870`].

[16] N. Cabibbo, *Unitary symmetry and leptonic decays*, *Phys.Rev.Lett.* **10** (1963) 531–533, [`doi: 10.1103/PhysRevLett.10.531`].

M. Kobayashi and T. Maskawa, *CP violation in the renormalizable theory of weak interaction*, *Prog.Theor.Phys.* **49** (1973) 652–657, [`doi: 10.1143/PTP.49.652`].

[17] R. Alkofer and J. Greensite, *Quark confinement: The hard problem of hadron physics*, *J.Phys.G* **G34** (2007) S3, [`hep-ph/0610365`], [`doi: 10.1088/0954-3899/34/7/S02`].

[18] J. Goldstone, *Field theories with superconductor solutions*, *Nuovo Cim.* **19** (1961) 154–164, [`doi: 10.1007/BF02812722`].

Y. Nambu, *Axial vector current conservation in weak interactions*, *Phys.Rev.Lett.* **4** (1960) 380–382, [`doi: 10.1103/PhysRevLett.4.380`].

[19] P. W. Higgs, *Broken symmetries, massless particles and gauge fields*, *Phys.Lett.* **12** (1964) 132–133, [`doi: 10.1016/0031-9163(64)91136-9`].

F. Englert and R. Brout, *Broken symmetry and the mass of gauge vector mesons*, *Phys.Rev.Lett.* **13** (1964) 321–323, [`doi: 10.1103/PhysRevLett.13.321`].

G. Guralnik, C. Hagen, and T. Kibble, *Global conservation laws and massless particles*, *Phys.Rev.Lett.* **13** (1964) 585–587, [`doi: 10.1103/PhysRevLett.13.585`].

[20] P. J. Mohr, B. N. Taylor, and D. B. Newell, *CODATA recommended values of the fundamental physical constants: 2006*, *Rev.Mod.Phys.* **80** (2008) 633–730, [`arXiv:0801.0028`], [`doi: 10.1103//RevModPhys.80.633`]. for updates see http://physics.nist.gov/cuu/Constants/.

[21] W. Heisenberg, *Die beobachtbaren Größen in der Theorie der Elementarteilchen III*, *Zeitschrift für Physik A Hadrons and Nuclei* **123** (1943) 93–112, [`doi: 10.1007/BF01375146`].

W. Heisenberg, *Die beobachtbaren Größen in der Theorie der Elementarteilchen II*, *Zeitschrift für Physik A Hadrons and Nuclei* **120** (1943) 673–702, [`doi: 10.1007/BF01336936`].

W. Heisenberg, *Die beobachtbaren Größen in der Theorie der Elementarteilchen*, *Zeitschrift für Physik A Hadrons and Nuclei* **120** (1943) 513–538, [`doi: 10.1007/BF01329800`].

[22] R. Feynman, *Space - time approach to quantum electrodynamics*, *Phys.Rev.* **76** (1949) 769–789, [`doi: 10.1103/PhysRev.76.769`].

[23] O. Nachtmann, *Elementary particle physics: Concepts and phenomena*, . Berlin, Germany: Springer (1990) 559 p.

M. E. Peskin and D. V. Schroeder, *An introduction to quantum field theory*, . Reading, USA: Addison-Wesley (1995) 842 p.

F. Mandl and G. Shaw, *Quantum field theory*, . Chichester, UK: Wiley (1984) 354 p.

C. Itzykson and J. Zuber, *Quantum field theory*, . New York, Usa: Mcgraw-hill (1980) 705 p.

[24] The LEP/Tevatron Electroweak Working Group, *Plots for summer **2011***, *http://lepewwg.web.cern.ch/LEPEWWG.*

[25] S. Dittmaier, C. Mariotti, G. Passarino, R. Tanaka, et al., *Handbook of LHC Higgs cross sections: 2. differential distributions*, `arXiv:1201.3084`.

[26] J. Schechter and J. Valle, *Neutrino masses in SU(2) x U(1) theories*, *Phys.Rev.* **D22** (1980) 2227, [`doi: 10.1103/PhysRevD.22.2227`].

R. N. Mohapatra and G. Senjanovic, *Neutrino mass and spontaneous parity violation*, *Phys.Rev.Lett.* **44** (1980) 912, [`doi: 10.1103/PhysRevLett.44.912`].

T. Yanagida, *Horizontal symmetry and masses of neutrinos*, *Prog.Theor.Phys.* **64** (1980) 1103.

[27] WMAP Collaboration, *Seven-Year Wilkinson microwave anisotropy probe (WMAP) observations: Cosmological interpretation*, *Astrophys.J.Suppl.* **192** (2011) 18, [`arXiv:1001.4538`], [`doi: 10.1088/0067-0049/192/2/18`].

[28] A. Buras, J. R. Ellis, M. Gaillard, and D. V. Nanopoulos, *Aspects of the grand unification of strong, weak and electromagnetic interactions*, *Nucl.Phys.* **B135** (1978) 66–92, [`doi: 10.1016/0550-3213(78)90214-6`].

[29] U. Amaldi, W. de Boer, and H. Furstenau, *Comparison of grand unified theories with electroweak and strong coupling constants measured at LEP*, *Phys. Lett.* **B260** (1991) 447–455, [`doi: 10.1016/0370-2693(91)91641-8`].

[30] Belgium, Denmark, France, Greece, Italy, Netherlands, Norway, Sweden, Switzerland, United-Kingdom, Western Germany, Yugoslavia, *Convention for the establishment of a european organization for nuclear research*, *http://council.web.cern.ch/council/en/governance/Convention.html.*

[31] O. S. Bruning, P. Collier, P. Lebrun, S. Myers, R. Ostojic, et al., *LHC design report. 1. The LHC main ring*, *CERN-2004-003-V-1, CERN-2004-003* (2004).

O. Buning, P. Collier, P. Lebrun, S. Myers, R. Ostojic, et al., *LHC design report. 2. The LHC infrastructure and general services*, *CERN-2004-003-V-2, CERN-2004-003* (2004).

[32] M. Benedikt, P. Collier, V. Mertens, J. Poole, and K. Schindl, *LHC design report. 3. The LHC injector chain*, *CERN-2004-003-V-3, CERN-2004-003* (2004).

[33] J.-L. Caron, *The LHC injection complex. L'ensemble d'injection du LHC*, *AC Collection. Legacy of AC. Pictures from 1992 to 2002.* (1993).

[34] L. Evans and P. Bryant, *LHC Machine*, *JINST* **3** (2008) S08001, [`doi: 10.1088/1748-0221/3/08/S08001`].

[35] ATLAS Collaboration, *ATLAS luminosity public results*, *http://twiki.cern.ch/twiki/bin/view/AtlasPublic/LuminosityPublicResults* (2012).

[36] Fermilab, *Interactive timeline*, *http://www.fnal.gov/pub/tevatron/milestones/interactive-timeline.html*.

[37] A. Martin, W. Stirling, R. Thorne, and G. Watt, *Parton distributions for the LHC*, *Eur.Phys.J.* **C63** (2009) 189–285, [`arXiv:0901.0002`], [`doi: 10.1140/epjc/s10052-009-1072-5`].

[38] D0 Collaboration, *Measurement of the ZZ production cross section in $p\bar{p}$ collisions at $\sqrt{s} = 1.96$ TeV*, *Phys.Rev.* **D84** (2011) 011103, [`arXiv:1104.3078`], [`doi: 10.1103/PhysRevD.84.011103`].

[39] CDF Collaboration, *First measurement of ZZ production in $p\bar{p}$ collisions at $\sqrt{s} = 1.96$-TeV*, *Phys.Rev.Lett.* **100** (2008) 201801, [`arXiv:0801.4806`], [`doi: 10.1103/PhysRevLett.100.201801`].

[40] ATLAS Collaboration, *Measurement of ZZ production in pp collisions at $\sqrt{s} = 7$ TeV and limits on anomalous ZZZ and ZZγ couplings with the ATLAS detector*, `arXiv:1211.6096`. submitted to JHEP.

[41] ATLAS Collaboration, *Measurement of the total ZZ production cross section in the four-lepton channel using 5.8 fb^{-1} of ATLAS data at $\sqrt{s} = 8$ TeV*, *ATLAS-CONF-2012-090* (2012).

[42] CMS Collaboration, *Measurement of the ZZ production cross section and search for anomalous couplings in $2\ell 2\ell'$ final states in pp collisions at $\sqrt{s} = 7$ TeV*, `arXiv:1211.4890`. submitted to JHEP.

[43] CMS Collaboration, *Measurement of ZZ production cross section in ZZ to $2\ell 2\ell'$ decay channel in pp collisions at $\sqrt{s} = 8$ TeV*, *CMS-PAS-SMP-12-014* (2012).

[44] LHCb Collaboration, *The LHCb Detector at the LHC*, *JINST* **3** (2008) S08005, [`doi: 10.1088/1748-0221/3/08/S08005`].

[45] ALICE Collaboration, *The ALICE experiment at the CERN LHC*, *JINST* **3** (2008) S08002, [`doi: 10.1088/1748-0221/3/08/S08002`].

[46] ATLAS Collaboration, *The ATLAS Experiment at the CERN Large Hadron Collider*, *JINST* **3** (2008) S08003, [`doi: 10.1088/1748-0221/3/08/S08003`].

[47] CMS Collaboration, *The CMS experiment at the CERN LHC*, *JINST* **3** (2008) S08004, [`doi: 10.1088/1748-0221/3/08/S08004`].

[48] ATLAS Collaboration, *ATLAS physics summary plots*, *`http://twiki.cern.ch/twiki/bin/view/AtlasPublic/CombinedSummaryPlots`* (2012). Status of figure: 30 Jun 2012 (ICHEP).

[49] J. Pequenao, *Computer generated image of the whole ATLAS detector*, *`http://cdsweb.cern.ch/record/1095924/`* (2008).

[50] ATLAS Collaboration, *ATLAS inner detector: Technical design report. Vol. 1*, *CERN-LHCC-97-16, ATLAS-TDR-4* (1997).

ATLAS Collaboration, *ATLAS inner detector: Technical design report. Vol. 2*, *CERN-LHCC-97-17* (1997).

[51] J. Pequenao, *Computer generated image of the ATLAS inner detector*, *`http://cdsweb.cern.ch/record/1095926`* (2008).

[52] ATLAS Collaboration, *ATLAS calorimeter performance: Technical design report*, *CERN-LHCC-96-40* (1996).

ATLAS Collaboration, *ATLAS liquid argon calorimeter: Technical design report*, *CERN-LHCC-96-41* (1996).

ATLAS Collaboration, *ATLAS tile calorimeter: Technical design report*, *CERN-LHCC-96-42* (1996).

[53] ATLAS Collaboration, *ATLAS muon spectrometer: Technical design report*, *CERN-LHCC-97-22, ATLAS-TDR-10* (1997).

[54] J. Pequenao, *Computer generated image of the ATLAS muons subsystem*, *`http://cdsweb.cern.ch/record/1095929`* (2008).

[55] K. Bachas, N. Benekos, F. Cerutti, M. Hoffmann, J. Meyer, and R. Nicolaidou, *Performance of the muon spectrometer in the high pseudo-rapidity region* $|\eta| > 2.5$, *ATL-MUON-INT-2012-002* (2012).

[56] ATLAS Collaboration, *ATLAS forward detectors for luminosity measurement and monitoring*, *CERN-LHCC-2004-010. LHCC-I-014* (2004).

[57] ATLAS Collaboration, *ATLAS forward detectors for measurement of elastic scattering and luminosity*, *CERN-LHCC-2008-004. ATLAS-TDR-018* (2008).

[58] ATLAS Collaboration, *Zero Degree Calorimeters for ATLAS*, *CERN-LHCC-2007-001. LHCC-I-016* (2007).

[59] ATLAS Collaboration, *Luminosity determination in pp collisions at* $\sqrt{s} = 7$ *TeV using the ATLAS Detector in 2011*, *ATLAS-CONF-2011-116* (2011).

[60] ATLAS Collaboration, *Luminosity determination in pp collisions at* $\sqrt{s} = 7$ *TeV using the ATLAS detector at the LHC*, *Eur.Phys.J.* **C71** (2011) 1630, [`arXiv:1101.2185`], [`doi: 10.1140/epjc/s10052-011-1630-5`].

[61] ATLAS Collaboration, *Data quality information for 2010 and 2011 data*, *http://twiki.cern.ch/twiki/bin/view/AtlasPublic/RunStatsPublicResults2010* (2012). Tables of 2011.

ATLAS Collaboration, *Approved plots ATLAS detector*, *http://twiki.cern.ch/twiki/bin/view/AtlasPublic/ApprovedPlotsATLASDetector* (2012). ATLAS Detector Status.

[62] I. Bird, K. Bos, N. Brook, D. Duellmann, C. Eck, et al., *LHC computing grid. Technical design report*, *CERN-LHCC-2005-024* (2005).

[63] ATLAS Collaboration, *ATLAS computing: Technical design report*, *CERN-LHCC-2005-022, ATLAS-TRD-017* (2005).

[64] J. Allison, K. Amako, J. Apostolakis, H. Araujo, P. Dubois, et al., *Geant4 developments and applications*, *IEEE Trans.Nucl.Sci.* **53** (2006) 270, [`doi: 10.1109/TNS.2006.869826`].

[65] ATLAS Collaboration, *The ATLAS simulation infrastructure*, *Eur.Phys.J.* **C70** (2010) 823–874, [`arXiv:1005.4568`], [`doi: 10.1140/epjc/s10052-010-1429-9`].

[66] H.-L. Lai, M. Guzzi, J. Huston, Z. Li, P. M. Nadolsky, et al., *New parton distributions for collider physics*, *Phys.Rev.* **D82** (2010) 074024, [`arXiv:1007.2241`], [`doi: 10.1103/PhysRevD.82.074024`].

[67] S. Frixione and B. R. Webber, *Matching NLO QCD computations and parton shower simulations*, *JHEP* **0206** (2002) 029, [`hep-ph/0204244`].

[68] M. L. Mangano, M. Moretti, F. Piccinini, R. Pittau, and A. D. Polosa, *ALPGEN, a generator for hard multiparton processes in hadronic collisions*, *JHEP* **0307** (2003) 001, [`hep-ph/0206293`].

[69] T. Gleisberg, S. Hoeche, F. Krauss, M. Schonherr, S. Schumann, et al., *Event generation with SHERPA 1.1*, *JHEP* **0902** (2009) 007, [`arXiv:0811.4622`], [`doi: 10.1088/1126-6708/2009/02/007`].

[70] S. Catani, F. Krauss, R. Kuhn, and B. Webber, *QCD matrix elements + parton showers*, *JHEP* **0111** (2001) 063, [`hep-ph/0109231`].

L. Lonnblad, *Correcting the color dipole cascade model with fixed order matrix elements*, *JHEP* **0205** (2002) 046, [`hep-ph/0112284`].

[71] M. L. Mangano, M. Moretti, F. Piccinini, and M. Treccani, *Matching matrix elements and shower evolution for top-quark production in hadronic collisions*, *JHEP* **0701** (2007) 013, [`hep-ph/0611129`], [`doi: 10.1088/1126-6708/2007/01/013`].

[72] S. Frixione, P. Nason, and C. Oleari, *Matching NLO QCD computations with parton shower simulations: the POWHEG method*, *JHEP* **0711** (2007) 070, [`arXiv:0709.2092`], [`doi: 10.1088/1126-6708/2007/11/070`].

P. Nason, *A new method for combining NLO QCD with shower Monte Carlo algorithms*, *JHEP* **0411** (2004) 040, [`hep-ph/0409146`], [`doi: 10.1088/1126-6708/2004/11/040`].

[73] T. Sjostrand, P. Eden, C. Friberg, L. Lonnblad, G. Miu, et al., *High-energy physics event generation with PYTHIA 6.1*, *Comput.Phys.Commun.* **135** (2001) 238–259, [`hep-ph/0010017`], [`doi: 10.1016/S0010-4655(00)00236-8`].

[74] G. Corcella, I. Knowles, G. Marchesini, S. Moretti, K. Odagiri, et al., *HERWIG 6: An Event generator for hadron emission reactions with interfering gluons (including supersymmetric processes)*, *JHEP* **0101** (2001) 010, [`hep-ph/0011363`].

[75] J. Butterworth, J. R. Forshaw, and M. Seymour, *Multiparton interactions in photoproduction at HERA*, *Z.Phys.* **C72** (1996) 637–646, [`hep-ph/9601371`], [`doi: 10.1007/s002880050286`].

[76] S. Jadach, Z. Was, R. Decker, and J. H. Kuhn, *The tau decay library TAUOLA: Version 2.4*, *Comput.Phys.Commun.* **76** (1993) 361–380, [`doi: 10.1016/0010-4655(93)90061-G`].

[77] P. Golonka and Z. Was, *PHOTOS Monte Carlo: A Precision tool for QED corrections in Z and W decays*, *Eur.Phys.J.* **C45** (2006) 97–107, [`hep-ph/0506026`], [`doi: 10.1140/epjc/s2005-02396-4`].

[78] G. Battistoni, S. Muraro, P. R. Sala, F. Cerutti, A. Ferrari, et al., *The FLUKA code: Description and benchmarking*, *AIP Conf.Proc.* **896** (2007) 31–49, [`doi: 10.1063/1.2720455`].

A. Ferrari, P. R. Sala, A. Fasso, and J. Ranft, *FLUKA: A multi-particle transport code (program version 2005)*, *CERN-2005-010, SLAC-R-773, INFN-TC-05-11* (2005).

[79] N. Amelin, E. Staubo, L. Csernai, V. Toneev, K. Gudima, et al., *Transverse flow and collectivity in ultrarelativistic heavy ion collisions*, *Phys.Rev.Lett.* **67** (1991) 1523–1526, [`doi: 10.1103/PhysRevLett.67.1523`].

L. Bravina, *Scaling violation of transverse flow in heavy ion collisions at AGS energies*, *Phys.Lett.* **B344** (1995) 49–54, [`doi: 10.1016/0370-2693(94)01560-Y`].

V. Lara and J. Wellisch, *Pre-equilibrium and equilibrium decays in Geant4*, *Proceedings of the CHEP 2000 conference* (2000) 52–55.

G. Folger and J. Wellisch, *String parton models in Geant4*, *eConf* **C0303241** (2003) MOMT007, [`nucl-th/0306007`].

[80] B. Andersson, G. Gustafson, and B. Nilsson-Almqvist, *A model for low p(t) hadronic reactions, with generalizations to hadron-nucleus and nucleus-nucleus collisions*, *Nucl.Phys.* **B281** (1987) 289, [`doi: 10.1016/0550-3213(87)90257-4`].

B. Nilsson-Almqvist and E. Stenlund, *Interactions between hadrons and nuclei: The Lund Monte Carlo, Fritiof Version 1.6*, *Comput.Phys.Commun.* **43** (1987) 387, [`doi: 10.1016/0010-4655(87)90056-7`].

[81] A. Heikkinen, N. Stepanov, and J. P. Wellisch, *Bertini intranuclear cascade implementation in Geant4*, *eConf* **C0303241** (2003) MOMT008, [`nucl-th/0306008`].

M. Guthrie, R. Alsmiller, and H. Bertini, *Calculation of the capture of negative pions in light elements and comparison with experiments pertaining to cancer radiotherapy*, *Nucl.Instrum.Meth.* **66** (1968) 29–36, [`doi: 10.1016/0029-554X(68)90054-2`].

[82] A. Rimoldi, A. Dell'Acqua, M. Gallas, A. Nairz, J. Boudreau, V. Tsulaia, and D. Costanzo, *The simulation of the ATLAS Experiment: Present status and outlook*, *ATL-SOFT-2004-004. ATL-COM-SOFT-2004-006. CERN-ATL-COM-SOFT-2004-006* (2004).

J. Boudreau and V. Tsulaia, *The GeoModel toolkit for detector description*, *Proceedings of the CHEP 2004 conference* (2005) 353–356.

[83] T. H. Kittelmann, V. Tsulaia, J. Boudreau, and E. Moyse, *The virtual point 1 event display for the ATLAS experiment*, *J.Phys.Conf.Ser.* **219** (2010) 032012, [`doi: 10.1088/1742-6596/219/3/032012`].

[84] L. Chevalier, *AMDB_SIMREC: A structured data base for the ATLAS spectrometer simulation program*, *ATL-MUON-97-148. ATL-M-PN-148* (1997).

[85] J. F. Laporte, L. Chevalier, C. Guyot, and M. Virchaux, *G4AGDD an AGDD based G4 application*, *ATL-SOFT-2001-002* (2001).

[86] L. Chevalier, A. Dell'Acqua, and J. Meyer, *An XML generic detector description system and geometry editor for the ATLAS detector at the LHC*, *ATL-SOFT-PROC-2012-053* (2012). accepted for the proceedings of the CHEP 2012 conference.

[87] L. Thomason, *TinyXML*, `http://www.grinninglizard.com/tinyxml/`.

[88] The Apache Software Foundation, *The Apache Xerces™ Project*, `http://xerces.apache.org/`.

[89] M. Virchaux and D. Pomarède, *The PERSINT Manual*, *ATL-SOFT-2001-003* (2001).

L. Chevalier, et al., *PERSINT event display for ATLAS: User's manual and tutorial*, *ATL-COM-SOFT-2012-156* (2012).

D. Pomarède and M. Virchaux, *The Persint visualization program for the ATLAS experiment*, *eConf* **C0303241** (2003) MOLT009, [`cs/0305057`].

[90] N. Benekos, G. Dedes, D. Rebuzzi, and M. Schott, *ATLAS muon spectrometer simulation and its validation algorithms*, *ATL-MUON-INT-2008-001. ATL-COM-MUON-2007-003* (2007).

[91] D. Rebuzzi, K. A. Assamagan, A. Di Simone, Y. Hasegawa, and N. Van Eldik, *Geant4 muon digitization in the ATHENA Framework*, *ATL-SOFT-PUB-2007-001. ATL-COM-SOFT-2007-001. CERN-ATL-COM-SOFT-2007-001* (2007).

W. Lampl, S. Laplace, M. Lechowski, D. Rousseau, H. Ma, S. Menke, and G. Unal, *Digitization of LAr calorimeter for CSC simulations*, *ATL-LARG-PUB-2007-011. ATL-COM-LARG-2007-008* (2007).

S. Gadomski, *Model of the SCT detectors and electronics for the ATLAS simulation using Geant4*, *ATL-SOFT-2001-005* (2001).

ATLAS Pixel Collaboration, *Pixel offline analysis for endcapA cosmic data*, *ATL-INDET-PUB-2008-003. ATL-COM-INDET-2007-018* (2007).

[92] A. Dell'Acqua, C. Maiani, Z. Marshall, and J. Penwell, *The simulation of cavern background in ATLAS using Geant4*, *ATL-COM-SOFT-2011-010* (2011).

[93] ATLAS Collaboration, *Expected electron performance in the ATLAS experiment*, *ATL-PHYS-PUB-2011-006* (2011).

[94] ATLAS Collaboration, *Electron performance measurements with the ATLAS detector using the 2010 LHC proton-proton collision data*, *Eur.Phys.J.* **C72** (2012) 1909, [`arXiv:1110.3174`], [`doi: 10.1140/epjc/s10052-012-1909-1`].

[95] R. Fruhwirth, *Track fitting with nonGaussian noise*, *Comput.Phys.Commun.* **100** (1997) 1–16, [`doi: 10.1016/S0010-4655(96)00155-5`].

[96] ATLAS Collaboration, *Muon momentum resolution in first pass reconstruction of pp collision data recorded by ATLAS in 2010*, *ATLAS-CONF-2011-046* (2011).

[97] S. Hassani, L. Chevalier, E. Lancon, J. Laporte, R. Nicolaidou, et al., *A muon identification and combined reconstruction procedure for the ATLAS detector at the LHC using the (MUONBOY, STACO, MuTag) reconstruction packages*, *Nucl.Instrum.Meth.* **A572** (2007) 77–79, [`doi: 10.1016/j.nima.2006.10.340`].

[98] N. Van Eldik, F. L. Linde, P. M. Kluit, and S. C. M. Bentvelsen, *The ATLAS muon spectrometer: calibration and pattern recognition.* . PhD thesis, Univ. Amsterdam, Amsterdam, 2007.

[99] M. Cacciari, G. P. Salam, and G. Soyez, *The anti-k(t) jet clustering algorithm*, *JHEP* **0804** (2008) 063, [`arXiv:0802.1189`], [`doi: 10.1088/1126-6708/2008/04/063`].

[100] S. D. Ellis and D. E. Soper, *Successive combination jet algorithm for hadron collisions*, *Phys.Rev.* **D48** (1993) 3160–3166, [`hep-ph/9305266`], [`doi: 10.1103/PhysRevD.48.3160`].

S. Catani, Y. Dokshitzer, and B. Webber, *The $k_\perp$-clustering algorithm for jets in deep inelastic scattering and hadron collisions*, *Physics Letters B* **285** (1992), no. 3 291 – 299, [`doi: 10.1016/0370-2693(92)91467-N`].

S. Catani, Y. L. Dokshitzer, M. Seymour, and B. Webber, *Longitudinally invariant K_t clustering algorithms for hadron hadron collisions*, *Nucl.Phys.* **B406** (1993) 187–224, [`doi: 10.1016/0550-3213(93)90166-M`].

[101] I. Antcheva, M. Ballintijn, B. Bellenot, M. Biskup, R. Brun, et al., *Root: A C++ framework for petabyte data storage, statistical analysis and visualization*, *Comput.Phys.Commun.* **180** (2009) 2499–2512, [`doi: 10.1016/j.cpc.2009.08.005`].

[102] L. Batkova, J. Meyer, and M. Verducci, *Preliminary studies of the heavy flavor estimation in the muon inclusive cross section at $\sqrt{s} = 7$ TeV at ATLAS*, *ATL-COM-PHYS-2010-997* (2010).

[103] T. Sjostrand, *High-energy physics event generation with PYTHIA 5.7 and JETSET 7.4*, *Comput.Phys.Commun.* **82** (1994) 74–90, [`doi: 10.1016/0010-4655(94)90132-5`].

[104] P. A. M. Eerola, *The inclusive muon cross-section in ATLAS*, *ATL-PHYS-98-120. ATL-GE-PN-120* (1998).

[105] ATLAS Collaboration, *Extraction of the prompt muon component in inclusive muons produced at $\sqrt{s} = 7$ TeV*, *ATLAS-CONF-2010-075* (2010).

[106] A. Favareto and A. Andreazza, *Measurement of the impact parameter resolution of charged particles: Plots for approval*, *ATL-COM-PHYS-2012-471* (2012).

[107] ATLAS Collaboration, *Performance of impact parameter-based b-tagging algorithms with the ATLAS detector using proton-proton collisions at $\sqrt{s} = 7$ TeV*, *ATLAS-CONF-2010-091* (2010).

[108] ATLAS Collaboration, *Performance of the atlas secondary vertex b-tagging algorithm in 7 tev collision data*, *ATLAS-CONF-2010-042* (2010).

[109] ATLAS Collaboration, *Soft muon tagging and D^*/μ correlations in 7 TeV collisions with ATLAS*, *ATLAS-CONF-2010-100* (2010).

[110] ATLAS Collaboration, *Calibrating the b-tag and mistag efficiencies of the SV0 b-tagging algorithm in 3 pb^{-1} of data with the ATLAS detector*, *ATLAS-CONF-2010-099* (2010).

ATLAS Collaboration, *b-Jet Tagging efficiency calibration using the System8 method*, *ATLAS-CONF-2011-143* (2011).

ATLAS Collaboration, *Measurement of the b-tag efficiency in a sample of jets containing muons with 5 fb^{-1} of data from the ATLAS detector*, *ATLAS-CONF-2012-043* (2012).

[111] ATLAS Collaboration, *Performance of the missing transverse energy reconstruction and calibration in proton-proton collisions at a center-of-mass energy of 7 TeV with the ATLAS detector*, *ATLAS-CONF-2010-057* (2010).

ATLAS Collaboration, *Data-quality requirements and event cleaning for jets and missing transverse energy reconstruction with the ATLAS detector in proton-proton collisions at a center-of-mass energy of $\sqrt{s} = 7$ TeV*, *ATLAS-CONF-2010-038* (2010).

[112] T. Sjostrand, S. Mrenna, and P. Z. Skands, *PYTHIA 6.4 physics and manual*, *JHEP* **0605** (2006) 026, [`hep-ph/0603175`], [`doi: 10.1088/1126-6708/2006/05/026`].

[113] A. Sherstnev and R. Thorne, *Parton distributions for LO generators*, *Eur.Phys.J.* **C55** (2008) 553–575, [`arXiv:0711.2473`], [`doi: 10.1140/epjc/s10052-008-0610-x`].

[114] W. Verkerke and D. P. Kirkby, *The RooFit toolkit for data modeling*, *eConf* **C0303241** (2003) MOLT007, [`physics/0306116`].

[115] ATLAS Collaboration, *Jet energy measurement with the ATLAS detector in proton-proton collisions at $\sqrt{s} = 7$ TeV*, `arXiv:1112.6426`.

[116] L. Batkova, J. Meyer, and M. Verducci, *Heavy flavor estimation in the muon inclusive production at $\sqrt{s} = 7$ TeV at ATLAS*, *ATL-COM-PHYS-2012-1519* (2012).

[117] A. Salvucci, *Measurement of muon momentum resolution of the ATLAS detector*, *European Physical Journal Web of Conferences* **28** (2012) 12039, [`arXiv:1201.4704`], [`doi: 10.1051/epjconf/20122812039`].

O. Kortner, E. Moyse, and A. Salvucci, *Muon resolution plots*, *ATL-COM-PHYS-2011-1504* (2011).

[118] C. Adorisio, G. Aielli, T. Alexopoulos, M. Alviggi, C. Amelung, et al., *Study of the ATLAS MDT spectrometer using high energy CERN combined test beam data*, *Nucl.Instrum.Meth.* **A598** (2009) 400–415, [`doi: 10.1016/j.nima.2008.09.031`].

[119] ATLAS Collaboration, *Expected performance of the ATLAS experiment - detector, trigger and physics*, `arXiv:0901.0512`.

M. Schott, G. Duckeck, and M. Obermaier, *Study of the sagitta resolution of MDT-chambers*, *ATL-MUON-PUB-2006-010. ATL-COM-MUON-2006-004* (2006).

[120] R. Gluckstern, *Uncertainties in track momentum and direction, due to multiple scattering and measurement errors*, *Nucl.Instrum.Meth.* **24** (1963) 381–389, [`doi: 10.1016/0029-554X(63)90347-1`].

[121] G. Avolio, F. Cerutti, E. Meoni, A. Policicchio, D. Rebuzzi, S. Rosati, and S. Ventura, *ATLAS muon barrel sagitta resolution versus momentum at 2004 H8 test beam and comparison with Geant4 simulation*, *ATL-MUON-PUB-2006-011. ATL-COM-MUON-2006-007* (2006).

[122] H. Bethe, *Moliere's theory of multiple scattering*, *Phys.Rev.* **89** (1953) 1256–1266, [`doi: 10.1103/PhysRev.89.1256`].

W. T. Scott, *The theory of small-angle multiple scattering of fast charged particles*, *Rev.Mod.Phys.* **35** (1963) 231–313, [`doi: 10.1103/RevModPhys.35.231`].

J. Motz, H. Olsen, and H. Koch, *Electron scattering without atomic or nuclear excitation*, *Rev.Mod.Phys.* **36** (1964) 881–928, [`doi: 10.1103/RevModPhys.36.881`].

[123] V. L. Highland, *Some practical remarks on multiple scattering*, *Nucl.Instrum.Meth.* **129** (1975) 497, [`doi: 10.1016/0029-554X(75)90743-0`].

V. L. Highland, *Erratum*, *Nuclear Instruments and Methods* **161** (1979), no. 1 171, [`doi: 10.1016/0029-554X(79)90379-3`].

G. R. Lynch and O. I. Dahl, *Approximations to multiple Coulomb scattering*, *Nucl.Instrum.Meth.* **B58** (1991) 6–10, [`doi: 10.1016/0168-583X(91)95671-Y`].

[124] ATLAS Collaboration, *Commissioning of the ATLAS muon spectrometer with cosmic rays*, *Eur.Phys.J.* **C70** (2010) 875–916, [`arXiv:1006.4384`], [`doi: 10.1140/epjc/s10052-010-1415-2`].

[125] ATLAS Collaboration, *Studies of the performance of the ATLAS detector using cosmic-ray muons*, *Eur.Phys.J.* **C71** (2011) 1593, [`arXiv:1011.6665`], [`doi: 10.1140/epjc/s10052-011-1593-6`].

[126] D. Adams, et al., *Track reconstruction in the ATLAS muon spectrometer with MOORE*, *ATL-SOFT-2003-007* (2003).

[127] L. Urban, *A model for multiple scattering in Geant4*, *CERN-OPEN-2006-077* (2006).

[128] H. Lewis, *Multiple scattering in an infinite medium*, *Phys.Rev.* **78** (1950) 526–529, [`doi: 10.1103/PhysRev.78.526`].

[129] G. Wentzel, *Zwei Bemerkungen über die Zerstreuung korpuskularer Strahlen als Beugungserscheinung*, *Zeitschrift für Physik - A Hadrons and Nuclei* **40** (1926) 590–593, [`doi: 10.1007/BF01390457`].

[130] A. Butkevich, R. Kokoulin, G. Matushko, and S. Mikheyev, *Comments on multiple scattering of high-energy muons in thick layers*, *Nucl.Instrum.Meth.* **A488** (2002) 282–294, [`hep-ph/0108016`], [`doi: 10.1016/S0168-9002(02)00478-3`].

[131] M. Smizanska, S. Baranov, J. Hrivnác, and E. Kneringer, *Overview of Monte Carlo simulations for ATLAS B-physics in the period 1996-1999*, *ATL-PHYS-2000-025, ATL-COM-PHYS-99-042, ATL-COM-PHYS-2000-007, CERN-ATL-PHYS-2000-025.*

ATLAS Collaboration, *Physics analysis tools for beauty physics in ATLAS*, *J.Phys.Conf.Ser.* **119** (2008) 032003, [`doi: 10.1088/1742-6596/119/3/032003`].

[132] G. Corcella, I. Knowles, G. Marchesini, S. Moretti, K. Odagiri, et al., *HERWIG 6.5 release note*, `hep-ph/0210213`.

[133] R. K. Ellis, W. J. Stirling, and B. Webber, *QCD and collider physics*, *Camb.Monogr.Part.Phys.Nucl.Phys.Cosmol.* **8** (1996) 1–435.

[134] K. Bachas and N. Benekos, *Z mass resolution studies using muons in* $|\eta| > 2.5$, *ATL-MUON-INT-2012-001* (2012).

[135] ATLAS Collaboration, *Determination of the muon reconstruction efficiency in ATLAS at the Z resonance in proton-proton collisons at* $\sqrt{s} = 7$ *TeV*, *ATLAS-CONF-2011-008* (2011).

[136] O. Kortner and E. Moyse, *Pile-up depedence of the ATLAS muon performance*, *ATL-COM-PHYS-2011-1640* (2011).

O. Kortner, A. Manfredini, and E. Moyse, *Pile-up effects on muon isolation variables in 2011 data*, *ATL-COM-PHYS-2011-1503* (2011).

[137] B. Lenzi and R. Nicolaidou, *Studies of muon energy loss and isolation in ATLAS calorimeters using cosmic-ray data*, *ATL-COM-PHYS-2010-073* (2010).

[138] ATLAS Collaboration, *Muon performance in minimum bias pp collision data at* $\sqrt{s} = 7$ *TeV with ATLAS*, *ATLAS-CONF-2010-036* (2010).

[139] B. Lenzi, R. Nicolaidou, and S. Hassani, *Developments on the software package for calorimetric isolation and energy loss measurements for muons in ATLAS*, *ATL-SOFT-INT-2009-002* (2009).

[140] ATLAS Collaboration, *Search for the Standard Model Higgs boson in the decay channel* $H \to ZZ(*) \to 4\ell$ *with* 4.8 *fb*$^{-1}$ *of pp collision data at* $\sqrt{s} = 7$ *TeV with ATLAS*, *Phys.Lett.* **B710** (2012) 383–402, [`arXiv:1202.1415`], [`doi: 10.1016/j.physletb.2012.03.005`].

[141] J. M. Campbell, R. K. Ellis, and C. Williams, *Vector boson pair production at the LHC*, *JHEP* **1107** (2011) 018, [`arXiv:1105.0020`], [`doi: 10.1007/JHEP07(2011)018`].

[142] G. Gounaris, J. Layssac, and F. Renard, *New and standard physics contributions to anomalous Z and gamma selfcouplings*, *Phys.Rev.* **D62** (2000) 073013, [`hep-ph/0003143`], [`doi: 10.1103/PhysRevD.62.073013`].

[143] K. Bachas, et al., *Measurement of the ZZ production cross section in proton-proton collisions at* $\sqrt{s} = 7$ *TeV with the ATLAS detector*, *ATL-COM-PHYS-2012-186* (2012).

[144] D0 Collaboration, *Search for doubly-charged Higgs boson pair production in* $p\bar{p}$ *collisions at* $\sqrt{s} = 1.96$ *TeV*, *Phys.Rev.Lett.* **108** (2012) 021801, [`arXiv:1106.4250`], [`doi: 10.1103/PhysRevLett.108.021801`].

N. Arkani-Hamed, A. Cohen, E. Katz, A. Nelson, T. Gregoire, et al., *The minimal moose for a little Higgs*, *JHEP* **0208** (2002) 021, [`hep-ph/0206020`].

R. N. Mohapatra and G. Senjanović, *Neutrino masses and mixings in gauge models with spontaneous parity violation*, *Phys. Rev. D* **23** (1981) 165–180, [`doi: 10.1103/PhysRevD.23.165`].

J. Gunion, J. Grifols, A. Mendez, B. Kayser, and F. I. Olness, *Higgs bosons in left-right symmetric models*, *Phys.Rev.* **D40** (1989) 1546, [`doi: 10.1103/PhysRevD.40.1546`].

N. Deshpande, J. Gunion, B. Kayser, and F. I. Olness, *Left-right symmetric electroweak models with triplet Higgs*, *Phys.Rev.* **D44** (1991) 837–858, [`doi: 10.1103/PhysRevD.44.837`].

J. Cieza Montalvo, N. V. Cortez, J. Sa Borges, and M. D. Tonasse, *Searching for doubly charged Higgs bosons at the LHC in a 3-3-1 model*, *Nucl.Phys.* **B756** (2006) 1–15, [`hep-ph/0606243`], [`doi: 10.1016/j.nuclphysb.2006.08.013`].

J. C. Montalvo, J. S. Borges, N. V. C. Jr., and M. Tonasse, *Erratum to: "Searching for doubly charged Higgs bosons at the LHC in a 3-3-1 model" [Nucl. Phys. B 756 (1-2) (2006) 1-15]*, *Nuclear Physics B* **796** (2008), no. 1-2 422 – 423, [`doi: 10.1016/j.nuclphysb.2008.01.003`].

[145] P. K. Das, *Neutral Z boson pair production due to radion resonance in the Randall-Sundrum model: Prospects at the CERN LHC*, *Phys.Rev.* **D72** (2005) 055009, [`hep-ph/0508103`], [`doi: 10.1103/PhysRevD.72.055009`].

[146] S. Bar-Shalom, G. Eilam, and B. Mele, *Sneutrino-Higgs mixing in WW and ZZ production in supersymmetry with R-parity violation*, *Phys.Lett.* **B500** (2001) 297–303, [`hep-ph/0005295`], [`doi: 10.1016/S0370-2693(01)00076-4`].

[147] L3 Collaboration, *Study of Z boson pair production in e^+e^- collisions at LEP at $\sqrt{s} =$ 189-GeV*, *Phys.Lett.* **B465** (1999) 363–375, [`hep-ex/9909043`], [`doi: 10.1016/S0370-2693(99)01065-5`].

[148] OPAL Collaboration, *Study of Z pair production and anomalous couplings in e^+e^- collisions at $\sqrt{s}$ between* 190-GeV *and* 209-GeV, *Eur.Phys.J.* **C32** (2003) 303–322, [`hep-ex/0310013`], [`doi: 10.1140/epjc/s2003-01467-x`].

[149] ALEPH Collaboration, *Measurement of the $e^+e^- \to ZZ$ production cross-section at center-of-mass energies of* 183-GeV *and* 189-GeV, *Phys.Lett.* **B469** (1999) 287–302, [`hep-ex/9911003`], [`doi: 10.1016/S0370-2693(99)01288-5`].

[150] DELPHI Collaboration, *ZZ production in e^+e^- interactions at $\sqrt{s} =$ 183-GeV to* 209-GeV, *Eur.Phys.J.* **C30** (2003) 447–466, [`hep-ex/0307050`], [`doi: 10.1140/epjc/s2003-01287-0`].

[151] The LEP collaborations ALEPH, DELPHI, L3, OPAL, and the LEP Electroweak Working Group, *A combination of preliminary electroweak measurements and constraints on the standard model*, `hep-ex/0612034`.

[152] The LEP collaborations ALEPH, DELPHI, L3, OPAL, and the LEP Working Group for Higgs boson searches, *Search for the Standard Model Higgs boson at LEP*, *Phys.Lett.* **B565** (2003) 61–75, [`hep-ex/0306033`], [`doi: 10.1016/S0370-2693(03)00614-2`].

[153] D0 Collaboration, *Observation of ZZ production in $p\bar{p}$ collisions at $\sqrt{s} = 1.96$-TeV*, *Phys.Rev.Lett.* **101** (2008) 171803, [`arXiv:0808.0703`], [`doi: 10.1103/PhysRevLett.101.171803`].

[154] D0 Collaboration, *Search for ZZ and $Z\gamma^*$ production in $p\bar{p}$ collisions at $\sqrt{s} = 1.96$ TeV and limits on anomalous ZZZ and $ZZ\gamma^*$ couplings*, *Phys.Rev.Lett.* **100** (2008) 131801, [`arXiv:0712.0599`], [`doi: 10.1103/PhysRevLett.100.131801`].

[155] ATLAS Collaboration, *Measurement of the ZZ production cross section and limits on anomalous neutral triple gauge couplings in proton-proton collisions at $\sqrt{s} = 7$ TeV with the ATLAS detector*, *Phys.Rev.Lett.* **108** (2012) 041804, [`arXiv:1110.5016`], [`doi: 10.1103/PhysRevLett.108.041804`].

[156] CMS Collaboration, *Measurement of the WW, WZ and ZZ cross sections at CMS*, *CMS-PAS-EWK-11-010* (2011).

[157] S. Alioli, P. Nason, C. Oleari, and E. Re, *A general framework for implementing NLO calculations in shower Monte Carlo programs: the POWHEG BOX*, *JHEP* **1006** (2010) 043, [`arXiv:1002.2581`], [`doi: 10.1007/JHEP06(2010)043`].

T. Melia, P. Nason, R. Rontsch, and G. Zanderighi, *W^+W^-, WZ and ZZ production in the POWHEG BOX*, *JHEP* **1111** (2011) 078, [`arXiv:1107.5051`], [`doi: 10.1007/JHEP11(2011)078`].

[158] T. Binoth, N. Kauer, and P. Mertsch, *Gluon-induced QCD corrections to $pp \to ZZ \to \ell\bar{\ell}\ell'\bar{\ell}'$*, `arXiv:0807.0024`.

[159] J. Butterworth, et al., *Single boson and diboson production cross sections in pp collisions at $\sqrt{s} = 7$ TeV*, *ATL-COM-PHYS-2010-695* (2010).

[160] J. Alwall, P. Demin, S. de Visscher, R. Frederix, M. Herquet, et al., *MadGraph/MadEvent v4: The new web generation*, *JHEP* **0709** (2007) 028, [`arXiv:0706.2334`], [`doi: 10.1088/1126-6708/2007/09/028`].

[161] ATLAS Collaboration, *Reconstruction and calibration of missing transverse energy and performance in Z and W events in ATLAS proton-proton collisions at 7 TeV*, *ATLAS-CONF-2011-080* (2011).

[162] G. Ordonez Sanz, *Muon identification in the ATLAS calorimeters.* PhD thesis, Nijmegen, U., Amsterdam, 2009.

[163] ATLAS Collaboration, *Measurement of the $W \to \ell\nu$ and $Z/\gamma^* \to \ell\ell$ production cross sections in proton-proton collisions at $\sqrt{s} = 7$ TeV with the ATLAS detector*, *JHEP* **1012** (2010) 060, [`arXiv:1010.2130`], [`doi: 10.1007/JHEP12(2010)060`].

ATLAS Collaboration, *Muon reconstruction efficiency in reprocessed 2010 LHC proton-proton collision data recorded with the ATLAS detector*, *ATLAS-CONF-2011-063* (2011).

N. Benekos, et al., *Measurement of the ZZ production cross section and limits on anomalous neutral triple gauge couplings in proton-proton collisions at $\sqrt{s} = 7$ TeV with the ATLAS detector*, *ATL-PHYS-INT-2012-021* (2012).

[164] T. Alexopoulos, et al., *Search for the Standard Model Higgs boson in the decay channel* $H \to ZZ^{(*)} \to 4\ell$ *with* $4.8\ fb^{-1}$ *of pp collisions at* $\sqrt{s} = 7\ TeV$, *ATL-COM-PHYS-2011-1715* (2011).

[165] ATLAS Collaboration, *Measurement of the total* ZZ *production cross section in the four-lepton channel with* $4.7\ fb^{-1}$ *of ATLAS data*, *ATLAS-CONF-2012-026* (2012).

[166] ATLAS Collaboration, *Measurement of the* ZZ *production cross section in the* $\ell\ell\nu\nu$ *channel in proton-proton collisions at* $\sqrt{s} = 7\ TeV$ *with the ATLAS detector*, *ATLAS-CONF-2012-027* (2012).

[167] K. Hagiwara, R. Peccei, D. Zeppenfeld, and K. Hikasa, *Probing the weak boson sector in* $e^+e^- \to W^+W^-$, *Nucl.Phys.* **B282** (1987) 253, [`doi: 10.1016/0550-3213(87)90685-7`].

G. Gounaris, J. Layssac, and F. Renard, *Signatures of the anomalous* $Z\gamma$ *and* ZZ *production at the lepton and hadron colliders*, *Phys.Rev.* **D61** (2000) 073013, [`hep-ph/9910395`], [`doi: 10.1103/PhysRevD.61.073013`].

G. Gounaris, J. Layssac, and F. Renard, *Off-shell structure of the anomalous* Z *and* γ *selfcouplings*, *Phys.Rev.* **D62** (2000) 073012, [`hep-ph/0005269`], [`doi: 10.1103/PhysRevD.62.073012`].

[168] U. Baur and D. L. Rainwater, *Probing neutral gauge boson selfinteractions in* ZZ *production at hadron colliders*, *Phys.Rev.* **D62** (2000) 113011, [`hep-ph/0008063`], [`doi: 10.1103/PhysRevD.62.113011`].

U. Baur, T. Han, and J. Ohnemus, WZ *production at hadron colliders: Effects of nonstandard* WWZ *couplings and QCD corrections*, *Phys.Rev.* **D51** (1995) 3381–3407, [`hep-ph/9410266`], [`doi: 10.1103/PhysRevD.51.3381`].

[169] U. Baur, T. Han, and J. Ohnemus, *QCD corrections and anomalous couplings in* $Z\gamma$ *production at hadron colliders*, *Phys.Rev.* **D57** (1998) 2823–2836, [`hep-ph/9710416`], [`doi: 10.1103/PhysRevD.57.2823`].

[170] ATLAS Collaboration, *Observation of an excess of events in the search for the Standard Model Higgs boson in the* $H \to ZZ^{(*)} \to 4\ell$ *channel with the ATLAS detector.*, *ATLAS-CONF-2012-092* (2012).

[171] ATLAS Collaboration, *Observation of a new particle in the search for the Standard Model Higgs boson with the ATLAS detector at the LHC*, *Phys.Lett.* **B716** (2012) 1–29, [`arXiv:1207.7214`], [`doi: 10.1016/j.physletb.2012.08.020`].

[172] CMS Collaboration, *Observation of a new boson at a mass of* 125 *GeV with the CMS experiment at the LHC*, *Phys.Lett.* **B716** (2012) 30–61, [`arXiv:1207.7235`], [`doi: 10.1016/j.physletb.2012.08.021`].

[173] ATLAS Collaboration, *Combined muon performance public results*, *https://twiki.cern.ch/twiki/bin/view/AtlasPublic/MuonPerformancePublicPlots*.